UNIVERSITÀ
DEGLI STUDI
DI TRIESTE

UNIVERSITÀ DEGLI STUDI DI TRIESTE

XXXVIII CICLO DEL DOTTORATO DI RICERCA IN FISICA

Characterisation and simulation of 65 nm CMOS imaging process Monolithic Active Pixel silicon Sensors for the ALICE ITS3 Upgrade

Settore scientifico-disciplinare: FIS/01

Dottoranda:
Anna Villani

Coordinatore:
Prof. Francesco Longo

Supervisore di tesi:
Prof. Giacomo Contin

Co-supervisore di tesi:
Prof. Paolo Camerini

ANNO ACCADEMICO 2024/2025

Abstract

The ALICE experiment at the CERN Large Hadron Collider (LHC) is designed to study strongly interacting matter, in particular the quark-gluon plasma (QGP), created at the extreme temperatures achieved in high-energy heavy-ion collisions. During the LHC Long Shutdown 2 (2018-2022), ALICE underwent a major upgrade of several of its detectors, enabling the reconstruction of rare physics channels that were previously inaccessible. The upgraded Inner Tracking System (ITS2) plays a central role in ALICE, providing the precise reconstruction of primary and secondary decay vertices and enabling accurate particle tracking close to the interaction point. The ITS2 consists of seven concentric layers of Monolithic Active Pixel Sensors (MAPS), with a total of roughly 12.5 billion pixels covering an active area of about $10\,\mathrm{m}^2$, representing the largest application of MAPS ever realised.

During the next LHC long shutdown (2026-2029), the ITS2 is scheduled to undergo an additional upgrade in preparation for LHC Run 4 (2029-2032), replacing its three innermost layers with a new fully cylindrical vertex detector, the ITS3. Such an innovative tracker will consist of two half-barrels, each featuring three self-supporting semi-cylindrical layers built from large-area, ultra-thin (50 µm) bent MAPS fabricated in a 65 nm CMOS process. By minimizing mechanical supports and eliminating cooling structures and material for power and data transmission, the ITS3 will reach an unprecedentedly low material budget of 0.09% X_0 per layer. Together with a reduced beam-pipe radius and the placement of the innermost layer at 19 mm from the interaction point, this design will significantly improve pointing resolution and tracking efficiency, especially for low-momentum particles. This will enhance precision measurements in the heavy-flavour sector, enabling the reconstruction of B_s^0, Λ_b^0, non-prompt D_s^+ and Ξ_c^+ decays, improving the study of low-mass di-electrons by reducing background, and potentially allowing for the direct tracking of charged strange baryons to reconstruct weakly decaying strange particles with novel techniques.

The wafer-scale sensors developed for ITS3 represents a major technological breakthrough in detector technology, made possible by stitched-circuit manufacturing and the 65 nm CMOS process. This thesis is part of the extensive characterisation campaign which has been planned for the ITS3 sensor prototypes. Specifically it is focused on the full characterisation of the Digital Pixel Test Structure (DPTS), designed to validate the 65 nm CMOS process, and the MOnolithic Stitched Sensor (MOSS), developed to demonstrate the stitching technology and evaluate the performance of different pixel and logic solutions in view of the final sensor design.

This thesis is structured as follows. The physics of heavy-ion collisions and the signatures of the quark-gluon plasma are first introduced, followed by a description of the ALICE apparatus, with particular emphasis on the ITS2 characteristics and the motivations for its upgrade. In particular, the expected performance improvements in

the measurements of Λ_c and thermal di-electrons are presented to illustrate the impact of the ITS3 upgrade.

A description of the ITS3 layout follows, including a general overview of the MAPS sensor and a detailed presentation of the prototypes characterised in this work. The main characterisation tests are discussed, and the procedure used to determine the optimal operating conditions of the sensors is outlined. Finally, results from in-beam measurements are presented to demonstrate the radiation tolerance of the ITS3 prototypes.

An extensive study of the noise sources in the prototypes was carried out to identify their origin and, where possible, reduce them in the final sensor. In fact, electronic noise, defined as the random output signal in the absence of incident particles, sets the lower bound for the detectable signal and affects both the detection efficiency and the energy resolution. Therefore, a thorough understanding of its underlying sources is crucial to minimise it and optimise the sensor performance. A thermal model was proposed to explain part of the observed noise, and additional frequency-dependent contributions were identified, one of which will be addressed in the final design.

The energy response of the DPTS was investigated using X-rays of well-defined energy. The measured spectra were analysed by evaluating the peak characteristics, such as the mean value and the energy resolution. This comprehensive study, including energy calibration up to high energies, provides both a strengthened characterisation of the prototypes for the ITS3 and an evaluation of their potential for applications beyond their intended use.

Finally, TCAD simulations were performed to model the electric field inside the pixels, analyse the charge collection properties of the ITS3 sensor, and explore its potential for energy-loss measurements using Garfield simulations. This approach also provided a validation of the results previously obtained in energy-loss studies.

Contents

Chapter 1

The physics of heavy-ion collisions

The Standard Model of particle physics is a theory that describes the electromagnetic, weak and strong forces. Through the mathematical language of quantum field theory, allows for quantitative predictions of phenomena involving elementary particles. Quantum Chromodynamics (QCD) [1] is a gauge field theory of the Standard model describing the strong interaction. QCD predicts a deconfined phase of strongly interacting matter arising at high temperatures and densities, the Quark-Gluon Plasma (QGP). According to the Big Bang cosmological theory, the early Universe existed in such a state. The relativistic heavy-ion collisions provided by the Large Hadron Collider (LHC) of the European Organization for Nuclear Research (CERN) are used as a tool to create and study the quark-gluon plasma. ALICE [2] is an experiment dedicated to the study of the heavy-ion and proton collisions that are provided by the LHC, specifically designed for the study of the quark-gluon plasma. ALICE performs particle identification and tracking through several detectors, among which the most important to study low momentum particles is the Inner Tracking System (ITS), which is the closest to the Interaction Point (IP). The currently-installed ITS, named ITS2, is composed by seven concentric approximately-cylindrical layers based entirely on silicon Monolithic Active Pixel Sensors (MAPS). ITS2 replaced the old ITS during the LHC Long Shutdown 2, LS2 (2018-22). Another upgrade is planned in the period 2026-2029 (LS3), that will replace the three innermost layers of ITS2 with a fully-cylindrical bent-silicon tracker, the ITS3.

The quark-gluon plasma formation in heavy-ion collisions is discussed in this chapter, with a description of the observables that can be measured to study its properties. A description of the ALICE experiment is also provided, focusing on the current ITS2. Finally, the improvements in the physics performance expected after the installation of the new tracker, the ITS3, are outlined.

1.1 The Quark Gluon Plasma

The quark-gluon plasma is a state of matter predicted by the QCD, existing at extremely high temperatures and densities, composed of quarks and gluons which are de-confined instead of being bound inside hadrons. Ultra-relativistic heavy-ion collisions are used to create the QGP in the laboratory.

1.1.1 The QCD phase transition

Asymptotic freedom is a distinctive feature of QCD which results in a dependence of the coupling constant α_S of the strong interaction on the momentum exchange between quarks and gluons. The interaction of such partons, is becoming weaker when their momentum exchange Q^2 increases, as shown in fig. 1.1. A perturbative approach (pQCD) can be used to investigate processes occurring at large momentum transfers ($Q > 100\,\text{GeV}$), where α_S is small ($\sim$0.1). Asymptotic freedom [4, 5] is observed in this regime, meaning that quarks can be treated as free particles instead of strongly bound inside the hadrons. Lattice QCD and Effective Field Theories can be used to describe the non-perturbative regime, which holds for low-momentum processes ($Q \sim 1\,\text{GeV}$) where the coupling constant becomes large ($\mathcal{O}(1)$). Such regime is characterised by the confinement [6], meaning that colour singlets quarks and gluons cannot be isolated and therefore observed directly, only colourless hadrons can be detected.

The QCD predicts a transition from the hadron gas phase, which is characterised by the confinement of quarks and gluons inside hadrons, to a state where quarks and gluons are deconfined: the quark-gluon plasma [7]. This transition is represented by the three-phase diagram of strongly-interacting matter shown in fig. 1.2 as a function of the temperature T and of the baryochemical potential μ_B. μ_B is proportional to the net baryon density of the system, and is equal to the energy needed to increase the baryon number of the system by one unit at fixed volume and entropy. The QCD vacuum is characterised by $T = \mu_B = 0\,\text{MeV}$, while the ordinary nuclear matter is characterised by $T = 0$ and $\mu_B = \sim 900\,\text{MeV}$. The QCD medium with $\mu_B = 0\,\text{MeV}$ corresponds to the situation of the early universe, where a smooth evolution of the system from an

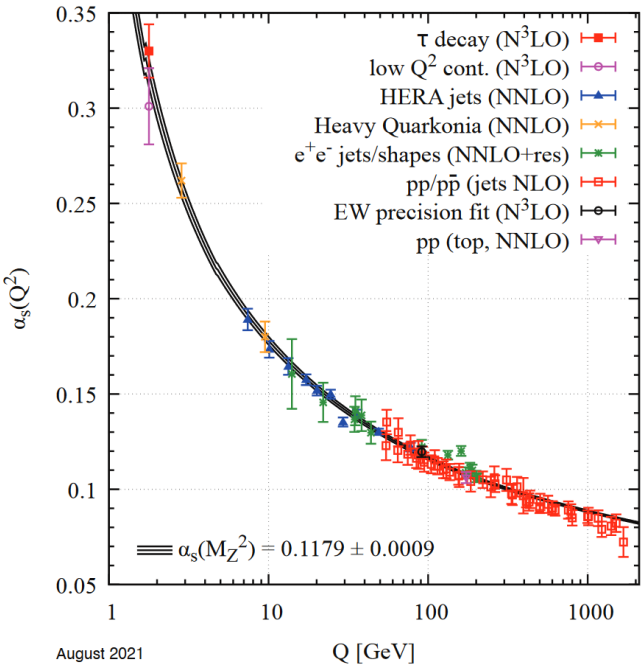

Figure 1.1: Measurements of the coupling constant α_S of the strong interaction as a function of the energy scale Q. Different measurements used to extract the α_S values are indicated by different colours. The respective degree of QCD perturbation theory used in the extraction of the constant is indicated in brackets. Figure taken from [3].

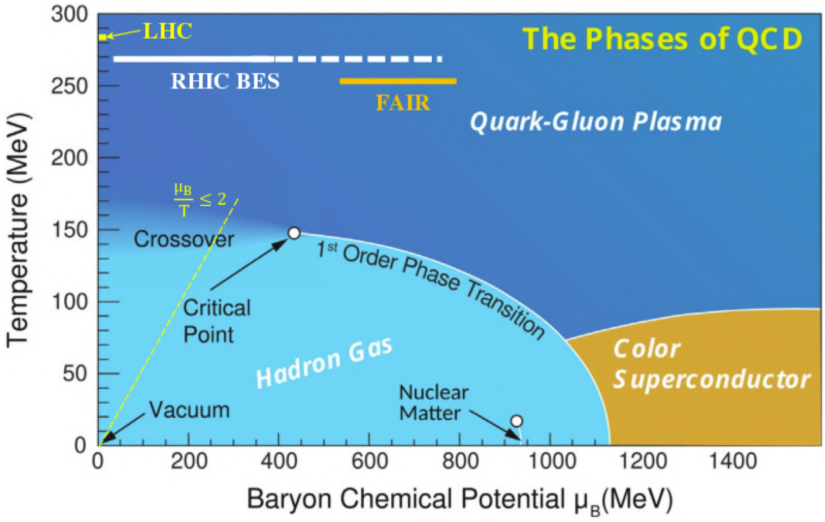

Figure 1.2: The phase diagram of QCD. Hadrons are dissolved into their quark constituents by increasing density and/or energy. The range of μ_B probed by different accelerator facilities is indicated on the top left.

hadronic state to the quark-gluon plasma occurs when the temperature is increased up to a critical value of $T_c = (156.5 \pm 1.5)$ MeV [8]. Similarly, the creation of the QGP may occur at large baryon density and low temperature, corresponding to the state in the core of the neutron stars [9].

The region of the QCD diagram at $\mu_B \approx 0$ is studied with heavy-ion collisions at the very high LHC centre-of-mass energies ($\sqrt{s_{NN}} \sim 5\,\text{TeV}$), while the RHIC BES-II programme [10] has recently investigated the phase transition region at higher μ_B using lower centre-of-mass energies. Such phase space diagram region will be probed by forthcoming experiments at the NICA [11, 12], FAIR [13] and SPS [14] facilities.

1.1.2 The space-time evolution of a heavy-ion collision

The evolution of a heavy-ion collision can be described as a sequence of stages, which are depicted in fig. 1.3 and described in detail in the following [15, 16, 17].

1. **Initial state:** the two nuclei are ultra-relativistically accelerated and are Lorentz contracted in the beam direction by a factor γ, which for Pb nuclei accelerated by the LHC at $\sqrt{s_{NN}} = 5.02\,\text{TeV}$ is approximately 2500. The collision takes place at the time $t = 0\,\text{fm}/c$. The distance between the centres of the two colliding nuclei is the impact parameter b, which is inversely proportional to the number of nucleons in the nuclei which participate in an inelastic interaction. The nucleons not participating in the collision, i.e. the spectator nucleons, continue travelling along the beam direction (fig. 1.4).

2. **Pre-equilibrium phase:** a weakly coupled pre-equilibrium stage is observed right after the collision for $t < 1\,\text{fm}/c$. Most of the interactions in the collision involve little transverse momentum transfer and thus are called *soft* interactions. They determine the initial density profile of the system, which is characterised by a lumpiness due to the nuclear fluctuations inside the incident nuclei. A minimal fraction of the incident partons undergoes hard perturbative interactions, which

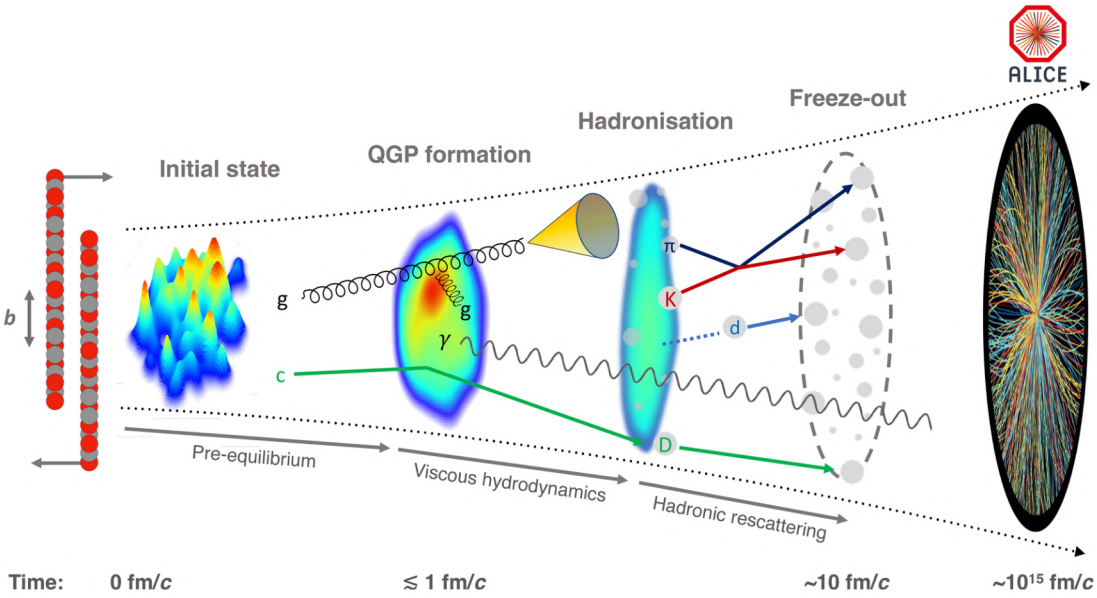

Figure 1.3: Stages of the evolution of a heavy-ion collision, from the projectiles to the production of hadrons, which are then detected. Figure from [18].

lead to the production of high momentum quarks and gluons as well as heavy quarks, such as the charm and the bottom quarks.

3. **QGP formation:** the system starts to thermalise and if the energy density and the temperature are sufficiently high, the quarks and gluons produced in the collisions form a collective medium that expands and flows as a relativistic hydrodynamic fluid, the quark-gluon plasma. The average energy density of the system, which is estimated for head-on LHC collisions with $\sqrt{s_{\mathrm{NN}}} = 2.76\,\mathrm{TeV}$, is of $12\,\mathrm{GeV/fm^3}$ [16], about twenty times the energy density of a hadron. It is comparable with the value of $12.7\,\mathrm{GeV/fm^3}$, expected from QCD lattice calculations for QGP matter in thermal equilibrium at a temperature of 300 MeV [19]. Hydrodynamic simulations show that the initial temperature of the quark-gluon plasma exceeds 450 MeV at the LHC energies [17]. As the quark-gluon plasma expands under pressure-driven forces, high momentum partons interact with it, loosing energy and offering information on the opaqueness of the quark-gluon plasma. The second stage in fig. 1.3 shows a radiative interaction of a high-momentum gluon with the quark-gluon plasma and an elastic interaction of a charm quark.

4. **Hadronisation:** a phase transition from the quark-gluon plasma to a hadron gas occurs when the medium cools down below the critical temperature value $\mathrm{T_C} = (156.5 \pm 1.5)$ MeV. Partons at lower momenta can combine into hadrons via coalescence, while high energy partons hadronise into collimated particle showers named jets, as can happen in elementary collisions.

5. **Chemical freeze-out:** inelastic interactions among hadrons cease at the chemical freeze-out temperature T_{chem}, fixing the particle yields. Statistical hadronisation models allow to extract T_{chem} from the hadron yields. Fig. 1.5 shows the fit results of different thermal model implementations on the yields of hadrons containing only light quarks measured in central (0-10%) Pb-Pb collisions at

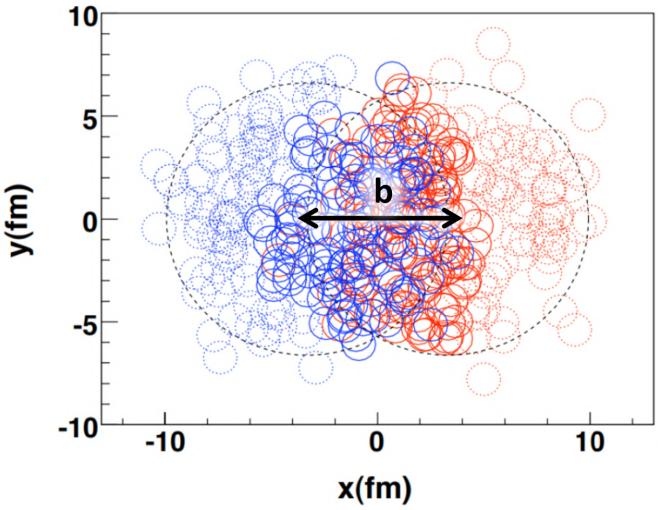

Figure 1.4: Example of a lead-lead collision at LHC with an impact parameter b of 7 fm. The nucleons of the two lead nuclei are represented in different colours. Solid line shows the participant nucleons, while dashed lines indicate the spectators. Figure from [16].

$\sqrt{s_{\mathrm{NN}}} = 2.76$ TeV. The obtained T_{chem} temperature is 156 MeV, comparable to the critical temperature $\mathrm{T_C} = (156.5 \pm 1.5)$ MeV for the transition between the quark-gluon plasma and the hadron gas at $\mu_{\mathrm{B}} = 0$.

6. **Kinetic freeze-out:** after 10 fm/c the kinetic freeze-out temperature T_{kin} is reached and the elastic interactions of hadrons stop. From that moment, the particle momenta are fixed and the hadrons travel until they reach the detector, where they are measured approximately 10^{15} fm/c after the collision.

LHC provides an unprecedented opportunity to study the hottest, densest, and longest ever lived quark-gluon plasma in the laboratory. The centre of mass energy per nucleon pair of $\sqrt{s_{\mathrm{NN}}} = 2.76$ TeV achieved in Pb-Pb collisions at the LHC, is so far the highest energy ever reached.

1.1.3 The QGP signatures

The quark-gluon plasma cannot be directly observed, as its life-time is of few fm/c. Physical quantities that have varying sensitivities to each phase of the quark-gluon plasma evolution are measured to study the quark-gluon plasma properties. The main known experimental probes are described in the following paragraphs.

1.1.3.1 Charged particle multiplicity

The charged particle multiplicity provides information on the centrality of the collision in the initial state. The centrality is defined based on the impact parameter b, when b is close to zero the collision is *central* and more particles are produced, when b is approximately two times the radius of the incident nuclei the collision is *peripheral* and fewer particles are produced. In the ALICE experiment during Runs 1 and 2,

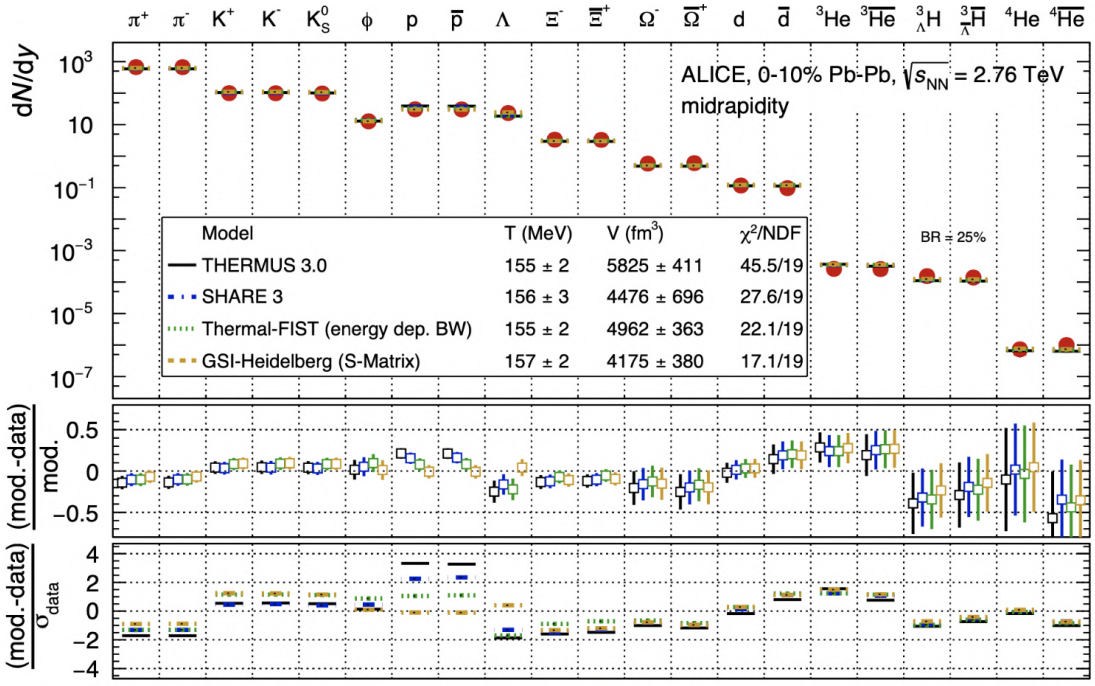

Figure 1.5: Yields of hadrons containing only light quarks measured in central (0-10%) Pb-Pb collisions at $\sqrt{s_{\rm NN}}$ = 2.76 TeV and results of four thermal model implementations (THERMUS [20], SHARE [21], Thermal-FIST [22] and GSI-Heidelberg [23]). The models contains three main parameters, the freeze-out temperature T_{chem}, the baryochemical potential $\mu_{\rm B}$ and the volume of the hadron gas V. Figure from [18].

the multiplicity of particles produced at forward rapidity[1] was measured with the V0 detector [24], which was composed by two array of scintillation counters placed on opposite sides of the collision point. The V0 signal amplitude distribution, proportional to the multiplicity, is used to define the centrality classes, as shown in fig. 1.6. The percentage of the total hadronic interaction cross section defines the centrality class. The signal distribution is fitted with the Glauber model [25], that allows for the extraction of the number of participants N_{part} and the number of binary collisions N_{coll} for each centrality class.

Figs. 1.7a and 1.7b show the average multiplicity of charged particles produced at midrapidity ($|\eta| < 0.5$) divided by the average number of participant nucleon pairs $\frac{2}{\langle N_{part}\rangle}\langle dN/d\eta\rangle_{|\eta|<0.5}$ as a function of $\langle N_{part}\rangle$ and $\sqrt{s_{\rm NN}}$ respectively. Data from A-A, pp and p-A collisions can be compared. Heavy-ion collisions show the largest values at the same $\sqrt{s_{\rm NN}}$, while the trend for pp and p-A is the same. Thus indicating that the more efficient particle production in A-A collisions is not due only to the multiple collisions of the participant nucleons, as this is true for protons in p-A collisions as well.

[1]The rapidity y for a particle with an energy E and longitudinal momentum p_z is defined as $y = 0.5\ \ln[(\mathrm{E} + p_z)/(\mathrm{E} - p_z)]$. In the relativistic limit, where the particle mass is small compared to its momentum, the rapidity can be approximated by the pseudorapidity η, which is defined as $\eta = -\ln(\tan(\theta/2))$, where θ is the polar angle of the particle in the reference frame whose z axis lies along the beam direction.

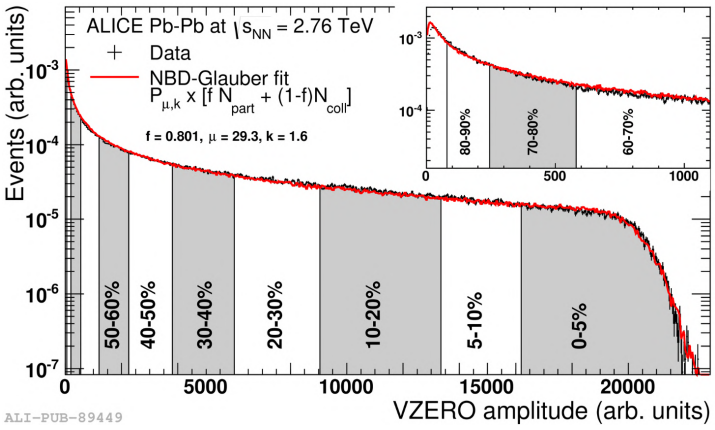

Figure 1.6: V0 signal amplitude distribution measured in Pb-Pb collisions at $\sqrt{s_{\mathrm{NN}}} = 2.76\,\mathrm{TeV}$ with centrality class definition. The Glauber model is used to fit the data. Figure from [26].

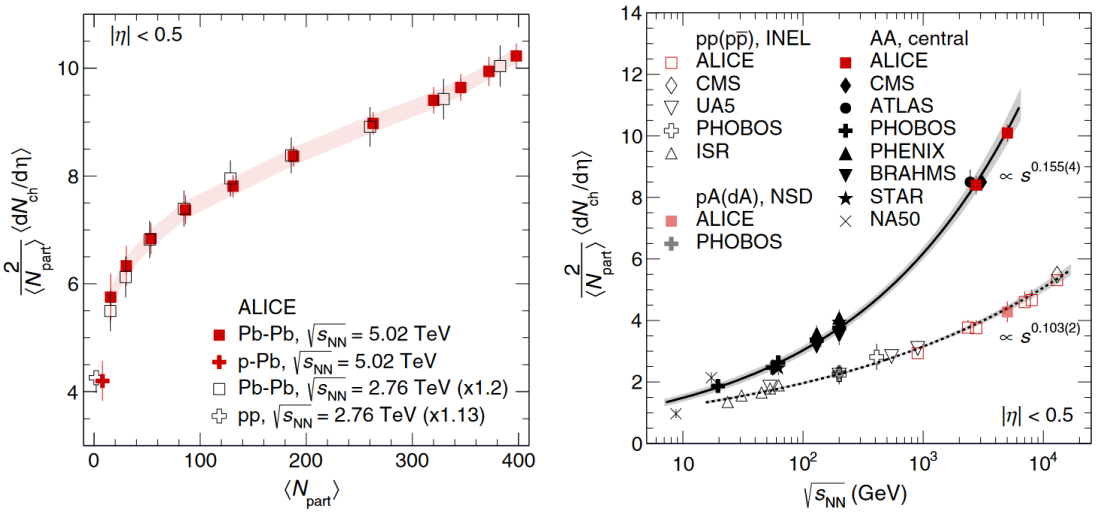

(a) (b)

Figure 1.7: Multiplicity of charged particles produced at midrapidity divided by the average number of participant nucleon pairs $\frac{2}{\langle N_{part}\rangle}\langle dN/d\eta\rangle_{|\eta|<0.5}$ as a function of $\langle N_{part}\rangle$ (a) and $\sqrt{s_{\mathrm{NN}}}$ (b). Results for A-A, p-A and pp collisions are compared. Figures from [27].

1.1.3.2 Collective flow

The collective flow is an observable that provides information about the evolution of the collision system. The collective motion of the particles produced in these collisions reflects the pressure-driven expansion of the quark-gluon plasma and is seen as a correlation between particles momenta. It has a radial and an anisotropic component [28]. The radial flow characterises central collisions, where the azimuthal symmetry of the initial system causes an isotropic azimuthal distribution of the final particles. Such effect can be quantified by measuring the mean transverse momentum $\langle p_{\mathrm{T}}\rangle$ distribution of identified particles, shown in fig. 1.8 for central (0-5%) and peripheral (80-90%) Pb-Pb collisions at $\sqrt{s_{\mathrm{NN}}} = 2.76\,\mathrm{TeV}$. The radial flow causes an increase in the trans-

verse momentum of higher-mass hadrons for p_{T} lower than 2 GeV/c. In accordance with the expectation of an increase in the radial flow with centrality, the $\langle p_{\mathrm{T}} \rangle$ is higher for central collisions. The $\langle p_{\mathrm{T}} \rangle$ distribution can be fitted with a function based on the Blast-Wave model [29] to retrieve the temperature of the kinetic freeze-out T_{kin}. In central collisions $\mathrm{T}_{kin} = 90$ MeV, while in peripheral collisions $\mathrm{T}_{kin} = 150$ MeV [30], suggesting an earlier kinetic freeze-out in the last case.

Non-central collisions are characterised by anisotropic flow, due to the almond shape of the overlap region of the two colliding nuclei, where pressure gradients are azimuthally asymmetric. This reflects into a flow of the nucleons which is maximised along the reaction plane, that is defined by the impact parameter and the beam axis. The particle density dependence on the azimuthal angle φ can be described with a Fourier series

$$\frac{dN}{d\varphi} \propto 1 + 2\sum_{n=1}^{\infty} v_n \cos[n(\varphi - \Psi_n)] \tag{1.1}$$

where v_n are the anisotropic flow coefficients, of which v_1, v_2 and v_3 are called directed, elliptic and triangular flow, respectively. Ψ_n is the n-order symmetry plane angle, that corresponds to the reaction plane in case of $n = 2$. v_2 is associated to the almond shaped quark-gluon plasma fireball, it is shown for charged particles as a function of p_{T} and of the centrality interval in fig. 1.9. v_2 reaches its maximum in the 40-50% centrality class, due to the larger eccentricity of the overlap region. In general, the elliptic flow v_2 increases with p_{T}, until it reaches a maximum around $p_{\mathrm{T}} \approx 2-3$ GeV depending on the centrality class. Moreover, for $p_{\mathrm{T}} < 2-3$ GeV/c, it shows an inverse proportionality with the particle mass, in agreement with the equal isotropic boost imposed by the radial flow to all particles.

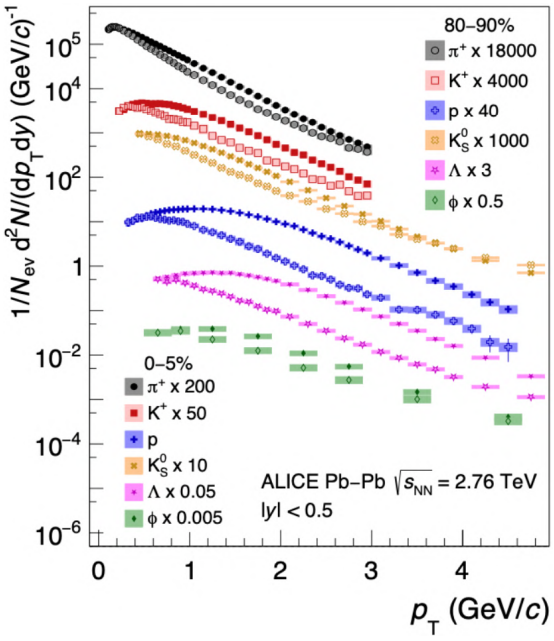

Figure 1.8: Mean transverse momentum $\langle p_{\mathrm{T}} \rangle$ for central (0-5%) and peripheral (80-90%) Pb-Pb collisions at $\sqrt{s_{\mathrm{NN}}} = 2.76$ TeV. Different colours represent different hadrons. Figure from [18].

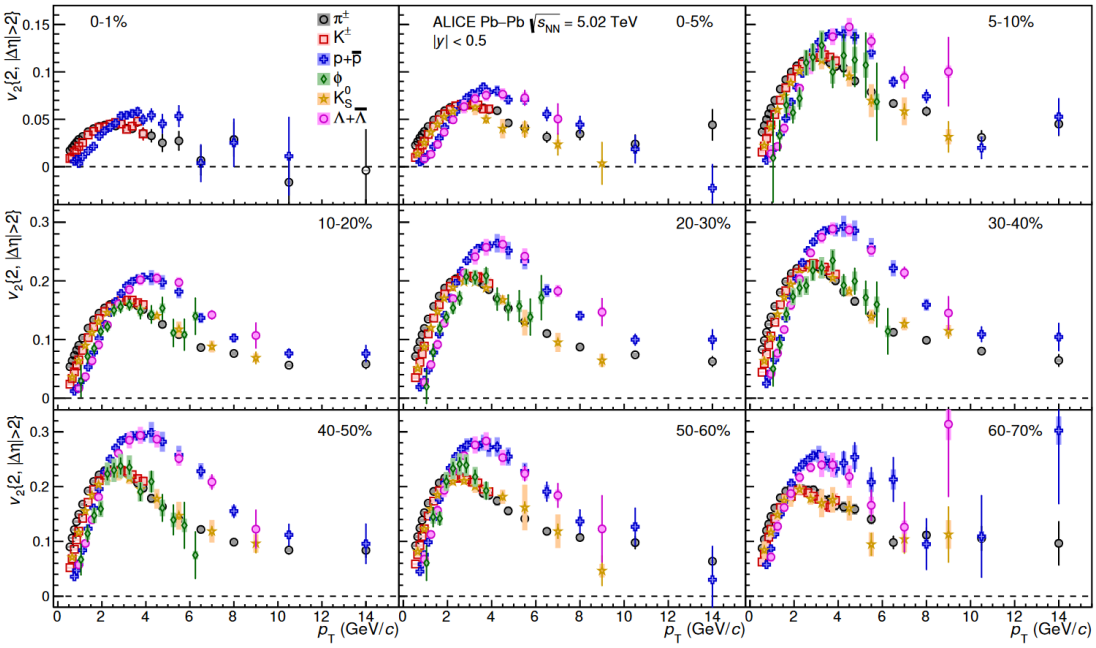

Figure 1.9: Elliptic flow v_2 as a function of the transverse momentum p_{T} in different centrality intervals of Pb-Pb collisions at $\sqrt{s_{\mathrm{NN}}} = 5.02\,\mathrm{TeV}$. Different particles are indicated by different colours. Figure from [31].

1.1.3.3 Strangeness enhancement

Another signature of the quark-gluon plasma is the strangeness enhancement. In the ordinary nuclear matter the production of strange particles is suppressed because of the larger mass of the s quark when compared to the u and d quark masses. In ultra-relativistic heavy-ion collisions, the production of strange hadrons is expected to be higher than in minimum bias pp collisions, given that the threshold for the production of $\mathrm{s\bar{s}}$ pairs, their bare mass ($\mathrm{m_s} \simeq 94\,\mathrm{MeV}/c^2$ [15]), is well below the quark-gluon plasma deconfinement temperature $\mathrm{T_C} = (156.5 \pm 1.5)$ MeV. As a consequence, an enhanced production of strange baryons is expected. The results in different collision systems at LHC for different species of particles are visible in fig. 1.10, where the ratio between strange hadron and pion yields as a function of the charged particle multiplicity is shown. The enhancement increases with the centrality of the collision and is systematically larger according to the strangeness content of the particle.

1.1.3.4 Hard probes energy loss

As mentioned before, hard probes, like heavy quarks and high-p_{T} partons, are produced in the earliest stage of the collision, thus they will experience the full quark-gluon plasma space-time evolution and provide information on the transport properties of the medium. The nuclear modification factor R_{AA} of the hard probes can be used to quantify the effect of the energy loss in the quark-gluon plasma. It is defined as:

$$R_{\mathrm{AA}} = \frac{dN_{\mathrm{AA}}/dp_{\mathrm{T}}}{\langle N_{coll}\rangle dN_{\mathrm{pp}}/dp_{\mathrm{T}}} \tag{1.2}$$

where N_{AA} and N_{pp} are the number of particles observed in nucleus-nucleus collisions and pp collisions respectively. R_{AA} is expected to be 1 if heavy-ion collisions were

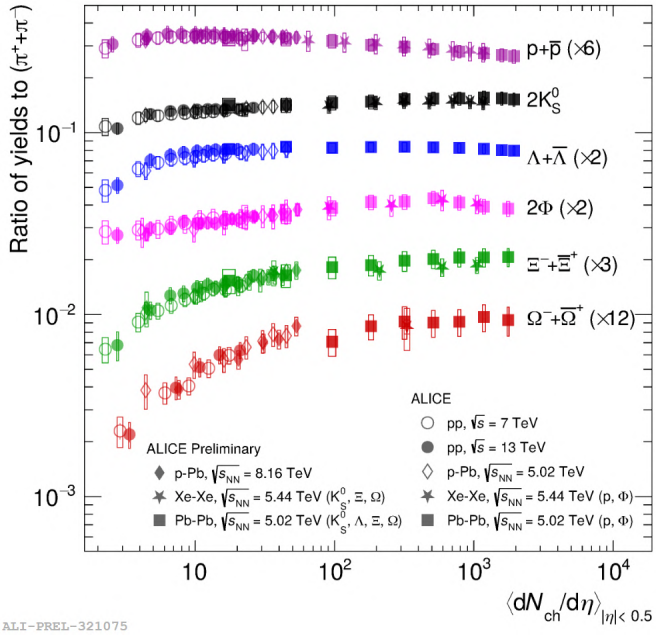

Figure 1.10: Ratio between strange hadron and pion yields as a function of the charged particle multiplicity in different collision systems, namely pp, p-Pb, Xe-Xe and Pb-Pb collisions. Different hadron species are indicated by different colours. Figure from the ALICE repository [32].

considered as a superposition of nucleon-nucleon collisions. Fig. 1.11 shows the ratio R_{AA} for charged particles as a function of the transverse momentum in central (0-5%) Pb-Pb collisions [33, 34]. The deviation to values lower than 1 indicates in-medium energy-loss. Its impact is stronger for the hadrons in Pb-Pb collisions, in accordance with the expectation of a larger volume of the quark-gluon plasma fireball. On the other hand, the nuclear modification factor of the photon and of the Z and $\mathrm{W}^{\pm}$ is compatible with one, as they are colour-neutral probes not interacting with the quark-gluon plasma.

1.1.3.5 Jet quenching

Jet quenching is an effect of the partons energy loss in the quark-gluon plasma medium. Jets consists of a cascade of consecutive emissions of partons, which are produced by hard parton scattering in the initial interaction phase, usually in a back-to-back configuration due to momentum conservation. A di-jet asymmetry can be observed when parents partons of two back-to-back jets travel different path inside the quark-gluon plasma medium and therefore can have a different energy loss. Fig. 1.12 shows the two-particle azimuthal distribution for pp, central d-Au and central Au-Au collisions measured by the STAR experiment at RHIC. In pp and d-Au collisions a peak at opposite azimuthal angles is observed. Instead, in Au-Au collisions the away-side peak is suppressed, i.e. jet quenching is observed.

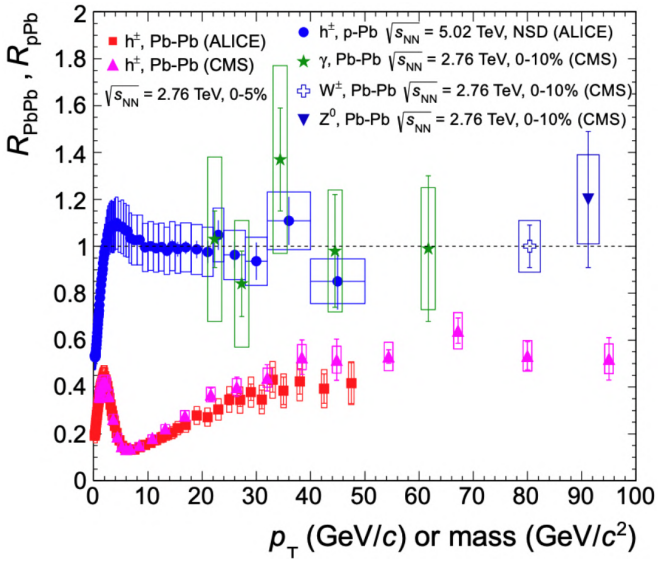

Figure 1.11: Nuclear modification factor R_{AA} as a function of the transverse momentum p_T. Different colours indicates the collision system and the particle species. Figure from [35].

1.2 The ALICE Experiment

A Large Ion Collider Experiment (ALICE) at CERN is dedicated to the study of the heavy-ion and proton collisions provided by the LHC. ALICE is optimised to study the properties of the quark-gluon plasma, a strongly interacting state of matter arising at high energies and densities, predicted by Quantum Chromodynamics (QCD). ALICE was designed to perform particle identification and tracking at high multiplicity over a wide range of transverse momenta p_T. The ALICE 1 apparatus [37], operated during the LHC Runs 1 and 2, has successfully recorded data from pp and Pb-Pb collisions [26], providing new insights on the quark-gluon plasma properties as well as many other aspects of the strong interaction [18]. During the LHC Long Shutdown 2, ALICE has undergone a major upgrade of several of its detectors [38, 39], to take data during LHC Runs 3 (2022-2026) and 4 (2030-2033). Such experimental apparatus,

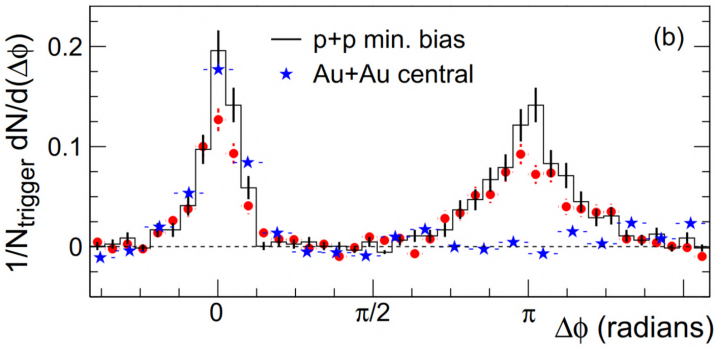

Figure 1.12: Two-particle azimuthal distribution for different collision systems measured by the STAR experiment at RHIC. Jet quenching can be observed in Au-Au collisions, where the away-side jet is suppressed. Figure adapted from [36].

called ALICE 2, started to record pp collisions data at $\sqrt{s_{\rm NN}} = 13.6\,\text{TeV}$ in July 2022. With respect to ALICE 1, the tracking reconstruction capability has improved, in particular for low-momentum particles. The readout rate has increased from 1 kHz to 50 kHz for Pb-Pb collisions in continuous readout mode. This makes it possible to record minimum-bias collision samples, corresponding to the full integrated luminosity of $13\,\text{nb}^{-1}$ delivered by the LHC during Runs 3 and 4. Two additional upgrades, the ITS3 [40] and FoCal [41] projects, are foreseen to be installed during the LHC Long Shutdown 3 to be ready for Run 4. ITS3 will consist of a new inner barrel for the Inner Tracking System, described in detail in Chapter 2. FoCal is a forward electromagnetic calorimeter with high readout granularity, optimised for photon detection in the range $3.4 < \eta < 5.8$ and coupled to a hadronic calorimeter.

An absolutely new upgrade of the experimental setup, named ALICE 3 [42], has been proposed for the LHC Runs 5 and 6.

1.2.1 The detector layout

The currently installed ALICE 2 apparatus is situated in one of the experimental caves of LHC 56 m deep. It is 16 m tall and covers an area of $26 \times 16\ \text{m}^2$. It comprises several detectors (fig. 1.13), organised in a central barrel embedded in a solenoidal magnet (in red in the figure, with a field of 0.5 T) to detect hadrons, electrons and photons in a polar angle between 45° and 135° and a forward muon spectrometer with a dipole magnet providing a total bending power of 3 Tm that covers polar angles from 2° to 9° [39]. The subsystems of the central barrel are placed with a cylindrical symmetry around the beam direction, enclosing the interaction point. They are designed to track particles in the high multiplicity environment of heavy-ion collisions, covering transverse momenta from approximately $100\,\text{MeV}/c$ to $100\,\text{GeV}/c$. Going from inside to outside, the detectors of the central barrel are:

- **Inner Tracking System (ITS2):** is responsible for primary and secondary vertex reconstruction and particle tracking in the vicinity of the interaction point. It has undergone a major upgrade during the LHC Long Shutdown 2 and another important upgrade, the ITS3, is foreseen for LHC Long Shutdown 3 The currently installed ITS2 is described in detail in sec. 1.3, while Chapter 2 is dedicated to ITS3.

- **Muon Forward Tracker (MFT):** is a high position resolution silicon detector, which provides charged particle tracking in the pseudorapidity interval $-3.6 < \eta < -2.45$, almost the same of the forward muon spectrometer (see next paragraph). The MFT was installed during LHC Long Shutdown 2 [43] as a vertex detector for the muon spectrometer to extend the muon physics program.

- **Time-Projection Chamber (TPC):** it extends from a radius of 0.85 m to 2.5 m over a length of 5 m, covering a symmetric pseudorapidity interval around central pseudorapidity ($|\eta| < 0.9$) at full azimuth. The gas mixture in use to operate the TPC is Ne-CO_2-N_2 (90-10-5). The readout is based on Gas Electron Multiplier (GEM) foils. The TPC has undergone a significant upgrade during the LHC Long Shutdown 2 as well [44].

- **Transition Radiation Detector(TRD):** it provides additional points for tracking from 2.8 m to 3.5 m in radius, contributing to the momentum determination

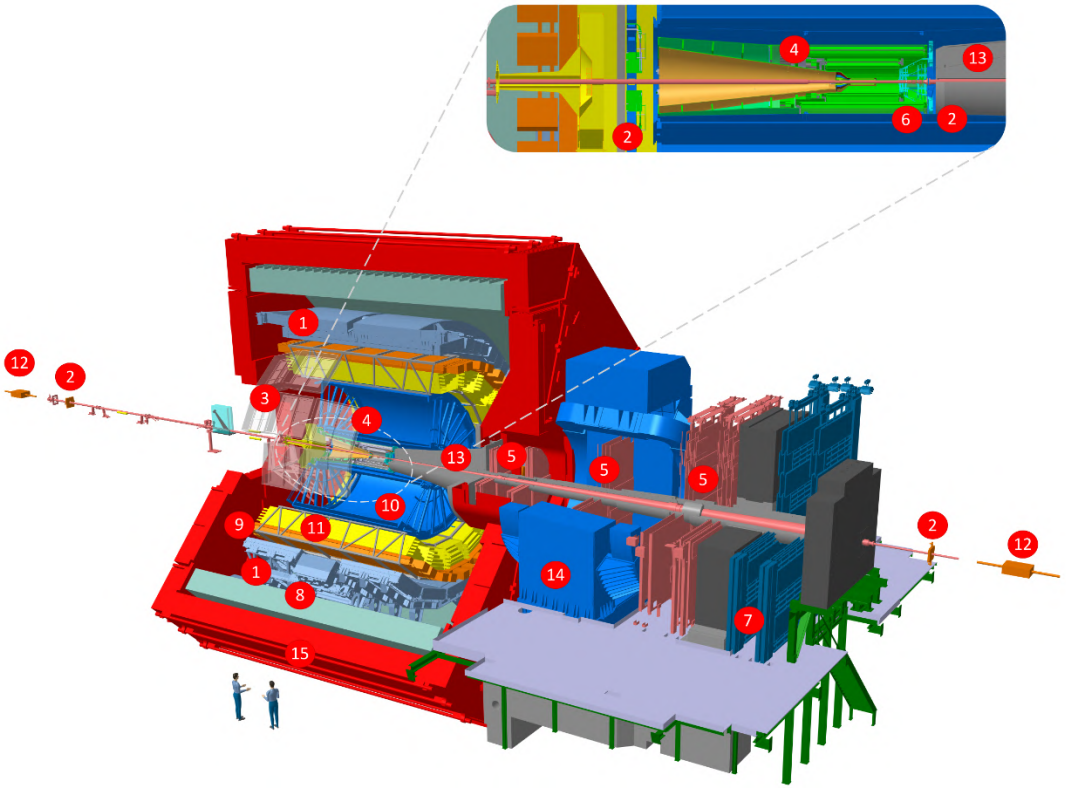

Figure 1.13: Schematic representation of the ALICE detector subsystems: (1) Electromagnetic Calorimeter (EMCAL); (2) Fast Interaction Trigger (FIT); (3) High Momentum Particle Identification Detector (HMPID); (4) Inner Tracking System (ITS); (5) Muon Tracking Chamber (MCH); (6) Muon Forward Tracker (MFT); (7) Muon Identifier (MID); (8) Photon Spectrometer (PHOS/CPV); (9) Time Of Flight (TOF); (10) Time Projection Chamber (TPC); (11) Transition Radiation Detector (TRD); (12) Zero Degree Calorimeter (ZDC); (13) absorber; (14) dipole magnet; (15) L3 magnet. Figure adapted from the ALICE repository [32].

of charged particles. The TRD allows dE/dx measurements for particle identification, as well as the detection of transition radiation for electron identification. A comprehensive description of the TRD can be found in [45].

- **Time Of Flight (TOF):** it consists of an array of Multi-gap Resistive-Plate Chamber (MRPC) strip detectors covering the central pseudorapidity region ($|\eta| < 0.9$). The TOF [46, 47] provides information for particle identification over a wide momentum range, below 2.5 GeV/c for pions and kaons, up to 4 GeV/c for protons and for low momentum electrons.

- **High Momentum Particle Identification Detector (HMPID):** it is a ring-imaging Cherenkov detector (RICH) composed by seven Multi-Wire Proportional Chambers (MWPCs) equipped with CsI segmented photocathodes. The HMPID [48] is designed to identify hadrons at $p_{\mathrm{T}} > 1$ GeV over a limited acceptance.

- **Electro-Magnetic Calorimeter (EMCal):** is a lead-scintillator sampling calorimeter with Avalance Photo Diode (APD) readout. The detector is segmented in two

parts, covering two different regions in azimuth. The EMCal [49, 50] was optimised to measure electrons from heavy-flavour hadron decays, electromagnetic component of jets, direct photons and neutral mesons.

- **PHOton Spectrometer (PHOS):** is an electromagnetic calorimeter equipped with $PbWO_4$ crystals and APD readout. It has a limited acceptance at midrapidity, the covered azimuthal angle is reduced as well. The PHOS [51] is specialised in the detection of photons in the energy range from 0.1 to 100 GeV.

The forward muon spectrometer [52] covers the pseudorapidity range $-4.0 < \eta < -2.5$. Besides the already mentioned dipole magnet and the MFT, which is comprised in the central barrel, downstream the interaction point it is composed by:

- A composite absorber with both high and low Z materials, for a total of about 10 interaction lengths.
- **Muon Tracking Chambers (MCH)**, five tracking stations equipped each with two Multi-Wire Proportional Chambers (MWPCs) with cathode pad readout.
- A second absorber made by iron, for a total of seven interaction lengths.
- **Muon IDentifier (MID)**, four planes of single gap Resistive Plate Chamber (RPC) detectors for a total detection area of about 150 m^2, used for muon identification. The RPC are operated with a gas mixture 89.7% $C_2H_2F_4$, 0.3% SF_6, 10% i-CH_{10}, humidified to 35%-40% relative humidity [53].

Some other detectors at small angles serve for global event characterisation and triggering, among which the Fast Interaction Trigger (FIT) and the Zero-Degree Calorimeters (ZDC).

The FIT [54] is a set of forward detectors used for triggering and for determining the collision time. It serves as an initial indicator of the vertex position and as a forward multiplicity counter as well. The FIT comprises three sub-detectors that are positioned along the beam line, FT0, FV0 and FDD (Forward Diffractive Detector). FT0 consists of two arrays of fast Cherenkov radiators, dedicated to the measure of the collision starting time. FV0 is a segmented scintillator disk, which provides the vertex location. Finally, FDD comprises two arrays of scintillator pads, and selects diffractive and ultra-peripheral events.

The ZDC [55] calorimeters are placed at approximately 100 m from the interaction point at both beam sides and detect spectator neutrons and protons emitted at very small angle. They serve mainly to determine the centrality of the collision and the event plane orientation.

The data produced by the detectors are transmitted through optical links to First Level Processors (FLPs), where they are assembled to time frames for further processing. Online reconstruction of all collisions is performed by a dedicated farm of Event Processing Nodes (EPNs), that is installed at the experiment site. These pre-analysed data are stored and subsequently undergoes an asynchronous reconstruction stage with an improved calibration to be ready for physics analysis. A dedicated software framework, named Online-Offline computing system (O^2) [56], was developed for the data processing from data reconstruction up to data analysis.

1.3 The Inner Tracking System

The ALICE Inner Tracking System (ITS) [57, 39] is responsible for primary and secondary vertex reconstruction and charged particle tracking in the vicinity of the interaction point. The current ITS2 was installed during the LHC Long Shutdown 2 in replacement of the previous ITS. It is completely based on the Monolithic Active Pixel silicon Sensor (MAPS) technology and has an active surface of 10 m^2 with nearly 12.5 Gpixels, thus making it the largest silicon pixel detector ever built. The ITS2 is equipped with the ALPIDE chip [58, 59, 60], a MAPS sensor implemented in a 180 nm CMOS technology, designed specifically for the ALICE ITS2.

With respect to the prior ITS, the ITS2 is characterised by:

- an higher impact parameter resolution in the transverse plane (up to three times) and in the longitudinal direction (up to six times) [39]. This was achieved thanks to an innermost layer closer to the interaction point (from 39 mm of the ITS to 22.4 mm of the ITS2), a smaller pixel size and a lower material budget (from 1.14% X_0 to 0.35% X_0 for the three innermost layers);
- a finer granularity and an additional tracking layer (from six to seven) that leads to a better tracking efficiency in the low transverse momentum range;
- a larger readout rate capability, 50 kHz in lead collisions and 400 kHz in protons collision.

Tab. 1.1 report a list of the main ITS2 parameters.

Table 1.1: Main ITS2 detector parameters. [39]

Technology	Monolithic Active Pixel silicon Sensor (MAPS)
No. of layers	7
Radius	22-395 mm
Pseudorapidity coverage	$\|\eta\| \leq 1.3$
Material budget/layer	inner barrel: 0.36% X_0, outer barrel: 1.10% X_0
Pixel size	$29.24 \times 26.88\,\mu m^2$
Spatial resolution	5 µm
Maximum rate	50 kHz (Pb-Pb), 400 kHz (pp)

1.3.1 ITS2 detector layout

The ITS2 is composed of seven cylindrical layers equipped with ALPIDE sensors [58, 59, 60]. The layers have a radius ranging between 22.4 mm and 391.8 mm and are placed coaxially around the beam pipe [57] (fig. 1.14). The three innermost layers are organized in the Inner Barrel (IB), while the outer four compose the Outer Barrel (OB). The sensors are thinned down to 50 µm and 100 µm in the IB and OB, respectively. A water cooling system keeps the temperature of the ITS2 stable around the room temperature 20−25° C). The radiation load expected after 10 years of operations is of 270 kGy of Total Ionising Dose (TID) and 1.7×10^{12} 1 MeV n_{eq} cm^{-2} of Non-Ionising Energy Loss (NIEL).

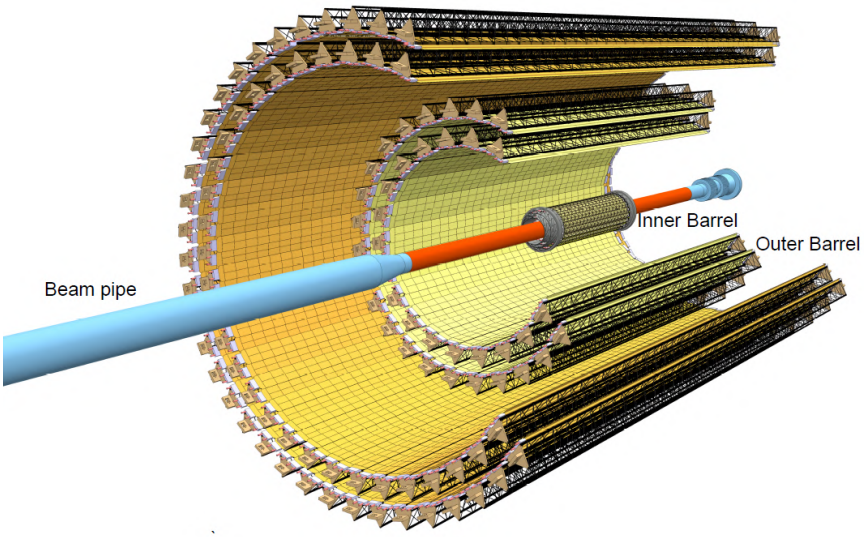

Figure 1.14: Schematic representation of the ALICE ITS2 detector.

Each layer is built up by functional independent units called staves, that make the overall structure azimuthally segmented (fig. 1.15).

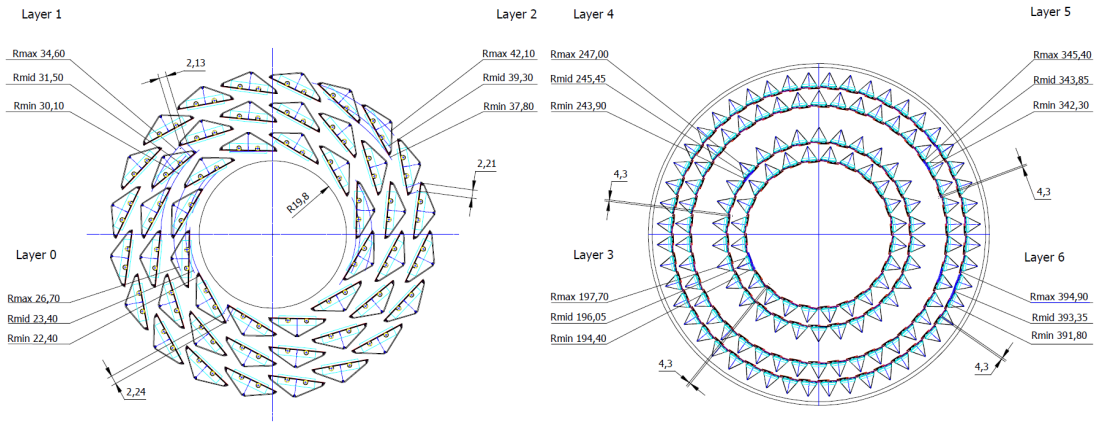

Figure 1.15: Schematic sections and dimensions of the ITS Inner Barrel (left) and of the ITS Outer Barrel (right). Units are in mm.

The IB staves are slightly different from the staves of the OB. Each stave comprises a Hybrid Integrated Circuit (HIC), a coldplate and a spaceframe, described in detail in

the following and displayed in fig 1.16. The main layout parameters of the ITS2 layers are reported in tab. 1.2.

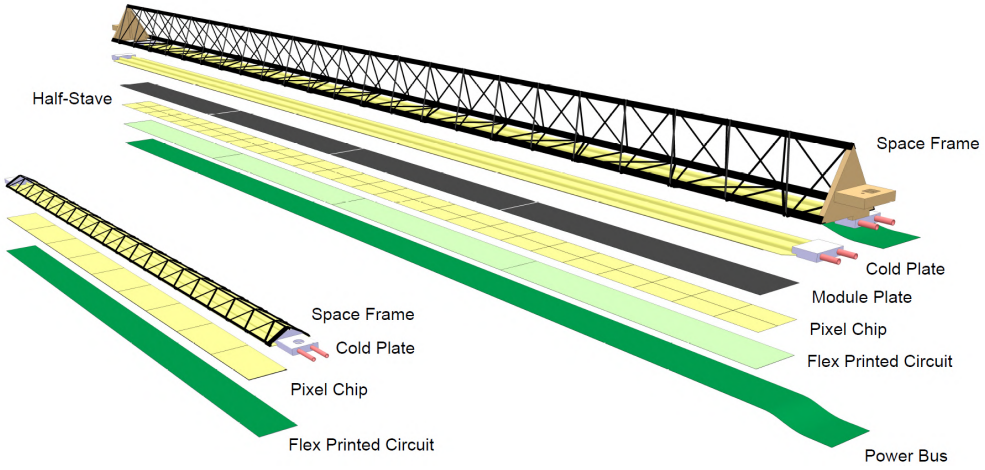

Figure 1.16: Exploded view of the IB stave (bottom left) and of the OB half-stave (top right). The stave components are indicated.

Table 1.2: Detailed parameters of the ITS2 layers.

Layer	Radius (cm)	Length (cm)	Staves	HICs/stave	Chips
0	2.3	27.1	12	1	108
1	3.1	27.1	16	1	144
2	3.9	27.1	20	1	180
3	19.6	84.4	24	8	2688
4	24.5	84.4	30	8	3360
5	34.4	147.8	42	14	8232
6	39.3	147.8	48	14	9408

Hybrid Integrated Circuit (HIC) The HIC consists of a Flexible Printed Circuit (FPC) for the sensor readout, control and power supply, on which the sensors are bonded via laser soldering. IB HIC comprises nine ALPIDE sensors in a row, OB HIC includes two rows of seven ALPIDE each (fig 1.16). The single IB stave consists of one HIC, covering a total area of 15 mm×270.8 mm. The middle layer and OB half-staves comprise four and seven HICs, respectively. Each OB HIC is covering an area of approximately 30 mm×210 mm. In the IB staves the sensors share the same aluminium power bus on the FPC. In the OB half-staves, all chips in one HIC are connected to the analogue and digital power lines of the FPC and an additional external aluminum power bus, in dark green in fig. 1.16, fed the FPCs of the half-stave. The electrical connections between the OB HICs and the dedicated external power bus is made by thin aluminum cables soldered on the the HIC. Aluminum was chosen as a conductor for the FPC of the IB, given the strict requirements on the material budget, whereas standard FPCs with copper conductor are used for the OB.

Space frame and cold plate The ITS2 stave mechanics consists of a space frame, a lightweight mechanical carbon support structure. The cooling is provided by the cold

plate, a highly thermally conductive carbon fiber laminate embedding the polyimide water-cooling pipes allowing for the removal by conduction of the heat generated by the chips (fig. 1.17). In the IB staves, the cold plate is integrated within the space frame and the HICs are glued directly on it with the sensor facing the cold plate to maximise the cooling efficiency. In the OB half-stave, the cold plate is attached to the space frame. The OB HICs are glued onto an additional 120 µm thick carbon plate that ensures the required stiffness to the module. The required power dissipation capability is about 47 mW/cm^2 for the IB modules and around 35 mW/cm^2 for the OB modules.

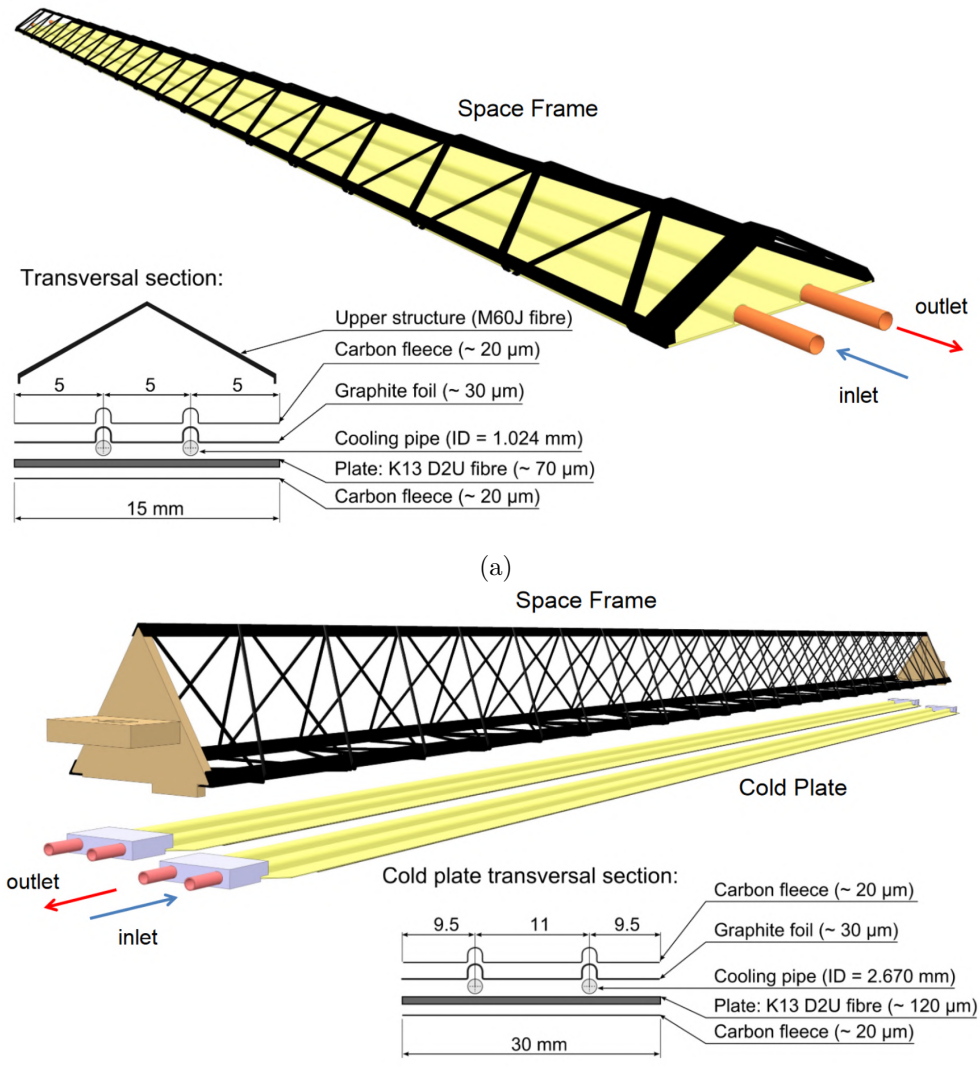

Figure 1.17: Schematic representation of the IB (a) and OB (b) mechanics and cooling system. Figures from [61].

Fig. 1.18 shows the material budget of an inner and outer layer of the ITS2. The contributions of the module components described in the previous paragraphs are indicated in different colours. The average material budget of 0.36% X_0 for the inner layer and of 1.10% X_0 for the outer layer, meets the stringent requirements of a very low material budget.

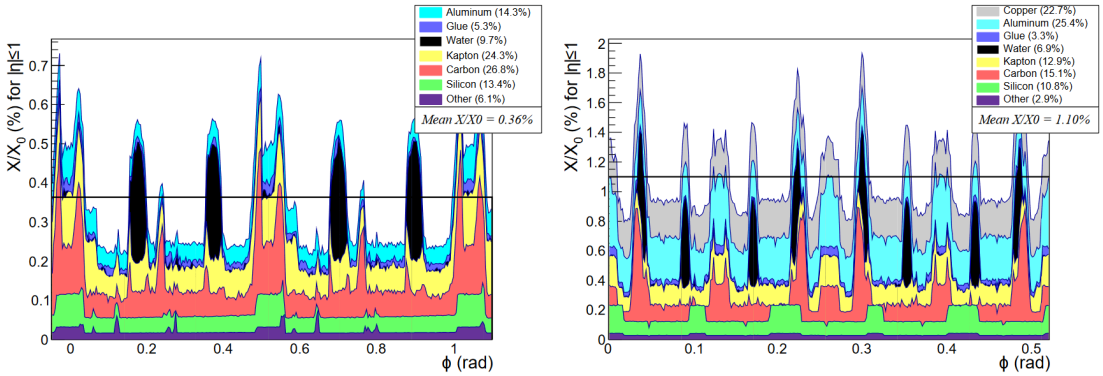

Figure 1.18: Azimuthal distribution (averaged over $|\eta| < 1$) of the material budget of an inner (left) and outer (right) ITS2 layer.

1.3.2 Global structures and services

The global mechanical support structures of the ITS2 must ensure a high accuracy in the position of the detector with respect to the TPC and the beam pipe, allowing the positioning of the first layer at a minimum distance to the beam pipe wall. Moreover, the thermo-mechanical stability over time must be guaranteed as well as the accessibility for maintenance and inspection. The requirements for the integration has to combine with those set by the other detectors installed very close to the ITS, i.e. the MFT and the FIT (fig. 1.13).

The ITS2 support structure is depicted in fig. 1.19, it comprises an inner barrel support structure (in yellow) and an outer barrel one (in green), divided in two halves. Four end-rings (in pink) provide the reference for the fixation of the structural components. Each half-barrel, made from carbon fiber composite, is composed of a half-cylindrical shell to support the detector layers and a half-conical structure for the signal and power cables routing to the ALICE miniframe. Such service barrels serve as a path for the cooling pipes as well.

1.3.3 Readout and powering system

The ITS2 readout and powering system is schematically represented in fig. 1.20. The readout system is organised in 192 autonomous Readout Units (RU), one for each stave, that provide control and trigger and read the ALPIDE chips. Each RU is connected to a Common Readout Unit (CRU) through a GBT link to transmit slow-control commands. The needed readout bandwidth of 1.2 Gbit/s (inner layers) and of 400 Mbit/s (outer layers) is achieved by transmitting data in parallel on up to three GBT links. An additional GBT link is used to receive the trigger from the Central Trigger Processor (CTP). The inner barrel chips are read-out individually, due to the higher occupancy rate, while the outer barrel ones are read grouped by seven. ITS2 can be operated

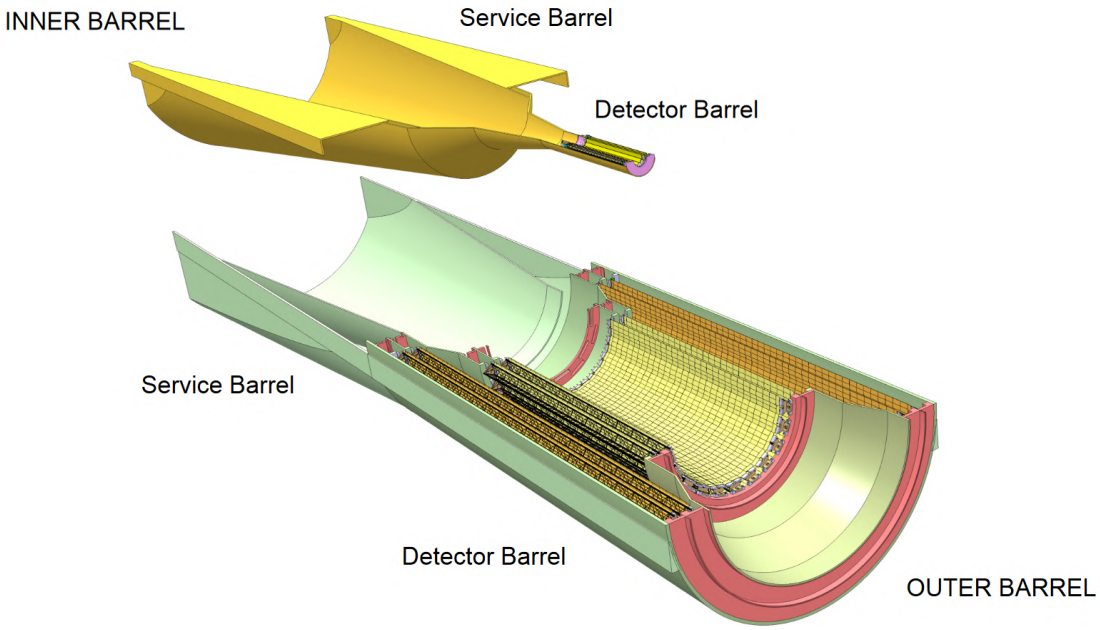

Figure 1.19: Half-barrel integration structures of the ITS2. The conical structures serves as a support for the services.

both in triggered and continuous mode. In triggered mode, the hits are stored in the sensor memory and read out only if a trigger command arrives within few μs after the hit occurs, while in continuous mode the data are continuously read out with a programmable frequency.

The powering system consists of 142 Power Boards (PB) physically placed near the RUs. It supplies the 1.8 V analogue and digital lines of the ALPIDEs, as well as the reverse bias that can be applied to the sensor substrate. Each PB has two power units, that contains 16 analogue and digital channels and 8 reverse bias channels. Thus each power units can power a single IB stave (1 HIC), a middle layer stave (8 HICs) or an

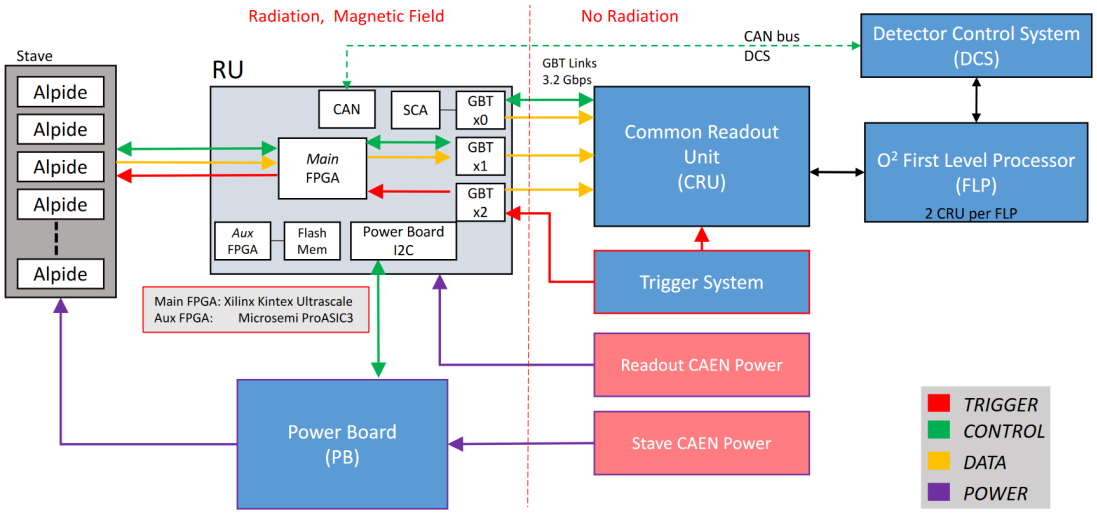

Figure 1.20: Schematic representation of the ITS2 readout and powering system.

outer layer half-stave (7 HICs). Each RU has full control over the power unit connected to its stave, therefore the power sequence, monitoring and tuning is managed via the GBT links of the RU.

Both RU and PB are located in the ALICE miniframe, inside the L3 magnet, therefore all system components were validated to operate in the 0.5 T magnetic field and in a radiation environment [62].

1.4 The physics motivation for the ITS3 Upgrade

The ITS2 will be upgraded during the LHC Long Shutdown 3 (LS3) [63, 64, 40], which is starting in mid 2026, to be ready for LHC Run 4. The upgrade foresees the replacement of the three innermost layers of the ITS2 with a truly cylindrical tracker, the ITS3 (see chapter 2). This innovative vertex detector will be composed of two half barrels, comprising each of three self-supporting cylindrical half-layers made of two large-area ($\mathcal{O}(10{\times}27\ \mathrm{cm}^2)$) ultra-thin (50 µm) bent stitched Monolithic Active Pixel silicon Sensors (MAPS) fabricated in a 65 nm CMOS process. The radius of the first layer of 19 mm and the unprecedented low material budget of 0.09% X_0 per layer will strongly improve the pointing resolution especially for low-momentum particles [65]. An improvement of a factor of 2 is foreseen for particles with a p_T lower than 1 GeV/c, thus allowing for the increase in the precision of measurements in the heavy-flavour sector and bringing another set of fundamental observables into reach.

The gain in performance will make accessible or largely improve the measurement of several observables which are among the main objectives of the ALICE physics program, i.e. B_s^0 and Λ_b^0 at low transverse momenta and of non-prompt D_s^+ and Ξ_c^+ decays in heavy-ion collisions. In addition, the study of low-mass di-electrons will benefit from the reduction of the background of electrons from photon conversion in the material and from semi leptonic charm-hadron decays. Finally, the direct tracking of charged strange baryons to reconstruct weakly decaying strange particles with novel techniques might be in reach. The expected performance improvements for the measurements of the Λ_c and thermal di-electrons will be presented in this section to demonstrate the impact of the ITS3 Upgrade. A comprehensive discussion of the ITS3 physics goals can be found in [65].

1.4.1 Heavy-flavour physics studies: Λ_c

Charm and beauty quarks are produced by hard-scattering processes only in the early stage of the heavy-ion collisions, as discussed in sec. 1.1.2. They interact with the medium constituents, exchanging energy but preserving their flavour. Hence, they can be used as probes to study the transport properties of the quark-gluon plasma. It was demonstrated by several measurements with heavy-ion collisions at RHIC (Au-Au) and at the LHC (Pb-Pb) that charm and beauty quarks interact strongly with the QGP. Two observables are usually measured to study the medium effects on heavy-flavour hadron production: the nuclear modification factor R_{AA} and the azimuthal anisotropy of open heavy-flavour signals, both discussed in detail in sec 1.1.3. The first one is defined for each considered centrality as the ratio of the yield measured in Pb-Pb collisions to the pp cross section scaled by the average nuclear overlap function $\langle T_{AA} \rangle$ [66]. The second one is characterised by the Fourier coefficients v_n of the distribution of the heavy-flavour hadron azimuthal angle with respect to the reaction plane. A precise measurement of

R_{AA} and v_2 of charm and beauty hadrons will help in constraining the modelling of the diffusion process.

The hadronization process and the system properties at hadronization time can be exploited thanks to heavy-flavour hadrons too. Given the large mass of the heavy quarks, their production in the soft processes occurring during the hadron-formation phase is assumed to be negligible. Instead, these processes determine the relative abundances of the different heavy-flavour hadron species, depending on the system properties. In particular, an increase of the production of heavy-flavour baryons relative to heavy-flavour mesons and of mesons with strange quarks relative to non-strange mesons is expected by both statistical hadronization and coalescence models.

The enhancement of the production of heavy-strange mesons with respect to non-strange ones was supported by the measurements of the production of prompt and non-prompt D_s^+ mesons [67, 68] and of B_s^0 mesons [69]. The installation of the ITS3 is fundamental to achieve the precision required to set important constraints to models.

Moreover, the measurement of the charm-strange baryon Ξ_c in Pb-Pb collisions will be possible with the ITS3, thus helping in studying the processes responsible for enhancing baryon production, as well as the abundant strange production in the medium, which influence the Ξ_c production. The data collected in Run 4 will allow for centrality studies of the heavy-flavour baryon-to-meson ratios, in particular the Λ_c^+/D_0 ratio at midrapidity from central to peripheral Pb-Pb collisions. In order to be able to distinguish between different models, the production and the azimuthal anisotropy of different hadron species must be measured down to the lowest possible p_T.

The identification of the decay particles of charm and beauty hadrons requires the best possible spatial resolution on the track trajectories in the vicinity of the collision point, given the short decay distance of these hadrons ($c\tau$ =59 µm for Λ_c^+). Otherwise, their decay vertices would be covered by the huge combinatorial background arising from the presence of thousands of particles in central Pb-Pb collisions.

Λ_c measurement The reconstruction of Λ_c^+ using the $\Lambda_c^+ \rightarrow pK^-\pi^+$ decay channel is an important benchmark channel to provide crucial information on the charm quark thermalisation and hadronization in the QGP, on the role of recombination and radial flow as well as on the deconfinement of charm quarks in the fireball [64]. In Pb-Pb collisions the production of charm and beauty baryons is expected to be enhanced, compared to pp collisions, in the low momentum region (below 10 GeV/c) because of the predicted thermalisation and hadronization via recombination of heavy quarks with light-flavour quarks inside the QGP.

Figure 1.21 shows the Λ_c^+/D_0 ratio, which was measured experimentally in Pb-Pb collisions at the LHC [75, 76, 77, 78] and in Au-Au collisions at RHIC [79]. An enhancement of the ratio in central Pb-Pb events for intermediate transverse momenta is observed. In peripheral collisions the enhancement is less pronounced, while it is not visible at all in pp collisions. Moreover, the ratio in different multiplicity intervals and different collision systems is compared to Catania [70], SHMc [71] and TAMU [72] model expectations. A discrimination between the models is not possible given the limited statistical precision. A more precise measurement of Λ_c^+ production was one of the main motivations for upgrading the ALICE detector for Run 3.

The short lifetime of Λ_c^+, 59 µm, is the main obstacle for the measurement of this baryon. Moreover, the first main decay channel, $\Lambda_c^+ \rightarrow pK^-\pi^+$, has a large three-prong combinatorial background. In the second decay channel, $\Lambda_c^+ \rightarrow pK_S^0$, ($K_S^0 \rightarrow \pi^+\pi^-$),

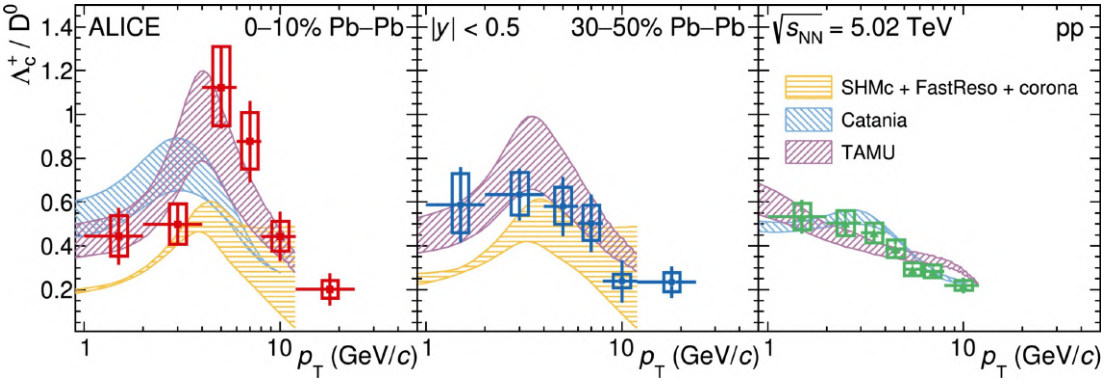

Figure 1.21: Experimental Λ_c^+ over D_0 cross section ratio as a function of p_T in 0-10% (left) and 30-50% (center) intervals in Pb-Pb collisions and in pp collisions (right). Expectations from the Catania [70], SHMc [71] and TAMU [72] models and from the PYTHIA8 event generator with the Monash [73] and CR Mode 2 [74] tunes are compared to the analysed data. Figure from [75].

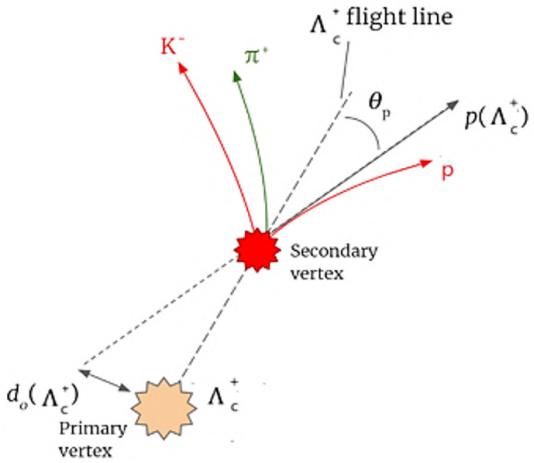

Figure 1.22: Decay channel $\Lambda_c^+ \rightarrow pK^-\pi^+$.

the long decay length (∼2.7 cm) of the K_S^0 affects negatively the determination of the decay vertex. The first one is considered the benchmark channel for the ITS3 Upgrade. Because of the very short Λ_c^+ lifetime, which makes secondary tracks displaced from the main interaction vertex by only a few tens of microns (fig. 1.22), a very precise tracking and impact parameter resolution are required.

The performance studies have been carried out for the ITS3 layout using the *hybrid* method described for the ITS2 in [61]: the tracks parameters in the full-simulation with the ITS2 geometry have been corrected to mimic the ITS3 impact parameter and momentum resolution.

In the evaluation of the simulated performance of the ITS3, the signal S and the background B yields are estimated in an invariant-mass interval of $\pm 3\ \sigma$ around the Λ_c^+ mass, where σ is its resolution. Figure 1.23 shows the comparison of the performance between ITS2 and ITS3 in terms of the significance (left), which is defined as $S/\sqrt{S+B}$, and of the signal-to-background ratio S/B (right) as a function of p_T in the 0-10% centrality class, where the physics effects are expected to be larger, for 8 billion events

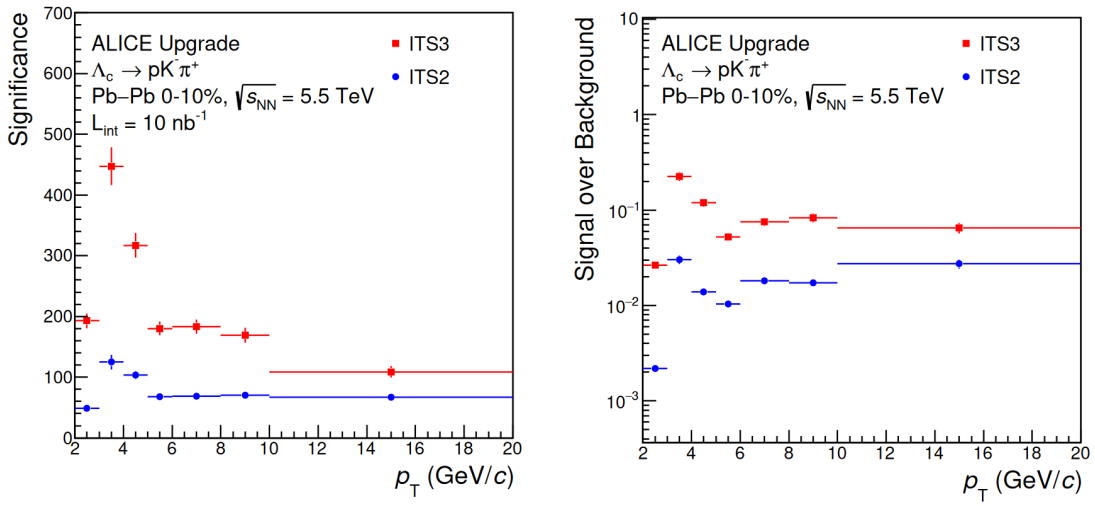

Figure 1.23: Significance $S/\sqrt{S+B}$ (left) and S/B ratio (right) as a function of p_T for the signal S and the background B estimated in the simulation of the decay channel $\Lambda_c^+ \rightarrow pK^-\pi^+$. Figures from [65].

corresponding to an integrated luminosity of $10\,nb^{-1}$. The better pointing resolution of the ITS3 allows for a higher rejection of the combinatorial background and for a higher efficiency in the signal selection, thus leading to an improvement of a factor of four in the significance and ten in the S/B ratio. The distribution of the Λ_c^+/D_0 ratio will benefit from the increased precision of the ITS3, especially in its lower p_T side. Moreover, p_T differential measurements with finer p_T intervals of 1 GeV/c or 0.5 GeV/c and the first significant measurements of Λ_c^+ elliptic flow v_2 will be possible thanks to the improved ITS3 performance. The former will improve the precision of the spectrum shape, that is important to determine precisely the total charm-production cross section. Therefore, the comparison between charm-hadron species will be improved, which is a test sensitive to the hadronization mechanism and to the effects of the radial flow.

1.4.2 Measurement of thermal di-electrons

Low momentum di-electron pairs can be used to detect the electromagnetic radiation produced by the QGP formed in heavy-ion collisions, thus allowing for gaining insight on the temperature of the medium. For this purpose, electrons with a transverse momentum down to 100 MeV/c are required to be detected. A very good electron identification is mandatory, since the production rate of thermal dileptons is low and the large combinatorial and physical background are the dominant sources of systematic uncertainties in the di-electrons measurements. The combinatorial background includes pairs in which one of the particles is a hadron misidentified as an electron, as well as electron pairs from π^0 Dalitz decays and from photon conversions, mainly $\pi^0 \rightarrow \gamma\gamma$. The physical background includes pairs of electrons generated by semi-leptonic charm decays. The ITS3 upgrade will reduce the material budget of the beam pipe by 30%, and the material budget of the first ITS layer by a factor of four, thus reducing the number of electrons from photon conversion before the first track measurement point. In addition, the tracking capability of the ITS3 down to very low p_T will improve the reconstruction efficiency of photon conversions in which one lepton has a very

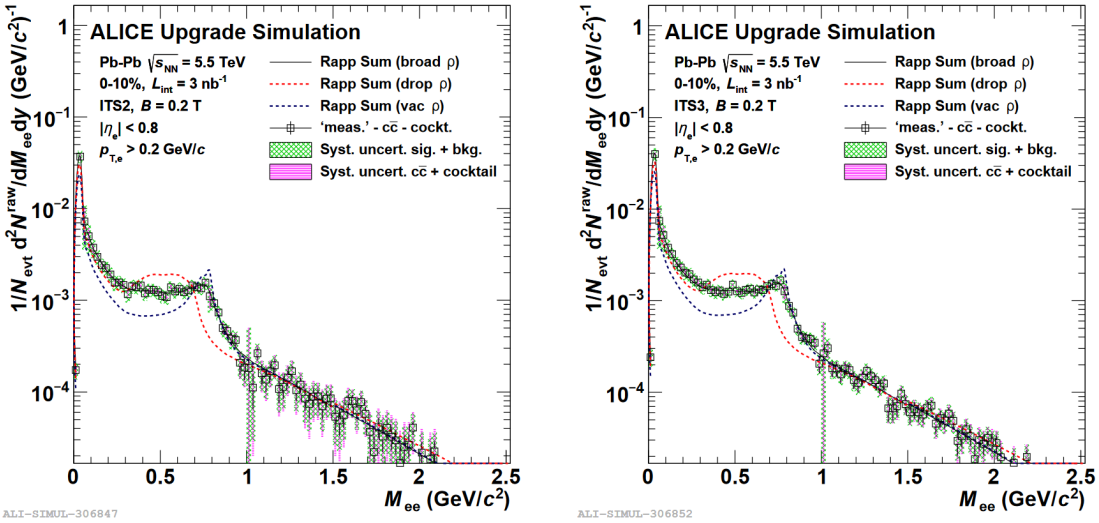

Figure 1.24: Physics performance simulation for ITS2 (left) and ITS3 (right). The distribution of the excess e^+e^- invariant mass for central (0-10%) Pb-Pb collisions at $\sqrt{s_{\rm NN}} = 5.5\,\text{TeV}$ with $\text{L}_{int} = 3\,\text{nb}^{-1}$ is represented by the black continuous line. The systematic uncertainties from the combinatorial background are represented by the green boxes, while the systematic uncertainties related to the subtraction of the cocktail and charm contribution are indicated by the magenta boxes. Figures from [65].

low momentum, thus helping in reducing the combinatorial background. Finally, the improved pointing resolution will reduce the background due to electrons from semi-leptonic charm decays, which will be efficiently tagged in advance.

Figure 1.24 shows the result of the physics performance simulation for 2.5×10^9 ($\text{L}_{int} = 3\,\text{nb}^{-1}$) central (0-10%) Pb-Pb collisions at $\sqrt{s_{\rm NN}} = 5.5\,\text{TeV}$ with a solenoid magnetic field of 0.2 T. The excess invariant-mass spectrum of e^+e^- after the subtraction of the background is shown on the left for ITS2 and on the right for ITS3. The dilepton yield at invariant masses $M_{ee} > 1.1$ GeV/c^2 is dominated by the thermal radiation from the QGP and can give information on the early temperature of the system, if the charm background can be effectively reduced. The function

$$\frac{dN_{ee}}{dM_{ee}} \propto M_{ee}^{3/2} e^{-\frac{M_{ee}}{T_{fit}}} \tag{1.3}$$

has been used to fit the simulated spectra in the region $1.1 < M_{ee} < 2.0$ GeV/c^2 to obtain the temperature parameter T_{fit}. The same function has been used to fit the input thermal spectrum to obtain the same parameter, called T_{real}. Figure 1.25 shows the comparison between the ratio T_{fit}/T_{real} for ITS2 and ITS3. For ITS3 it can be observed that, with respect to the ITS2, the statistical uncertainty is reduced by a factor of 1.3, the systematic uncertainty from the subtraction of the combinatorial background is reduced by a factor of 2 and the systematic uncertainty from the subtraction of the light-hadron background is reduced by a factor of 2.

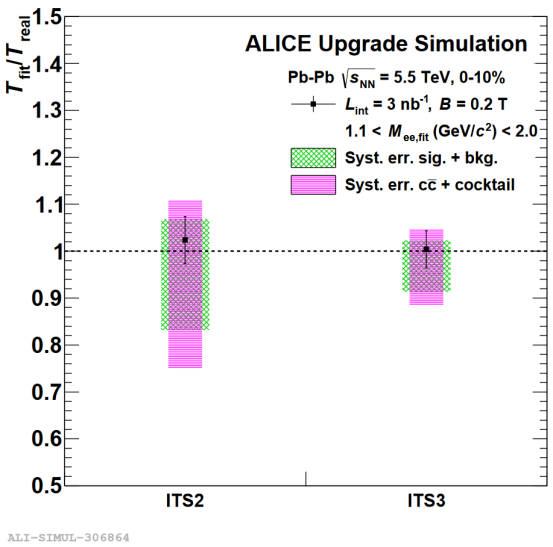

Figure 1.25: Comparison of the ratio between the parameters T_{fit} and T_{real} obtained from a fit to the invariant mass excess spectrum for ITS2 and ITS3. The statistical uncertainties are represented by the error bars, the systematic uncertainties from the combinatorial background are represented by the green boxes, the systematic uncertainties related to the subtraction of the charm contribution are indicated by the magenta boxes. Figure from [64].

Chapter 2

The Monolithic Active Pixel silicon Sensor prototypes for the ITS3

The first development of Monolithic Active Pixel silicon Sensors (MAPS) began in the 90s [80], when a detector fabrication process compatible with integrated circuit was designed, thus allowing for the production of monolithic devices comprising both high-quality electronics and sensitive volume [81]. Thirty years later the MAPS technology is established to be the most suitable one for trackers in high-energy physics where lightweight, low-power, low-noise and high-resolution sensors are needed. A benchmark application of the most advanced MAPS technology will be the ALICE ITS3 Upgrade, that foresees the replacement of the three innermost layers of the current ALICE Inner Tracking System (ITS2) by a truly cylindrical tracker, the ITS3, to be ready for LHC Run 4 (2029-2032). The ITS3 will be composed of three layers, each made by two flexible MAPS sensors of large area ($\mathcal{O}(10{\times}26\ \mathrm{cm}^2)$).

In this chapter the MAPS technology is described, followed by the delineation of the ITS3 layout and of the challenges that such advanced structure poses on the sensor characteristics. Finally, a detailed description of the sensor prototypes which are studied in this thesis (sec. 2.3) and their preliminary characterisation techniques (sec. 2.4 and 2.4) are outlined.

2.1 Monolithic Active Pixel silicon Sensors

Monolithic active pixel silicon sensors are semiconductor detectors. They are usually employed as position-sensing devices, thanks to their micron-scale pattering capabilities, but can be used also for energy-loss measurement, given their excellent energy resolution. The most advanced silicon detectors can now achieve a very low thickness, as they can be thinned down to approximately 50 µm, a low power consumption, a high granularity given the small pixel pitch of 10 µm multiples, and a low noise/signal ratio, hence satisfying the requirements for high-energy collision trackers. In this section the operating principles of silicon detectors are described, focusing on the MAPS technology.

2.1.1 Silicon properties

Silicon semiconductors are crystalline materials whose macroscopic arrangement exhibits an energy band structure, which is characterised by a valence band and a conduction band separated by an energy gap of $E_g = 1.12$ eV at room temperature. Electrons in the conduction band are free to roam about the entire crystal, whereas electrons in the valence band are bound to their respective lattice atoms. Silicon has four valence electrons, hence four covalent bonds are formed. At room temperature, a valence electron can be excited to the conduction band by thermal energy, leaving a hole in the valence band. Thus, an electric current can be generated in the semiconductor due to the movement of electrons in the conduction band and the movement of holes in the valence band. Electron/hole (e^-/h^+) pairs are continuously generated, reaching a concentration n_i in stable conditions. At T = 300 K the pairs concentration in silicon is $n_i = 1.5 \times 10^{10}\,\mathrm{cm}^{-3}$, meaning that only $1/10^{12}$ cm^{-3} atom is ionised.

In intrinsic semiconductors, n_i is the same for both electrons and holes. However, this equilibrium can be changed by adding pentavalent (donors) or trivalent (acceptors) atoms to the silicon crystal, to create respectively n-type and p-type silicon. The n-type silicon has an excess of electrons, whereas the p-type has an excess of holes. The concentration of the donors or of the acceptors in extrinsic semiconductors ranges from 10^{12} cm^{-3} up to 10^{20} cm^{-3} in highly doped silicon, which is denoted by adding a "+" sign after the material type as n+ and p+. In doped semiconductors the resistivity of the material is decreased, given the inverse proportionality between the concentration of the dopant and the resistivity.

2.1.2 The p-n junction

MAPS detectors functionalities rely on the p-n junction, which is obtained by joining together a p-type semiconductor and a n-type semiconductor. As shown in fig. 2.1, when the contact occurs an initial diffusion of electrons towards the p-region and a diffusion of holes towards the n-region takes place, until a stable condition is reached. Thus, a charge build-up arises in the semiconductor region near the interface: the p-type becomes negatively charged and the n-type becomes positively charged. This creates an electric field gradient and so a potential difference, known as the contact potential, across the junction.

The charged volume is known as the depletion region as it is empty of mobile charge carriers. It is a key element for ionizing radiation detection: a charge particle crossing the depletion region will liberate e^-/h^+ pairs, which are then driven by the electric field and create a signal proportional to the ionisation.

The width of the depletion zone depends on the concentration of n and p donors and can be increased by applying a reverse bias voltage, known as *back bias voltage*, allowing for the enlargement of the sensitive volume for radiation detection and thus improving the signal.

2.1.3 MAPS detectors

Monolithic active pixel sensors represent the state-of-the-art of silicon pixel detectors. They are characterised by the coexistence of the sensitive volume and of the pixel readout circuitry in the same silicon crystal. Their cross section consists of three layers as shown in fig. 2.2: a highly doped p^{++} substrate acting as mechanical support, a p^-

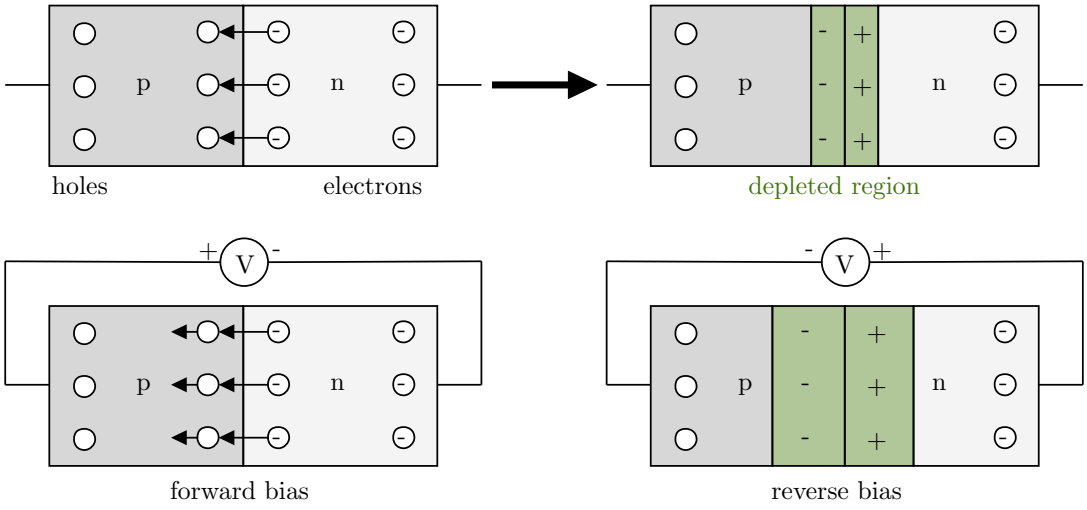

Figure 2.1: Depletion process of a p-n junction: when the two-type silicon are joined the positive free carriers in the p-type that are near the interface moves to the n-type, similarly act the holes in the n-type, hence a built in potential arises, generating a depletion zone which can be enlarged by applying a reverse bias voltage.

epitaxial layer which is used as the active volume and some *well* implants that are used to place the in-pixel circuitry. MAPS sensors are characterised by an high resistivity, that allows to achieve a large depletion volume in the epitaxial layer through a low back bias voltage, thus meaning that the epitaxial layer has a low doping concentration. The CMOS electronics, instead, requires to be placed in a highly doped region. Therefore, thanks to the deep pwell implants, that allows for the placing of PMOS transistors onto the pixel avoiding the competition in the charge collection between the collection diode and the nwell, the usage of a complete CMOS (Complementary Metal Oxide Semiconductor) circuity is permitted. A back bias voltage can be applied to the collection diode (nwell diode in the figure) to enlarge the depleted region.

MAPS technology provides low-power consumption thin detectors with high granularity and fast response.

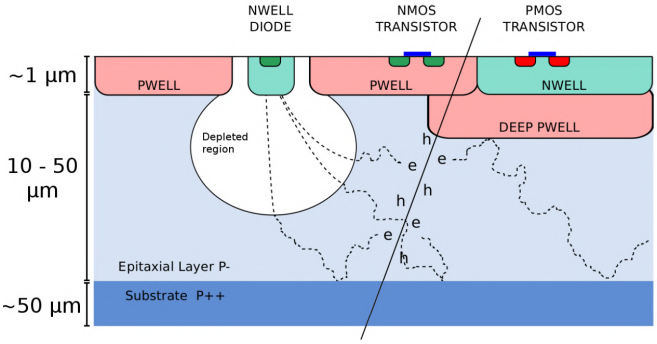

Figure 2.2: Schematic section of a MAPS pixel. A charge particle crossing the detector is represented. It generates e^-/h^+ pairs in the epitaxial layer. Electrons that reach by diffusion the depleted region are then collected mainly by drift.

2.2 The ITS3 layout

The upgrade project of the ALICE vertex detector provides for the use of state-of-the-art MAPS sensors. In this section the ITS3 structure and its challenges are presented.

The layout of the ITS3 includes two half barrels, each comprising three half-layers, as shown in fig. 2.3. The outermost layer is attached to an external Cylindrical Structural Shell (CYSS), which provides the main mechanical support to the entire structure. Each half-layer will consist of a single large-area ($\mathcal{O}(10\times26$ cm^2)) MAPS sensor fabricated in a 65 nm CMOS process, which will be flexible, thanks to its reduced thickness of 50 µm, and will be bent in a half-cylindrical shape, held in place by a series of half-wheel and longeron spacers made of ultra-lightweight open cell carbon foam. The reduction of the beam pipe outer radius, from 19.4 mm to 16.5 mm, and the cylindrical shape of the detector will allow placing the tracker closer (minimum radius of 19.0 mm) to the Interaction Point (IP) compared to the current ITS2 (minimum radius of 24.0 mm). A forced airflow between the layers and the carbon foam rings in thermal contact with the sensors will remove the heat generated by the sensors. The key parameters for the ITS3 are reported in tab. 2.1.

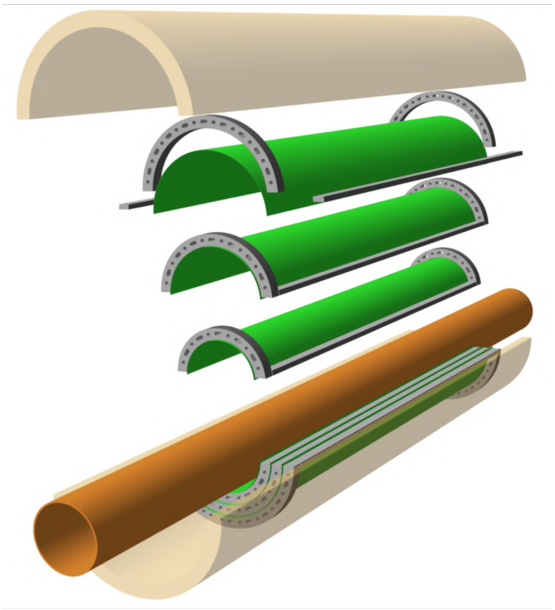

Figure 2.3: Schematic representation of the ITS3 layout. It consists of two half-barrels, each composed of three truly semi-cylindrical self-supporting layers. Each half-layer is made of one large-area ($\mathcal{O}(10\times26$ cm^2)) ultra-thin ($\leq$50 µm) bent stitched MAPS sensor, which is held in position by an ultra-light carbon foam support structure.

The overall design of the ITS3 will be significantly simplified if compared to the one of the ITS2 described in sec. 1.3, thus resulting in a marked reduction of the material budget. The azimuthal distribution of the material budget of a single inner layer of the ITS2, reported on the left in fig. 1.18, shows that the silicon sensor, which is the only component ideally needed, contributes less than 15% to the mean total value of 0.36% X_0 [64]. Moreover, the distribution is not homogeneous along ϕ because of support structures, cooling system and stave overlaps. The removal of the materials associated with the non-silicon components envisaged for the ITS3, will allow the achievement of an unprecedented low material budget of 0.09% X_0 per layers, along

	Layer 0	Layer 1	Layer 2
Radius (mm)	19.0	25.2	31.5
Sensor dimension (cm^2)	26.6×5.87	26.6×7.83	26.6×9.78
Pseudo-rapidity coverage	±2.5	±2.3	±2.0
Material budget (% X_0 / layer)		0.09	
Silicon thickness (µm / layer)		$< 50\,\mu m$	
Pixel size (μm^2 / layer)		$\mathcal{O}(20\times22.5)$	
Power density (mW/cm^2)		40	
NIEL (1 MeV n_{eq} cm^{-2})		10^{13}	
TID (kGy)		10	

Table 2.1: Key parameters of the future ITS3 [40].

with a more uniform distribution in φ (fig. 2.4).

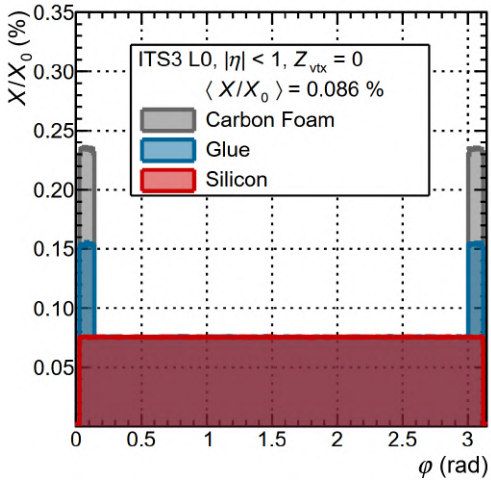

Figure 2.4: Azimuthal distribution of the material budget of a single ITS3 layer for tracks of particles originating from the interaction point. Figure from [40]

A Fast Monte Carlo Tool (FMCT) was used to study the pointing resolution and the tracking efficiency of the ITS3 [64]. The pointing resolution is defined as the dispersion of the Distance of Closest Approach (DCA) of the reconstructed primary tracks to the interaction point and represents the capability of the vertex detector to distinguish between primary and secondary vertices. The comparison of the ITS3 and the ITS2 pointing resolution, given in fig. 2.5a for primary charged pions, shows that for $p_T \simeq 1$ GeV the pointing resolution of the ITS3 is a factor of two better than that of the ITS2. Similarly, the comparison of the ITS3 and ITS2 tracking efficiency given in fig. 2.5b, shows that for low transverse momentum the ITS3 performance is better than that of the ITS2.

The expected radiation load for ITS3 will increase by $60 - 70$ % [64] with respect to the ITS2 load because of the reduced distance from the interaction point, although it will still be below the ALPIDE reference tolerance of 10^{13} 1 MeV n_{eq} cm^{-2} (Non Ionizing Energy Loss, NIEL) and 10 kGy (Total Ionizing Dose, TID), which will be maintained if not improved in a new sensor.

The detector components of the new vertex detector must meet the requirements

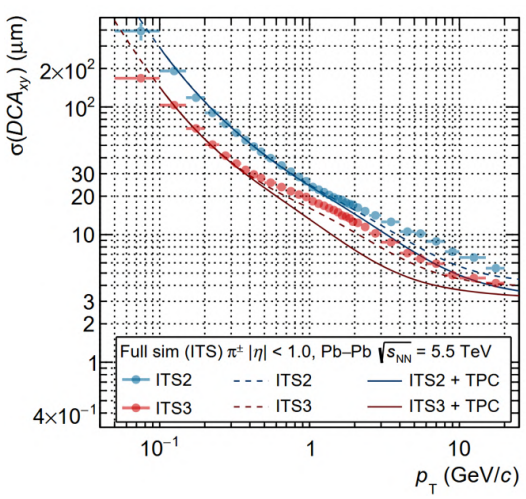

(a) Pointing resolution for primary charged pions with $|\eta| < 1$ in the transverse plane as a function of p_{T}. The line of interest is the continuous one. Figure adapted from [40].

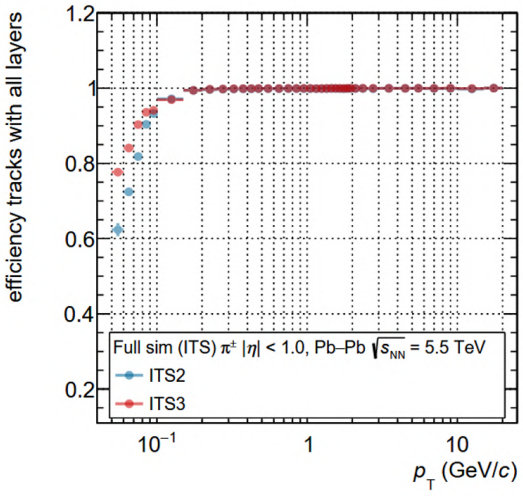

(b) Tracking efficiency for charged pions with $|\eta| < 1$ as a function of p_{T}. Only tracks with a hit on each layer are considered. Figure adapted from [40].

Figure 2.5

set out in tab. 2.1, moreover they must ensure high accuracy in the relative position of the detector sensors and a stability of the system lower than the sensor resolution.

Each half-layer of the ITS3 is made of the following components (fig. 2.6):

- a single bent wafer-scale silicon sensor;
- a polyimide Flexible Printed Circuit (FPC) on each side of the half-layer. The A-side FPC provides the data and powering transmission, the C-side FPC provides only powering. The powering lines reach the C-side FPC from the A-side, traveling along the CYSS;
- two lightweight carbon-foam longerons, placed along the sensor's long edges, that provide mechanical support along the beam direction, and two half-rings to keep the FPCs bent and aligned to the sensor;
- a manifold, which acts as gas distributor for the air-cooling system and that provides additional support to the A-side FPC. The A-side half-ring also acts as a thermal radiator.

An engineering model of half-ITS3, made of three half-layers bonded together to achieve an ultralight and stable assembly, is shown in fig. 2.7. It is used to finalise the assembly procedure, the technical specifications and drawings.

2.2.1 Mechanics and cooling

The mechanics must ensure the stability of the sensor positions over time while minimising the inactive material, to satisfy the stringent requirements (<0.09% X_0) on the material budget. The air cooling system, which was chosen to avoid introducing liquid coolant pipes into the active area, must guarantee a stable operation of the detector by

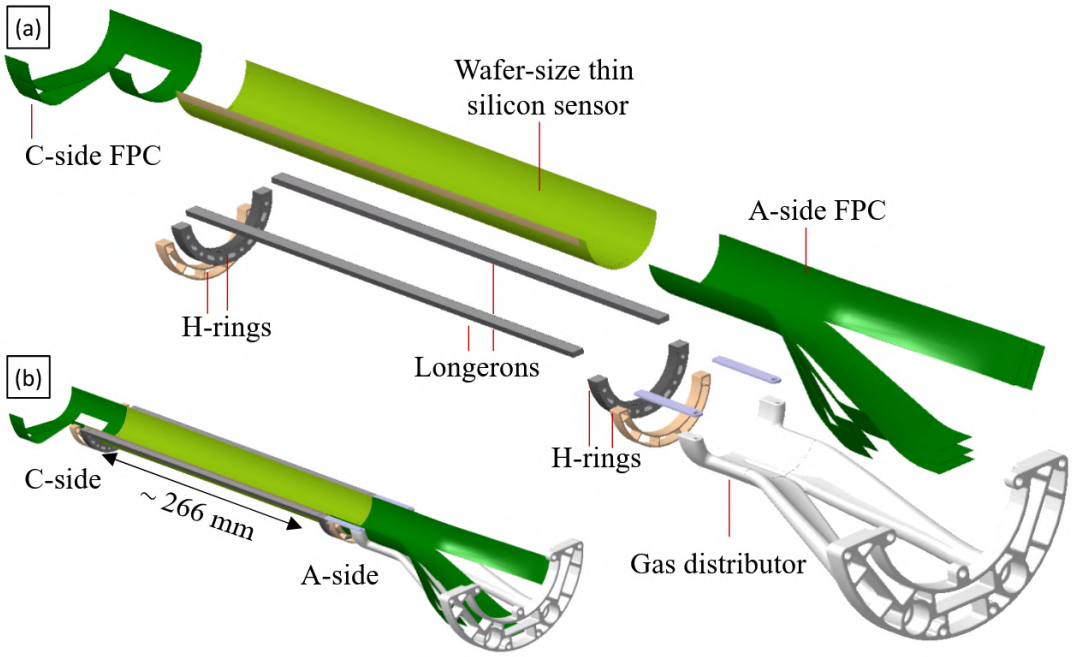

Figure 2.6: Exploded view and assembled view of an ITS3 half-layer. Figure from [40].

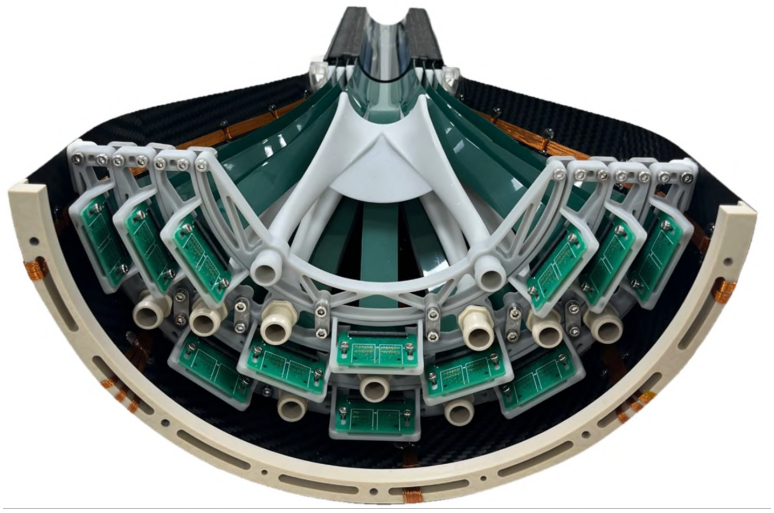

Figure 2.7: Qualification model of half ITS3.

keeping the operating temperature of the sensor lower than 30 °C and the maximum temperature gradient in the pixel matrix region lower than 5 °C.

Two types of open-cell Reticulated Vitreous Carbon (RVC) foam were chosen for the support structures due to their mechanical and thermal properties. The half-rings on the C-side and the longerons (fig. 2.6) will be made with RVC with low density and high Young's modulus (Duocel® RCV). An RCV with added graphite coating (Allcomp K9 standard density) with high thermal conductivity will be used for the half-rings on the A-side, which will act as radiators, to increase the surface area in contact with the airflow.

The air cooling system must provide effective dissipation of the heat produced by

both the sensor endcap (see sec. 2.3.2) and matrix. The carbon foam ring on top of the sensor endcap efficiently conducts the significant localised heat generated in this area to the surrounding air, where it is dissipated by convection. Instead, the heat produced by the sensor matrix is removed through direct forced convection, with airflow passing through the holes and slots in the half-ring

An ITS3 breadboard model, with detection half-layer mock-ups consisting of dummy silicon embedded in polyimide heaters, was assembled to evaluate the thermal performance of the final detector. Two copper serpentines are integrated in the dummy half-layers to simulate the heat generated in the endcap and in the matrix. An airflow from the C-side to the A-side is supplied to the system through a wind tunnel. The thermal tests conducted with this setup and the comparison of the results with Computational Fluid Dynamics (CFD) simulations, demonstrated that the detector can be operated at a temperature of 5 °C above the inlet air temperature using an average airflow velocity of about 8 m/s. The temperature gradient across the sensor can be kept within 5 °C (fig. 2.8). The results were obtained with a surface power density of 1000 mW/cm^2 for the endcap and of 50 mW/cm^2 for the matrix, for which a target of 40 mW/cm^2 is envisaged.

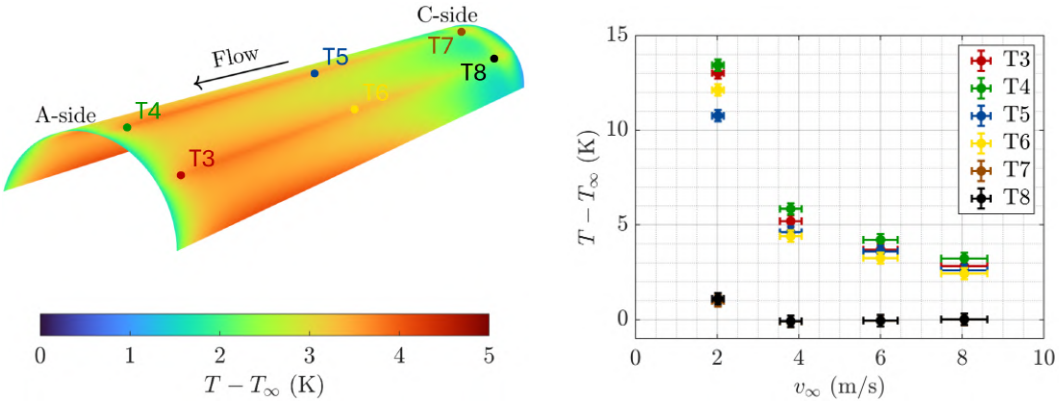

(a) Temperature gradient on a single ITS3 half layer simulated using a CFD model. T is the temperature of the detector and T_∞ is the air temperature. The dots represent the temperature sensor locations.

(b) Measured temperatures on a single half-layer of the ITS3 breadboard model in the positions indicated in fig. 2.8a as a function of the airflow velocity.

Figure 2.8

2.2.2 Interconnections and off-detector electronics

The detector is connected to the external readout electronics and power supply via Flexible Printed Circuits (FPC). Ultrasonic wire-bonding is used to connect the FPC to the sensor.

Three stacked double-sided FPCs connect each layer from the detector A-side (see fig. 2.9). This configuration was chosen to facilitate the passive component, i.e. decoupling capacitors and connectors, assembly on the FPC tail. Each FPC consists of 3, 4 or 5 equal sections, mirroring the number of chip segments of the half layer it belongs to. Each section provides analogue and digital power, bias voltage, six high-speed (10.24 Gb/s) lines for data transmission and six lines for clock (160 MHz) and control

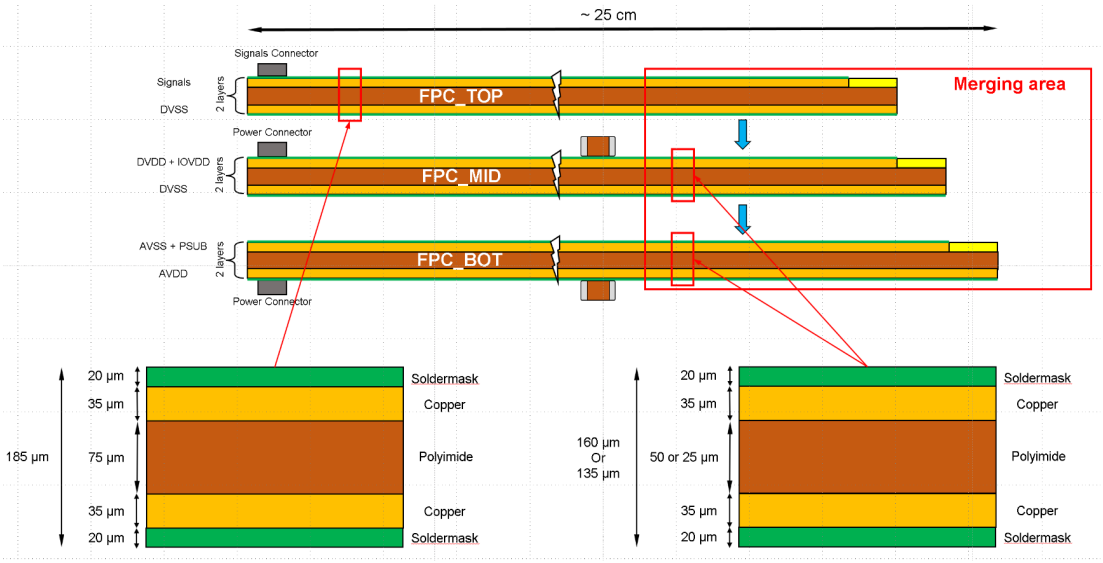

Figure 2.9: On top a schematic representation of three double-sided FPCs (top, dedicated to signal transmission; middle and bottom, dedicated to the power distribution), which are stacked and interconnected to serve one ITS3 half-layer. The two magnifications on the bottom show in detail the material cross-section of the FPC, for the top (*left*), and middle and bottom (*right)* FPC layers, highlighting the difference in polyimide substrate thicknesses.

(5 Mbit/s). FPCs connected on the C-side of the detector provide only powering. A stacked FPC for the innermost layers, with three segments is shown in fig. 2.10a. A detail of the wire-bonds connecting the FPC to the sensor is shown in fig. 2.10b

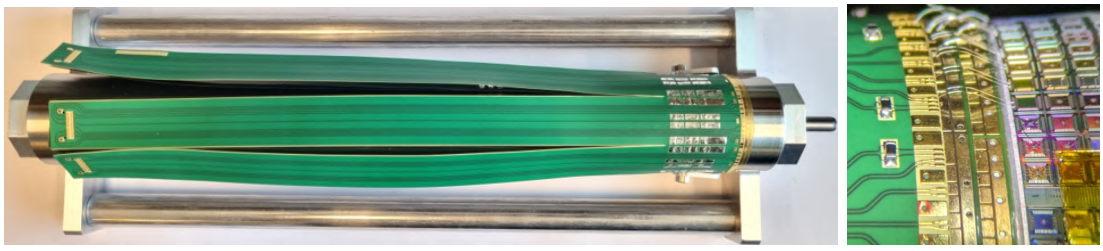

(a) (b)

Figure 2.10: (a) Stacked FPC for an innermost half-layer, mounted on a mandrel. The three segments are visible. (b) Wire-bonding test between an FPC mounted on a mandrel and some bent ITS3 prototypes.

The FPCs connect the sensor to the off-detector electronics, which is responsible for powering, controlling and monitoring each sensor segment and data transmission. Fig. 2.11 shows a schematic representation of the off-detector electronics. Starting from the right, the Central Trigger Processor (CTP), the Detector Control System (DCS) and the data processing farm are connected to the Detector Service Electronics (DSE) via the Common Readout Unit (CRU), which provides trigger, control and readout connections. The ITS2 FPGA-based readout is removed, while 12 ITS2 CRUs will be reused for the ITS3, although a firmware upgrade is required. The DSE is split

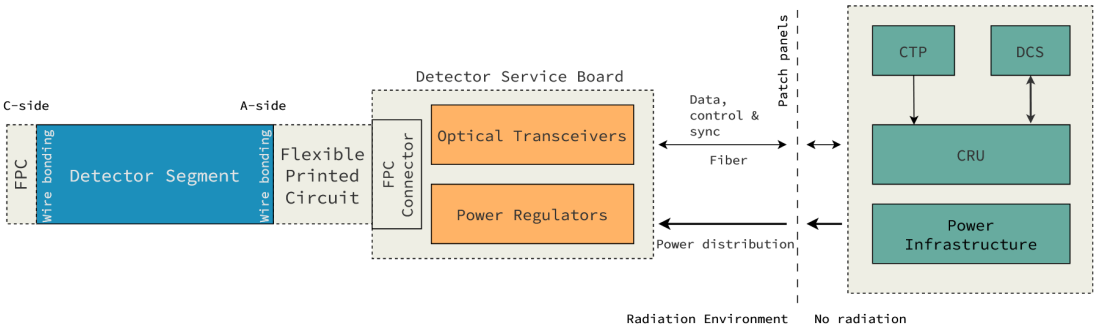

Figure 2.11: Schematic representation of the off-detector electronics for one detector segment.

in several sub-units, the Detector Service Boards (DSB). The DSB are placed in the service barrel, as close as possible to the detector to allow a data rate of 10.24 Gb/s. Each DSB is connected to a subset of the chip segments of the half-barrel.

The power distribution is made via the DSB as well, which will be supplied in turn by commercial rack power supplies. Additionally, the DSE will provide the reverse-substrate bias.

2.2.3 Silicon sensor bending

Wafers for the ITS3 prototypes are thinned down to 50 µm by back-grinding process. The reduced thickness enhances the silicon flexibility and facilitates the curvature of the sensor. The mechanical stability and the performance of bent chip fabricated in a 180 nm and 65 nm CMOS process has been investigated.

The prototypes were systematically bent down to radii much smaller than the ITS3 target radii to measure the force applied as a function of the displacement, which is defined as the distance between the original position and the bent position of the sensor centre, and the point of breakage. Fig. 2.12 shows these quantities for ALPIDE and ITS3 chips (indicated as 65 nm processed) with different thickness. The point of breakage is reached only for the 50 µm sensors, at radii much below the ITS3 innermost layer radius.

The performance of bent ALPIDEs and bent 65 nm CMOS prototypes was evaluated, to verify the effect of bending on both analogue and digital parts. Results obtained with both sensor series show that bending does not significantly alter the performance of the chip [82, 40].

2.3 The sensor prototypes for the ITS3

The ITS3 sensor development represents a major R&D challenge due to its uniqueness in terms of large area and flexibility. The key idea behind the development of a wafer-scale MAPS sensor is to make use of the *stitching*, a process used in semiconductor manufacturing to create large-scale chips by "stitching" together smaller regions of a chip design, overcoming the size limits of the photolithographic equipment. Moreover, the need to remove the external electrical busses providing power distribution and data transmission to reduce the material budget, requires to embed all these functionalities in the stitched sensor. For a further description of the stitching technology, see sec. 2.3.2.

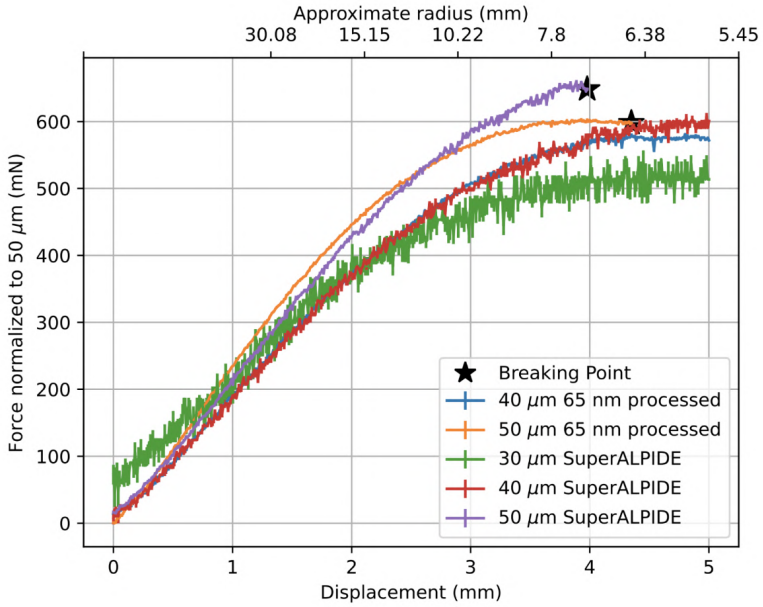

Figure 2.12: Force applied to bend silicon sensors of different thickness as a function of the displacement and of the approximate radius. Different colours represent different thicknesses and sensors.

A single MAPS-based silicon sensor which is large enough to cover the dimensions of a ITS3 half-layer and with the required features is only available in the 65 nm CMOS process standard, which allows for the production of 30 cm diameter wafers and the application of the stitching technique. Since sensors in such process were never used before in high-energy physics experiments, the ITS3 R&D program includes a wide campaign to test the technology performance and radiation hardness. A robust sensor development plan has been envisioned to accomplish the design and production of the final ITS3 sensor within schedule. The plan includes four productions:

- the Multiple Layer Reticle 1 (MLR1), including multiple small-scale test structures to validate the 65 nm CMOS imaging technology for this application; the chips were received in 2021 and fully characterised;
- the Engineering Run 1 (ER1), including the first large-scale stitched MAPS to validate the stitching technique, and multiple test structures; the chips were delivered in 2023 and are now fully characterised;
- the Engineering Run 2 (ER2), including the full-scale and fully functional sensor prototype; the chips are expected to be delivered at the end of 2025 and the characterisation will start immediately after dicing;
- the Engineering Run 3 (ER3), dedicated to the final ITS3 sensor production, expected for delivery in 2027.

This thesis work is part of the activities carried out for the MLR1 and ER1 prototypes characterisation.

2.3.1 The Digital Pixel Test Structure

The first ITS3 prototype characterised within this thesis work is the Digital Pixel Test Structure (DPTS), a silicon MAPS sensor included in the ITS3 MLR1 production. It represents a proof of concept for the usage of the 65 nm CMOS imaging technology in digital MAPS sensors. Moreover, the initial analogue and digital stages of the DPTS in-pixel logic resembles the ones expected for the final ITS3 sensor.

The DPTS consists of a matrix of 32×32 pixels plus an additional monitor pixel. The pixel pitch is of 15 µm and the sensor is 50 µm thick. The overall dimensions are $1.5 \times 1.5 \times 0.05$ mm^3. It features an asynchronous digital readout, a time-based encoding of hit position and a Time-over-Threshold (ToT) encoding of the signal amplitude, which retains the analogue information about the detected signal after the digitisation [83, 84].

From the photo of a DPTS showed in fig. 2.13a, it is possible to identify the detector matrix, which occupies the squared region at the centre, with a visible pixel structure. All around the matrix a series of guard rings prevent the diffusion of electrons generated outside the main array towards the pixel area. In the outermost part it is possible to identify 12 pads for each side. Each interconnection pad is then wire-bonded to the carrier card to operate by powering, configuring and reading out the chip (fig. 2.13b). There are three power domains:

- **Analogue:** AVDD and AVSS indicate the reference voltage and ground levels for the pixel analogue front-end, comprising amplifier and discriminator, and for the monitor pixel power domain.
- **Digital:** DVDD and DVSS indicate the reference voltage and ground levels for the pixel digital readout and peripheral configuration circuitry.
- **CML buffer:** BVDD and BVSS indicate the reference voltage and ground levels for the Current Mode Logic (CML) buffer that gives the digital output.

The reverse bias voltage applied to the substrate and the bias for the pixels p-wells are provided via the pads placed on the carrier card.

The functional diagram of the DPTS is shown in fig. 2.14, where the main building blocks are highlighted. Starting from the left, the in-pixel amplifier receives the signal that can be either generated in the collection diode that represents the sensor p-n junction or artificially created by the injection capacitance C_{inj}. The amplified signal is then shaped and compared to a voltage level, i.e. the sensor threshold. If the signal amplitude is larger than the threshold then the signal is digitised and, if the pixels is not masked via the shift register, the hit position and its ToT are time-encoded by the pixel address generator. The hit merger in the sensor periphery will combine the digital signals of the 1024 pixels in a single output then passed to the Current Mode Logic (CML) driver, which generates the final output signals in a positive/negative polarity that is then read out with an external oscilloscope (see sec. 2.3.1.4). The single monitor pixel sends directly the analogue shaped signal to an analogue buffer that transmits this signal to the output. A detailed description of the in-pixel front-end can be found in sec. 2.3.1.1

2.3.1.1 DPTS in-pixel front-end

The analogue in-pixel front-end circuit is shown in fig. 2.15 [83]. The amplification and reset stage and the discrimination stage are pointed out. Four currents (I_{bias}, I_{biasn},

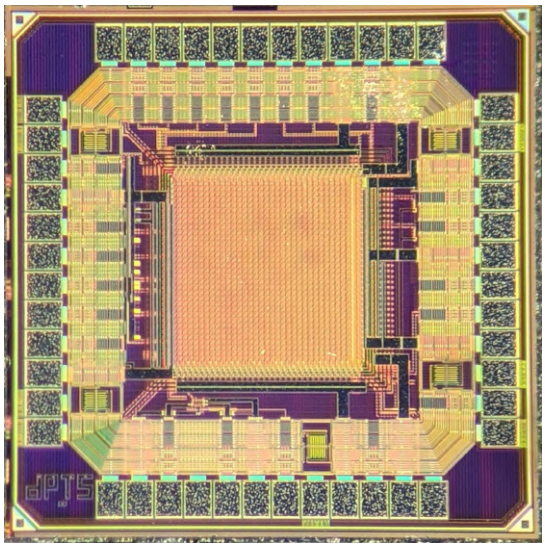

(a) Photo of a DPTS.

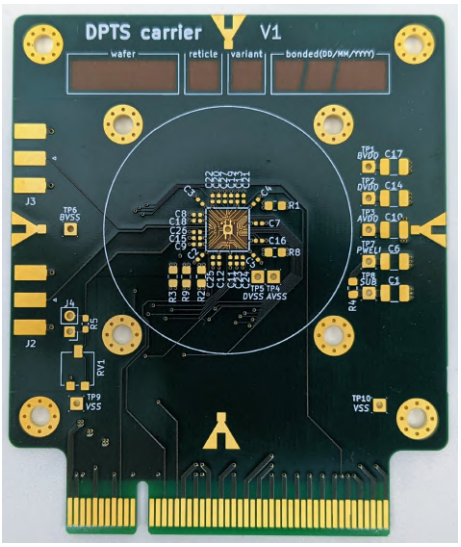

(b) Carrier card specifically developed to operate the DPTS sensors.

Figure 2.13

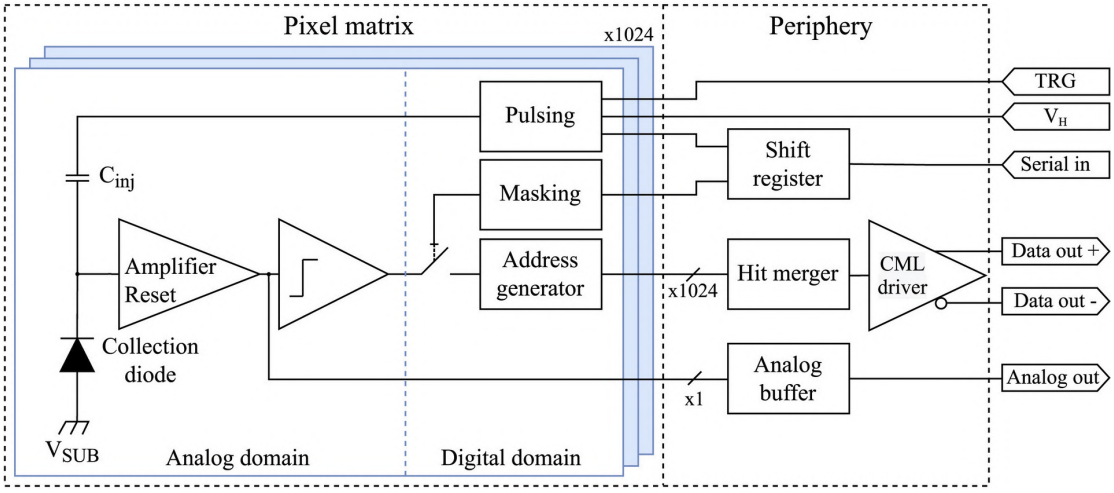

Figure 2.14: Functional diagram of the DPTS, figure from [83].

I_{reset} and I_{db}) and two voltages (V_{casb} and V_{casn}) control the circuit, by providing the reference levels to the transistors. These currents and voltages are externally generated and provided via the interface pads on the chip. The circuit [85] is based on a two-stage (cascoded) high gain inverting amplifier. Thanks to the cascoded topology, such amplifier is very fast and stable. Its input requires a direct feedback from the output to avoid saturation of the output and to correctly define the amplifier operating point inside its linear region. The V_{casb} transistor M6 and the I_{reset} transistor M5 are part of the feedback loop and automatically set the correct voltage on the collection electrode. In particular, the feedback balances the current passing through the V_{casb} transistor, so that the total current entering the node is equal to the current leaving the node, equal to the difference between I_{reset} and the leakage current on the collection electrode.

When charge is collected on the collection diode, the circuit responds dynamically.

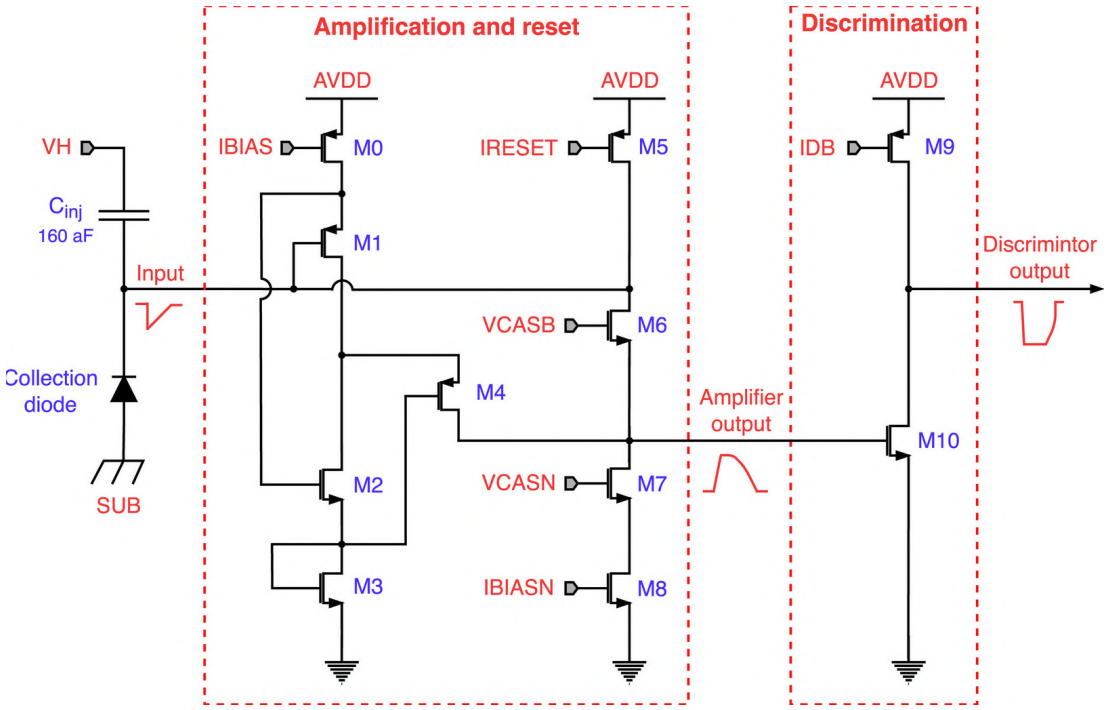

Figure 2.15: Analogue in-pixel front-end of the DPTS. Figure from [83].

The incoming charge generates a negative voltage drop on the input node, such signal is then amplified and inverted by the inverting amplifier. The positive voltage excursion output of the inverting amplifier is connected to the source of the V_{casb} transistor, making it switch off. The I_{reset} current then resets the voltage at the input node linearly, since the current is constant, resulting in a close to linear time-over-threshold behaviour.

The output of the amplification and reset stage is the input to the discrimination stage, a common-source stage comprising the transistors M9 (I_{db}) and M10. Once the amplifier output reaches a threshold voltage and makes the transistor M10 to overcome I_{db}, the voltage at the output of the discrimination stage will suddenly drop from the supply voltage AVDD to ground, generating a digital signal. The additional monitoring pixel of the DPTS features a source follower instead of the common-source stage, buffering the analogue output directly to the interface pad.

The main branch of the front-end (I_{bias}, M0-M3) operates with currents between 10 nA and 5 µA. The I_{biasn} current, operated at one-tenth of the I_{bias} current, and the V_{casn} voltage further control the operating margin of the amplifier. Moreover, the reverse bias V_{pwell} applied to the sensor affects the NMOS transistor, thus V_{casb} and V_{casn} require to be adjusted to V_{pwell} and current levels in the circuit.

The main power consumption contribution is given by the I_{bias} current in the main branch, since the I_{reset} current is orders of magnitude lower and the I_{db} current is flowing only when transistor M10 is active.

An additional capacitance C_{inj}, with a design value of 160 aF, can be used to inject a test charge in the collection electrode. The external voltage reference level V_h regulates the amount of charge injected.

2.3.1.2 The matrix readout via the CML output

A pixel fires when it is hit by a particle or when it is manually pulsed with the internal capacitance. The produced signal goes through the circuit described in the previous sections up to the CML buffer. The CML output can be read with an oscilloscope. It consists in two differential digital outputs, one positive and one negative. The superposition of the two signals (fig. 2.16) gives two trains with four crossings for each hit. The first train is generated when the pixel analogue signal overcomes the threshold and therefore it is addressed to as "rising". The time distance between the first and the second crossing is fixed. Instead, the time distance T_PID between the first crossing and the third varies according to the firing pixel position in the column. Likewise, the time distance T_GID between the third crossing and the fourth varies according to the firing pixel position in the row. The same time encoding scheme is repeated between the four crossings of the second train. The second train is generated when the pixel analogue signal returns below the threshold and therefore it is addressed to as "falling". The time distance between the first train and the second train is equal to the *Time-over-Threshold* (ToT) of the pixel analogue signal. The order of magnitude of the time distance encoding positions is of ns, instead the ToT can go up to several tens of µs according to the analogue signal. A linear relation holds between T_PID, T_GID and respectively the number of the column (x) and the number of the row (y):

$$T\_PID = T_x + \delta_x x \tag{2.1}$$

$$T\_GID = T_y + \delta_y y \tag{2.2}$$

Where T_x and T_y are two fixed offset and δ_x and δ_y are respectively the x and y encoder step.

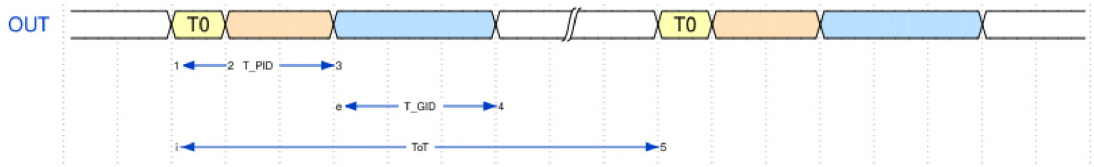

Figure 2.16: Schematic representation of the superposition of the positive and negative CML buffer outputs.

The matrix is organised in 32 columns and 32 rows. Nevertheless, from the readout point of view, it behaves as a single column of 1024 pixels with a continuous readout sharing the same CML output. The readout sequence is represented in fig. 2.17a. First the events coming from the columns under the red dashed line are collected. After a delay dTx also the events coming from the columns under the green dashed line are collected.

This alternate readout was implemented to avoid as much as possible signal overlaps due to charge sharing in horizontal direction. However, overlaps due to charge sharing or multiple events in vertical direction are still possible. A possible output is shown in fig. 2.18 for the simultaneous firing of two pixels i and j belonging both to the pixels group under the red dashed line or under the green dashed line in fig. 2.17. The output is an XOR coincidence of the signals of the two pixels. The position of the hit and the ToTs are no more decodable.

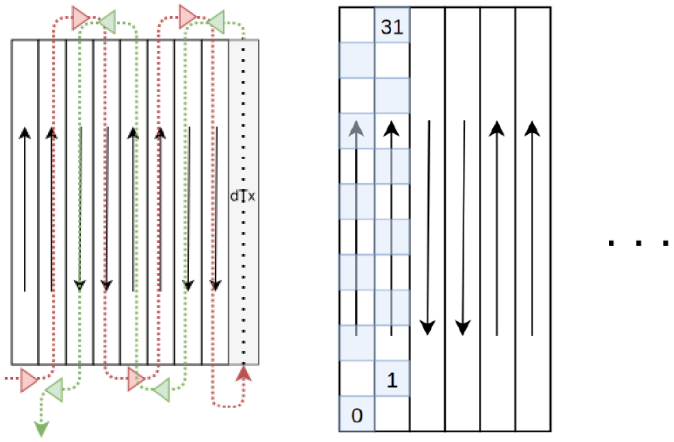

(a) Readout scheme of the DPTS matrix.

(b) X version readout scheme of the DPTS matrix.

Figure 2.17

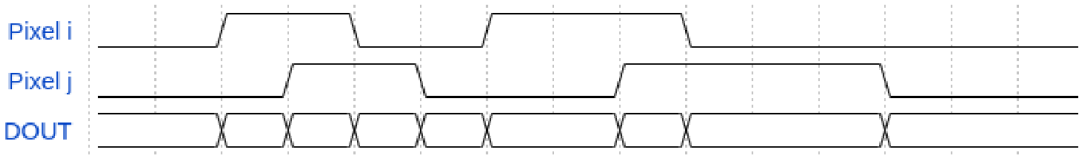

Figure 2.18: Possible output in case of multiple pixel firing.

The DPTS is available in three readout versions, named **X**, O and S, the overlap due to charge sharing in vertical direction is partially avoided in the X version readout, where the pixels are read with a chessboard pattern. An example is provided in fig. 2.17b, where a column for the digital readout is represented by the light blue pixels. Since the laboratory testing revealed no difference in the performance of different readout versions, no distinction will be made.

2.3.1.3 Doping profile

MLR1 prototypes were produced in three different versions with respect to the doping implants in the sensing volume, named *standard*, *modified* and *modified with gap* respectively (fig.2.19).

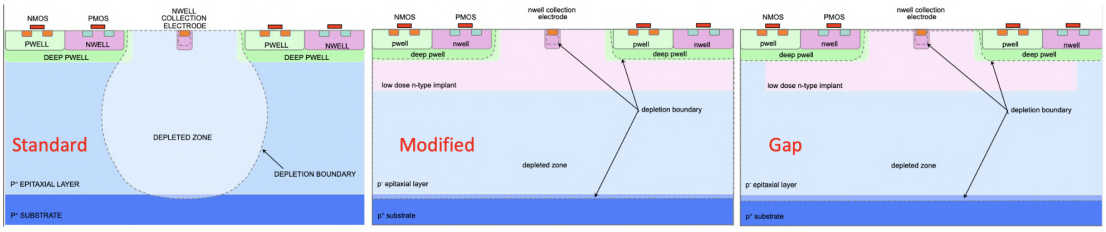

Figure 2.19: Schematic representations of the three version of the MLR1 doping profile.

Standard process. The standard version is the one realized with a doping profile which was extensively used for existing MAPS silicon sensors, like the ALPIDE chip [58, 59, 60]. The chip cross section is characterised by a highly p-doped (p^+) substrate that provides mechanical support to the structure, a p-doped (p^-) epitaxial layer used as the active volume and the CMOS circuitry layer where the in-pixel readout electronics is implemented. *Nwell* implants in the circuitry layer act as collection diodes for the signal released in the active volume. The depletion of the epitaxial layer depends on the back bias voltage applied to the collection diode. The depletion extends almost radially from the collection electrode (fig. 2.19 left). Even the maximum applied back bias voltage is not expected to deplete the whole epitaxial layer volume.

Modified process. The modified process differs from the standard process for an additional low dose n-doped implant between the circuitry layer and the epitaxial layer. This modification makes it possible to uniformly extend the depleted region to the whole epitaxial layer, allowing for a more efficient charge collection process.

Modified process with gap. The most recent version results from the optimisation of the previously described processes. As the modified process, it is characterized by an additional low dose n-doped implant between the circuitry layer and the epitaxial layer, this time with a small gap between different pixels. The depleted region is still covering the whole epitaxial layer, and the gap helps to avoid unwanted effects of charge sharing.

The DPTS implements the modified with gap process, which has been produced in four so-called splits named 1, 2, 3, 4, which gradually modify the doping concentrations of the various implants [86]. Split 1 applies the standard doping profiles. Split 2 has an improved deep p-well to allow a better isolation between sensor and circuitry and to prevent punch-through between deep p-well and circuitry, for a larger operating margin. Split 3 has an adjustment of the deep n-well to allow full depletion. Split 4 shows the most aggressive modification to the doping with respect to split 1, the deep-p well is further modified to prevent potential wells created by the circuitry.

All the DPTS studied in this work implement the split 4 modified process with gap.

2.3.1.4 The DPTS test system

An electronic test system is used to operate the DPTS and conduct standard laboratory test. The same system can be integrated into a tracking telescope for synchronised in-beam data-taking.

The setup is composed of a computer, an oscilloscope, a power supply, a Data-AQuisition (DAQ) board, a proximity board and a carrier card hosting the chip under test. The core components of this setup are the DAQ board (fig. 2.20a) and the proximity board (fig. 2.20b), both custom made by the ALICE ITS3 Collaboration specifically to test these sensors. The system is controlled by the Field Programmable Gate Array (FPGA) on the DAQ board. The power to the chip is provided via the connection on the DAQ board. The reference levels in voltage or current for the settings to operate the chip are controlled by the DAQ board via the proximity board.

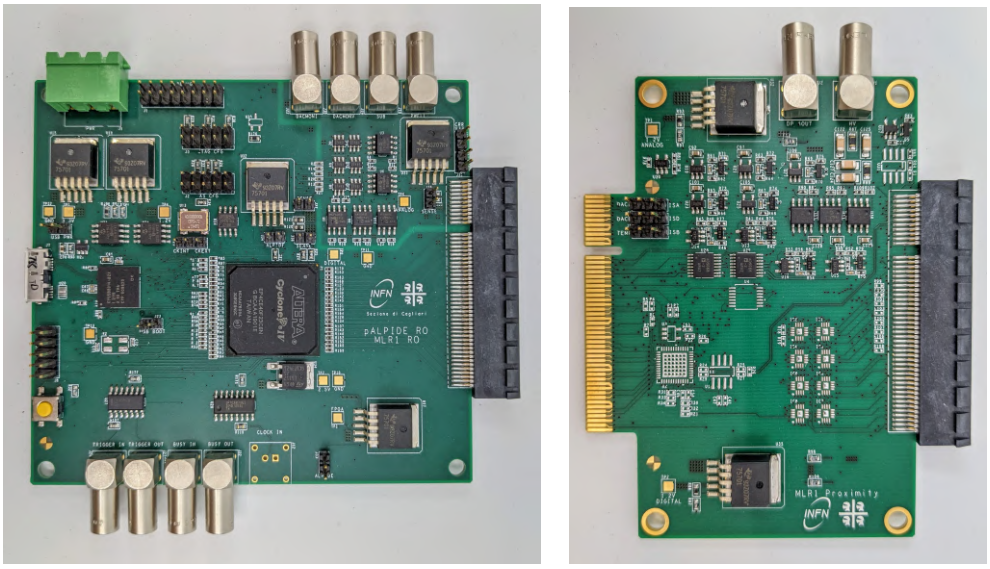

(a) *DAQ board.* (b) *Proximity board.*

Figure 2.20

2.3.2 The MOnolithic Stitched Sensor

The second ITS3 prototype characterised within this thesis work is the MOnolithic Stitched Sensor (MOSS), a silicon MAPS detector included in the ITS3 ER1 production and fabricated with the 65 nm CMOS technology. MOSS is the first large-area (1.4×26 cm^2) sensor prototype for the ITS3, aimed at the implementation and validation of the stitched design, and at the characterisation of different possible solutions in terms of pixel pitch and front-end layout. Indeed, it includes 10 Repeated Sensor Units (RSU), each comprising eight regions organized in two half units, named *top* and *bottom*, with pixel arrays of different dimensions (256×256 and 320×320) and pitches (18 µm and 22.5 µm). Endcaps placed at the two ends complete the chip. Fig. 2.21 shows a MOSS schematic representation.

The two half-units differ in circuit density and in widths and spacing of the interconnecting metal structures. The eight regions differ in the front-end (see sec. 2.3.2.3).

The MOSS is also available in a smaller structure comprising a single Readout Sensor Unit, that is named *babyMOSS*. Although smaller than the MOSS, the babyMOSS is a fully functional sensor, to be used for the ER1 characterisation.

2.3.2.1 Stitching technology

The stitching technology allows for the fabrication of a sensor that is larger than the reticle size, which in standard CMOS circuit manufacturing defines the limit in the sensor dimensions, by placing the reticles on the wafer with high precision achieving a well-defined overlap. In-silicon interconnections and peripheral structures along the outer edges of the resulting large-area chip allow for the routing of the power and the data to be embedded in the chip. The three layout components of the MOSS design reticle are shown in fig. 2.22a: a Left End-Cap (LEC), a Right End-Cap (REC) and the Repeated Sensor Unit. The MOSS sensor consists of ten RSU placed side by side with one LEC and one REC placed at the corresponding ends, as shown in fig. 2.22b,

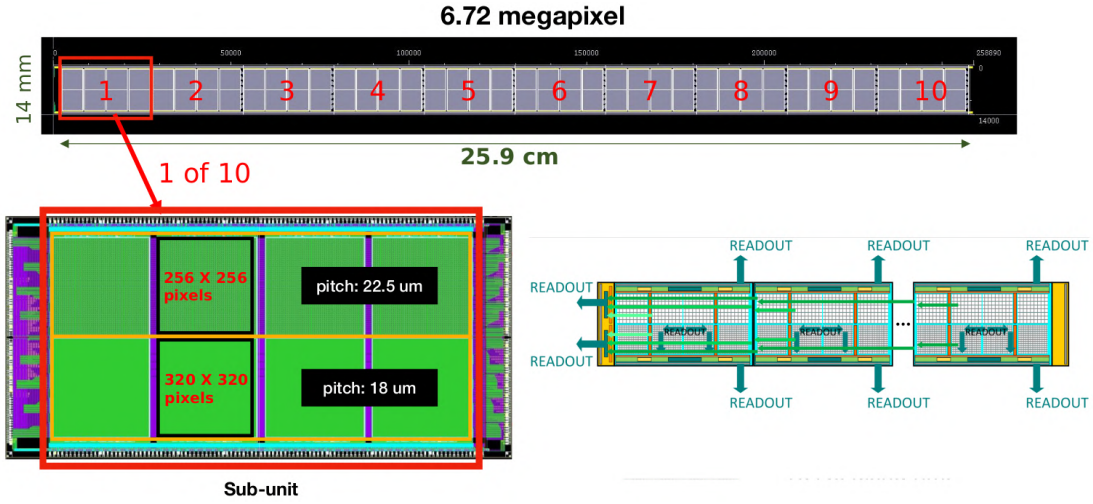

Figure 2.21: Schematic representations of the MOSS sensor. A repeated sensor unit is magnified and one region for each half-unit is highlighted.

resulting in a one-dimensional stitched layout.

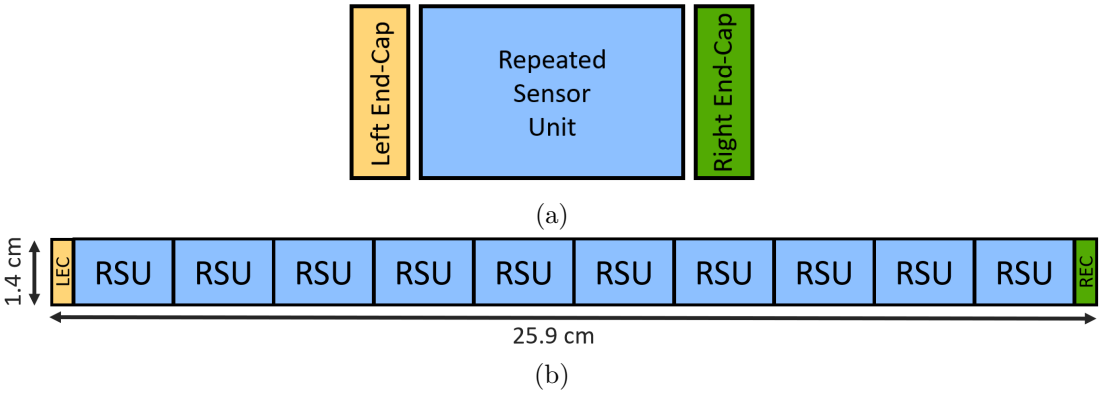

Figure 2.22: (a) Schematic design reticle with the MOSS components, i.e the Left End-Cap (LEC), the Right End-Cap (REC) and the Repeated Sensor Unit (RSU). (b) Schematic representation of the Monolithic Stitched Sensor (MOSS), fabricated with the layout components shown in (a).

2.3.2.2 MOSS architecture

Fig. 2.23 shows the functional block diagram of a MOSS bottom half-unit. The block diagram of the top half-unit is symmetrical. Half of the three layout components, the LEC, the RSU and the REC, is visible. The four regions are highlighted, illustrating the contained blocks. Supply, control and readout connections are schematically indicated. The sensor can be operated either from the long edge or from the short edge. In the first case each half unit can be operated individually via the peripheral wire bond pads. In the second case the sensor is operated via the LEC, that provides supply, control and readout connections, and REC, that provides only powering. In the MOSS sensors only the rightmost and leftmost RSUs can be powered via the end-caps, due

to conductivity limitations of the in-silicon transmission lines. The stitched backbone, indicated on the bottom in the figure, is a set of transmission lines that allows for inter stitching communication when the sensor is operated from the LEC. The half-units can be electrically disconnected from the stitched backbone to be controlled from the peripheral pads (fig. 2.24a). A grid on top of the entire chip distributes powering (fig. 2.24b).

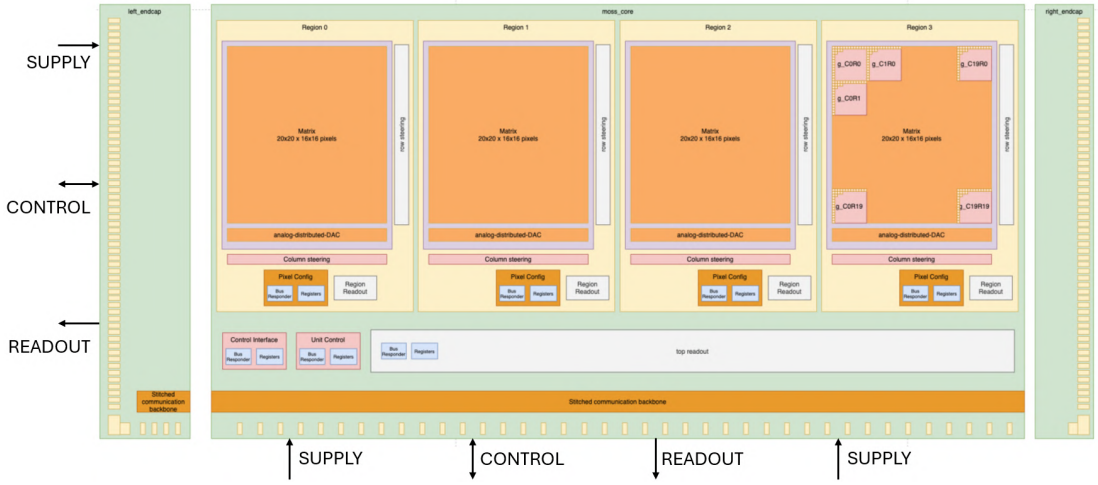

Figure 2.23: Architecture of a MOSS bottom half-unit.

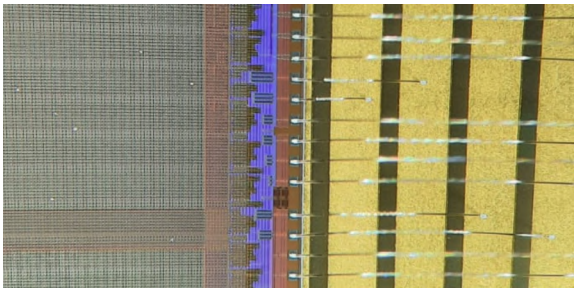

(a) Close up of the connection via the peripheral pads of the sensor. The stitched backbone is visible on the bottom.

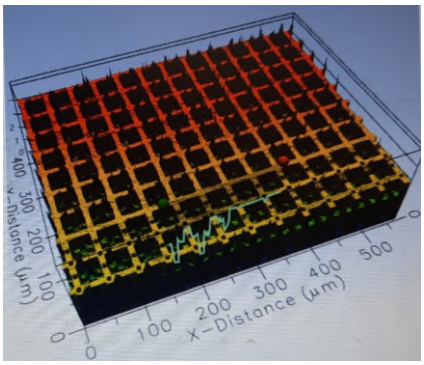

(b) Power distribution grid on top of the sensor.

Figure 2.24

The analogue and digital power domain are individual for each half-unit, while the reverse bias is global for the entire chip.

2.3.2.3 MOSS in-pixel front-end

The in pixel front-end is shown in fig. 2.25. It is derived from the logic of the DPTS described in sec. 2.3.1.1. An additional voltage reference level, V_{shift}, controls the bias on the collection diode thus reducing the main front-end biasing current. The other operating principles of the circuit are the same described for the DPTS logic.

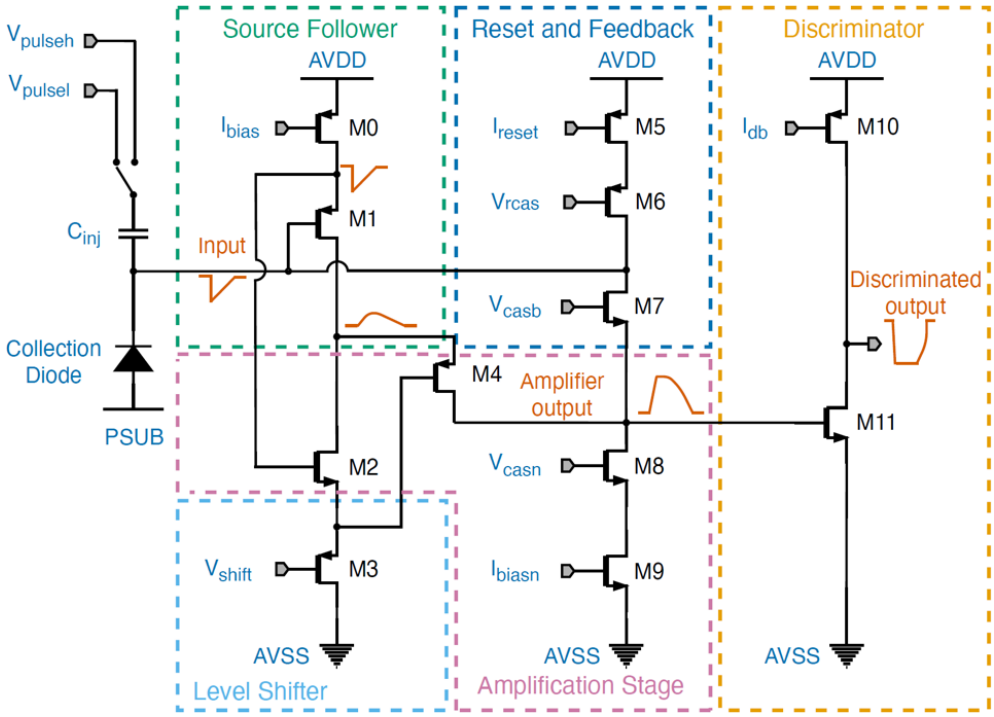

Figure 2.25: In pixel front-end of a MOSS pixel.

The functional diagram of the in-pixel digital logic is schematised in fig. 2.26. The circuit is based on an active-low logic. During normal operation of the sensor, the key step of the first stage of the circuit is the NOR operation between the DISCR_OUT signal, that is the discriminated output of the in-pixel front-end, and the STROBE signal, which is a matrix global signal that controls the sampling of the pixel output. Given that both signals are active when low, this operation is effectively an AND operation between them, that thus returns a signal only when both the pixel discriminated output and the strobe signal are active. Both signals DPULSE and PULSE_EN are disabled when the sensor is used to detect particles, thus their NOR returns a "0". Following the circuit in the image, the NOR operation between the outputs of the first two NOR will return a digital pulse that corresponds to the coincidence between the pixel discriminated output and the strobe signal. This signal is then fed to the in-pixel latch memory, that remains active until a reset signal $\bar{R}$ is sent. When a readout command is sent through the slow control, the pixels are read out based on a priority encoder that makes use of row and column steering. The procedure is described below for a bottom region, referring to fig. 2.23 and 2.26, it is symmetrical for the top regions:

1. The pixels that are not masked send a ROW_OR signal to the row steering block, that encodes the address of the pixel and flags the firing pixels with the signal SELECT_ROW. The row priority encoder communicates the row address to the periphery starting from the top row with at least one pixel hit.

2. The pixels that received the SELECT_ROW flag transmits the COL_PIXEL_OUT signal to the column steering block, whose priority encoder transmit to the periphery the column index of the firing pixels starting from the first on the left.

3. The region readout block in the periphery registers each pixel address from the

row and column steering and every time a pixel is read out the readout block generates a clear pulse. Such signal is received by the column steering, that transmits a CLEAR_COL command only to the selected column.

4. The pixel with an active SELECT_ROW signal in the column that received the CLEAR_COL command resets its latch memory and thus resets its ROW_OUT output.

5. The matrix readout is completed once all the ROW_OR signals are de-asserted.

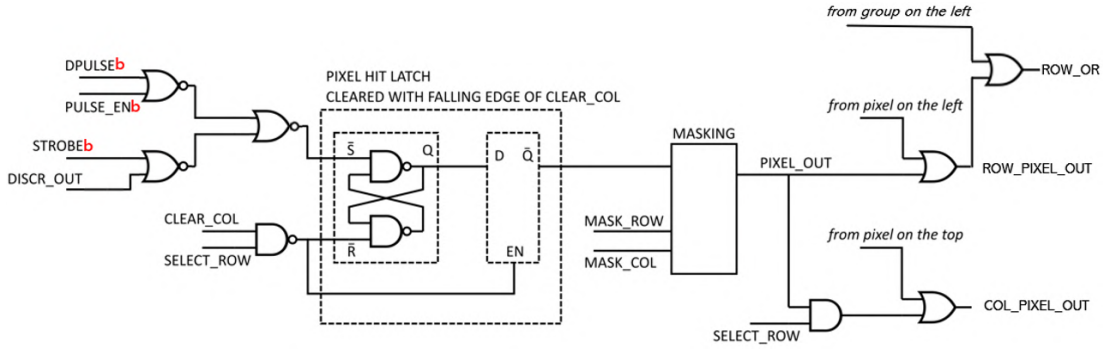

Figure 2.26: Schematic of the digital in-pixel logic of the MOSS sensor.

The strobe signal actually defines the duration in time of the acquisition window. Usually the sensor is operated with a strobe of few µs and the readout command is sent only once the strobe signal ended. Thus, the firing pixel addresses are recorded only after the acquisition ended. The Time-over-Threshold of the analogue pixel signal can be retrieved using a different readout logic. A strobe signal which is around ten times larger than the expected ToT is sent. Then, the sending of the readout command is triggered by the region *testout* signal. Such trigger is sent right after a pixel of the selected region fired, while the strobe signal is still active. Thus, the priority encoder starts the matrix reading while the acquisition is still ongoing. The readout procedure described previously is followed until point 3, then the CLEAR_COL command is sent and the firing pixel resets its latch memory, however, being the STROBE and the DISCR_OUT signals still active, the latch memory is activated again and the ROW_OR signal is not de-asserted. Therefore, the same pixel is selected again by the priority encoder to be read out. Because of its operating procedure, this readout type is called *stuck readout method*. More details about the stuck readout can be found in [87].

2.3.2.4 The MOSS test system

A DAQ-board-based test system derived from the one described in sec. 2.3.1.4 is used to operate the babyMOSS. As the DPTS setup, it can be integrated in a telescope for beam test measurements.

The setup is composed by a computer, a power supply, a DAQ board, a raiser board and a carrier card hosting the chip under test. The same DAQ board used for the DPTS setup is used in the babyMOSS setup. The core components of the setup are shown in fig. 2.27. An additional water cooling system can be used to keep the sensor temperature constant during testing via an aluminium cooling jig connected to a chiller that can be placed on the bottom of the carrier card. The power and the reverse bias voltage are provided to the chip by the DAQ board via the raiser board.

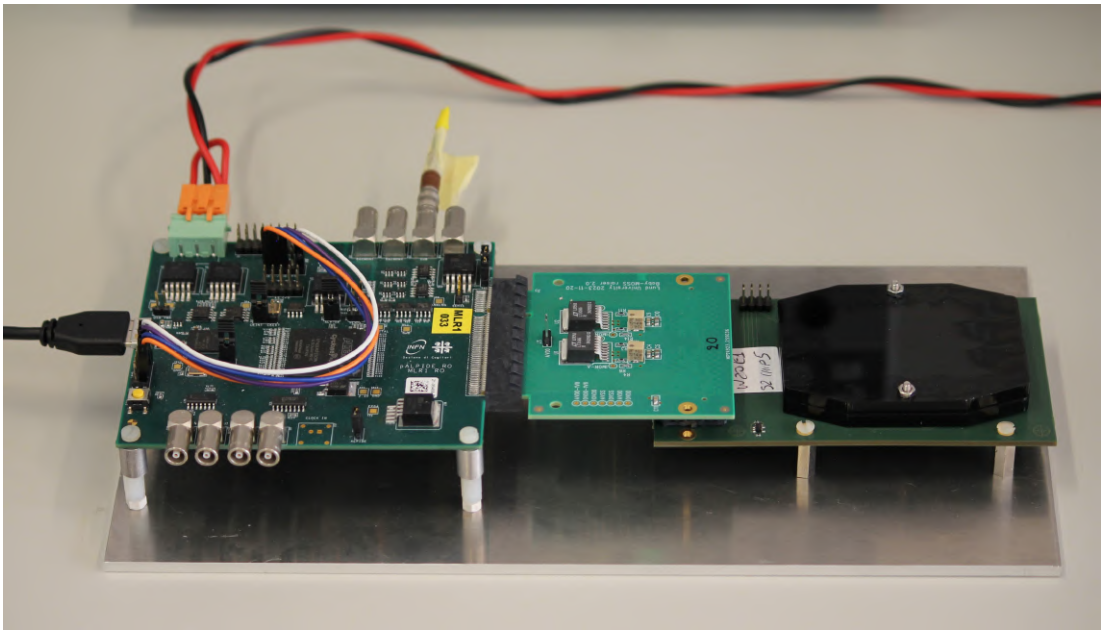

Figure 2.27: Main components of the babyMOSS test system, starting from the left there is the DAQ board, the raiser board and the carrier board with the sensor mounted on top and protected by a black plastic cover.

2.4 Laboratory characterisation

The first step for the MAPS sensor characterisation is the definition of the front-end parameter *operating ranges*, namely the value ranges for which the in-pixel logic transistor reference voltages and currents ensure the required sensor performance (see sec. 2.3.1.1 and 2.3.2.3). In this section the two main test routines that are executed for each set of operating parameters to evaluate the sensor performance are described: the threshold scan and the fake-hit rate scan. The threshold scan measures the effective threshold applied to each pixel of the matrix, where the threshold is the reference voltage level that defines whether the detected analogue signal is digitised or not, as a function of the parameter settings. The fake-hit rate scan measures the probability to have a noise event per pixel with a random trigger while varying the same parameters.

Two additional test routines that are fundamental for the energy response characterisation of the prototypes are described as well in this section: the DPTS decoding calibration scan and the ToT calibration scan.

This work contributed to the development of the data acquisition and analysis software, which was carried out within the ALICE ITS3 collaboration.

Once the operating range of the sensor has been defined with standalone tests, the detector response to external particles can be investigated with the goal of validating the operating range which was found and verify that the sensor satisfies the requirements of the final detector. Such measurements are described in the following chapters.

2.4.1 Definition of the operating range

2.4.1.1 The threshold measurement

The DPTS and the babyMOSS are digital detectors, thus meaning that the analogue signal in input to the discrimination stage of the in-pixel front-end circuitry is sent in output as a digital response only if it overcomes a voltage reference level named *threshold*. The threshold is adjusted via the parameters to set the reference voltage levels for the transistors of the in-pixel circuitry. In this work the parameter V_{casb} is used to regulate the threshold. The parameter V_{casn} is used together with V_{casb} to adjust the threshold when the reverse bias is changed, as explained in sec. 2.3.1.1.

The threshold scan measures the effective threshold applied for each pixel. The measurement procedure consists in the injection of a test charge in the in-pixel circuitry through the application of a potential difference V_h across the internal capacitance C_{inj} (see fig. 2.15 and 2.25). The injected charge varies within a user-defined range, that in the standard procedure is between $20 - 300\ e^-$ in steps of $\sim 10\ e^-$. For each value the charge is injected 25 times. The detector response is evaluated by enumerating the number of times that a digital output is given out of the total 25 injection for each charge value. Fig. 2.28 shows the result of a threshold scan on a single pixel: when the charge is low the analogue signal never overcomes the threshold, thus the counts are zero. Some signals are detected as the injected charge increases, until the charge is high enough so that all analogue signals overcome the threshold and thus the number of counts is equal to the number of injections for each charge value. The thermal noise from the sensitive volume of the sensor causes a fluctuation in the counting. Given the random origin of this noise, its distribution is assumed to be Gaussian around zero, for more details on the noise see chapter 3.

The cumulative distribution function associated to the thermal noise Gaussian distribution can be used to fit the data as shown in fig. 2.28

$$y(x) = \frac{p_0}{2}\left[1 + erf\left(\frac{x - p_1}{p_2\sqrt{2}}\right)\right] \tag{2.3}$$

where erf is the error function, defined as

$$erf(z) = \frac{2}{\sqrt{\pi}}\int_0^z e^{-t^2}dt \tag{2.4}$$

the parameter p_0 is the number of injections for each charge value, while p_1 and p_2 are respectively the mean value and the standard deviation of the Gaussian distribution defining the error function. p_1 is expected to coincide with the threshold, as the noise Gaussian distribution is centred in zero. p_2 is referred to as the noise of the pixel.

The measured threshold and noise are different from pixel to pixel, their distribution for the entire matrix follow a Gaussian function as depicted in fig. 2.29a and 2.29b for the DPTS chip. The mean values define the threshold and the noise of the device. A full scan of the matrix takes around 30 minutes for the DPTS and around 5 minutes for the babyMOSS, thus only a subset of pixels is usually scanned for quick checks.

The mean threshold and noise as a function of the operating parameter V_{casb} are measured to define the operating range of the sensor. The threshold is required to be high enough to reduce the probability of detecting noise events (see sec. 2.4.1.2), but low enough not to impact the efficiency of the detector (see sec. 2.5.2). A good trade-off is reached with a threshold between 100 e^- and 140 e^-. Fig. 2.30 shows an

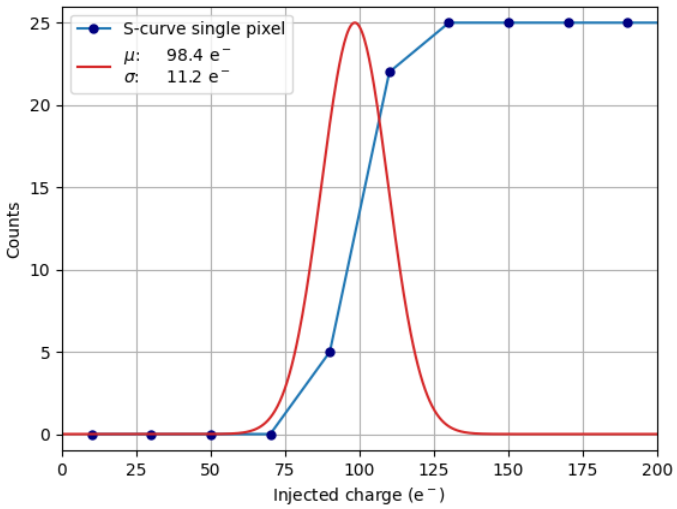

Figure 2.28: Results of the threshold scan for a single pixel and the Gaussian distribution representing the noise associated to the thermal noise. The mean of the Gaussian is the threshold, while the standard deviation is the noise.

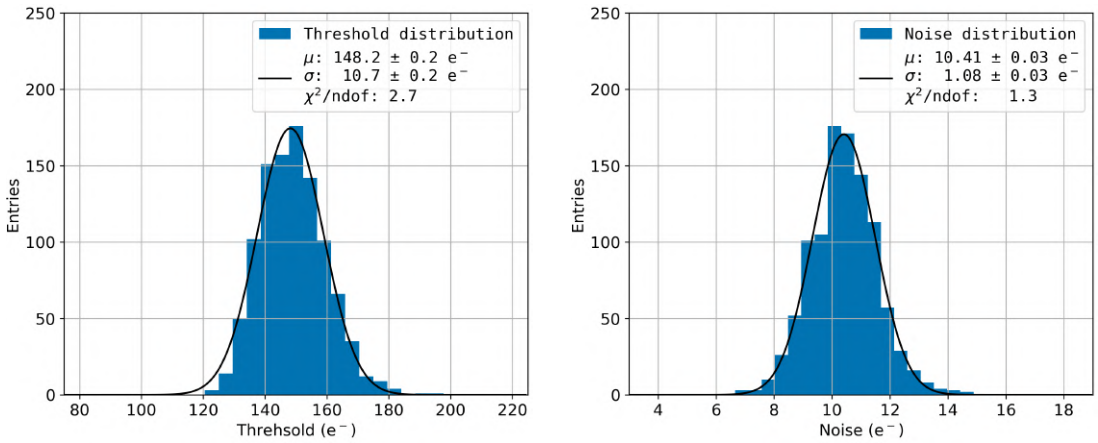

(a) (b)

Figure 2.29: Typical pixel threshold (left) and noise (right) distributions of a DPTS chip measured with a threshold scan. The black line represents the Gaussian fit.

example of the measured threshold and noise as a function of V_{casb} for a DPTS chip operated with three different reverse bias voltage. V_{casn} was adjusted for each reverse bias. The threshold decreases when V_{casb} increases, while the noise remains constant, except for some points at the boundaries of the explored V_{casb} range, indicating that the operating range limit of the detector has been reached and thus instabilities in the in-pixel circuit might influence the result. At a V_{sub}=V_{pwell} of -1.2 V the detector shows the best performance in terms of mean threshold and mean noise: indeed at this bias voltage, the sensor can be operated at a threshold as low as 100 e^- with some margin while the noise is the lowest measured between the three reverse bias voltages that have been investigated.

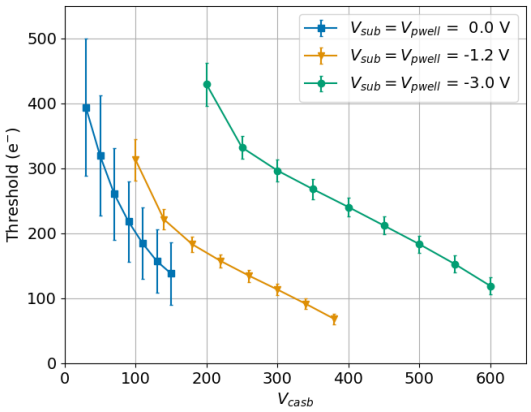

(a) DPTS mean threshold as a function of the operating parameter V_{casb} for different reverse bias voltages V_{BB}. Figure adapted from [83].

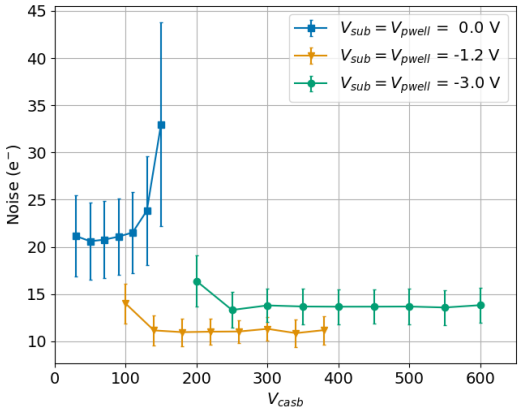

(b) DPTS mean noise as a function of the operating parameter V_{casb} for different reverse bias voltages V_{BB}. Data from [83].

Figure 2.30

2.4.1.2 The fake-hit rate measurement

The fake-hit rate scan measures, as a function of the varying configuration parameters, the probability to have a noise event in a pixel, defined as a randomly triggered acquisition, in absence of incident particles, which results in a signal above threshold. The configuration yielding the lowest possible fake-hit rate is favoured, to reduce the possibility of miss assigning fake hits to tracked particles. An in-depth study of the noise origins is presented in chapter 3. The fake-hit rate FHR is defined as

$$FHR = \frac{n_{hits}}{n_{pixel} \cdot n_{trigger} \, \Delta t} \tag{2.5}$$

where n_{hits} is the number of detected noise events, n_{pixel} is the number of pixels in the matrix, $n_{trigger}$ is the number of random triggers and Δt is the time duration of the acquisition window. The number of triggers is user-defined and set in order to have a sensitivity of the measurement reasonably smaller than the ITS3 fake-hit rate requirement of 10 pixel^{-1} s^{-1}. The sensitivity s is defined as the minimum fake-hit rate that can be measured with the chosen operating conditions, that is given by eq. 2.5 if n_{hits} is set to 1. The sensitivity limit for the DPTS and for the babyMOSS top and bottom matrices is shown in tab. 2.2 for $n_{trigger} = 10^5$, the default value for the reported measurements.

Table 2.2: Sensitivity limit of the DPTS and of the two matrix type of the babyMOSS in the fake-hit rate measurements for 10^5 random triggers $n_{trigger}$.

Matrix	n_{pixel}	$n_{trigger}$	Δt (µs)	Sensitivity (s)
DPTS	32×32	10^5	40	2.4×10^{-4}
babyMOSS top	256×256	10^5	6	2.5×10^{-5}
babyMOSS bottom	320×320	10^5	6	1.6×10^{-5}

A different estimate of the error on the fake-hit rate is done for the DPTS and the babyMOSS. Due to its readout (see sec. 2.3.1.2), the error on the DPTS fake-hit rate

has both statistical and systematic contributions. The first one is computed as

$$\sigma_{FHR} = \frac{\sqrt{n_{hits}}}{n_{pixel} \cdot n_{trigger} \Delta t} \tag{2.6}$$

The systematic uncertainty in the measured fake-hit rate is related to possible clashes in the CML output when more than one pixel fires, thus giving a digital output that cannot be decoded uniquely. The total systematic error is estimated as the difference between the maximum and the minimum fake-hit rate, derived as follows. The maximum fake-hit rate is computed assuming that n_{hits} is equal to the total number of detected trains. Instead, the minimum fake-hit rate is computed assuming that n_{hits} is equal to the number of non-empty triggered events.

On the babyMOSS, the fake-hit rate uncertainty is computed assuming a binomial statistics. The confidence interval corresponding to a confidence level of 68.3%, which is equivalent to one standard deviation, is used to define the uncertainty.

The fake-hit rate as a function of the threshold set through the V_{casb} parameter, is combined with the threshold measurements to define the operating range to be used for the in-beam characterisation. Fig. 2.31a shows the measured fake-hit rate as a function of the operating parameter V_{casb} for three different reverse bias voltages. The same data are shown in fig. 2.31b as a function of the applied threshold that was measured for each V_{casb}. The best performance of the detector is obtained with a reverse bias voltage of -1.2 V: the sensor can be operated in a wide range of threshold from the lowest target value of 100 e^- while keeping a fake-hit rate lower than 10 $^{-2}$ pixel^{-1} s^{-1}. As an example, for this chip the operating range at a V_{sub}=V_{pwell} of -1.2 V is defined between 90 e^- and 220 e^-, which guarantees minimal and stable noise level. This operating range is used for in beam measurements and updated following the detection efficiency results (see sec.2.5).

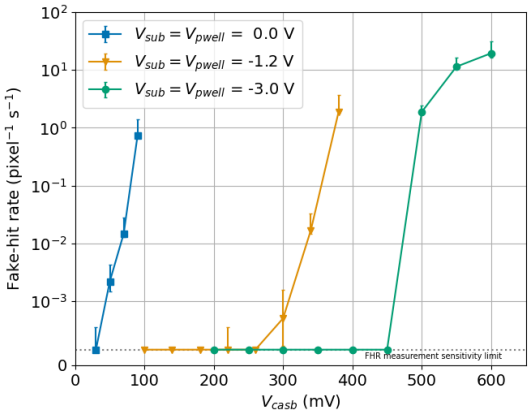

(a) DPTS fake-hit rate as a function of the operating parameter V_{casb} for different reverse bias voltages V_{BB}. Figure adapted from [83].

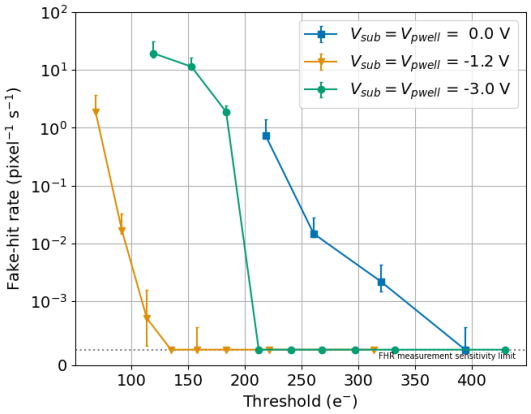

(b) DPTS fake-hit rate as a function of the applied threshold tuned with the operating parameter V_{casb} for different reverse bias voltages V_{BB}. Data from [83].

Figure 2.31

Since both threshold and fake-hit rate measurements prove that the sensor shows the best performance at a reverse bias voltage of -1.2 V, this value was decided to be kept as the default one for the DPTS and for the babyMOSS.

2.4.2 The DPTS pixel position decoding calibration

The digital output of the DPTS encodes in the time intervals named PID and GID the position of the detected hit, as explained in sec. 2.3.1.2. The aim of the pixel position decoding calibration is to measure the PID and GID of each pixel, so that the pixels can be uniquely identified when other routine tests are done. The procedure of the position decoding calibration consists in pulsing 100 times each pixel with a fixed pulse and record the digital output. The mean PID and GID are computed for both rising and falling edges and associated to the corresponding pixel. Fig. 2.32 shows the output of the position decoding calibration for the rising edge (a) and falling edge (b). Each cluster visible in the plot corresponds to one pixel and comprises 100 data points. The black cross indicates the mean time position associated to the pixel. The same pixel shows a different mean time position in the rising and in the falling edge.

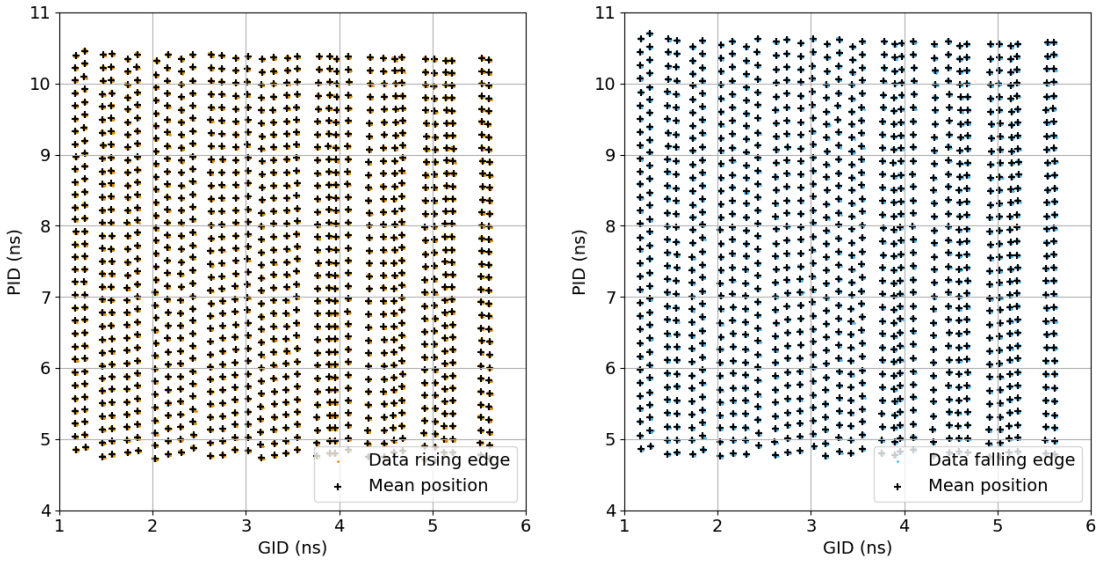

(a) Results of the DPTS position decoding calibration for the rising edge.

(b) Results of the DPTS position decoding calibration for the falling edge.

Figure 2.32

The position decoding calibration allows to decode the position of the hit from a digital signal by comparing pixel by pixel the PID and GID in the digital output to the know mean time position. If both PID and GID are compatible with the corresponding means, the hit is associated to the related pixel. An algorithm that compares both rising and falling edge PIDs and GIDs with the calibration ones was developed to associate a pixel to each hit when multiple pixels fire at the same time [88].

The mean PID and GID of each pixel are variable under operating parameter changes, thus a position decoding calibration is necessary for each set of parameters that is used. Moreover, the time distance associated to the pixel position in the matrix is temperature dependent, as it is shown in fig. 2.33. A data-driven correction of the position decoding calibration was developed within this thesis work to account for the modification in the pixels PID and GID over time due to temperature changes in long ($>$ 1h) measurements. The correction algorithm requires knowledge of the mean PID and GID associated to each pixel, as obtained from the position decoding calibration, as well as the PID and GID of the events acquired with externally incident particles.

The mean PID and GID of all events within a squared window centred on the mean GID and PID coordinates associated with each pixel are then computed and used as the new position calibration for that pixel. Fig. 2.34 shows the result of the data-driven correction of the position decoding calibration, where the red crosses represent the corrected time-position of the pixels. The data-driven correction of the position decoding is fundamental in in-beam measurements and energy-loss measurements where the temperature of the sensor is not easily controllable, and the knowledge of the hit position is essential.

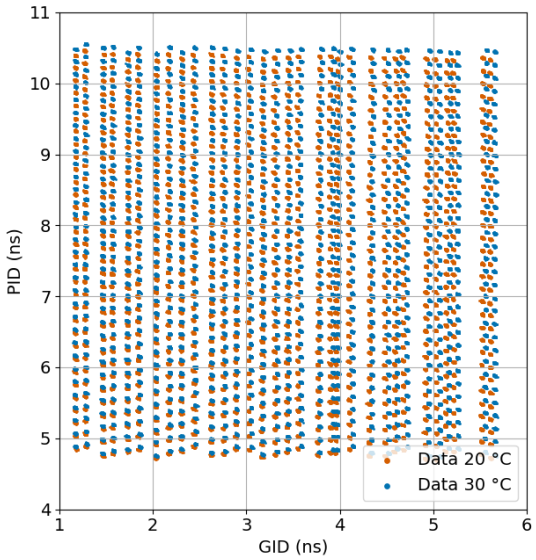

Figure 2.33: Position decoding calibration for the rising edge at 20 °C and 30 °C.

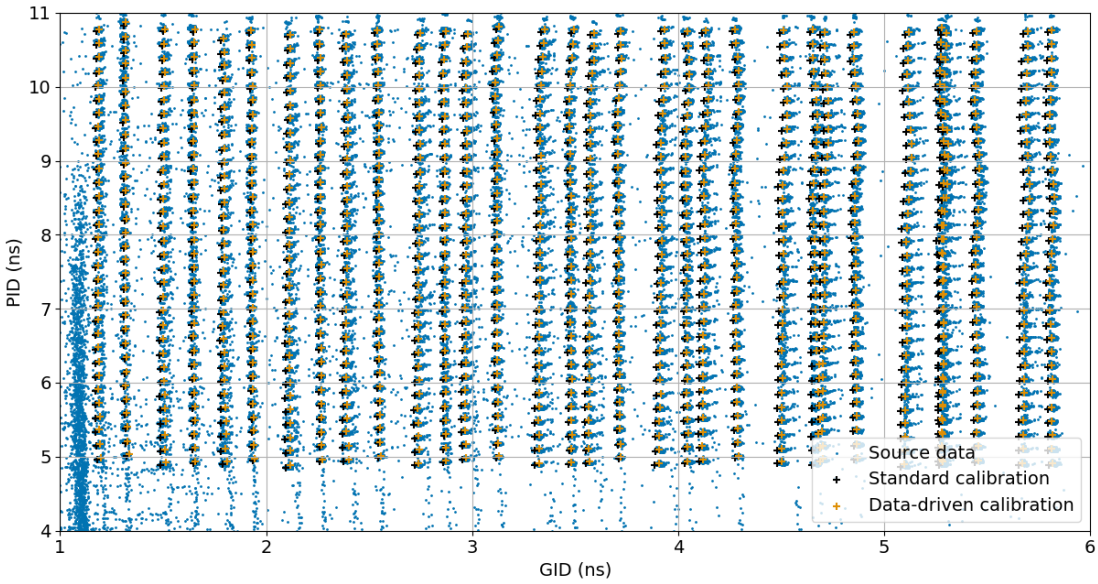

Figure 2.34: Data-driven correction of the position decoding calibration performed on the data taken with a radioactive source of ^{55}Fe.

2.4.3 The time-over-threshold calibration

The time-over-threshold (ToT) of the analogue signal in input to the in-pixel front-end digital stage of both DPTS and babyMOSS can be retrieved as explained in sec. 2.3.1.2 and 2.3.2.3, respectively. The ToT depends on the shape and amplitude of the analogue signal, which in turn depends on the amounts of energy released within the active volume of the device and on the response of the first stage of the in-pixel front-end that amplifies and shapes the signal. The released energy is independent from the pixel, however the response of the in-pixel circuitry can differ from pixel to pixel. Such pixel-dependence of the measured ToT can be avoided by expressing the ToT as a function of the voltage V_{pulseh} applied across the pulsing capacitance necessary to obtain the same output. Very similar results are obtained for the babyMOSS. The measurement procedure consists in the repeated injection of a fixed test charge in the in-pixel front-end for each pixel. The injected charge value ranges from 100 e^- to 1000 e^- for the DPTS and from 250 e^- to 2000 e^- for the babyMOSS, reflecting the operative upper limits of the V_{pulseh} parameter for the two sensors. For each injected charge value the mean measured ToT is recorded for each pixel and compared to the V_{pulseh} applied to obtain the corresponding analogue signal. The result of the time-over-threshold calibration is shown in fig. 2.35 for the DPTS sensor. The result obtained for the babyMOSS sensor is similar and thus it is not shown. The blue points represent the cumulative measurement for all the pixels in the matrix. The spread of the ToT response increases with increasing V_{pulseh}. However, as demonstrated by the yellow and orange points referred to individual pixels, the spread in the ToT is due to a pixel-to-pixel variability of the response rather than to a general worsening of the ToT response.

An empirical function was used to fit the data for each pixel (continuous and dashed lines in the figure)

$$ToT = aV_{pulseh} + b - \frac{c}{V_{pulseh} - d} \tag{2.7}$$

where a, b, c and d are the fit parameters. The linear part of the function describes well the trend of the data for V_{pulseh} higher than 200 e^-, while the hyperbolic part describes the data below 200 e^-. Since the range of injection for the babyMOSS starts above 200 e^-, a linear function is used to fit the babyMOSS data. As the minimum energy loss we aim to measure correspond to 400 e^- signals, this is not expected to be a limitation.

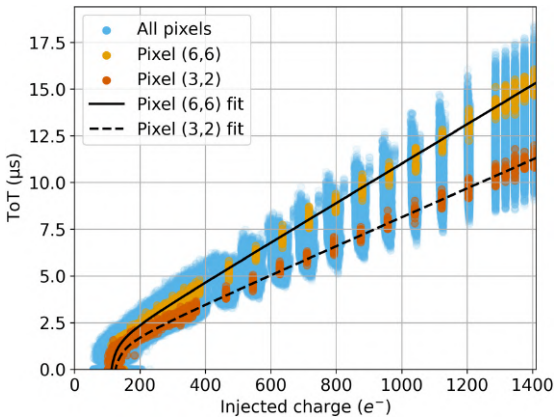

Figure 2.35: Time-over-Threshold calibration for the DPTS sensor. Figure from [83].

The inverse of eq. 2.7 that express V_{pulseh} as a function of the measured ToT is used to normalise the pixel response over the matrix in energy-loss measurements presented in chapter 4.

After all the preliminary characterisation steps described in this section, the sensor prototypes can be used for particle detection. In the following section the in-beam measurements to complete the definition of the sensor operating range are presented.

2.5 In-beam characterisation

The general characterisation of the ITS3 prototypes response is completed with the investigation of the in-beam performance using Minimum Ionising Particles (MIP), which assure straight trajectories and a known and minimum energy released by the particle crossing the detector. In this section the beam test setup and the analysis framework are detailed and the measured detection efficiency is discussed to define the final operating range of the detector.

2.5.1 Testbeam setup

Multiple test campaigns took place at the CERN PS and SPS testbeam facilities from November 2022 to April 2025 to test both DPTS and MOSS. The results presented in this section are based on data taken at the CERN PS with a set of representative babyMOSS chips and a beam of 7 GeV negative hadrons. The schematic representation of the beam telescope is shown in fig. 2.36. Six ALPIDE chips [58, 59, 60] serve as reference planes and are used to reconstruct particle tracks. The MOSS sensor is placed in between the reference arms. The sensor under test is kept at a constant temperature of 27 °C by an aluminium cooling jig placed on the back of the MOSS carrier. Such operating conditions correspond to the ones foreseen for the ITS3 [40]. The carrier board and the cooling jig feature a hole corresponding to the location of the chip to limit multiple scattering. The data acquisition is triggered by the coincidence of the amplified and discriminated signals of two scintillators.

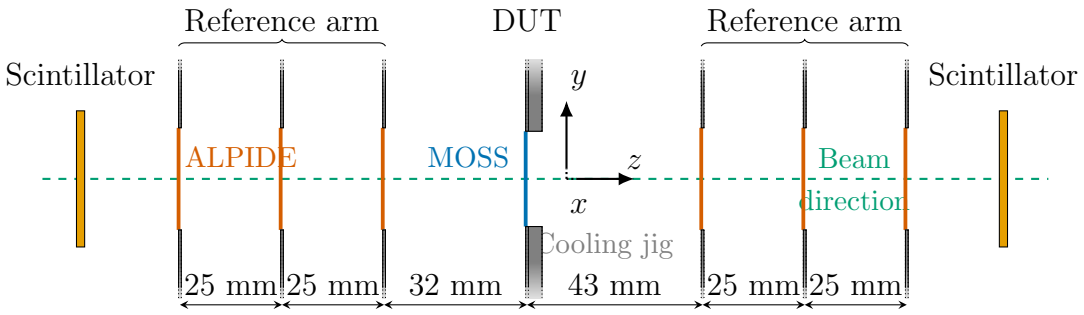

Figure 2.36: Schematic diagram of the telescope used for in-beam measurement with the MOSS chip (not to scale). Three ALPIDE sensors placed upstream of the Device Under Test (DUT) and three ALPIDE placed downstream are used as reference planes. The coincidence of two scintillator signals is used for triggering.

The EUDAQ [89] framework is used for data acquisition and the Corryvreckan [90] test beam reconstruction software framework is used to process offline the data. Particle

tracks are reconstructed by fitting the positions of the clusters found in the reference planes with General Broken Lines [91]. Clusters on the DUT are associated with tracks if they are located within a circular region of 100 µm radius, centred on the interpolated intersection of the track with the DUT. An event selection was applied requiring exactly one reconstructed track per event, a single hit on each reference plane, and a satisfactory track fit quality ($\chi^2 < 3$).

2.5.2 Detection efficiency

The goal of the in-beam measurements is to evaluate the sensor detection efficiency for different thresholds and operating conditions, with the aim of verifying compliance with the target performance for the ITS3 sensors, which is a detection efficiency higher than 99%, while keeping a fake-hit rate lower than 10 hits/pixel/s [40].

This performance must be maintained after the radiation doses expected during ITS3 operation, which, including a safety factor, are of 10 kGy Total Ionising Dose (TID) and 10^{13} 1 MeV n_{eq} cm^{-2} Non-Ionising Energy Loss (NIEL).

The detection efficiency ε of a detector is defined as:

$$\varepsilon = \frac{\text{number of detected events}}{\text{number of tracked events}} \tag{2.8}$$

For the present analysis, the number of tracked events corresponds to the number of reconstructed tracks passing through all the ALPIDE reference planes and the DUT. Possible inefficiencies of the DUTs under study are expected to be mainly related to a too high threshold or to malfunctions induced by the radiation damage.

The impact of the different MOSS chip characteristics (see sec. 2.3.2) on the detection efficiency is discussed in the following.

Fig. 2.37 compares the detection efficiency and fake-hit rate as a function of the applied threshold for matrices with pixel pitches of 22.5 µm (light blue) and 18 µm (yellow). The detection efficiency increases for the larger pitch, in agreement with the expectation that larger pixels have proportionally less border area than smaller ones, thus hits on the pixel edges are statistically more likely to be below threshold due to charge sharing. The same result was obtained with other ITS3 sensor prototypes [92].

A larger pixel pitch is observed to increase the fake-hit rate. The increased pixel volume is expected to raise the leakage current, and consequently the shot noise. However, the fake-hit rate increase estimated with the thermal model described in chapter 3 is insufficient to account for the experimental difference. Another possible explanation is that the larger number of pixels in the matrix with the smaller pixel pitch increases the capacitive load on the distribution net of the digital signal, thus reducing the impact of the perturbation from the strobe signal, which is described in detail in sec. 3.4.

Fig. 2.38 compares the detection efficiency and fake-hit rate as a function of the applied threshold for a 2.5 µm gap (yellow) and a 5.0 µm gap (blue shadows) for a matrix with 22.5 µm pixel pitch. A smaller gap exhibits a slightly higher detection efficiency, in agreement with the expectation that when the gap size is decreased, the electric field at the border of the pixel is increased, reducing the charge sharing between neighbouring pixels [93]. The fake-hit rate is not systematically affected by the gap size variation.

Moreover, the two data sets which are shown in shades of blue were taken at different times. Their compatibility validates the reproducibility of the measurements.

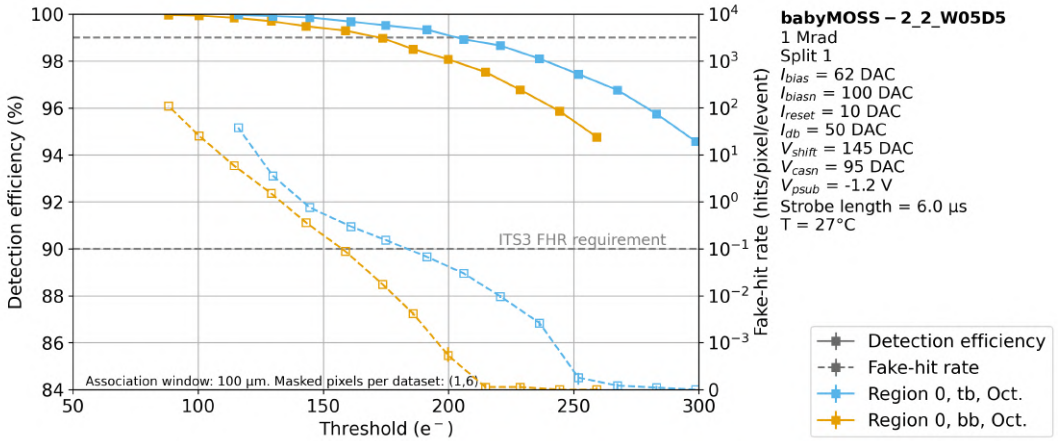

Figure 2.37: Detection efficiency and fake-hit rate as a function of the applied threshold, comparing the 22.5 µm (light blue) and the 18.0 µm (yellow) pixel pitch.

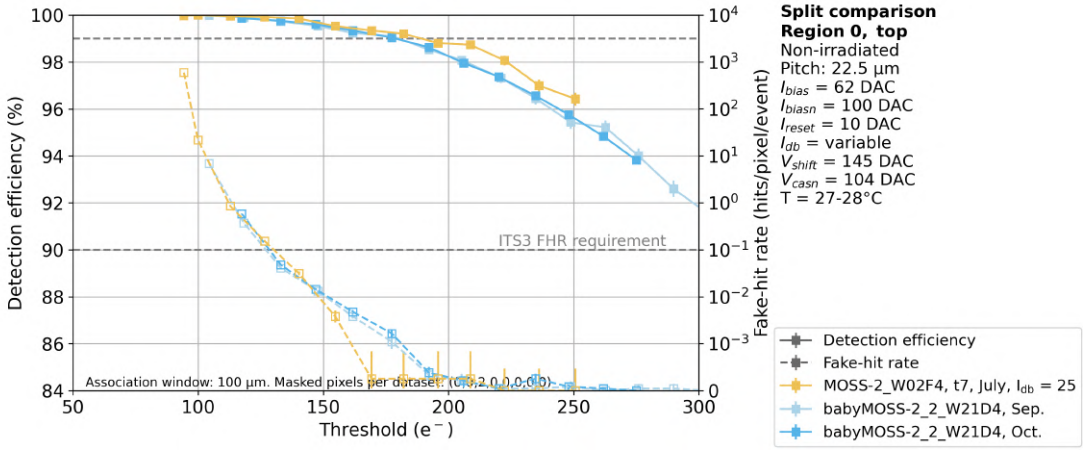

Figure 2.38: Detection efficiency and fake-hit rate as a function of the applied threshold, comparing a 2.5 µm gap (yellow) and a 5.0 µm gap (blue shadows) for a matrix with 22.5 µm pixel pitch.

Overall, a larger pixel pitch achieves the target performance over a wider threshold range.

The detection efficiency and fake-hit rate as a function of the threshold for a matrix with a 22.5 µm pixel pitch with a 5.0 µm gap, are shown in fig. 2.39 for different irradiation levels. The sensors have been irradiated with ionising radiation doses of 10 kGy and 100 kGy and non-ionising radiation doses of 10^{13} 1 MeV n_{eq} cm^{-2} and 10^{14} 1 MeV n_{eq} cm^{-2}. The results for a non-irradiated sensor are shown for reference.

The TID-irradiated samples show an increase of the fake-hit rate with the dose, in accordance with the expectation that ionising radiation affects the in-pixel front-end performance, thus worsening the signal-to-noise ratio. The efficiency is not affected at 10 kGy, the expected ionising dose for the ITS3, however it decreases at 100 kGy, although the sensor remains operational.

The niel-irradiated samples show an increase of the fake-hit rate with the dose as well, attributable to a larger leakage current from the pixel volume, and thus a

higher shot noise, due to irradiation damage. The expected ionising dose for the ITS3, 10^{13} 1 MeV n_{eq} cm^{-2}, does not impact the efficiency. At a higher dose of 10^{14} 1 MeV n_{eq} cm^{-2}, the detection efficiency drops below 99%, however the sensor can still function.

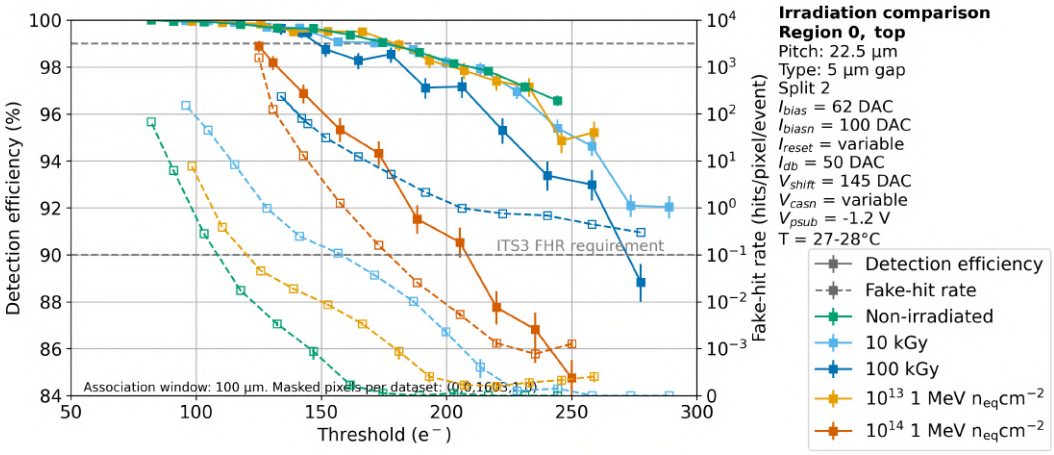

Figure 2.39: Detection efficiency and fake-hit rate for a matrix with a pixel pitch of 22.5 µm as a function of applied threshold for different irradiation levels: non-irradiated, ionising radiation doses of 10 kGy and 100 kGy and non-ionising radiation doses of 10^{13} 1 MeV n_{eq} cm^{-2} and 10^{14} 1 MeV n_{eq} cm^{-2}.

Overall, the operational margin after irradiation, defined as the threshold range where the ITS3 requirements are met, is reduced as expected. In detail, for the non-irradiated sample the operational margin is between 110 e^- and 175 e^- for a total range of ∼65 e^-, while the non-ionising radiation dose of 10^{13} 1 MeV n_{eq} cm^{-2} reduces it to ∼55 e^- and the ionising dose of 10 kGy reduces it to less than 30 e^-. Higher irradiation doses deteriorate both the detection efficiency and the fake-hit rate to the point where no operational margin remains, however the senors remain functional.

In summary, despite the operational margin reduction, sensors irradiated at the expected ITS3 levels of either TID or NIEL can be still operated.

Chapter 3

Noise characterisation of the ITS3 prototypes

Electronic noise in detectors is usually described as a random output signal in the absence of incident particles. The noise plays a key role in defining the lower bound on the detectable signal level, namely the threshold, which has to be set by doing a trade-off between the need to reject noise events and the goal of achieving near 100% detection efficiency, as discussed in sec. 2.4.1. Moreover, the noise can impact on the energy resolution of the detector, hence affecting the detector sensitivity in energy-loss measurements. Therefore, a thorough understanding of the underlying causes of the fake-hit rate is crucial to minimize it as effectively as possible. One approach to quantify the noise of a MAPS detector is to measure the fake-hit rate, which is defined as the number of hits per pixel per seconds in the absence of external stimuli, as described in sec. 2.4.1.2. One of the key requirements for the final ITS3 sensor is to maintain a fake-hit rate below 10^{-1} pixel^{-1} s^{-1}, for the reasons just mentioned.

This chapter provides an overview of the noise components which are expected to affect the sensor performance. A model is developed to predict the expected contribution of temperature-dependent noise to the fake-hit rate. The noise measurements performed on the small-scale Digital Pixel Test Structure (DPTS) at 20 °C are compared to the thermal model. A masking procedure is developed to selectively identify pixels exhibiting thermal noise. The time-measurement capabilities of the DPTS are utilised to study the Time-of-Arrival (ToA) and Time-over-Threshold (ToT) of noise events. The dependence of the fake-hit rate on temperature is investigated using three dataset acquired at 20 °C, 25 °C and 30 °C. The influence of the acquisition window duration on fake-hit rate is studied using the large area-prototype MOnolithich Stitched Sensor (MOSS). The larger matrix size of the MOSS, relative to the DPTS, is leveraged to investigate the influence of the on-chip signal distribution network by examining potential matrix position-dependent correlations in the noise.

3.1 Noise in semiconductor devices

The noise in electronic devices is commonly observed as a random fluctuation in time of the output voltage or current. Thus it is known as a stochastic process, characterised by statistical properties [94]. The three most common types of noise in semiconductor devices are thermal noise, shot noise and $1/f$ noise. This last one is referred to also as current noise, flicker noise, contact noise or excess noise. Generation-recombination

noise and burst noise can also occur. Thermal noise and shot noise with large statistics have a Gaussian distribution, and Bell's measurement [95] demonstrated that $1/f$ noise exhibits a Gaussian distribution as well.

3.1.1 Thermal and shot noise

Thermal noise, i.e. Johnson noise [96, 97], arises from the Brownian motion of the charge carriers (electrons and holes) due to the thermal energy in their resistive material. When the material is in thermal equilibrium with its surroundings, a deviation from such equilibrium is followed by a relaxation back towards it. The sum of many of these microscopic events gives rise to the macroscopic variation of voltage or current in the electronic device. Thermal noise is an inevitable feature of electrical circuits.

Shot noise [98] is a non-equilibrium form of noise which is due to the quantization of charge and therefore of current. It is frequently encountered in solid-state devices when a net current flows across a potential barrier such as the depletion layer of a p-n junction.

Thermal and shot noise can be depicted as a train of random pulses with a decaying exponential shape and a Poisson distribution in time[1]. In the limit case of very narrow noise signals the random pulse train is known as an impulse process [99] and its power spectral density is:

$$\overline{S_x(\omega)} = 2\nu\overline{a^2} \tag{3.1}$$

where ω is the angular frequency, ν is the mean rate of events and $\overline{a^2}$ is the mean-square value of the pulse amplitude. This shows that the spectrum is flat, thus the process on the base of it, is said to be white. For real signals, which have a non-zero width, the power spectral density rolls-off rapidly at frequencies beyond the reciprocal of the pulse width. The thermal and shot noise shows a flat power density up to frequencies comparable with the reciprocal of the pulse widths. The power spectral densities for the thermal noise and for the shot noise can be deduced from considerations on the noise mechanism [100]. Given a resistance R at an absolute temperature T the spectral current noise density of thermal noise is:

$$i_{tn}^2 = \frac{4kT}{R} \tag{3.2}$$

where k is the Boltzmann constant. While the spectral noise density of shot noise is:

$$i_{sn}^2 = 2eI \tag{3.3}$$

where e is the electronic charge and I is the average current.

3.1.2 $1/f$ noise

$1/f$ noise can be represented as a random pulse train with a specific pulse shape [101, 102]:

$$f(t) = t^{-\frac{1}{2}}u(t) \tag{3.4}$$

where $u(t)$ is the unit step function. This type of noise is a relaxation process, whose characteristic is the exponentially decaying autocorrelation function:

$$\overline{\Phi_x(\tau)} = \overline{\Phi_x(0)}e^{-\frac{|\tau|}{\tau_1}} \tag{3.5}$$

[1]The statistic is poissonian because the events are independent. Given T the duration of a train, the probability density function of the event time is $1/T$.

where $\overline{\Phi_x(\tau)}$ is the variance of the process and τ_1 is the decay constant. The power spectral density is given applying the inverse of the Wiener-Khintchine theorem:

$$\overline{S_x(\omega)} = 4\int_0^\infty \overline{\Phi_x(\tau)}\cos\omega\tau d\tau = \frac{4\overline{\Phi_x(0)}\tau_1}{(1+\omega^2\tau_1^2)} \tag{3.6}$$

It results that when the frequency $\omega << 1/\tau_1$ the spectrum is flat and when $\omega >> 1/\tau_1$ it rolls off as $1/\omega^2$. The power spectral density of the $1/f$ noise varies with frequency as $|f|^{-\alpha}$, with α between 0.8 and 1.2. Frequencies down to 10^{-6} Hz have shown this dependence, instead, an upper limit is difficult to establish as other noise contributions usually mask it. $1/f$ noise for example occurs when carriers are trapped and then released with a time constant τ_f. An infinite number of uniformly distributed time constants τ_f gives a spectral power density with a pure $1/f$ distribution.

3.1.3 Generation-recombination noise

Random trapping of charge carriers in semiconductor materials leads to generation-recombination noise. Centres of recombination are known as Hall-Shockley-Read (HSR) centres from the scientists who formulated the statistics of the generation-recombination events [103, 104]. This type of noise is significant in FET when the generation-recombination process is occurring in the channel-gate depletion region: electrons and holes are emitted alternately from HRS centres and are then swept out of the junction by the electric field. Thus, a local modulation of the depletion layer width, *i.e.* the channel width, is produced and in turn a fluctuation of the current flowing in the external circuit occurs [94].

3.1.4 Burst noise

Solid state devices sometimes feature electrical noise in the form of random bursts. This type of noise is also known as Random Telegraph Noise (RTN) and manifests itself as a random step waveform with uniform amplitude. MOS transistors of minimum size can exhibit RTN noise due to single traps near the substrate-oxide interface [105]. Fig. 3.1 shows an example of RTN two-level fluctuation of a MOS drain current. Fig. 3.2 shows as multiple traps result in $1/f$ noise [106].

3.1.5 Noise of in-pixel electronics

The analogue signal generated in the p-n junction of the detector must be processed to perform measurements. In Monolithic Active Pixel silicon Sensors (MAPS) the in-pixel read-out electronics (see sec. 2.3.1.1 and 2.3.2.3) process the signal. The sensitive layer of the sensor absorbs the incident radiation and converts it into an electrical signal. This signal is then amplified, shaped and digitised, following the scheme in fig. 3.3. The sensor and the read-out electronic are subject to the different type of noise discussed above. The overall noise must be minimized to avoid smears of the quite small sensor signal: the charge released by Minimum Ionising Particles (MIP) inside the active layer of the sensor is $\mathcal{O}(10^{-16}$ C), statistically fluctuating. The total capacitance in parallel with the input, that is the sensor capacitance and the capacitance of the amplifier, is a critical parameter that impacts on the Signal-to-Noise Ratio (SNR).The pulse shaper is the next stage, and its primary function is to improve the SNR by applying subsequent filters that gives to the signal the shape of a smooth cusp. The maximum of the pulse

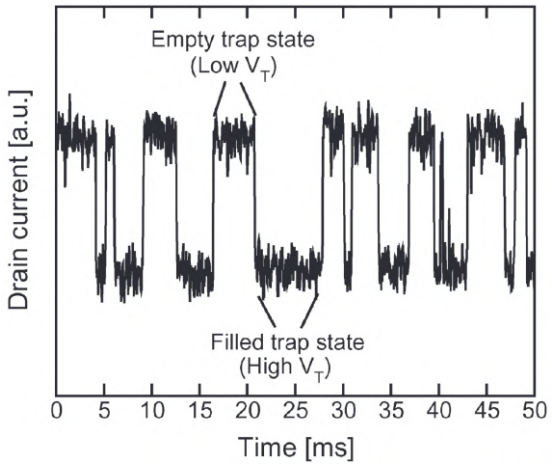

Figure 3.1: Drain current fluctuations due to RTN noise in a MOS device. A filled-trap (high threshold voltage V_T) state turns into a low current level, whereas an empty-trap (low V_T) state turns into a high current level [105].

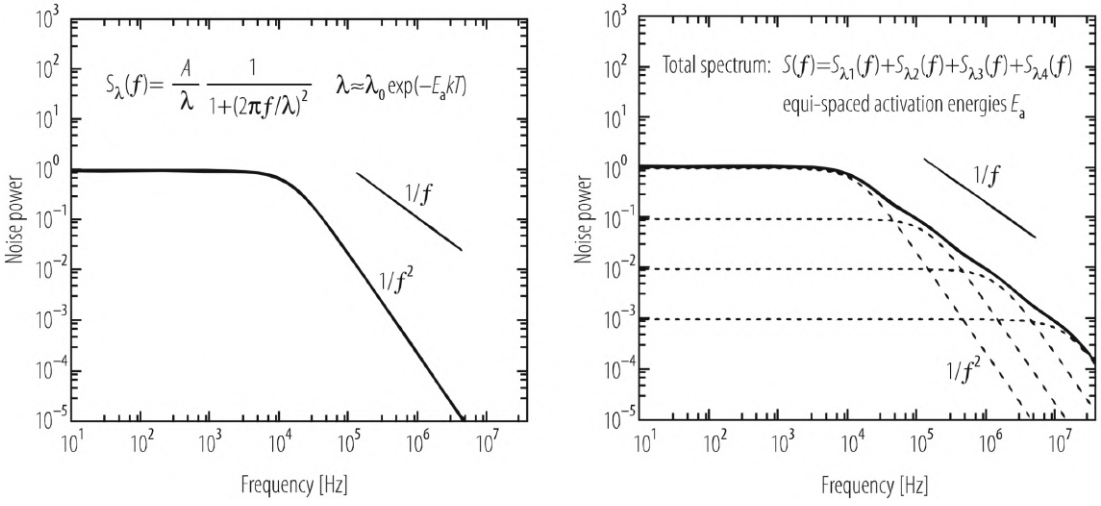

Figure 3.2: A single trap generates RTN noise (left), whereas a superposition of multiple trapping-detrapping events with uniform distribution of life times generates a noise spectrum very close to $1/f$ (right) [106].

must be held for a proper time to be compatible with the digitiser. After the digitisation the signal is stored for subsequent analysis.

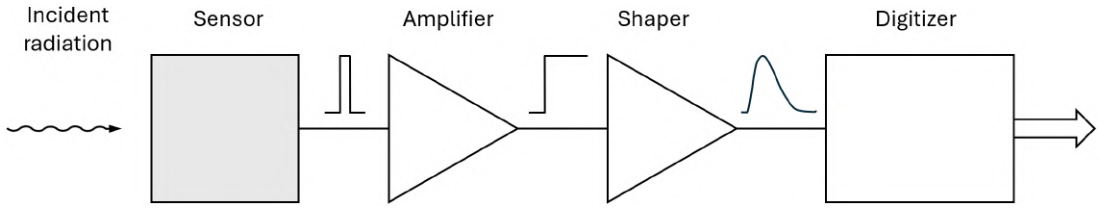

Figure 3.3: Generic scheme of sensor functionalities, that in the ITS3 sensor prototypes are included in the in-pixel logic. The incident radiation is absorbed by the sensor and then amplified and shaped before being digitalised and transmitted to the data BUS.

The electronic noise of the in-pixel circuitry can be either addressed to voltage or current sources. Fig. 3.4 shows the equivalent circuit for the noise analysis of a typical MAPS front-end. The capacitor C_d represents the detector, a current generator in parallel with C_d accounts for the fluctuations in the leakage current of the detector, which are described as a shot noise current i_{nd}. The bias voltage supply and its thermal noise are modelled as a resistor R_b with an i_{nb} current generator in parallel. R_s represents the sum of all resistances present in the input signal path and its thermal noise is represented as an e_{ns} voltage generator.

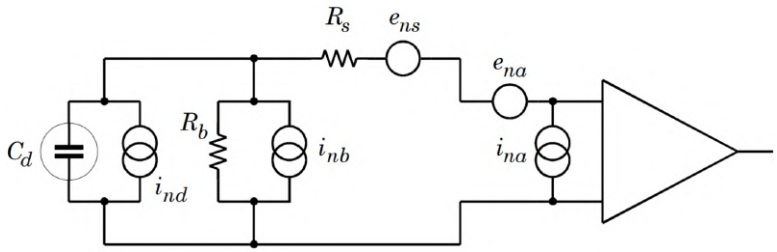

Figure 3.4: Circuit for noise analysis of a typical detector front-end [100].

The noise of the amplifier and of the pulse shaper is a combination of voltage and current sources, e_{na} and i_{na}.

Thermal and shot noise have a Gaussian distribution of amplitudes, following eq. 3.2 and eq. 3.3 their spectral density are:

$$\begin{aligned} i_{nd}^2 &= 2eI_d \\ i_{nb}^2 &= 4kT/R_b \\ e_{ns}^2 &= 4kTR_s \end{aligned} \tag{3.7}$$

where e is the electronic charge, I_d the detector bias current, k the Boltzmann constant and T the temperature.

The noise introduced by the amplifier and shaper can have multiple contributions, mainly due to trapping and de-trapping processes, which lead to an overall $1/f$ behaviour of the noise spectrum. Thus, the spectral density is:

$$e_{nf}^2 = \frac{A_f}{f} \tag{3.8}$$

where A_f is a noise coefficient device specific.

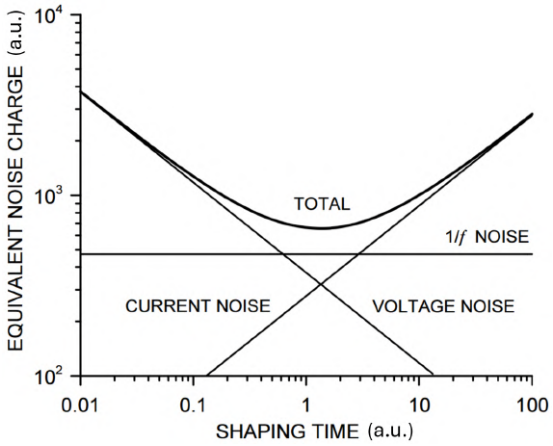

Figure 3.5: Noise contributions as a function of the shaping time, *i.e.* pulse duration [100].

In the case of uncorrelated noise contributions, they can be added in quadrature. The total noise is found by integrating over the full bandwidth of the system. The noise is usually expressed as an equivalent noise charge, equal to the detector signal that yields a SNR of one.

Fig. 3.5 shows the contribution of $1/f$, current and voltage noise as a function of shaping time for a typical detector system [106, 107, 108, 109, 110]. The $1/f$ noise depends on the ratio of upper to lower cut-off frequencies of the shaper, thus it is independent of the shaping time. On the other hand, the contribution of noise current increases with shaping time and the contribution of voltage noise decreases with shaping time. If the detector capacitance is increased, the voltage noise is increased, and the noise minimum is shifted to longer shaping times [100].

3.2 Fake-hit rate white noise model

All the types of noise discussed in sec. 3.1 impact on the sensor fake-hit rate. The contributions can be classified as white noise, e.g. thermal noise and shot noise, and as frequency dependent noise, i.e. $1/f$ noise, Random Telegraph Noise (RTN), generation-recombination noise. A model of the fake-hit rate given by the only contribution of the white noise is depicted below.

The probability density function (*pdf*) of the white noise signals amplitude is a Gaussian distribution centred in zero[2]. Given a pixel with a standard deviation of the noise distribution n_p, the probability of a fake hit with an amplitude greater than the pixel threshold t_p occurring in the pixel is:

$$f_p(t_p, n_p) = \int_{t_p}^{+\infty} \mathcal{N}(x|0, n_p) = \int_{t_p}^{+\infty} \frac{1}{\sqrt{2\pi} n_p} e^{-\frac{x^2}{(2n_p^2)}} dx = \frac{1}{2} erfc\left(\frac{t_p}{\sqrt{2} n_p}\right) \tag{3.9}$$

where $erfc$ indicates the complementary error function.

The variation of the pixel threshold and noise must be considered to compute the mean fake-hit rate of the sensor matrix. In the hypothesis of Gaussian *pdf* for both

[2]If we assume the pedestal of the MAPS detector under test to be null, we can use a normal distribution with mean zero as the distribution of the thermal noise

threshold and noise (sec. 2.4.1.1), named respectively $\mathcal{N}(t;\mu_t,\sigma_t)$ and $\mathcal{N}(n;\mu_n,\sigma_n)$, the expected value of fake-hits per pixel can be computed as:

$$E[f_p(t_p,n_p)] = \int_0^{+\infty}\int_0^{+\infty} f_p(t,n)\ \mathcal{N}(t;\mu_t,\sigma_t)\ \mathcal{N}(n;\mu_n,\sigma_n)\ dtdn \tag{3.10}$$

The Poisson distribution in time of the noise events has to be considered to compute the expected fake-hit rate. For a given τ, defined as the characteristic pixel noise time at zero threshold, the probability to measure one event in an interval Δt is:

$$P_1(\Delta t,\tau) = \int_0^{\Delta t} \frac{1}{\tau} e^{-\frac{t}{\tau}} = 1 - e^{-\frac{\Delta t}{\tau}} \tag{3.11}$$

thus, the expected number of fake-hits per pixel can be computed as:

$$\mathrm{N_{fake\text{-}hits}} = E[f_p(t_p,n_p)]\ P(\Delta t,\tau) \tag{3.12}$$

assuming $\Delta t >> \tau$ then:

$$\lim_{\Delta t>>\tau} P(\Delta t,\tau) = 1 \tag{3.13}$$

so the mean number of fake-hits per pixel expected in the acquisition time window t_{strobe} is equal to:

$$\mathrm{N_{fake\text{-}hits}} = E[f_p(t_p,n_p)] \tag{3.14}$$

Thus, the expected fake-hit rate per pixel is:

$$\text{fake-hit rate} = \frac{\mathrm{N_{fake\text{-}hits}}}{t_{\mathrm{strobe}}} = \frac{1}{t_{\mathrm{strobe}}}\int_0^{+\infty}\int_0^{+\infty} f_p(t,n)\ \mathcal{N}(t;\mu_t,\sigma_t)\ \mathcal{N}(n;\mu_n,\sigma_n)\ dtdn \tag{3.15}$$

3.2.1 Analytical evaluation

Parameter extraction The fake-hit rate white noise model is derived under the hypothesis of a Gaussian distribution of the sensor threshold and noise, which is a valid assumption for the DPTS and the babyMOSS sensors as shown in fig. 2.29b in the previous chapter.

The model input parameters can be measured through threshold scans, as described in sec. 2.4.1.1, which yield average threshold μ_t, average noise μ_n, and the corresponding dispersions σ_t and σ_n, as a function of the applied VCASB. In fig. 3.6 the VCASB dependence of the four parameters is shown. The distributions are fitted with a second order polynomial function:

$$y = ax^2 + bx + c \tag{3.16}$$

which is then used with the obtained parameters a, b and c to compute the model input parameters in a continuous range of thresholds.

Simulated fake-hit rate A Python program specifically developed allows for the analytical evaluation of the model. The algorithms provided by the Python library SciPy [111] are used to compute the Gaussian functions and the integral.

Fig. 3.7 shows the fake-hit rate as a function of the threshold as analytically evaluated from the model described by eq. 3.14. As expected, the number of fake-hits decreases as the threshold increases.

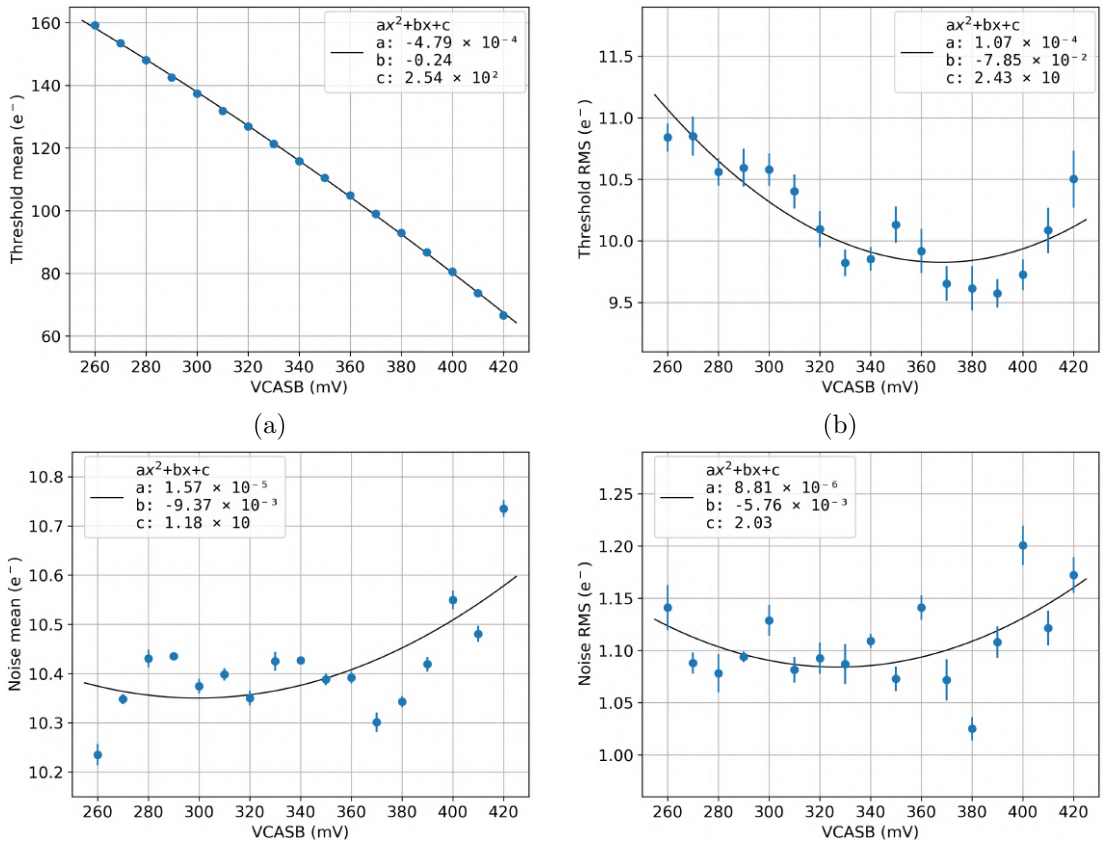

Figure 3.6: DPTS threshold mean (a) and standard deviation (b) and noise mean (c) and standard deviation (d) as a function of the operating parameter VCASB. A second order polynomial function is used to interpolate the data.

The computation of eq. 3.14 requires to reduce the integral limits, to allow the correct convergence of the Python algorithm for the integration. Therefore, the region where the integrand function is not negligible is identified (fig. 3.8) and the limits are chosen accordingly.

3.3 DPTS fake-hit rate investigation

The fake-hit rate of the DPTS has been measured at the nominal operating temperature of 20 °C as a function of the applied threshold and has been compared to the thermal noise model described in sec. 3.2 to assess the thermal contribution to the measured fake-hit rate. Moreover, the temperature dependence of the thermal noise component, which is expected to increase with temperature, has been investigated by measuring the fake-hit rate of the DPTS as a function of the applied threshold at 25 °C and 30 °C as well.

3.3.1 Comparison with the thermal model

The fake-hit rate thermal model described by eq. 3.15 is analytically evaluated for all the measured thresholds at 20 °C for four DPTS. In the following, the results from the

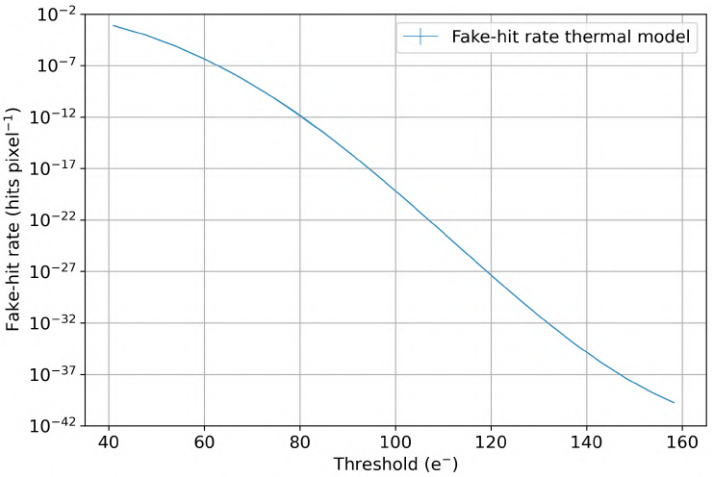

Figure 3.7: Fake-hits modelled as a function of the threshold value. Computed by a Python program that evaluates eq. 3.15 using data from a DPTS sensor.

first tested chip are discussed, as they are compatible with those obtained with the other sensors. The procedure described in sec. 3.2.1 is used. The number of triggers ($N_{trigger}$) to measure the fake-hit rate was fixed to $5{\times}10^6$, and the time acquisition window (t_{strobe}) for each trigger was of 40.01 μs. Thus, the corresponding sensitivity limit of the measurement was of:

$$S = \frac{1}{N_{trigger} \cdot t_{\text{strobe}} \cdot n_{pixels}} = 4.88 \times 10^{-6}\ pixel^{-1} s^{-1} \tag{3.17}$$

The comparison between the thermal model and the measured fake-hit rate is shown in fig. 3.9. Both quantities are plotted as a function of the applied threshold. Both measured fake-hit rate and model show a decreasing trend as the threshold increases, however, a difference of several orders of magnitude between the model and the data is observed in the whole threshold range. The fake-hit rate measurement sensitivity limit

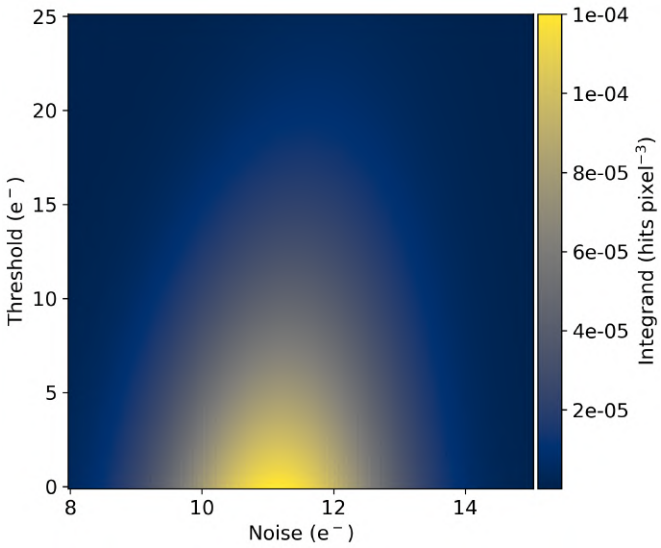

Figure 3.8: Integrand function of eq. 3.15 computed within the chosen integral limits.

is represented by the dotted line.

The difference between the thermal model and the measured fake-hit rate indicates possible contributions to the noise which are not taken into account by the model, i.e. frequency dependent noise as 1/f, RTN and generation recombination noise.

The hit multiplicity is studied to identify possible outliers. Fig. 3.10 shows the pixel hit multiplicity for fake-hit rate measurements taken with 5 M random triggers at three different thresholds. Single pixels can fire more than once for a single trigger. At the lowest threshold, 74 e^-, a few pixels are firing more than 10^5 times, while most of the pixels exhibit a hit multiplicity which is below 100. These noisy pixels are possibly affected by frequency dependent noise. Following this observation, a masking of the pixels based on the pixel hit multiplicity is applied with the method described in the following. Fig. 3.11 shows the fake-hit rate for three different thresholds as a function of the number of masked pixels. The pixels are masked based on their firing rate, from the most active to the least active one. Events that are not assignable to a pixel because of clashes in the signal trains encoding the pixel position, are accounted for in the undecodable event contribution, represented by the dotted line in the plot. Masking less than 1% of the most frequently firing pixels causes the fake-hit rate to drop by more than one order of magnitude. An inflection point in the fake-hit rate trend can be observed between 1% and 10% of masked pixels at a threshold of 80 e^-, indicating a possible change in the type of dominant noise contribution. The mask which is excluding 4.8% pixels (49 pixels) at a threshold of 80 e^-, is applied to all the measured thresholds. The resulting masked fake-hit rate is compared to the thermal model in fig. 3.12. The non-masked fake-hit rate is shown too, as well as the undecodable event contribution as a function of the threshold. The masking of the pixels makes the fake-hit rate to decrease by two orders of magnitude. Although reduced, a difference by more than one order of magnitude from the model remains, indicating a persistence of a residual non white component which is not easy to remove.

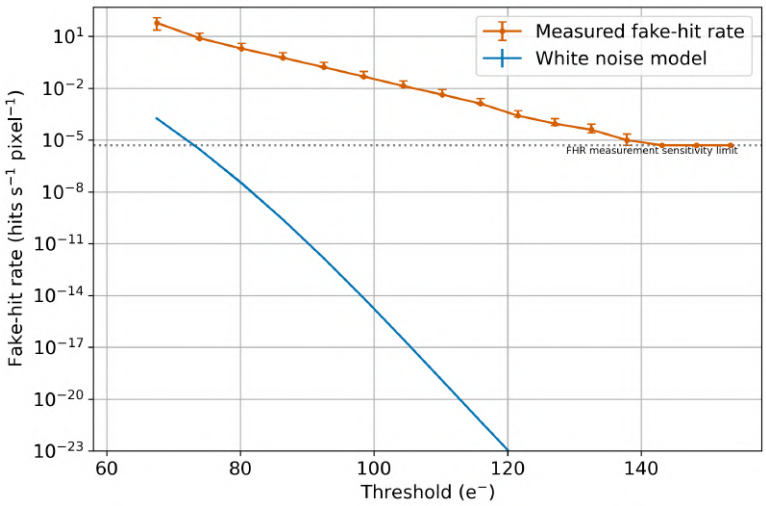

Figure 3.9: Comparison between the fake-hit rate thermal model and the measured fake-hit rate as a function of the applied threshold for a DPTS chip kept at 20 °C. The fake-hit rate measurement sensitivity limit is represented by the dotted line.

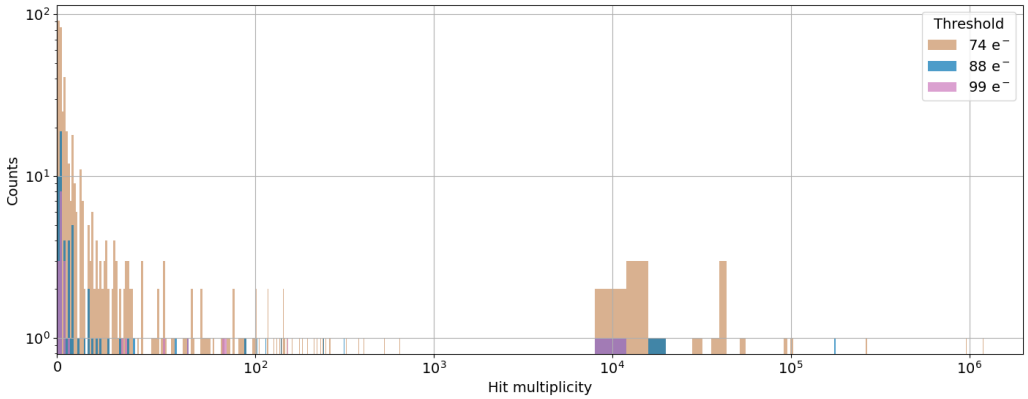

Figure 3.10: Hit multiplicity per pixel at three different thresholds.

3.3.2 Temperature dependence of DPTS fake-hit rate

The fake-hit rate of the DPTS is studied as a function of the temperature at 20 °C, 25 °C and 30 °C. The threshold and noise mean and standard deviation are studied as well to highlight possible correlation with the fake-hit rate. Fig. 3.13a shows the threshold mean as a function of the operating parameter VCASB at the three temperatures. All data sets show the expected (fig. 3.6) decreasing threshold trend for increasing VCASB, with a temperature dependence clearly visible as well, with the threshold mean at 30 °C being systematically lower than for 20 °C and 25 °C. The noise as a function of the threshold is shown in fig. 3.13c. The noise at 30 °C is systematically higher than for 20 °C and 25 °C. No systematic difference is observed in the threshold standard deviation (fig. 3.13b) and in the noise standard deviation (fig. 3.13d).

The fake-hit rate as a function of the applied threshold at 20 °C, 25 °C and 30 °C is shown in fig. 3.14. The three data sets are compatible, meaning that the expected increase in the thermal noise component is negligible if compared to the frequency

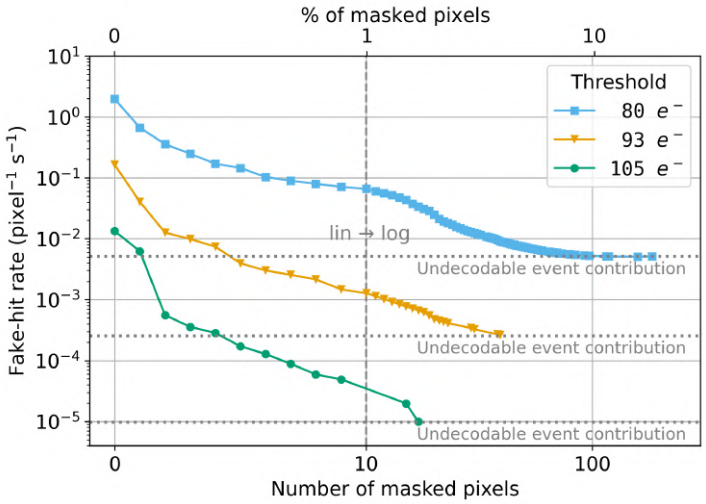

Figure 3.11: Fake-hit rate as a function of the number of masked pixels for three threshold values. Pixels are masked based on their firing rate, from most active to least active. The undecodable event contribution is highlighted by the dotted line.

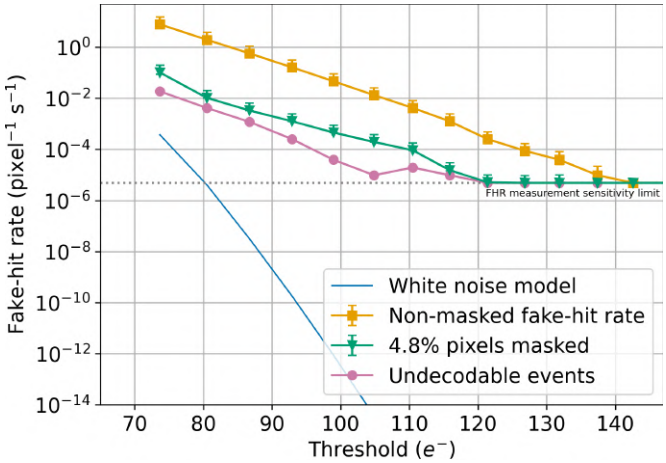

Figure 3.12: Non-masked fake-hit rate (yellow) as a function of the applied threshold compared to the fake-hit rate which is obtained masking 4.8% of the noisiest pixels (green) and to the model (blue). The undecodable events contribution is shown in pink.

dependent source of noise, which are dominating the fake-hit rate.

3.4 MOSS fake-hit rate measurements

The impact of the acquisition window duration on the fake-hit rate is studied with the MOSS at varying thresholds. The matrix position dependence of the fake-hits is studied as well, to investigate possible correlations with the on-chip signal distribution net. A timing analysis to be compared to simulations is presented.

3.4.1 Impacts of the acquisition window duration

The duration of the time interval that is used to measure the fake-hit rate of the sensor is defined by the strobe length. As discussed at the end of sec. 3.2, in the hypothesis of white noise only and of a strobe signal much longer than the characteristic time of the noise events at zero threshold, the fake-hit rate exhibits an inverse proportionality to the strobe duration. The fake-hit rate of the MOSS as a function of the strobe length at different thresholds is shown in fig. 3.15. The fake-hit rate follows a decreasing trend as the strobe length is increasing, except for a jump around a strobe length of 1.2 μs, which is observed for all the thresholds. The expected inverse proportionality is not respected. These observations support the hypothesis of a dominant non-thermal contribution to the noise. As expected, the fake-hit rate is higher for lower threshold values.

A possible matrix position dependence of the fake-hit rate is studied by analysing the fake-hit profiles along rows and columns for different strobe duration, which are shown respectively in fig. 3.16a and 3.16b. The profiles along rows are almost flat, as expected in case of no matrix position dependence, except for a slight increase in the right side. Instead, the profiles along columns show a more significant asymmetry. For strobe lengths lower than 1.5 μs the column fake-hit rate profile exhibits a broad peak on the right side. The asymmetry disappears for a strobe length of 1.5 μs, where the

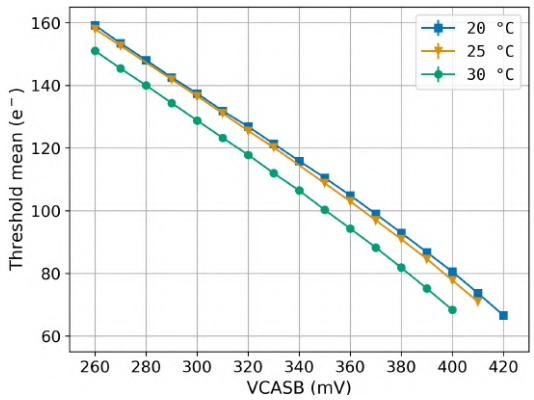

(a) Threshold mean as a function of the operating parameter VCASB at 20 °C, 25 °C and 30 °C.

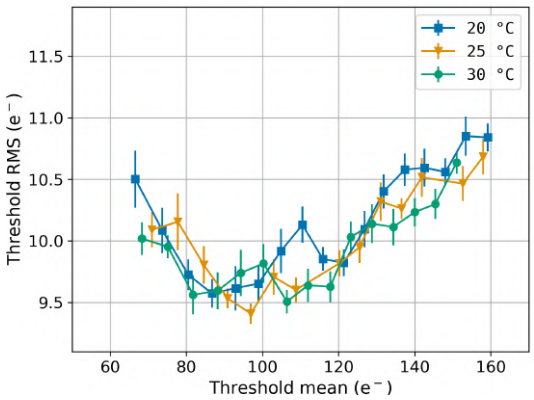

(b) Threshold standard deviation as a function of the threshold at 20 °C, 25 °C and 30 °C.

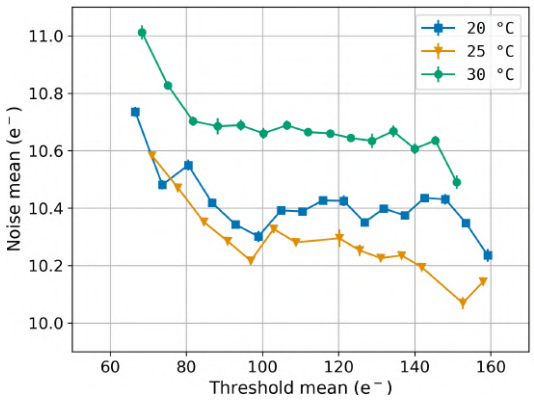

(c) Noise mean as a function of the threshold at 20 °C, 25 °C and 30 °C.

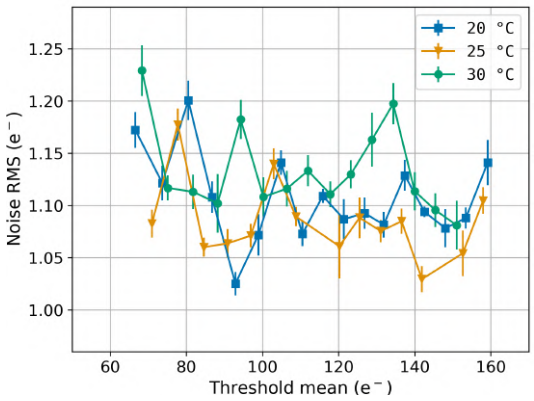

(d) Noise standard deviation as a function of the threshold at 20 °C, 25 °C and 30 °C.

Figure 3.13

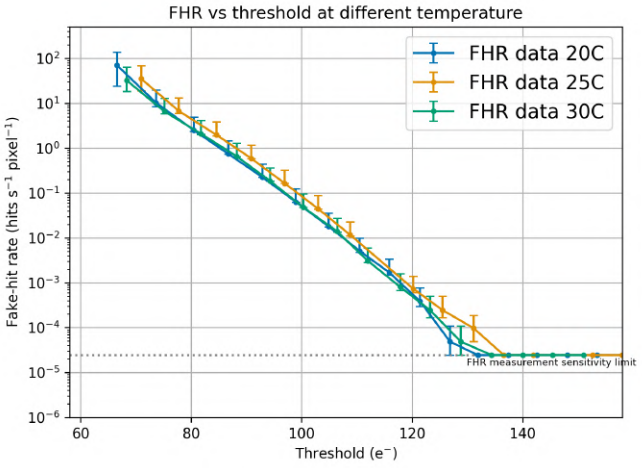

Figure 3.14: Fake-hit rate as a function of the threshold at 20 °C, 25 °C and 30 °C.

profile is constant. An asymmetry occurs again for strobe lengths longer than 1.5 μs,

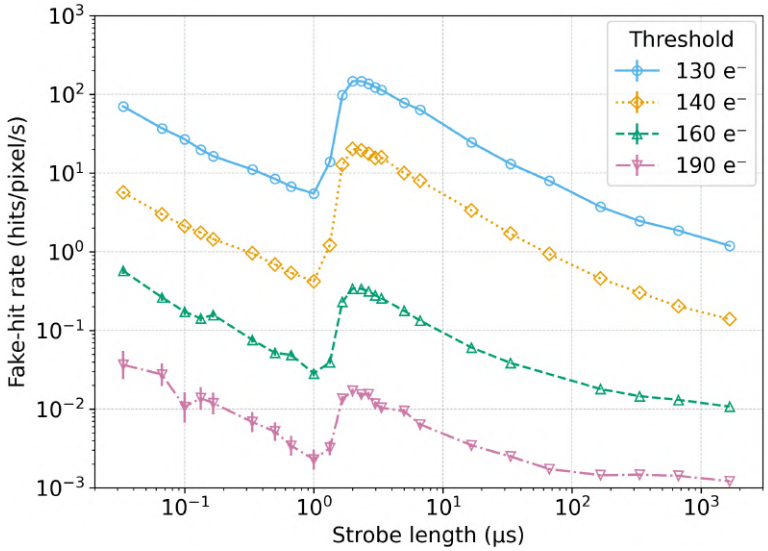

Figure 3.15: Fake-hit rate as a function of the strobe length for the MOSS sensor at four different thresholds.

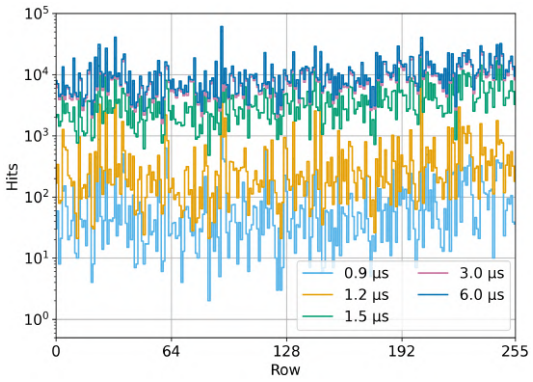

(a) Fake-hits profiles along rows at different acquisition window time duration.

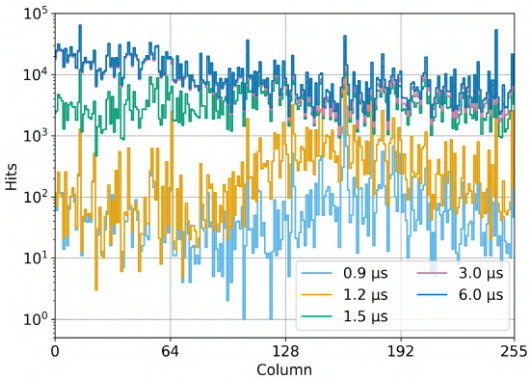

(b) Fake-hits profiles along columns at different acquisition window time duration.

Figure 3.16

where the right side shows a noise occupancy lower than the left.

3.4.2 Timing characteristics of the MOSS fake-hit rate

Given the asymmetry in the fake-hit rate column profiles, the fake-hit rate as a function of the strobe length is studied on single columns. The fake-hit rate is expressed in 10^{-1} pixel^{-1} event^{-1} instead of 10^{-1} pixel^{-1} s^{-1} to allow the fit with an error function.

Fig. 3.17 shows the result for column 32 (a), which is placed in the plateau on the left of the fake-hit column profile shown in fig. 3.16b, and for column 150 (b), which is placed in the broad peak on the right. The mean value given by the error function fit shows that the position of the rising edge of the fake-hit rate is shifted between the two columns for all the threshold values. The rising time is larger for column 32 than for column 150.

The column position-dependence of the fake-hit rate rise time is further investigated

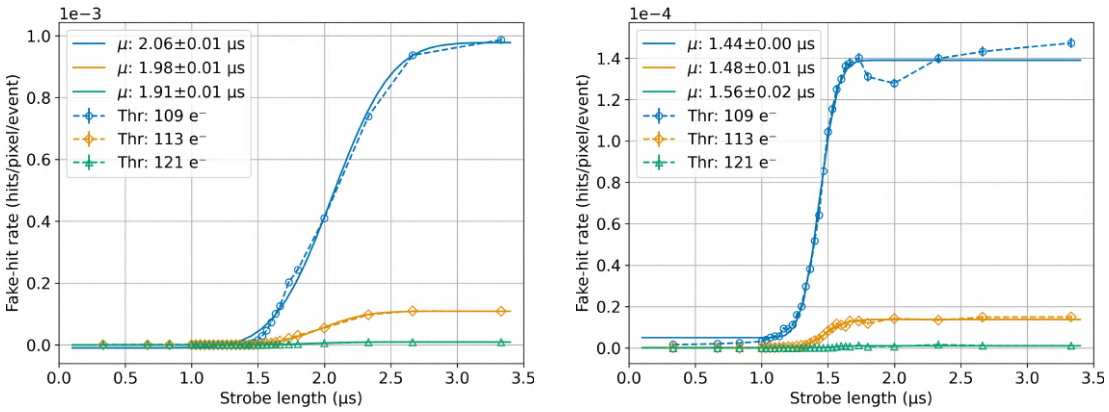

(a) (b)

Figure 3.17: Fake-hit rate as a function of the strobe length for column 32 (a) and for column 151 (b) at different thresholds. The continuous lines represent the error function fit.

by studying the mean (fig. 3.18a) and the standard deviation (fig. 3.18b) given by the fit as a function of the column number for three different thresholds. A clear dependence from the column position is visible. The mean has a minimum around column 150 and increases towards column 256 as well as towards column 50. Between columns 1 and 50 a plateau can be observed. The standard deviation follows a similar behaviour, except for a plateau between columns 150 and 256. Column 150 correspond to the position where the distribution net of the bias VSHIFT starts. VSHIFT is first distributed horizontally and then routed vertically along the columns as schematically represented in fig. 3.19. Other analogue biases are distributed similarly. The strobe signal, instead, comes from the right side of the matrix and is transmitted to the matrix every two rows. A possible coupling between the metal layers of the analogue signal distribution lines and the strobe distribution lines can explain the features observed in the fake-hit column profile, as it might generate noise signals.

A coupling between the strobe lines and the VSHIFT lines is hypothesised in a Cadence Virtuoso [112] simulation of the chip matrix distribution nets. A perturbation on the analogue output node of the in-pixel circuit is observed (fig. 3.20). The simulation is for a region of the MOSS bottom unit, but a similar result is expected for a region of the top unit. The perturbation has the shape of a damped oscillation, that changes polarity going from the first column to the last one. The column corresponding to the position where VSHIFT is distributed to the matrix shows the oscillation with the faster rising edge. The shape of the perturbation allows to explain the trend in the mean in fig. 3.18a. The perturbation arrives earlier at column 150 and so does the mean position of the rising edge of the fake-hit rate as a function of the strobe duration. Going from column 150 to column 50 the mean time increases, as the perturbation is slowly changing polarity, decreasing its ToA as well. After column 50, towards column 0, the mean time remains stable. It is possible that this behaviour not completely explained by the shape of the perturbation in these columns is related to some other couplings between the distribution lines. From column 150 to column 256 the mean time increases, following the increase in the rise time of the perturbation.

The mean position of the jump observed in the fake-hit rate as a function of the

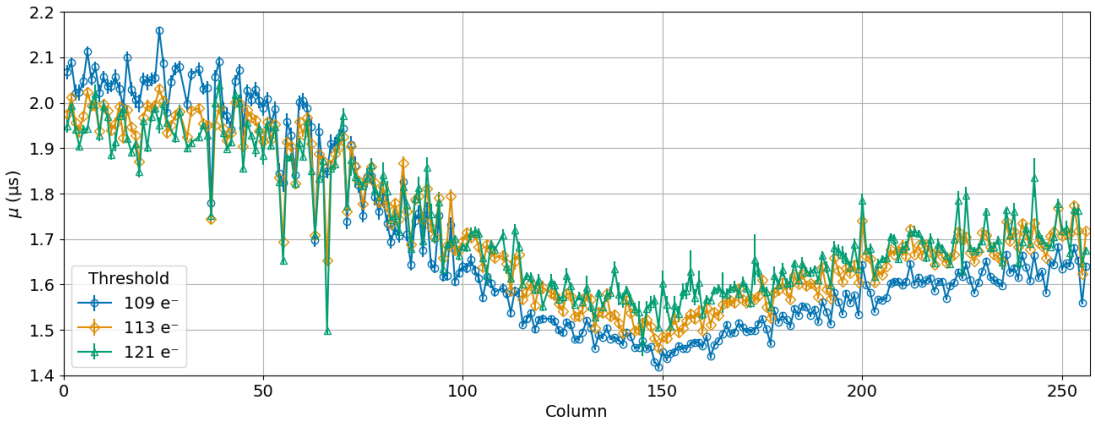

(a)

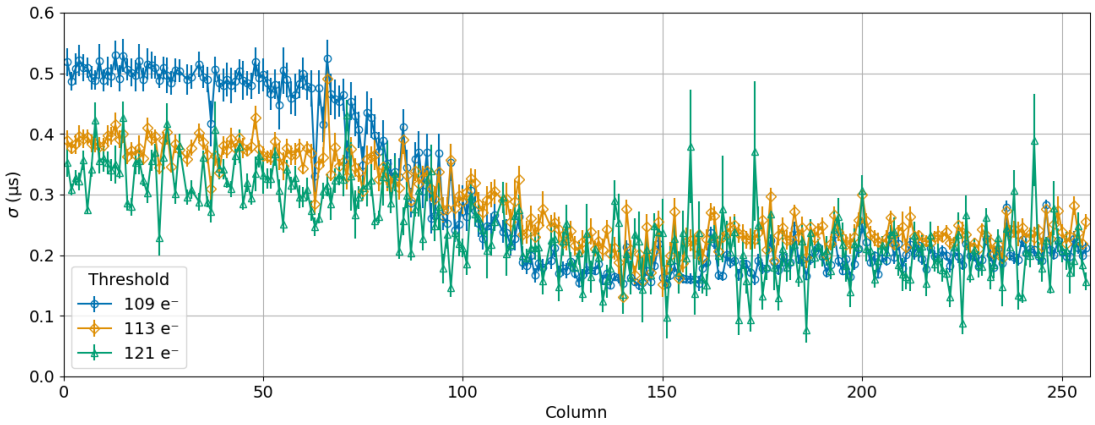

(b)

Figure 3.18: Mean (a) and standard deviation (b) given by the error function fit on single column data (fig. 3.17) as a function of the column number for three different threshold.

strobe length (fig. 3.15) is explained as well by the presence of the perturbation, as the simulation showed that the mean reaction time of the in-pixel circuit when a signal arrives is around 1.2 μs.

3.5 Fake-hit rate study summary

The studies presented in this chapter show that in the MAPS prototypes for the ITS3 there are multiple sources of noise. A thermal model of the noise is developed and compared to the data, showing that the thermal component is not the dominant one in the four tested DPTS. Frequency dependent noise sources are present as well.A study of the dependence of the fake-hit rate on the temperature shows that the frequency-dependent noise component is predominant at 20 °C, 25 °C and 30 °C. The study on the impact of the acquisition window time duration on the fake-hit rate shows an unexpected peak, that with further investigations is associated to a perturbation created by a coupling between the metal lines for the distribution of the analogue bias VSHIF and of the strobe signal, providing important feedback to designers for the final ITS3 sensor design.

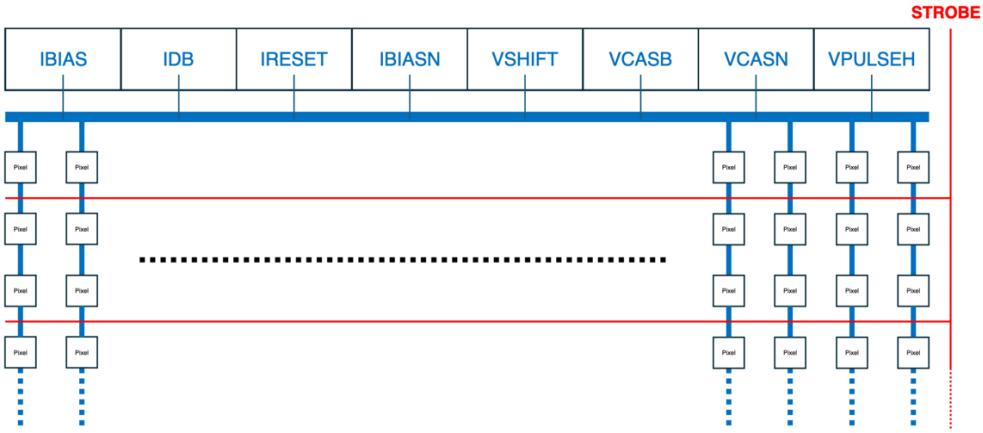

Figure 3.19: Schematic representation of the biases distribution and strobe signal distribution to the matrix. Analogue biases are distributed first horizontally and then routed vertically along columns. The strobe signal is first distributed vertically and then transmitted to the matrix every two rows.

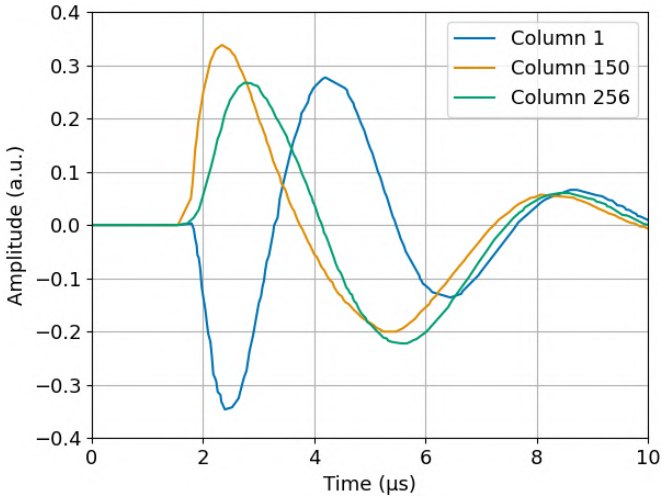

Figure 3.20: Simulation of the perturbation on the pixel analogue output node due to the coupling between the VSHIFT and the strobe distribution lines. The plot has been adapted from a simulation for a MOSS bottom region, which is courtesy of Giacomo Ripamonti.

Chapter 4

Energy-loss measurements

Designed for high detection efficiency and excellent spatial resolution, the DPTS and babyMOSS chips also enable measurement of energy loss in the sensitive volume by encoding the analog signal's Time-over-Threshold information into the digital output. In this chapter a study of the energy response of these ITS3 sensor prototypes is presented in detail.

An introduction on the particle interaction with matter is given in the first part, with particular attention to the processes of interest for this thesis work. The Bethe-Bloch formula, which describes the energy loss of charged particles in matter, is presented, and the specific case of heavy-ion interaction with a thin silicon sensor is outlined. The interaction of photons with matter is described as well, focusing on the processes occurring in silicon in the photon energy range which was explored with this thesis ($< 50\ keV$): photoelectric effect, Compton scattering and coherent scattering are described. The emissions of the radioactive sources $^{55}_{26}$Fe and $^{241}_{95}$Am are depicted in detail.

In the second part of the chapter, the performance of DPTS sensors irradiated with monochromatic X-rays from two radioactive sources ($^{55}_{26}$Fe and $^{241}_{95}$Am) and with fluorescence X-rays emitted from targets (titanium, manganese, iron, palladium, tin) is studied. A detailed analysis of the measured spectra is presented and the calibration of the energy response from 1.73 keV up to 28.5 keV is performed. The temperature effect on the energy calibration and on the energy resolution is investigated, as well as the pixel-to-pixel variability of the energy response.

In the last part of the chapter, the in-beam babyMOSS energy response to heavy-ions is presented. The setup which was used for a dedicated beam test at the GSI/FAIR facility with a mixed ion beam of helium and carbon is described. An ALPIDE telescope was used to track the beam particles and a custom-made scintillator setup with Time Of Flight (TOF) and energy loss measurement capabilities was used to characterise the beam and select the particle type in the offline analysis.

4.1 Radiation energy-loss in silicon

In this section the interaction of particles with matter is described, focusing on the processes of interest for the characterisation measurements of the ITS3 prototypes. Firstly, the interaction of charged particles with matter is discussed. In particular, the Bethe-Bloch formula is presented and the case of heavy-ion energy loss in thin absorber is explored. Secondly, the interaction of photons is described. The photoelectric effect is outlined first, as it is the one of greatest interest for the characterisation of the energy

response, since it leads to the release of all the photon energy in the medium. Subsequently the Compton scattering and the Rayleigh scattering are discussed as possible source of background in the X-Ray Fluorescence (XRF) measurements discussed in the following sections. The characteristics of two radioactive sources $^{55}_{26}$Fe and $^{241}_{95}$Am , which are used to investigate the ITS3 prototype energy response to X-rays, are described.

4.1.1 Interaction of charged particles

Charged particles lose energy in matter manly through ionisation, i.e. many inelastic collisions with the atomic electrons of the material [113]. Other energy-loss processes can occur, as the Cherenkov radiation emission, nuclear reactions and braking radiation or Bremsstrahlung, but are not of interest for the particles and the energy range exploited in this thesis.

4.1.1.1 The Bethe-Bloch formula

The average energy loss by ionisation per unit path length (dE/dx), usually referred to as *stopping power*, is described by the Bethe-Bloch formula, to which the density effect correction δ and the shell correction C are added:

$$-\frac{dE}{dx} = 2\pi N_a r_e^2 m_e c^2 \rho \frac{Z}{A}\frac{z^2}{\beta}\left[ln\left(\frac{2m_e\gamma^2 v^2 W_{max}}{I^2}\right) - 2\beta^2 - \delta - 2\frac{C}{Z}\right] \tag{4.1}$$

with the variables reported in tab. 4.1. The maximum energy transfer for a particle of mass $M >> m_e$ in a single collision is defined [113] as:

$$W_{max} = 2m_e c^2 \beta^2 \gamma^2 \tag{4.2}$$

Table 4.1: Summary of variables used in the Bethe-Bloch formula (eq. 4.1).

N_a	Avogadro's number (6.022×10^{23} mol^{-1})
r_e	classical electron radius (2.817×10^{-13} cm)
m_e	electron mass
c	light speed
ρ	absorbing material density
Z	absorbing material atomic number
A	absorbing material atomic weight
z	incident particle charge in units of e^-
v	incident particle speed
β	incident particle v/c
γ	incident particle $1/\sqrt{1-\beta^2}$
W_{max}	maximum energy transfer in a single collision
I	mean excitation potential
δ	density correction
C	shell correction

The Bethe-Bloch formula (eq. 4.1) gives results which are valid within a few percent in the region $0.1 < \beta\gamma < 1000$ for elementary particles which are more massive than the electron and for H and He nuclei. For heavier nuclei some charge-dependent

corrections are needed [114, 115, 116] and discussed further below. Fig. 4.1 shows the mass stopping power of muons in copper. For $\beta\gamma$ between 0.1 and 1 the stopping power falls as $1/\beta^2$ until it reaches a minimum at $\beta\gamma \sim 3$. Particles with this $\beta\gamma$ are called *Minimum Ionising Particles* (MIP). For increasing $\beta\gamma$ up to 1000, the stopping power increases, as the logarithmic term increases. At high energies, the density correction term *delta* takes into account the reduction of the energy loss, which is due to the polarisation of the medium by the passage of the charged particle. The green dashed line shows the stopping power without the shell correction.

The Bethe-Bloch formula assumes that the incident particle interacts with a gas of free electrons. This condition is true if the speed of the incident particle is larger than the speed of the atomic electrons. When the projectile speed is lower, the shell correction C accounts for the occurring effects. Together with other two corrections terms proposed by Baraks [117] and Bloch [118], the corrected Bethe-Bloch formula is accurate down to $\beta\gamma \sim 0.05$. For $0.01 < \beta\gamma < 0.05$ no theory is able to describe the measurements, and the data which were tabulated for protons by Andersen and Ziegler [117, 119] are used. For $\beta\gamma$ below 0.01, Lindhard theory [120, 121] provides an accurate description.

4.1.1.2 Heavy-ion energy loss

The total energy loss by heavy-ions in matter has a contribution coming from the interaction of the projectile with the target electrons, called electronic stopping, and a contribution due to the interaction with the target nuclei, named nuclear stopping [122, 123]. The nuclear stopping is negligible for ion energies above 200 keV/amu. Since this energy is well below the one of the ions which were used for this work (225 MeV/amu), the nuclear stopping contribution will not be discussed further.

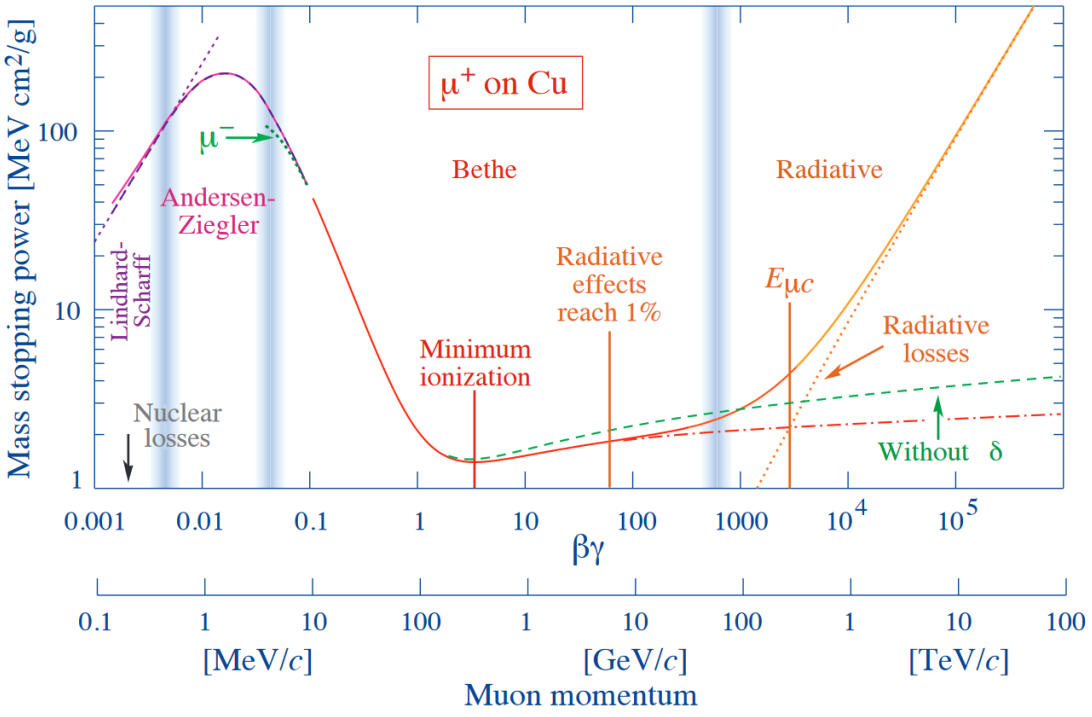

Figure 4.1: Positive muon mass stopping power (solid line) in copper. Figure from [3].

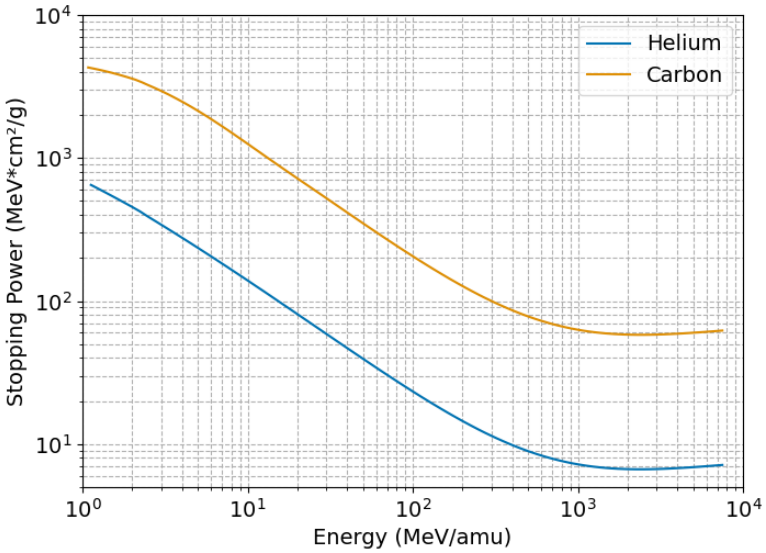

Figure 4.2: Electronic stopping power of helium and carbon ions in silicon. The ions used to characterise the ITS3 prototypes have an energy of 225 MeV/amu. Plot done using data from the SRIM software [125].

The heavy-ion scaling rule is usually applied to retrieve the stopping power of the ions (S_{HI}) from the one of the protons (S_p). The rule states that the ratio between the stopping power of the protons at two different velocities v_1 and v_2 is equal to the ratio between the stopping power of the ions (S_{HI}) at the same velocities in the same material:

$$\frac{S_p(v_1, Z)}{S_p(v_2, Z)} = \frac{S_{HI}(v_1, Z)}{S_{HI}(v_2, Z)} \tag{4.3}$$

with Z the atomic number of the material. Given that:

$$\frac{S_{HI}(v, Z)}{S_p(v, Z)} = \tilde{z} \tag{4.4}$$

eq. 4.3 can be simplified as:

$$S_{HI} = S_p \cdot \tilde{z}^2 \tag{4.5}$$

where $\tilde{z}$ is the heavy-ion effective charge. The Thomas-Fermi atomic theory can be used to estimate $\tilde{z}$, which is expressed by Northcliffe as:

$$\tilde{z} = z \sqrt{1 - exp\left(- \frac{v_1}{v_0 z^{2/3}} \right)} \tag{4.6}$$

where z is the ion atomic number, v_1 is its speed and v_0 is the Bohr speed.

Fig. 4.2 shows the electronic stopping power as a function of the energy for helium (in blue) and carbon (in yellow) ions in silicon computed by the software SRIM [124, 125]. The energy of interest for this thesis is of 225 MeV/amu, i.e. 0.9 GeV and 2.7 GeV for He and C respectively. The energy lost by the two ions differs by about one order of magnitude, making them easily identifiable by a system with energy-loss measurement capabilities.

4.1.1.3 Energy loss fluctuations

The Bethe-Bloch formula (eq. 4.1) gives the mean energy which is lost by a charged particle passing through a medium. The statistical fluctuations in the collision number and in the energy transferred for each collision will cause the energy lost by the particle to follow a certain statistical distribution. Usually, such distribution is derived for thick and thin absorbers separately.

In thick absorbers the number of collisions is large enough to apply the Central Limit Theorem, thus the sum of the energy transferred in each collision, ΔE shows a Gaussian distribution, which is centred in the mean value ΔE_{BB} predicted by the Bethe-Bloch formula:

$$f_{\Delta E}(x) \propto e^{-\frac{(\Delta E - \Delta E_{BB})^2}{2\sigma^2(x)}} \tag{4.7}$$

where σ is [113]:

$$\sigma^2(x) = 4\pi N_a r_e^2 (m_e c^2)^2 \rho \frac{Z}{A}\left(\frac{1-\frac{\beta^2}{2}}{1-\beta^2}\right)x = 0.1569\ MeV^2 \cdot \rho \frac{Z}{A}\left(\frac{1-\frac{\beta^2}{2}}{1-\beta^2}\right)x \tag{4.8}$$

where x is the absorber thickness and the parameters are those summarised in tab. 4.1.

The condition on the Gaussianity $\sigma >> W_{max}$, where W_{max} (eq. 4.2) is the maximum energy transfer in a single collision, leads to a minimum thickness required to consider an absorber "thick":

$$x >> \frac{2m_e c^2 \beta^2 \gamma^2}{0.1569\ MeV^2 \cdot \rho} \frac{A}{Z}\left(\frac{1-\beta^2}{1-\frac{\beta^2}{2}}\right) = x_{min} \tag{4.9}$$

In the case of interest for this thesis, i.e. Helium and Carbon ions of 225 MeV/amu, x_{min} in silicon is 330 μm, several times larger than the thickness of the sensitive layer of the ITS3 prototypes ($\sim$10 μm).

Therefore the reduced number of collisions of the incident particle with the absorber electrons does not allow to use the Central Limit Theorem and the absorber cannot be considered thick. The expected distribution is asymmetric with a tail towards high energies. Such distribution was described by Landau and Vavilov [126, 127]. The Most Probable Value (MPV) of energy loss differs from the mean value given by the Bethe-Bloch formula and was defined by Landau [128] as:

$$\Delta E_{MPV} = \xi(x)\left[ln\frac{2mc^2\beta^2\gamma^2}{I} + ln\frac{\xi(x)}{I} + 0.2000 - \beta^2 - \delta\right] \tag{4.10}$$

where ξ is equal to:

$$\xi = 4\pi N_a r_e^2 m_e c^2 \frac{1}{2}\left\langle\frac{Z}{A}\right\rangle z^2 \frac{x}{\beta^2}\ \text{MeV} \tag{4.11}$$

Fig. 4.3 shows the ratio between the MPV in silicon and the mean loss of a minimum ionizing particle, 1.66 MeVg^{-1}cm^2, for different thicknesses of silicon.

A Landau distribution, convoluted with a Gaussian distribution, which takes into account fluctuations in the detector response due to noise, is used in the following to fit the energy distribution measured with the ITS3 prototypes.

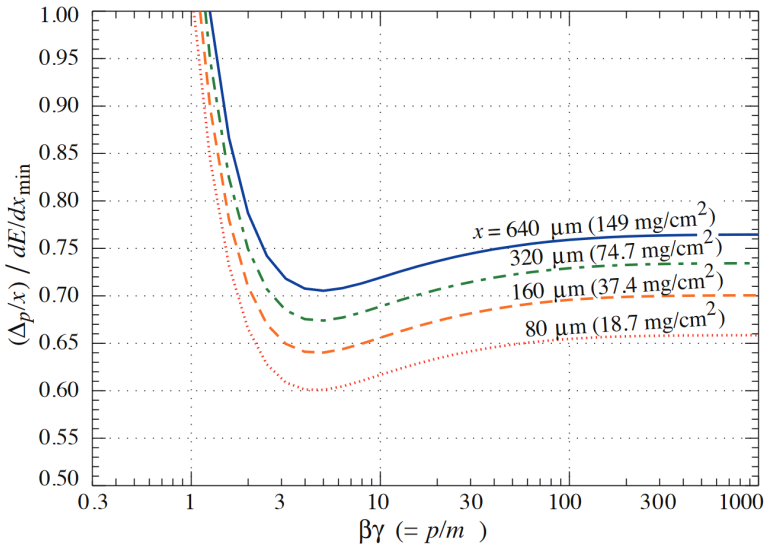

Figure 4.3: Ratio between the most probable energy loss in silicon and the mean loss of a minimum ionizing particle, 1.66 MeV g^{-1}cm^2. Colours represent different silicon thickness. Figure from [3].

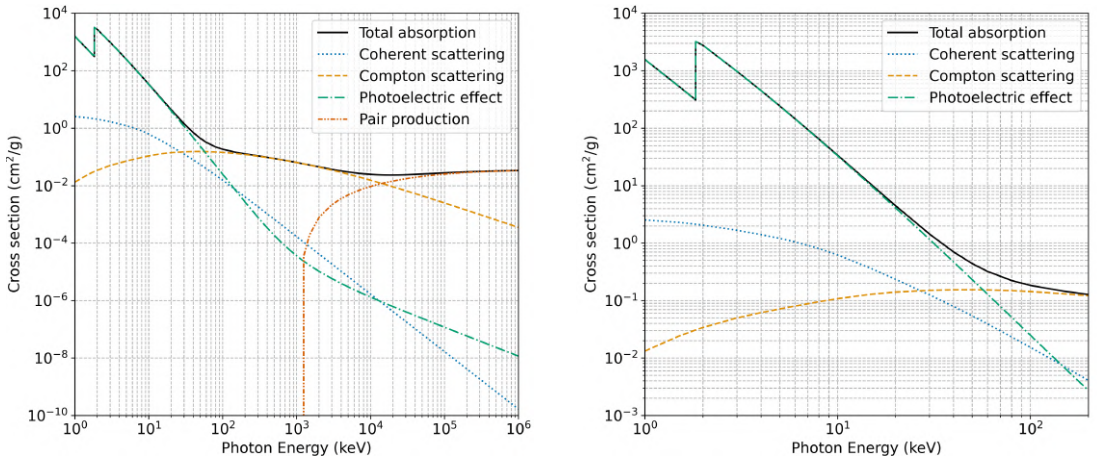

(a) (b)

Figure 4.4: Total absorption coefficient of silicon and contributions of different type of interactions with respect to the incident photon energy (a). The photoelectric effect is dominant in the energy range used in the measurements of this thesis (b), followed by coherent scattering and Compton scattering. Data is from [130].

4.1.2 Interaction of photons

Photons in matter undergo mainly photoelectric absorption, Compton scattering and pair production, depending on the energy of the photon and on the material of the detector [113, 129]. Coherent or elastic scattering, which includes Rayleigh, Thomson and Delbrück scattering, can occur as well. Fig. 4.4a shows the contributions to the total absorption coefficient of silicon, while fig. 4.4b shows a magnification of the same absorption coefficient in the energy range of interest for the measurements presented in this thesis. The production of an electron-positron pair can take place only

if the incident photon has an energy higher than 1.022 MeV. Since the energy of the X-rays which were used to characterise the ITS3 prototypes are below 50 keV, only photoelectric absorption, Compton scattering and coherent scattering are expected to occur.

In general, given N_0 incident X-rays, the number N of photons interacting with the detector is equal to:

$$N = N_0\left(1 - e^{-\mu\rho x}\right) \tag{4.12}$$

where ρ is the density of the material and μ is its absorption coefficient, equal to the sum of the absorption coefficients of each interaction type that can occur.

4.1.2.1 Photoelectric effect

The photoelectric effect is the interaction of most interest for the characterisation of the sensor response, as all the photon energy is released into the detector. It consists in the absorption of the incident photon by an atomic electron. If the binding energy E_B of the electron is lower than the energy of the photon E_γ, the electron is ejected from the atom with a kinetic energy:

$$E_{kin} = E_\gamma - E_B \tag{4.13}$$

In tab. 4.2 the electron binding energies for K, L and M shells of Silicon are reported. In the most probable case, the incoming photon interacts with electrons of the M

Table 4.2: Electron binding energies of ^{14}Si [131] [132] for K, L and M shell.

	K 1s $[eV]$	L 2s $[eV]$	L 2p $[eV]$	M $[eV]$
^{14}Si	1839	150	100	8.15

shell. The silicon ionization energy for M shell, around 10 eV, is negligible and the released electron has an energy equal to the one of the incoming photon. Instead, when the interaction is with an electron of the L shell, the binding energy is not negligible. However, the subsequent rearrangement of the electrons inside the atom can produce de-excitation X-rays which are photoelectrically absorbed and so the total energy detected is equal again to the one of the incoming photon. Sometimes it can also occur that the main photoelectric effect takes place involving one electron of the silicon K shell. A hole is left in the K shell, then filled by the de-excitation of an electron from the L shell. This leads to the production of a characteristic X-ray, that for silicon has an energy of 1.74 keV [133]. This process is called X-Ray Fluorescence (XRF) and is exploited for the measurements described in sec. 4.2 to produce photons of well-known energy from single element targets. The fluorescence photon can undergo photoelectric absorption in turn. When it is not detected because it escapes the active region, the overall energy seen by the detector is decreased by 1.74 keV: this originates the silicon escape peak [134, 135].

The absorption coefficient μ of the photoelectric effect increases with the atomic number Z of the medium. The mean free path of a photon in a medium of density ρ before interacting by photoelectric effect is defined as:

$$\lambda_{ph} = \frac{1}{\rho\ \mu_{ph}} \tag{4.14}$$

Fig. 4.5a shows the mean free path λ_{ph} in silicon for photons up to 100 keV. Since the thickness of the ITS3 prototypes is of 50 μm, photons with an energy less than ~10 keV are expected to be easily absorbed within the detector. However, the sensitive layer thickness is of only 10 μm, so the percentage of photons detected will be lower than that of the absorbed ones. Fig. 4.5b shows the percentage of photons that undergo photoelectric absorption in 10 μm of silicon. As expected from eq. 4.12, the percentage follows an exponential decrease, becoming less than 1 % for photons with an energy above 20 keV. In fig. 4.5c the Continuous Slowing-Down Approximation (CSDA) range in silicon is reported for photoelectron energies of interest. The pixel pitch of the studied ITS3 prototypes is of 15 μm, thus photoelectrons with an energy up to ~35 keV are expected to be collected by single pixels. However, it must be noted from the plot in fig. 4.5b that the number of absorbed photons with this energy is very little (< 0.3 %).

4.1.2.2 Compton scattering

The Compton scattering is the interaction between a photon and a free electron. Atomic electrons are considered free if their binding energy is much lower than the incident photon energy. Fig. 4.6 shows the kinematics of the Compton scattering. Given an incident photon with an initial energy E_γ, which after the scattering at an angle φ becomes $E_{\gamma'}$, the energy transferred to the electron, which is scattered at an angle θ, will be:

$$E_\gamma - E_{\gamma'} = \frac{E_\gamma E_{\gamma'}}{m_e c^2}\big(1 - cos(\varphi)\big) \tag{4.15}$$

where m_e is the electron mass, c is the light speed. This relation comes out from the energy and momentum conservation. It must be noted that the incident photon releases only partially its energy into the detector, thus making the Compton scattering not ideal for the characterisation of the sensor response.

The angular distribution probability of the scattered photons can be derived from the Klein-Nishina differential cross-section ($d\sigma/d\Omega$) [113]:

$$\frac{d\sigma}{d\varphi} = 2\pi sin(\varphi)\frac{d\sigma}{d\Omega} = 2\pi sin(\varphi)\frac{r_e^2}{2}\frac{1}{[1+y(1-cos\varphi)]^2}\left(1 + cos^2\varphi + \frac{y^2(1-cos\varphi)^2}{1+y(1-cos\varphi)}\right) \tag{4.16}$$

where $y = E_\gamma/(m_e c^2)$. Such cross section is represented in fig. 4.7 as a function of the incident angle for different photon initial energies. There are two maxima for almost all the energies, one between 40° and 60° and one between 110° and 130°. The second one is less pronounced for high incident photon energies (> 50keV). Rather than for detection, the Compton scattering is important in the measurements presented in sec. 4.2 to have an indication on the primary beam photons that undergo Compton scattering in the target used for XRF.

4.1.2.3 Coherent scattering

Rayleigh or coherent scattering is the elastic interaction of the incident photon with atoms as a whole. The characteristic of this interaction is that no energy is transferred to the medium, only the direction of the photon is changed. The understanding of this type of interaction is important for the evaluation of the background seen by the sensor in XRF measurements (see sec. 4.2). The Rayleigh scattering occurs for low photon

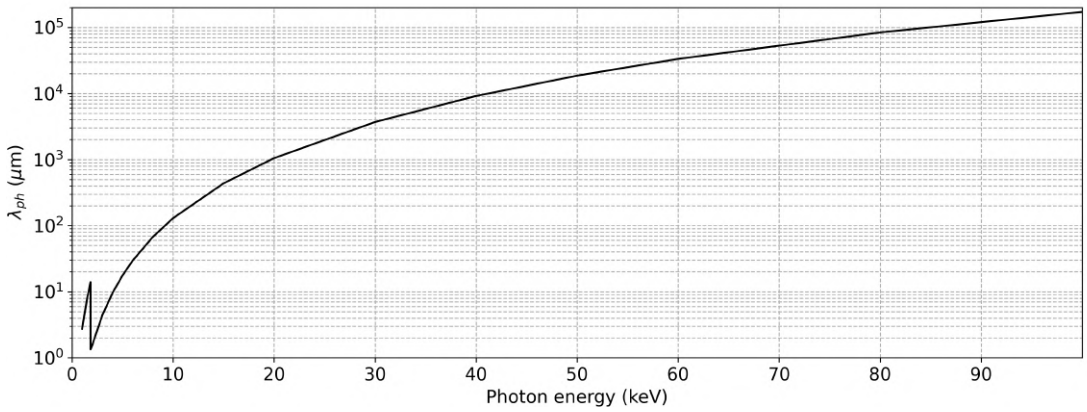

(a) Photon mean free path in silicon as a function of energy. Data from [130].

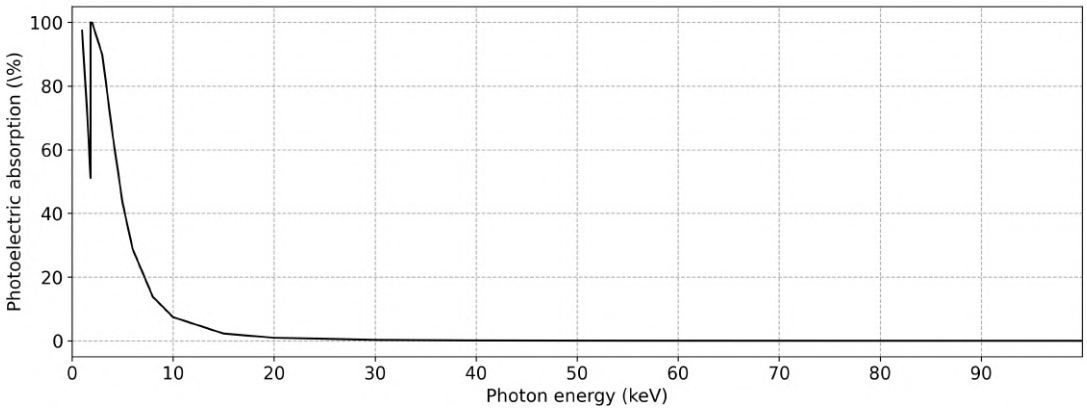

(b) Percentage of photons absorbed by photoelectric effect in 10 μm of silicon. Data from [130].

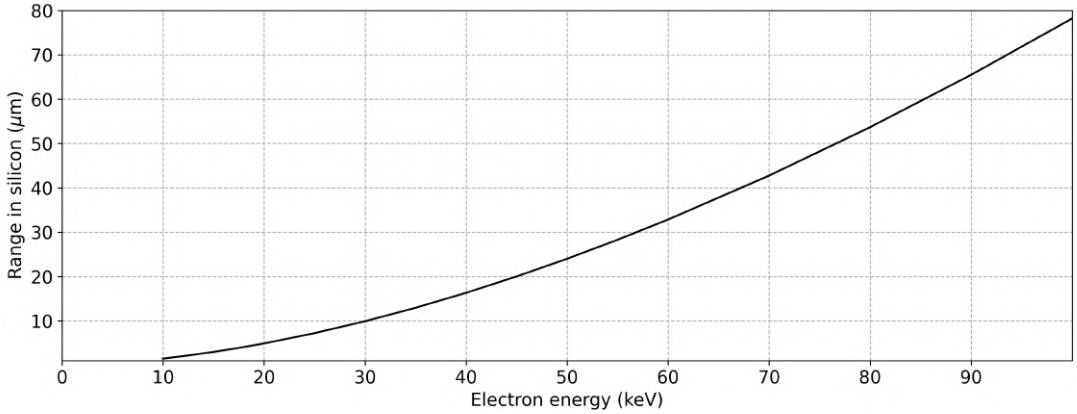

(c) Electron mean Continuous Slowing-Down Approximation (CSDA) range in silicon. Data from [136].

Figure 4.5

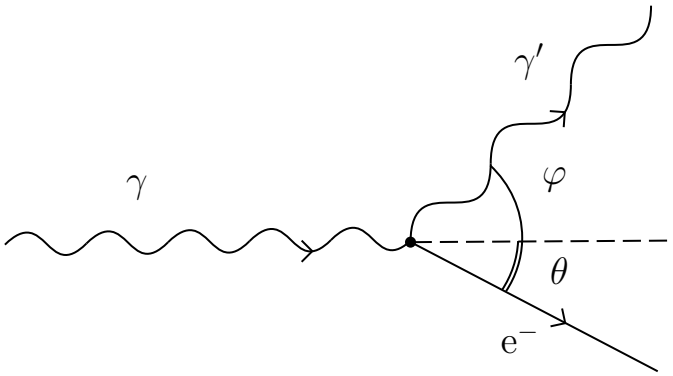

Figure 4.6: Schematic representation of Compton scattering. An incident photon γ interacts with an electron and is scattered by an angle φ with respect to the original direction.

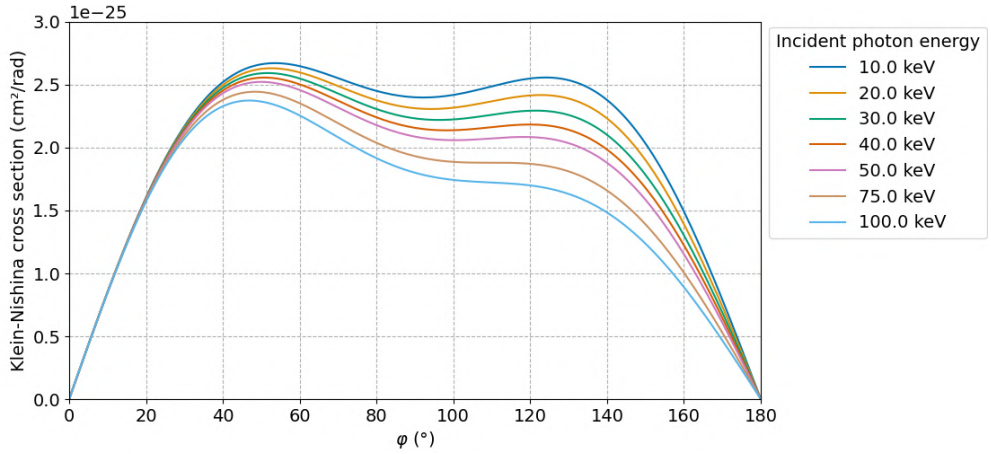

Figure 4.7: Klein-Nishina cross section as a function of the photon scattering angle φ. When ε=0° the photon continues traveling along its initial trajectory, when ε=180° the photon is back scattered. Colours represent different energies of the incident photon.

energy and in high-Z materials. The Rayleigh differential cross section is [137]:

$$\frac{d\sigma_R}{d\Omega} = F^2(q,Z)\frac{r_e^2}{2}(1+cos^2\varphi) \tag{4.17}$$

where the quantities are summarised in tab. 4.1, $F(q,Z)$ is the atomic form factor and q is the momentum transfer:

$$q \approx 2\frac{E_\gamma}{m_e c^2} sin\left(\frac{\theta}{2}\right) \tag{4.18}$$

Assuming constant the atomic form factor, which is true in the classical limit, eq. 4.17 reduces to:

$$\frac{d\sigma_R}{d\Omega} = \frac{r_e^2}{2}(1+cos^2\varphi) \tag{4.19}$$

thus meaning that the scattering is maximum for φ=0°,180° and minimum for φ=90°.

4.1.3 Radioactive sources

Two radioactive sources have been used to characterise the energy response of the ITS3 prototypes to X-rays, the $^{55}_{26}$Fe and the $^{241}_{95}$Am . They are described in the following.

4.1.3.1 $^{55}_{26}$Fe source characteristics

$^{55}_{26}$Fe disintegrates by electron capture with a half-life time of $2.73y$ [3] according to the following decay scheme:

$$^{55}_{26}Fe + e^- \rightarrow {}^{55}_{25}Mn + \bar{\nu}_e \tag{4.20}$$

The captured electron leaves a vacancy in the K shell of the resulting atom, which can be filled by deexcitation from the upper shells. If the deexcited electron comes from the L shell, the resulting characteristic X-ray is called $K\alpha$, if the electron comes from the M shell it is called $K\beta$ [138]. A further distinction between the two emissions can be done according to the spin of the decaying electron, so that some substructures are distinguishable. Besides X-ray emissions, also a γ transition can be observed as well as a continuous background up to 231.21 keV due to inner Brehssmtrahlung and Auger electrons. In tab. 4.3 the energies and the rates normalized to 100 disintegrations are reported.

Table 4.3: Energies and rates normalized to 100 disintegrations of main $^{55}_{26}$Fe emissions [139].

	Energy $[keV]$	Emissions per 100 disint.
Auger e^-	0.47-0.67	140.2±0.8
	4.95-6.53	60.1±0.5
$K\alpha_2$	5.89	8.45±0.14
$K\alpha_1$	5.90	16.57±0.27
$K\beta_{1-3}$	6.49	3.40±0.01
$K\beta_{5-4}$	6.53	
γ	125.9	$0.13 \pm 0.01 \times 10^{-6}$

For this work, the emissions of interest are the X-rays, as they are monochromatic and easily detectable. The difference between the energies of $K\alpha_1$ and $K\alpha_2$ is negligible, like the one between $K\beta_{1-3}$ and $K\beta_{5-4}$. This leads to two main emissions, $K\alpha$ with an average energy of 5.9 keV and a decay probability of $25.02 \pm 0.41\%$ and $K\beta$ with an average energy of 6.5 keV and a decay probability of $3.40 \pm 0.07\%$. γ rays give a negligible contribution to the detected spectrum, due to their low emission probability. Regarding Auger e^-, in air the mean range for a 10 keV e^- is $2.9 \cdot 10^{-4} g/cm^2$ [136], that means 0.24 cm, smaller than the distance between the source and the detector (> 1 cm).

The Kα and Kβ emissions of $^{55}_{26}$Fe will be mainly absorbed by photoelectric effect in silicon, given that the photoelectric absorption coefficient is the dominant one at their energies (see sec. 4.1.2.1). Considering the effects described in sec. 4.1.2.1, we expect the release of electrons of four energies within the detector, summarized in tab. 4.4. The range in silicon for an electron of 10 keV is 1.5 μm [136], therefore we can assume that all the created electrons remain inside the detector. Released electrons lose energy by ionization, generating e-h pairs. In silicon the mean energy necessary to produce

a pair is about 3.6 eV at room temperature, therefore it is possible to compute the average expected number of pairs created for each signal (tab. 4.4).

Table 4.4: Expected peaks and their energies in keV and in terms of created pairs in depleted silicon. The statistical error on the number of pairs is calculated as its square root.

	Energy $[keV]$	Created pairs
Si_{fl}	1.74	483±22
Si_{es}	4.16	1156±34
K_{α}	5.90	1639±41
K_{β}	6.51	1808±43

The effective signal collected depends also on the geometry of the detector [140] (fig. 4.8). If the electron loses its energy in the depleted region, all the produced pairs are collected. If the electron is created in the substrate, only charges that reach the depleted region by diffusion are collected. This results in a continuum background up to 6.5 keV. If the electron loses energy in the CMOS circuitry layer it is difficult to make a prediction of the resulting signal without a simulation.

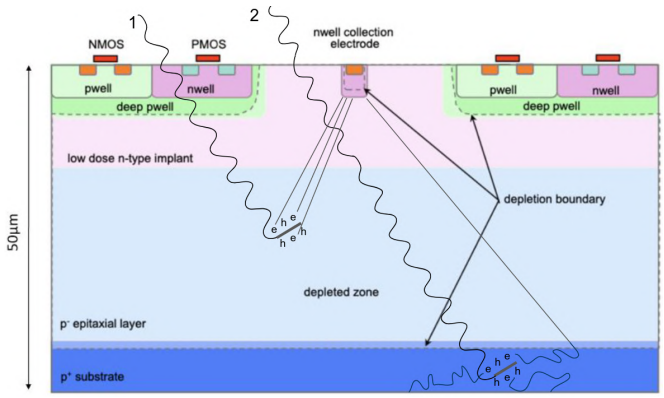

Figure 4.8: Two cases of photoelectric absorption in a silicon depleted detector. If the X-ray is absorbed in the depleted region the created electrons reach the collection diode mainly by drift. If the X-ray is absorbed in the substrate only electrons reaching the depleted region by diffusion are collected.

4.1.3.2 $^{241}_{95}$Am source characteristics

$^{241}_{95}$Am decays via alpha emission with a half-life time of 432.6 y [3] according to the following nuclear reaction:

$$^{241}_{95}Am \rightarrow ^{237}_{93}Np + \alpha \tag{4.21}$$

the $^{237}_{93}$Np daughter nucleus is typically not produced in its ground state, but rather in one of its excited states, thus the emitted alpha particle can have different energies, as reported in tab. 4.5. In the 84.4% of the cases the emitted alpha particle has an energy of 5.486 MeV and the excited $^{237}_{93}Np$ is populated in its level with an energy of 59.5 keV [141].

Table 4.5: Energies and emission probabilities of alpha particles emitted by $^{241}_{95}$Am [141].

Energy $[MeV]$	Emissions probability
5.479	1.7%
5.534	13.2%
5.578	84.4%
5.604	0.23%
5.637	0.38%

The excited $^{237}_{93}Np^*$ undergoes a γ decay to reach a stable state

$$: {}^{237}_{93}Np^* \rightarrow {}^{237}_{93}Np + \gamma \tag{4.22}$$

Depending on the excited state of Neptunium, the produced photon can have different energies. In tab. 4.6 are reported the most probable transitions and the energy of the emitted photon, considering also the characteristic emissions of neptunium due to the re-arrangement of the shell electrons.

Table 4.6: Emitted photon energy for the most probable transitions in the $^{237}_{93}Np^*$ decay [141, 142, 143]. The characteristic emissions Lα_1, Lβ_1 and Lγ_1 are accounted as well.

Transition	Photon energy (keV)
Lα_1	13.9
Lβ_1	17.8
Lγ_1	20.8
$\gamma_{2,1}$(Np)	26.3
$\gamma_{1,0}$(Np)	33.2
$\gamma_{2,0}$(Np)	59.5

The $^{241}_{95}$Am source which is used for the measurement is contained in a thin plastic shell, thus the alpha particle are stopped and only the emitted photons reach the detector.

4.2 DPTS energy response characterisation with X-rays

The performance of the DPTS (sec. 2.3.1) irradiated with X-rays was studied. In most cases, X-rays release all of their energy inside the detector by photoelectric effect, hence it is possible to associate a well-known energy to a given response of the device. Different sources of X-rays were used to characterise the DPTS, i.e. a $^{55}_{26}$Fe radioactive source, an $^{241}_{95}$Am radioactive source and fluorescence photons created from targets in a dedicated X-Ray Fluorescence (XRF) setup. In this section the response of DPTS to a wide range of X-rays energies, from 1.73 keV to 28.5 keV, is presented in detail: in the first part a description of the experimental setup used for XRF measurements

is provided. Then, a detailed analysis of the measured spectra is outlined, to obtain an energy calibration of the response up to 28.5 keV. The influence of the temperature on the energy calibration and on the resolution is investigated as well. Lastly, a single pixel calibration is performed to assess the contribution of the pixel-to-pixel energy response variation to the measured threshold.

4.2.1 Setups for X-ray measurements

The DPTS test system, described in sec. 2.3.1.4, was used to acquire data with radioactive sources and XRF. The radioactive source measurements were conducted at the INFN laboratories in Trieste, by adding a source holder to the carrier card to keep the radioactive source at about 2 cm above the sensor. Fig. 4.9 shows the $^{55}_{26}$Fe source mounted on the support.

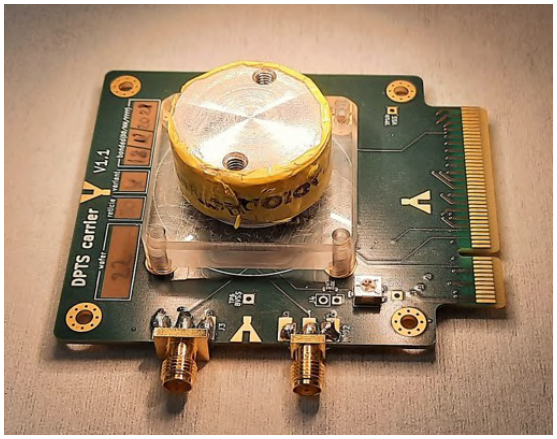

Figure 4.9: DPTS carrier card with an additional plastic source holder mounted on top of the sensor to keep in position the $^{55}_{26}$Fe source.

The XRF measurements took place at two facilities located at Elettra Sinctrotrone Trieste [144], namely the Instrumentation & Detectors Laboratory [145] and the OptImaTo (Optimal Imaging and Tomography) laboratory [146].

In the first laboratory, an X-ray tube with a copper anode was used to produce the primary X-ray beam, which was characterised by a continuum Bremsstrahlung background up to 40 keV and by the copper characteristic Kα and Kβ emissions at 8.0 keV and 8.9 keV, respectively. The beam has a diameter of 1-2 mm. Fig. 4.10 shows the setup from above. The primary beam coming out from the X-ray tube hits the target, placed at an angle smaller than 45° relative to the beam direction. This angle is chosen to reduce Compton scattering of the primary beam in the detector direction. The DPTS was facing the target at 2.3 cm. This setup was used to acquire high statistics for evaluating the pixel-to-pixel variation of the energy response, as described in sec. 4.2.5. A tin and an iron foil were placed side by side and used as targets to acquire the fluorescence spectrum characterised by their emission lines, which are listed in tab. 4.8.

In the OptImaTo laboratory a microfocus liquid metaljet X-ray source (Excillum D2+, 160 kV, Sweden) with a Galinstan alloy anode was used to produce the primary X-ray beam. A conical X-ray beam exits the source through a window with a 13-degree opening angle, and a copper collimator is used to further reduce the beam divergence.

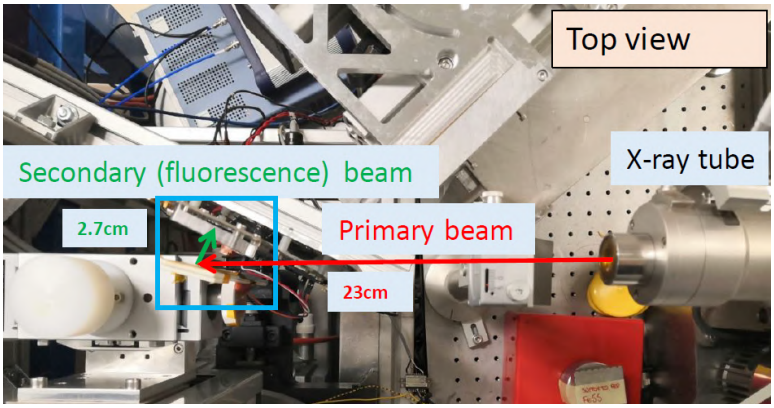

Figure 4.10: Setup used at the Instrumentation & Detectors Laboratory [145] for XRF measurements with the DPTS. The primary beam is hitting a titanium-iron target, whose fluorescence emission are used to evaluate the performance of the DPTS, which is placed few centimetres in front of the target.

The energy spectrum of the beam is a continuum Bremsstrahlung, adjustable in the range 30-160 kV (see fig. 4.11) and containing characteristic lines of gallium, indium and tin emissions (tab. 4.7).

A picture of the setup is shown in Fig. 4.12. Foils of tin, manganese, palladium and titanium were used as targets and placed in the beam with an angle of 45° relative to the beam direction. The characteristic emissions of all the targets and of the copper in the collimator are reported in Tab. 4.8. The DPTS was placed parallel to the target at approximately 10 cm, with the top side facing the incoming fluorescence emissions. This position was chosen to reduce the probability of hits on the detector from the primary beam Compton scattered photons and to better shield the detector from the conical beam.

4.2.2 Measurement and preliminary analysis procedure

Two fully functional DPTS were tested. One was used to measure the spectrum of different X-ray sources to study the linearity of the device response in an energy range from 1.73 keV to 28.5 keV. The same DPTS was tested to study the energy response of the device at different temperatures. Another DPTS was used to investigate the pixel-to-pixel variation of the energy response. The operating settings of the DPTS were chosen to have the desired operational point using the procedure described in

Table 4.7: Energies of the characteristic peaks [147] of the primary beam at the laboratory OptImaTo [146].

Peak	Energy (keV)
Ga Kα	9.25
Ga Kβ	10.26
In Kα	24.2
In Kβ	27.3
Sn Kα	25.2
Sn Kβ	28.5

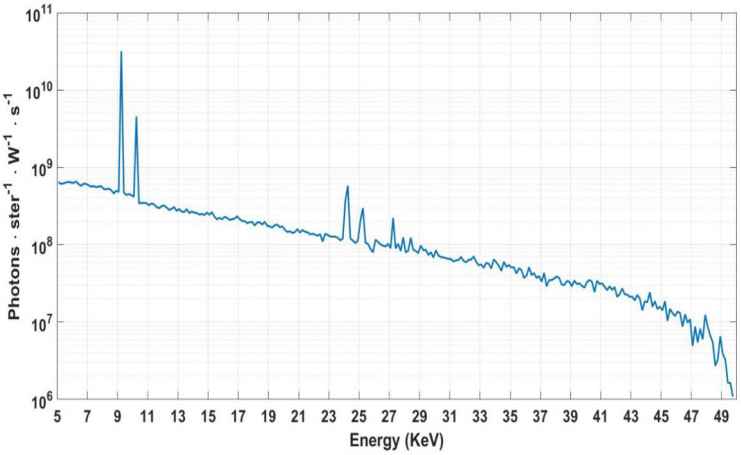

Figure 4.11: Spectrum produced by the microfocus liquid metaljet X-ray source at the laboratory OptImaTo [146]. The characteristic emission peaks of the Galinstan alloy anode are visible on top of the continuous Brehmsstrahlung background, from the left there are the gallium, indium and tin Kα and Kβ lines, whose energies are reported in tab. 4.7.

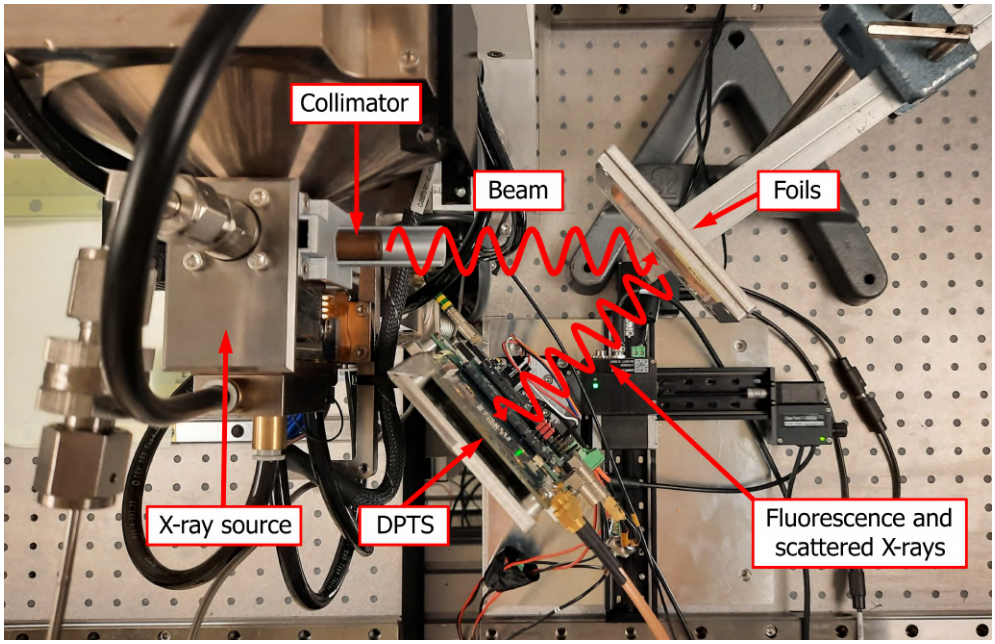

Figure 4.12: Setup used at the OptImaTo [146] laboratory to take XRF measurements with the DPTS. The primary beam, collimated with a copper cylinder, hits the target. The DPTS faces the target, at $\sim$ 10 cm from it, and detects the target fluorescence photons.

sec. 2.4.1. A sequence of preliminary measurements, that are detailed in sec. 2.4, was defined to validate the settings for each chip configuration:

- **Threshold scan:** verification of the applied pixel threshold distribution. In most of the cases the device is operated under standard conditions, with a threshold of around 100 e^-.

Table 4.8: Energies of the characteristic peaks [147] of the targets which were used in XRF measurements and of the copper contained in the collimator.

Peak	Energy (keV)
Pd Lα	2.84
Ar Kα	2.96
Sn Lα	3.44
Ti Kα	4.51
Ti Kβ	4.93
Mn Kα	5.90
Fe Kα	6.40
Mn Kβ	6.49

Peak	Energy (keV)
Fe Kβ	7.06
Cu Kα	8.05
Cu Kβ	8.90
Pd Kα	21.2
Pd Kβ	23.8
Sn Kα	25.3
Sn Kβ	28.5

- **Fake Hit Rate scan:** noise event rate measurement with random trigger. A fake hit rate lower than 10 $pixel^{-1}$ s^{-1} is required.
- **Decoding calibration:** mapping of the position encoding.
- **ToT calibration scan:** ToT response calibration at the pixel level.

Some preliminary analysis steps are then needed to select the events of interest for each spectrum. These steps include matching of rising and falling edge encoded position, selection of single pixel cluster events, rejection of noisy pixel events. After the events have been selected, a tuning of the matrix ToT response is done. They are described below. All analyses were performed using Python/ROOT scripts developed specifically for this purpose.

Matching of rising and falling edge encoded position When a single pixel is firing, the CML output signal consists of two trains of binary signals. The first train corresponds to the analogue signal rising edge and the second corresponds to the analogue signal falling edge. Both trains encode the hit position. When more than one pixel fires at once, the data includes two trains for each firing pixel. A sanity check on the data is done to select only events for which the position encoded in the rising edge train matches the one encoded in the falling edge train [88]. About 30% of the data are usually discarded. The encoding of the position is temperature dependent. Thus, the data-driven procedure to adjust the decoding calibration described in sec. 2.4.2 is used for the X-ray measurements with the DPTS, aiming at taking into account the variation of the time-encoding of the position.

Selection of single pixel cluster events When an event has only one pixel firing, all the energy of the incoming particle is assumed to be deposited in that pixel, hence there is a one-to-one relationship between the detector output and the released energy. This is one of the reasons to select only single pixel cluster events. The second reason is the DPTS intrinsic inaccuracy in detecting multiple pixel cluster events, due to the position decoding scheme (see sec. 2.3.1.2). Moreover, the electric field in the depleted region of the detector is designed specially to favour the single pixel charge collection. A simple clustering algorithm was executed on the pre-selected events. The resulting cluster size distribution (fig. 4.13) shows that 23.2% of the events have multiple pixel clusters.

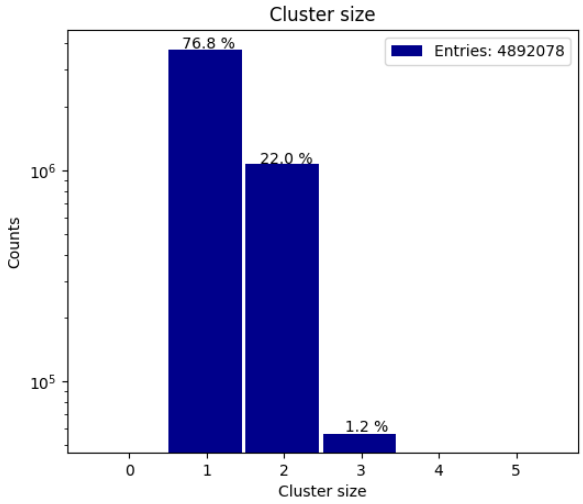

Figure 4.13: Cluster size distribution for the pre-selected events of one dataset.

Rejection of noisy pixel events For source measurements the data acquisition is triggered by the signal coming from the matrix, the noisy pixels contribution is not negligible if their rate is comparable with that of the source. A cut based on the single pixel hit multiplicity distribution for single pixel cluster events was implemented to discard all the data coming from noisy pixels. A Gaussian interpolation is performed on the main peak of the distribution (fig. 4.14a). All the pixels that have a multiplicity of hits above five standard deviations from the mean are not considered for further analysis. This algorithm allows discarding also signals from the matrix edge pixels (fig. 4.14b), as these pixels can collect signals also from just outside the matrix and so they have a multiplicity of events slightly higher than the innermost pixels. These signals are rejected since the response of the edge pixels is not consistent with the rest of the matrix.

Calibration of the ToT response The ToT response to a monochromatic energy release within the detector will change from pixel to pixel (fig. 4.15) due to process variations in the fabrication of the pixel circuitry. The single pixel ToT response must be calibrated to treat the whole matrix data in a consistent way. The parameters a, b, c and d obtained from the ToT calibration scan (sec. 2.4.3) are used for this purpose, so that it is possible to obtain the calibrated ToT ($ToT_{calibrated}$) expressed in mV from the relation:

$$ToT_{calibrated} = a \cdot V_H + b - \frac{c}{V_H - d} \tag{4.23}$$

where V_H is the operating parameter that defines the amplitude of the pulse. This conversion is applied pixel by pixel to all data to obtain the calibrated spectrum, reported in orange in fig. 4.16 for one of the datasets, in comparison with the non-calibrated spectrum in blue. The non-calibrated spectrum shows only one broad peak on the right and a smaller one on the left. In the calibrated spectrum instead, more peaks are resolved. The complete analysis of the calibrated spectrum shown in the figure is presented in the following section.

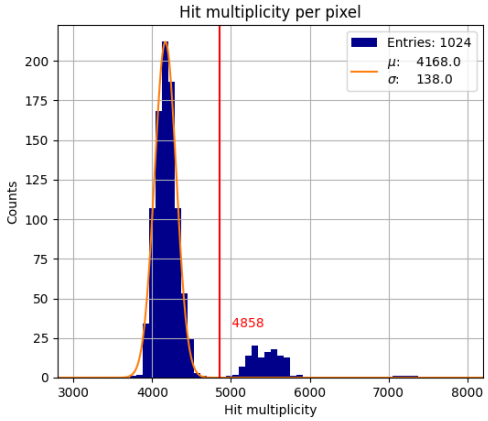

(a) Hit multiplicity distribution for single pixel cluster events. The red line represents the cut above which pixels are considered noisy. The group of entries right above the cut corresponds to the edge pixels.

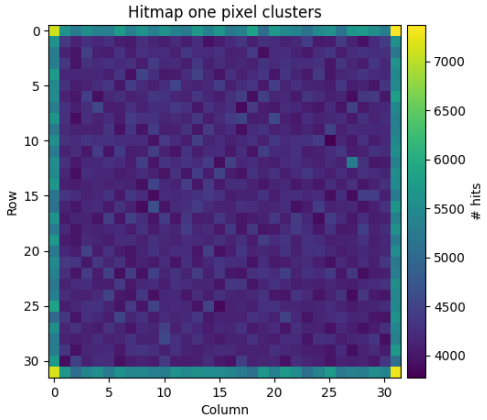

(b) Hitmap of single pixel cluster events.

Figure 4.14

4.2.3 Energy calibration

Six spectra were measured with the same DPTS sample to investigate the sensor performance when irradiated by monochromatic X-rays, for a total of 11 energy points measured between 1.73 keV and 28.5 keV. Two out of six spectra result from the radioactive sources of $^{55}_{26}$Fe and $^{241}_{95}$Am . Three other spectra correspond to the fluorescence photons from a manganese target, a combined titanium-palladium target, and a tin target, respectively. The last spectrum corresponds to the direct beam from the OptImaTo source. In most cases, the peaks in each spectrum are fitted using the sum of a Gaussian distribution and a parametrised background function. When the background cannot be adequately described by a simple continuous function, the peaks are fitted with a Gaussian fit alone. The Gaussian fit of the peak gives information on the mean position μ and the standard deviation σ of the signal distribution. The integral of the Gaussian distribution gives the abundance N_i of events identified with the corresponding process. These quantities are then used to compute the energy resolution ε as:

$$\varepsilon = \frac{2.35\sigma}{\mu} \tag{4.24}$$

and the yield y_i of each $i-$peak of the spectrum as:

$$y_i = \frac{N_i}{\sum_j N_j} \tag{4.25}$$

where N_j is the event multiplicity of all the other peaks in the spectrum.

The calibration of the sensor energy response is carried out separately for each spectrum, by comparing the mean peak position μ with the corresponding expected photon energy and assuming a linear relation between the two.

In the following the analysis for the most relevant measured spectrum are presented, the analysis of the remaining ones is discussed in app. A. Eventually, the overall results

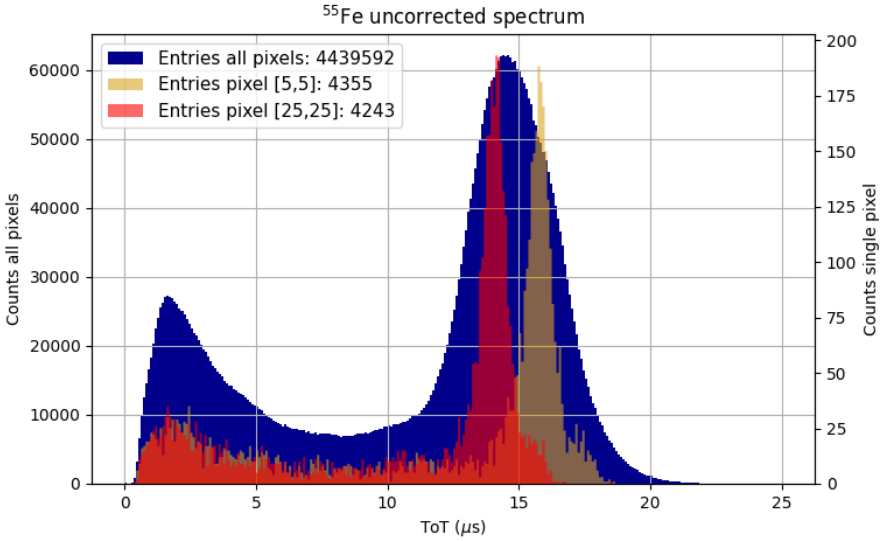

Figure 4.15: In blue the uncalibrated spectrum for the whole matrix. In orange and red the uncalibrated spectra for two different single pixels.

on the energy response are discussed in terms of the energy calibration and of the energy resolution as a function of the incident photon energy.

4.2.3.1 $^{55}_{26}$Fe source and manganese target spectra

The $^{55}_{26}$Fe source spectrum and the spectrum from fluorescence photons from the manganese target are expected to be characterised by the same peaks, as the main emissions of $^{55}_{26}$Fe correspond to the Kα and Kβ emissions of manganese. Therefore, the two spec-

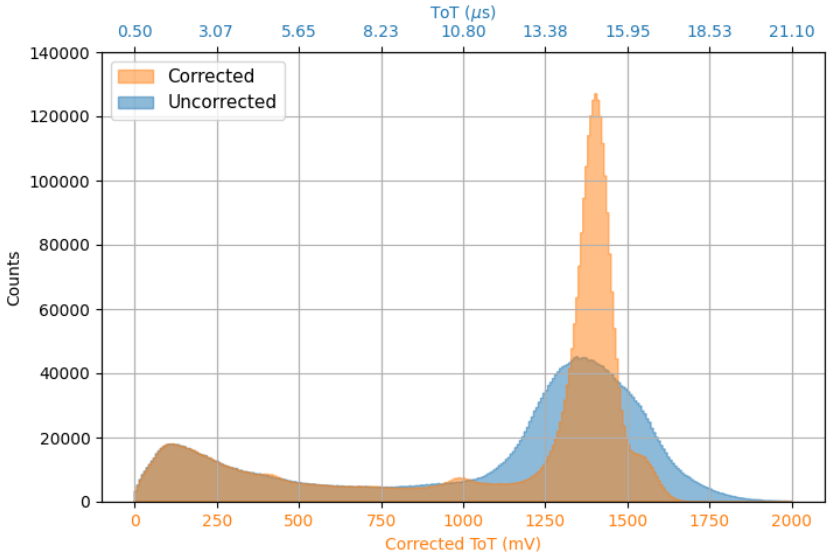

Figure 4.16: In light blue the uncalibrated spectrum for the whole matrix, in orange the ToT calibrated spectrum. Only single pixel cluster events were considered.

tra are compared to check the response consistency in the two different data taking conditions. Fig. 4.17 shows the calibrated spectrum from the $^{55}_{26}$Fe radioactive source, while 4.18 shows the calibrated spectrum from the manganese target fluorescence photons. A continuous background characterises the spectrum, which is possibly related to photons that were photo-absorbed outside the depleted region and thus the energy released inside the detector was only partially collected. The four peak structure, which was described in sec. 4.1.3.1, is visible in both calibrated spectra on top of the continuous background: the silicon fluorescence peak Si_{fl} is centerd around 450 mV, the silicon escape peak Si_{es} is placed around 1200 mV and the manganese $K\alpha$ and $K\beta$ monochromatic emissions are falling in the range $1500 - 1900$ mV.

The spectrum from the XRF measurements with the manganese target shows another additional peak in the range $750 - 1000$ e^-, which is compatible with the argon Kα emission (see tab. 4.8), in the hypothesis of fluorescence photons emitted by argon atoms naturally present in the air, excited by the primary beam.

The fits of the peaks are described in detail in the following paragraphs.

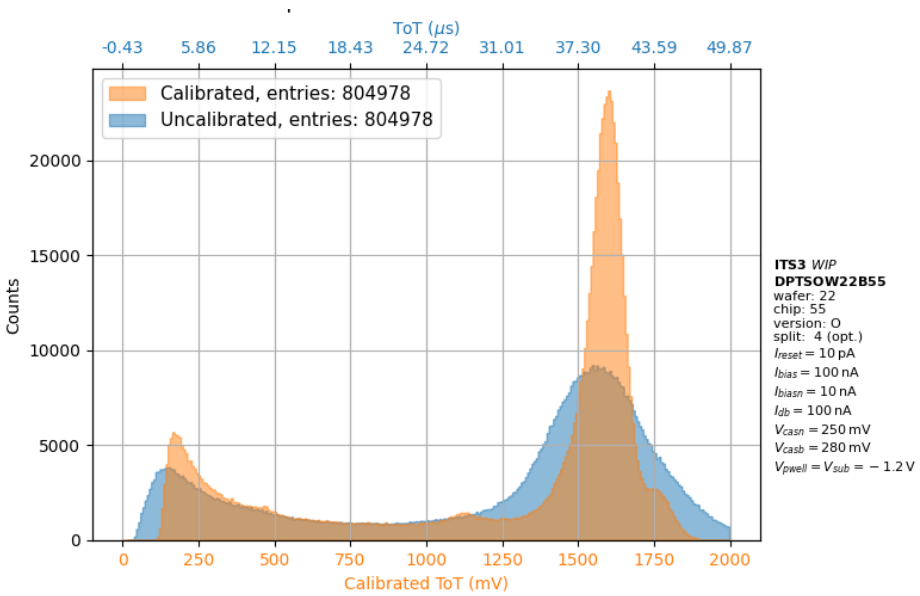

Figure 4.17: Measured spectrum of a $^{55}_{26}$Fe radioactive source. The manganese characteristic emission peaks (Mn-K$_\alpha$ and Mn-K$_\beta$), the corresponding escape peak (Mn-K$_{\alpha,\beta}$ − Si-K$_{\text{edge}}$) and the silicon fluorescence peak (Si-K$_{\alpha,\beta}$) are resolved.

Silicon fluorescence peak from $^{55}_{26}$Fe and Mn target spectra The silicon fluorescence emission has an energy of 1.74 keV. It is identified with the peak at around 400 mV in the spectrum shown in fig. 4.17 and fig. 4.18. The background underlying the peak is described by an exponential parametrised distribution:

$$bkg(x) = p_0 + p_1 \; e^{-\frac{x}{p_2}} \tag{4.26}$$

where p_0, p_1 and p_2 are the parameters to be estimated. This function is used to fit the spectrum in a range around the peak, excluding the peak itself (fig. 4.19 and 4.20 left). The signal is fitted with the sum of a Gaussian distribution and the previously

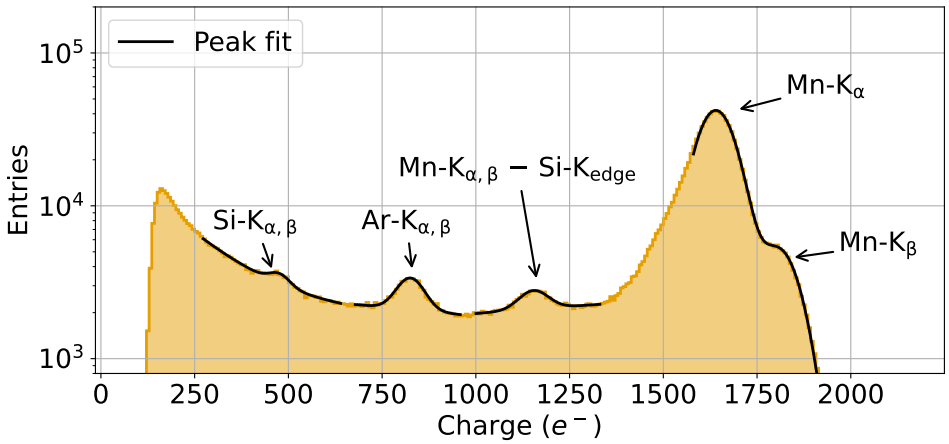

Figure 4.18: Measured spectrum of fluorescence X-rays emitted from a manganese target. The manganese characteristic emission peaks (Mn-K$_\alpha$ and Mn-K$_\beta$), the corresponding escape peak (Mn-K$_{\alpha,\beta}$ − Si-K$_{\text{edge}}$) and the silicon fluorescence peak (Si-K$_{\alpha,\beta}$) are resolved. Additionally, the spectrum shows the argon characteristic emission peak (Ar-K$_{\alpha,\beta}$).

evaluated exponential background (fig. 4.19 and fig. 4.20 right):

$$f(x) = bkg(x) + A\ e^{-\frac{(x-\mu)^2}{2\sigma^2}} \tag{4.27}$$

The variables of interest and the derived quantities for the silicon fluorescence peak are reported in tab. 4.9 and tab. 4.10 for the iron source and the manganese target spectrum, respectively.

Argon fluorescence peak from Mn target spectrum The argon characteristic emission has an energy of 3.0 keV and is associated with the peak between 750 mV and 1000 mV, which is visible in fluorescence X-ray spectrum from the manganese target and not in the $^{55}_{26}$Fe spectrum. The background underlying the peak is described by a linear function:

$$bkg(x) = p_0 + p_1 x \tag{4.28}$$

where p_0 and p_1 are the parameters to be estimated. This function is used to fit the spectrum in a range around the peak, excluding the signal itself (fig. 4.21 left). Then the peak is fitted with a Gaussian distribution summed with the linear background which was previously evaluated (fig. 4.21 right):

$$f(x) = bkg(x) + A\ e^{-\frac{(x-\mu)^2}{2\sigma^2}} \tag{4.29}$$

The variables of interest and the derived quantities for the argon fluorescence peak are reported in tab. 4.10.

Silicon escape peak from $^{55}_{26}$Fe and Mn target spectra The silicon escape peak from the manganese Kα and $K\beta$ emissions has an expected energy of 4.16 keV. It is

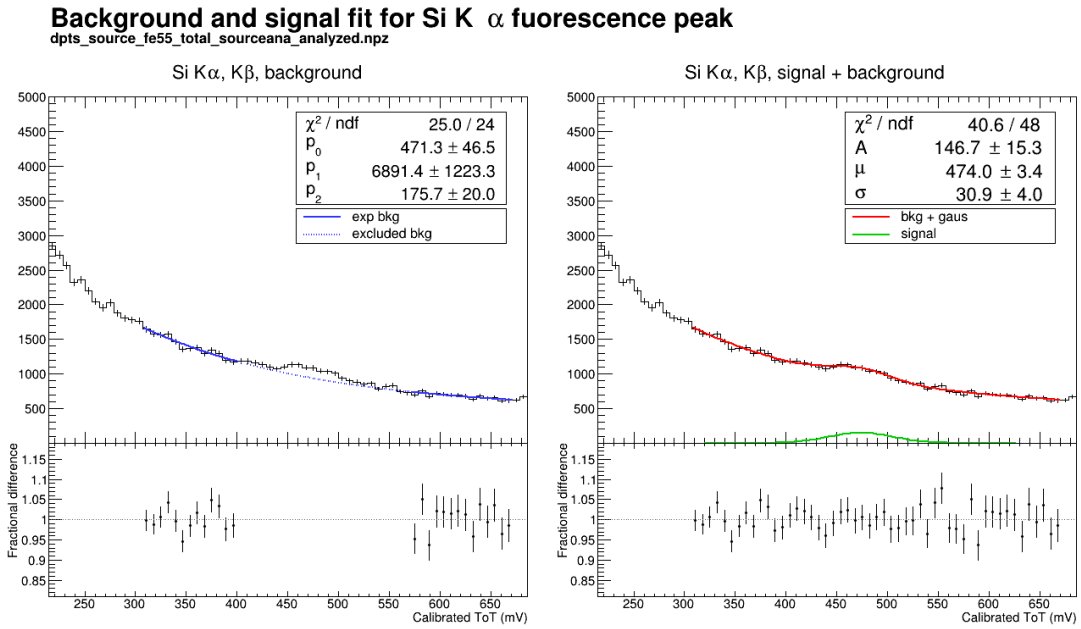

Figure 4.19: Fit of exponential background (left) and sum of background and signal (right) for the silicon fluorescence peak in the spectrum of a $^{55}_{26}$Fe radioactive source. The data under the dashed line was excluded in the fit of the background.

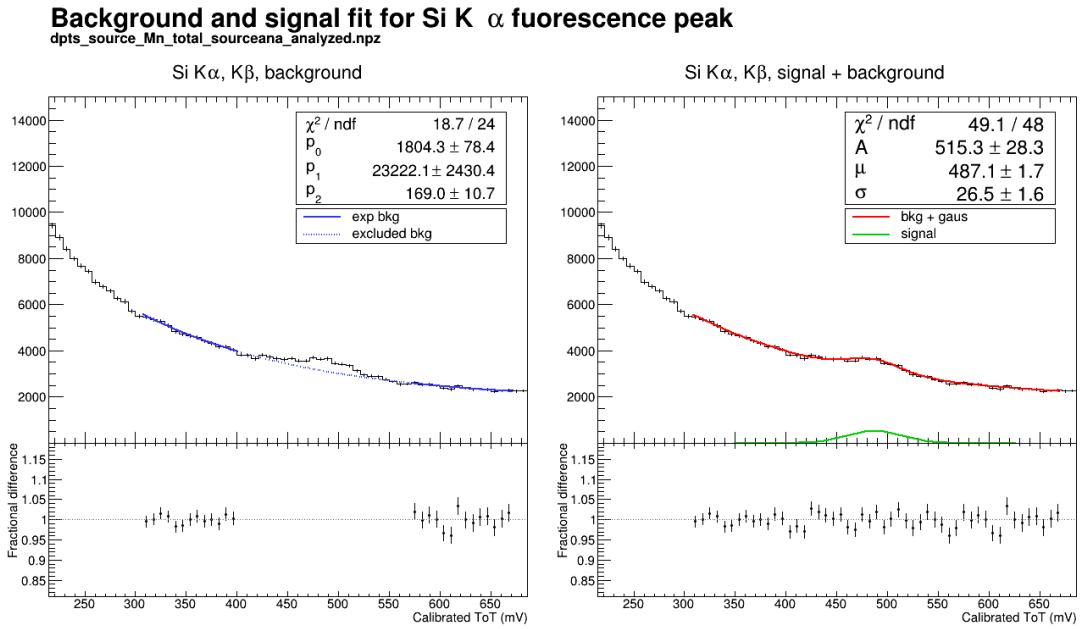

Figure 4.20: Fit of exponential background (left) and sum of background and signal (right) for the silicon fluorescence peak in the spectrum of fluorescence X-rays emitted from a manganese target. The data under the dashed line was excluded in the fit of the background.

associated to the peak between 1000 mV and 1250 mV in the spectra in fig. 4.17 and

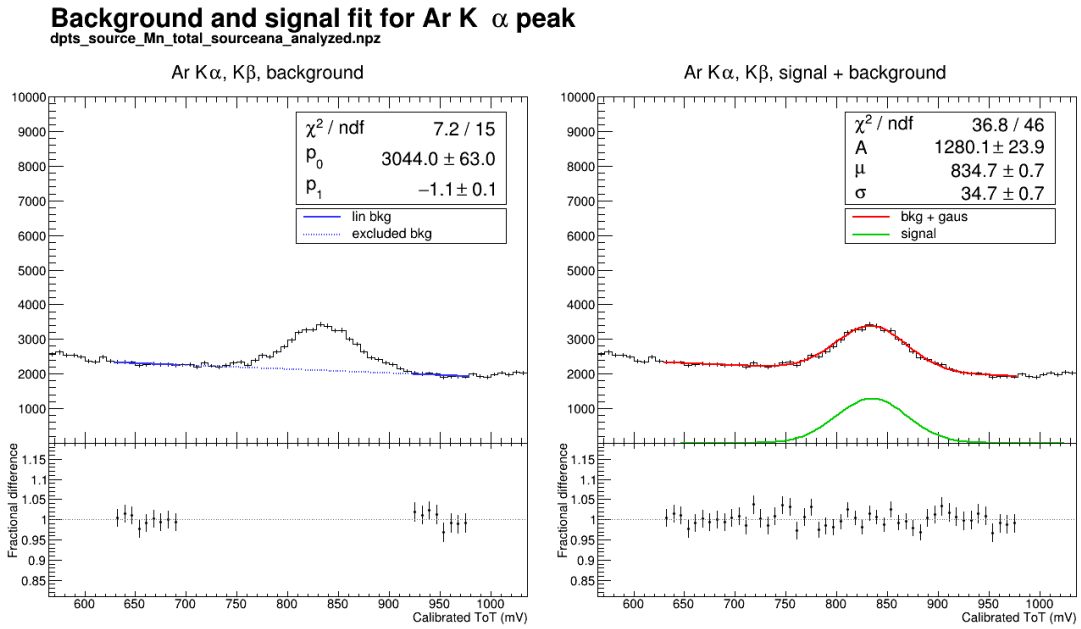

Figure 4.21: Fit of linear background (left) and sum of background and signal (right) for the argon fluorescence peak in the spectrum of fluorescence X-rays emitted from a manganese target. The data under the dashed line was excluded in the fit of the background.

4.18. The background is described well by the linear function:

$$bkg(x) = p_0 + p_1 x \tag{4.30}$$

where p_0 and p_1 are the parameters to be estimated. This function is used to fit the data in the side bands of the signal, excluding the peak itself (fig. 4.22 and 4.23 left). The signal is fitted with the sum of a Gaussian distribution and the linear background which was previously evaluated (fig. 4.22 and fig. 4.23 right):

$$f(x) = bkg(x) + A\ e^{-\frac{(x-\mu)^2}{2\sigma^2}} \tag{4.31}$$

The variables of interest and the derived quantities for the silicon escape peak are reported in tab. 4.9 and tab. 4.10 for the iron source and the manganese target spectrum, respectively.

Manganese Kα, Kβ from $^{55}_{26}$Fe and Mn target spectra The manganese characteristic X-rays Kα and Kβ have an energy of 5.90 keV and 6.49 keV, respectively. They are associated with the two overlapping peaks between 1500 mV and 1900 mV in the spectra in fig. 4.17 and 4.18. They are fitted with a sum of two overlapping Gaussian distributions (fig. 4.24 and 4.25):

$$f(x) = A_1\ e^{-\frac{(x-\mu_1)^2}{2\sigma_1^2}} + A_2\ e^{-\frac{(x-\mu_2)^2}{2\sigma_2^2}} \tag{4.32}$$

No background was considered for the fit of these peaks, given the lack of a region of the spectrum at the sides of the peaks with only the background contribution. This

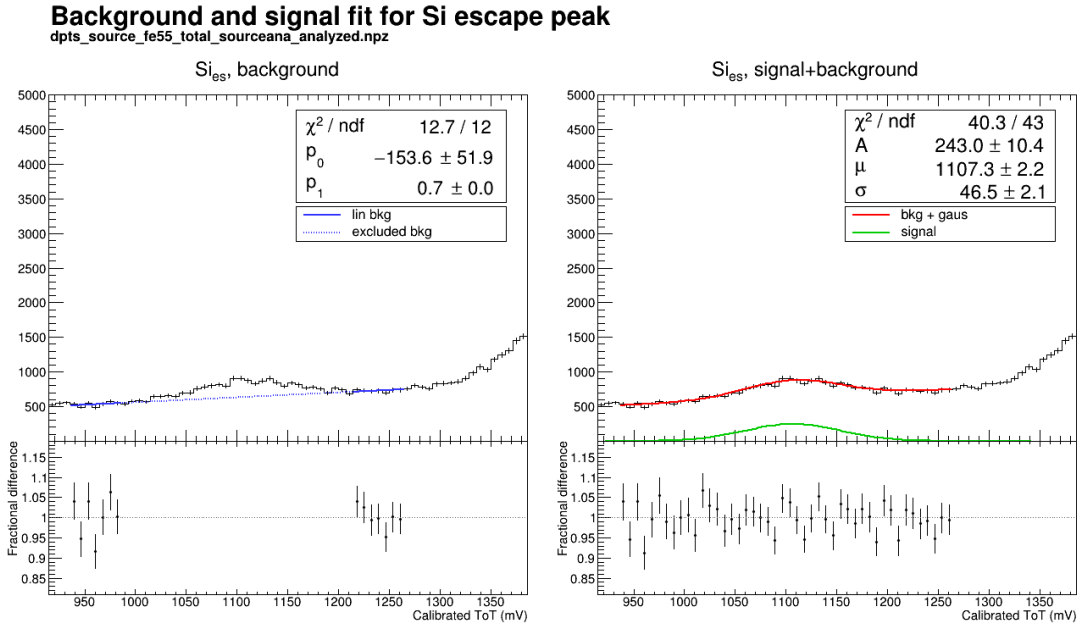

Figure 4.22: Fit of linear background (left) and sum of background and signal (right) for the silicon escape peak from the manganese Kα and $K\beta$ emissions in the spectrum of a $^{55}_{26}$Fe radioactive source. The data under the dashed line was excluded in the fit of the background.

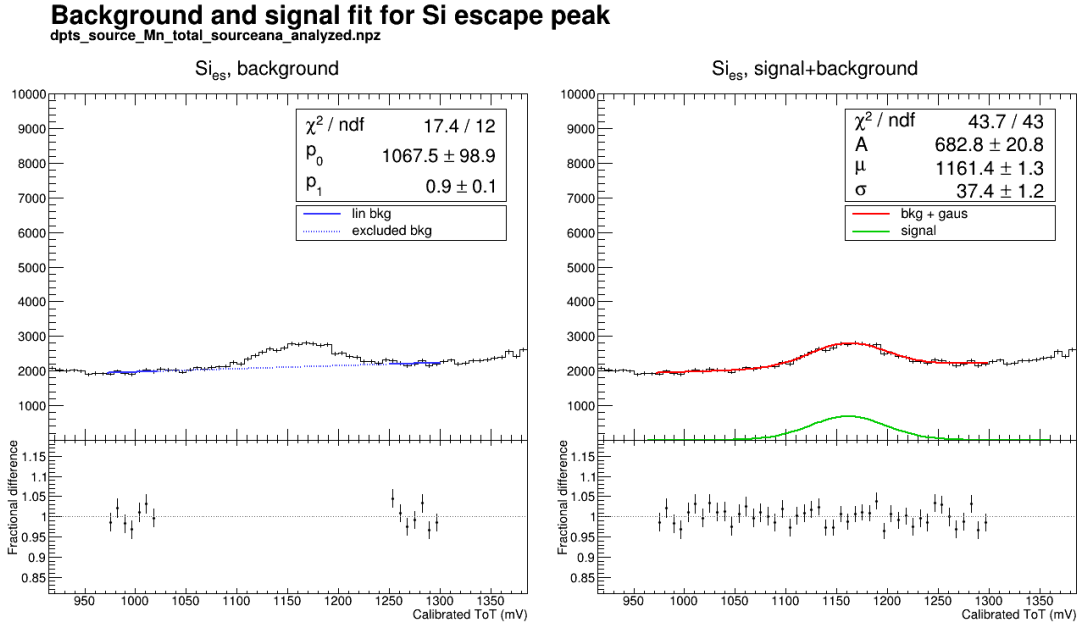

Figure 4.23: Fit of linear background (left) and sum of background and signal (right) for the silicon escape peak from the manganese Kα and $K\beta$ emissions in the spectrum of fluorescence X-rays emitted from a manganese target. The data under the dashed line was excluded in the fit of the background.

brings to a fit of the peaks that describes well the peaks region, but is deviating from the data on the low energy tail of the Mn-$K\alpha$ peak.

The variables of interest and the derived quantities for the manganese characteristic emissions Kα and Kβ are reported in tab. 4.9 and tab. 4.10 for the iron source and the manganese target spectra, respectively.

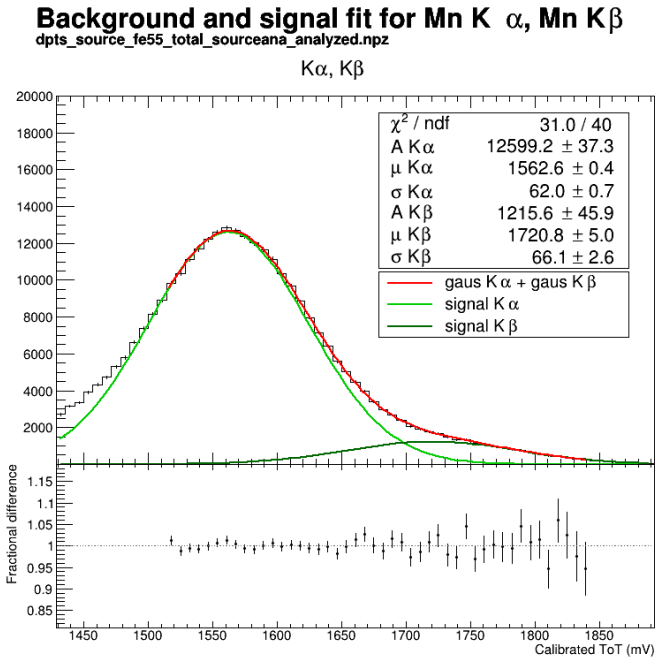

Figure 4.24: Fit with the sum of two Gaussian signals of the manganese Kα and $K\beta$ characteristic X-rays in the spectrum of a $^{55}_{26}$Fe radioactive source.

Table 4.9: Summary of the key parameters of the peaks in the X-ray spectrum of a $^{55}_{26}$Fe radioactive source.

Peak	Photon energy (keV)	μ (mV)	σ (mV)	Yield (%)	Energy resolution (%)
Si_{fl}	1.74	474.0 ± 3.4	30.9 ± 4.0	0.52 ± 0.01	15.33 ± 1.97
Si_{es}	4.16	1107.3 ± 2.2	46.5 ± 2.1	1.29 ± 0.02	9.86 ± 0.44
$K\alpha$	5.90	1562.6 ± 0.4	62.0 ± 0.7	89.04 ± 0.23	9.33 ± 0.10
$K\beta$	6.51	1720.8 ± 5.0	66.1 ± 2.6	9.16 ± 0.06	9.03 ± 0.35

Energy calibration with the $^{55}_{26}$Fe and Mn target spectra The comparison between the mean peak position μ and the corresponding photon energy (see tab. 4.9 and 4.10) is shown in fig. 4.26a and 4.26b for the $^{55}_{26}$Fe spectrum and Mn target spectrum, respectively. The parameters for the linear calibration differ between the two spectra, however, remain compatible within the error. A difference is observed in the energy resolution as well, which is systematically worse for the spectrum obtained with the ^{55}Fe source than for the spectrum from fluorescence X-rays emitted by a manganese target. The worsening of the energy resolution might be caused by a variation of the

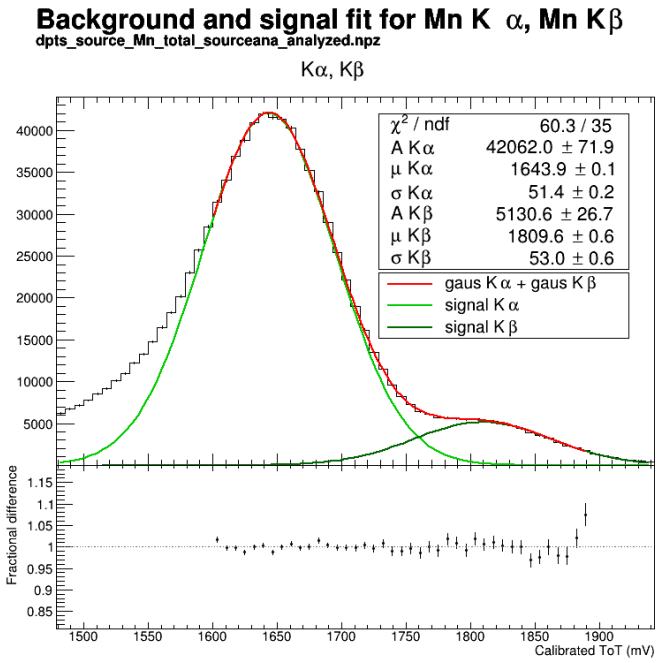

Figure 4.25: Fit with the sum of two Gaussian signals of the manganese Kα and $K\beta$ characteristic X-rays in the spectrum of fluorescence X-rays emitted from a manganese target.

Table 4.10: Summary of the key parameters of the peaks in the spectrum of fluorescence X-ray emitted by a manganese target.

Peak	Photon energy (keV)	μ (mV)	σ (mV)	Yield (%)	Energy resolution (%)
Si_{fl}	1.74	487.1 ± 1.7	26.5 ± 1.6	0.54 ± 0.01	12.77 ± 0.78
$K\alpha$	2.96	834.7 ± 0.7	34.7 ± 0.7	1.77 ± 0.01	9.78 ± 0.19
Si_{es}	4.16	1161.4 ± 1.3	37.4 ± 1.2	1.01 ± 0.01	7.57 ± 0.25
$K\alpha$	5.90	1643.9 ± 0.1	51.4 ± 0.2	85.88 ± 0.13	7.35 ± 0.03
$K\beta$	6.51	1809.6 ± 0.6	53.0 ± 0.6	10.80 ± 0.04	6.88 ± 0.08

temperature during the acquisition, which was longer for the ^{55}Fe source, and might have caused a shift of the mean detected value, thus broadening the peaks.

4.2.3.2 Tin target spectrum

The spectrum of fluorescence X-rays emitted from a tin target is shown in fig. 4.27. The expected characteristic emission peaks of tin are visible in the spectrum: the Sn-K$_\alpha$ and Sn-K$_\beta$ are centred around 7000 e$^-$ and 7900 e$^-$ respectively, while the Sn-L$_\alpha$ is partially overlapping with the Ar-K$_{\alpha,\beta}$ peak in the range from 700 e$^-$ to 1300 e$^-$. The silicon fluorescence peak Si-K$_{\alpha,\beta}$ is resolved at ∼400 e$^-$. The peaks in the spectrum between 1500 mV and 3200 mV, that are attributed to Compton and Rayleigh scattered X-rays from the primary beam, are excluded in the following analysis, as their exact energy cannot be determined precisely. The peak at ∼6200 mV is analysed together with the

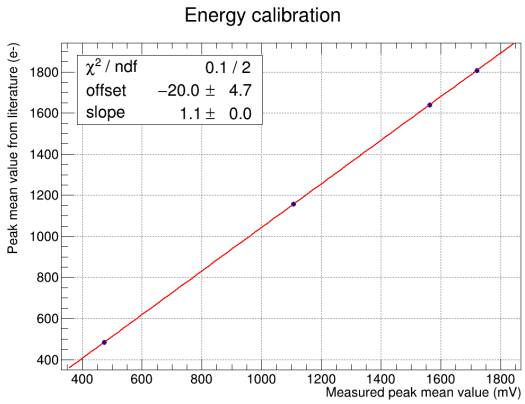

(a) Energy calibration plot for the $^{55}_{26}$Fe spectrum.

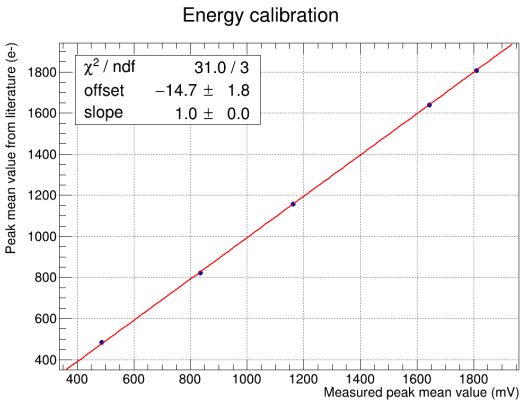

(b) Energy calibration plot for the manganese target spectrum.

Figure 4.26

Sn-K$_\alpha$ and Sn-K$_\beta$ peaks and a possible interpretation as due to Compton scattered In-Kα photons from the primary beam is outlined.

A continuous background characterises the spectrum, as observed in all the previous spectra. This feature is possibly related to partial charge collection of photons that converted outside the depleted region of the sensor.

The fits of the peaks are described in detail in the following.

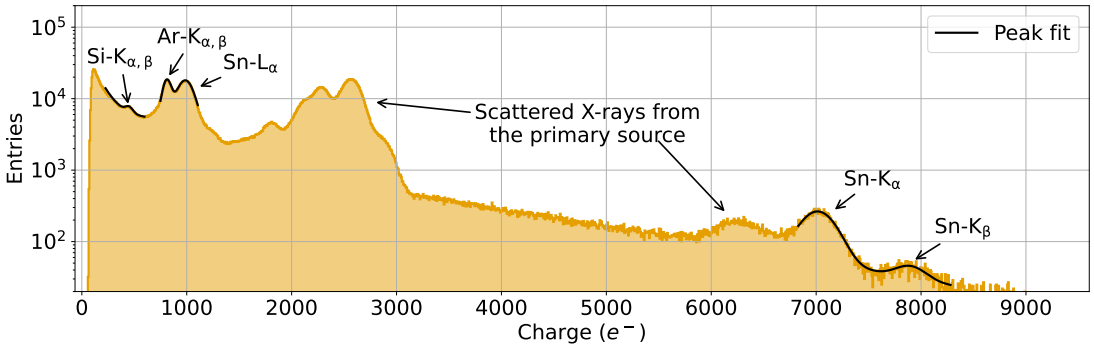

Figure 4.27: Measured spectrum of fluorescence X-rays emitted from a tin target. The tin characteristic emission peaks (Sn-K$_\alpha$, Sn-K$_\beta$ and Sn-L$_\alpha$), the silicon fluorescence peak (Si-K$_{\alpha,\beta}$) and the argon characteristic emission peak (Ar-K$_{\alpha,\beta}$) are resolved. Additional peaks in the spectrum are attributed to Compton and Rayleigh scattered X-rays from the primary beam.

Silicon fluorescence peak from Sn target spectrum The silicon fluorescence emission has an energy of 1.74 keV. In the tin fluorescence spectrum, it is associated to the peak around 400 e$^-$. The fit of the signal and of the background is done as previously discussed in sec. 4.2.3.1. An exponential function is used to describe the background (fig. 4.28 left), to which a Gaussian distribution is added for the signal description (fig. 4.28 right).

The variables of interest and the derived quantities for the silicon fluorescence peak are reported in tab. 4.11.

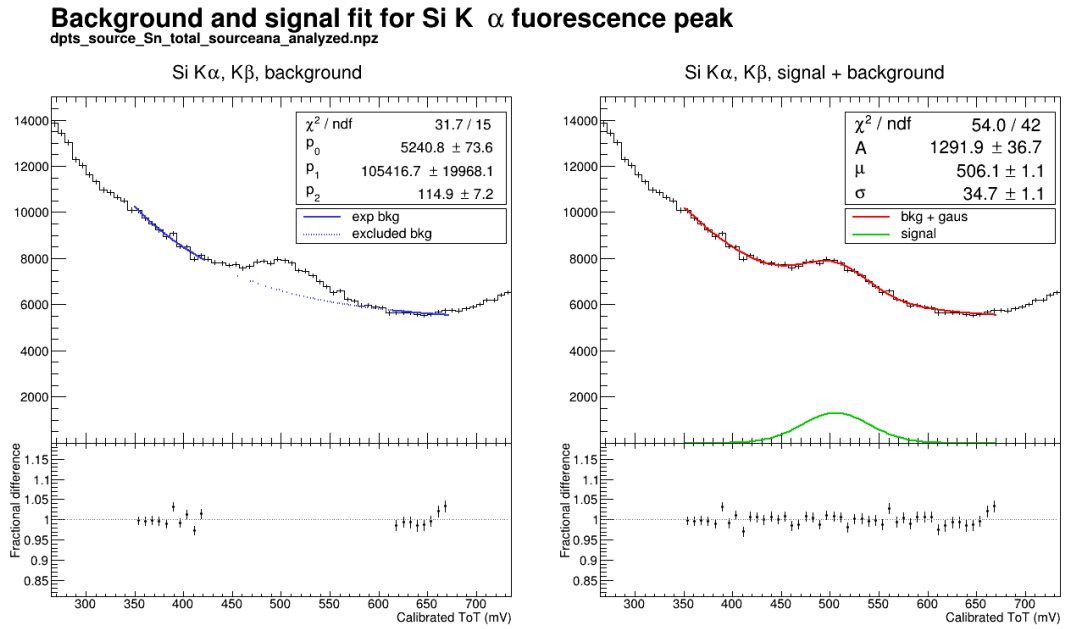

Figure 4.28: Fit of exponential background (left) and sum of background and signal (right) for the silicon fluorescence peak in the spectrum of fluorescence X-rays emitted from a tin target. The data under the dashed line was excluded in the fit of the background.

Argon fluorescence and Sn-Lα peaks from Sn target spectrum The argon fluorescence emission has an energy of 3.0 keV, while the Sn-Lα emission has an energy of 3.4 keV. These two emissions are associated to the two peaks in the energy range between 700 e^- and 1300 e^-. The background that is underlying the peaks is parametrised by a linear relation:

$$bkg(x) = p_0 + p_1 x \tag{4.33}$$

that was used to fit the histogram in the sidebands of the two peaks (fig. 4.29 left). The signals are fitted with a sum of two Gaussian distributions on top of the background which was previously evaluated (fig. 4.29 right):

$$f(x) = bkg(x) + A_1\ e^{-\frac{(x-\mu_1)^2}{2\sigma_1^2}} + A_2\ e^{-\frac{(x-\mu_2)^2}{2\sigma_2^2}} \tag{4.34}$$

The variables of interest and the derived quantities for the argon Kα peak and the tin Lα peak are reported in tab. 4.11.

Sn-Kα and Sn-Kβ peaks from Sn target spectrum The Kα and Kβ emissions of tin have an energy of 25.3 keV and 28.5 keV respectively. They are associated to the peaks in the tin calibrated spectrum above 6700 e^-. Another peak is resolved just below the Sn-Kα, possibly associated to the indium Kα photons of the primary source,

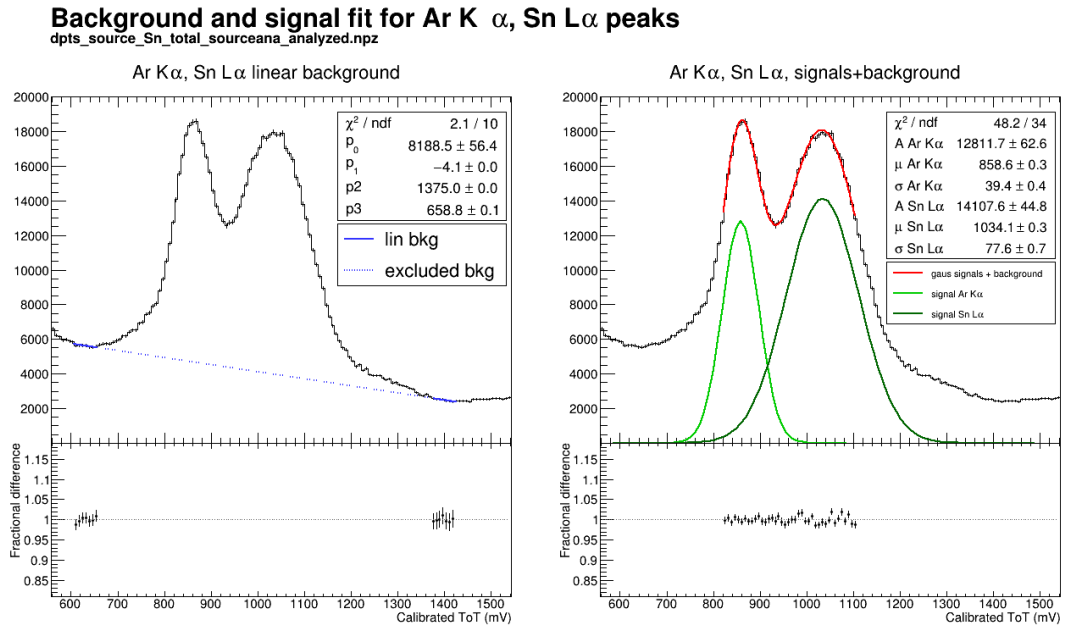

Figure 4.29: Fit of linear background (left) and sum of background and signals (right) for the argon fluorescence peak and the Sn-Lα peak in the spectrum of fluorescence X-rays emitted from a tin target. The data under the dashed line was excluded in the fit of the background.

which are Compton scattered on the tin target. The background underlying the three peaks is described by an exponential function:

$$bkg(x) = p_0 + p_1 \; e^{-\frac{x}{p_2}} \tag{4.35}$$

that is used to fit the spectrum in a region around the peaks (fig. 4.30 left), excluding the signals. Then the sum of three Gaussian distribution and the exponential background, that was previously evaluated, is used to fit the signals (fig. 4.30 right):

$$f(x) = bkg(x) + A_1 \; e^{-\frac{(x-\mu_1)^2}{2\sigma_1^2}} + A_2 \; e^{-\frac{(x-\mu_2)^2}{2\sigma_2^2}} + A_3 \; e^{-\frac{(x-\mu_3)^2}{2\sigma_3^2}} \tag{4.36}$$

The variables of interest and the derived quantities for the tin Kα and Kβ peaks are reported in tab. 4.11.

Energy calibration with the Sn target spectrum The comparison between the mean peak position μ and the corresponding photon energy (see tab. 4.11) is shown in fig. 4.31 for the tin target spectrum.

Compton scattered photons from the primary beam The peak associated to In-Kα photons (leftmost peak in fig. 4.30) of the primary beam which are Compton scattered, has a mean value of 6251.2±5.6 mV. It can be converted in 22.3 keV by using the energy calibration described in previous paragraph. The In-Kα emission has an energy of 24.2 keV. Given a mean angle φ of 133° between the direction of

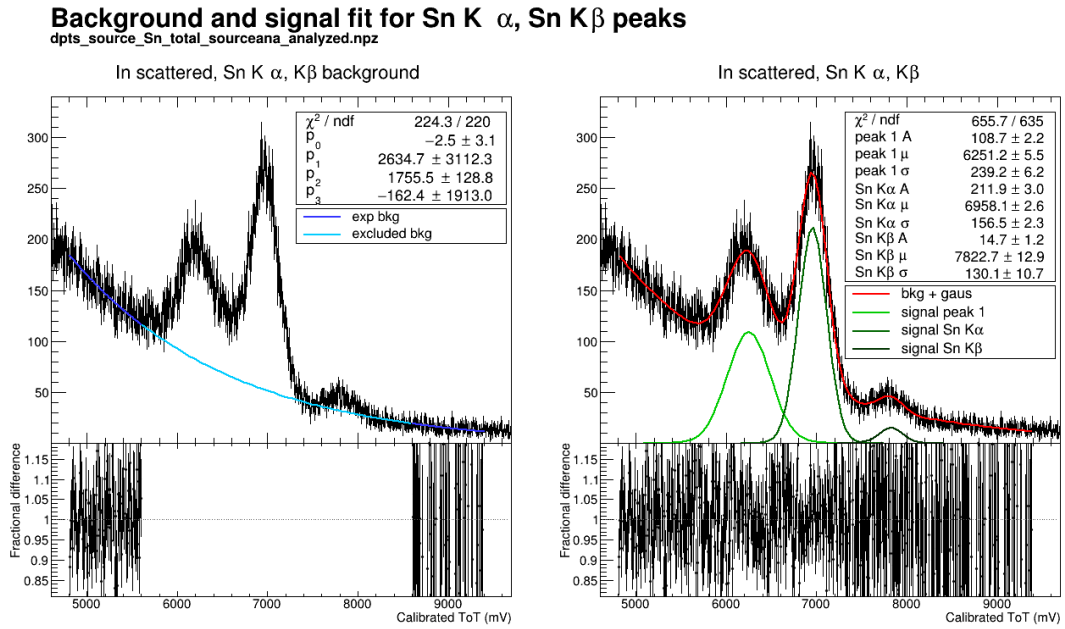

Figure 4.30: Fit of exponential background (left) and sum of background and signals (right) for the Sn-Kα and Sn-Kβ peaks in the spectrum of fluorescence X-rays emitted from a tin target. The data under the dashed line was excluded in the fit of the background. The leftmost fitted peak is possibly associated with Compton scattered photons from the primary source.

Table 4.11: Summary of the key parameters of the peaks in the spectrum of fluorescence X-ray emitted by a tin target.

Peak	Photon energy (keV)	μ (mV)	σ (mV)	Yield (%)	Energy resolution (%)
Si Ka	1.74	506.1 ± 1.1	34.7 ± 1.1	2.67 ± 0.02	16.09 ± 0.51
Ar Ka	2.96	858.6 ± 0.3	39.4 ± 0.4	30.06 ± 0.08	10.79 ± 0.11
Sn La	3.44	1034.1 ± 0.3	77.6 ± 0.7	65.19 ± 0.14	17.64 ± 0.15
Sn Ka	25.30	6958.1 ± 2.6	156.5 ± 2.3	1.97 ± 0.02	5.29 ± 0.08
Sn Kb	28.50	7822.7 ± 12.9	130.1 ± 10.7	0.11 ± 0.00	3.91 ± 0.32

the primary beam and the scattered beam (see fig. 4.12), the expected energy of the Compton scattered photon $E_{\gamma'}$ can be obtained by rearranging eq. 4.15:

$$E_{\gamma'} = \frac{E_\gamma}{1 + \frac{E_\gamma}{m_e c^2}\left(1 - cos(\varphi)\right)} \tag{4.37}$$

where E_γ is the energy of the In-Kα. Thus, the expected energy of the scattered peak is $E_{\gamma'} = 22.6$ keV, that is compatible with the measured value of the peak.

4.2.3.3 Energy response results

The results of the analyses presented in the previous sections for each spectrum (tabs. 4.9, 4.10, A.1, A.2, 4.11 and A.3) have been collected to draw some general conclusions.

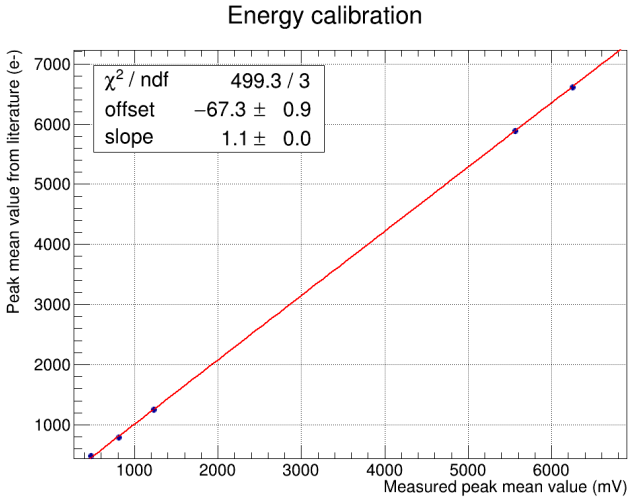

Figure 4.31: Energy calibration plot for the tin target spectrum.

The energy resolution as a function of the incident photon energy for all the measured peaks is shown in fig. 4.32. Different colours and shapes identify the spectrum from which the points are obtained. The resolution gets better as the incident photon energy increases, becoming less than 10% for photon energies larger than 5 keV, thus indicating that the energy resolution performance of the detector is enhanced at higher energies.

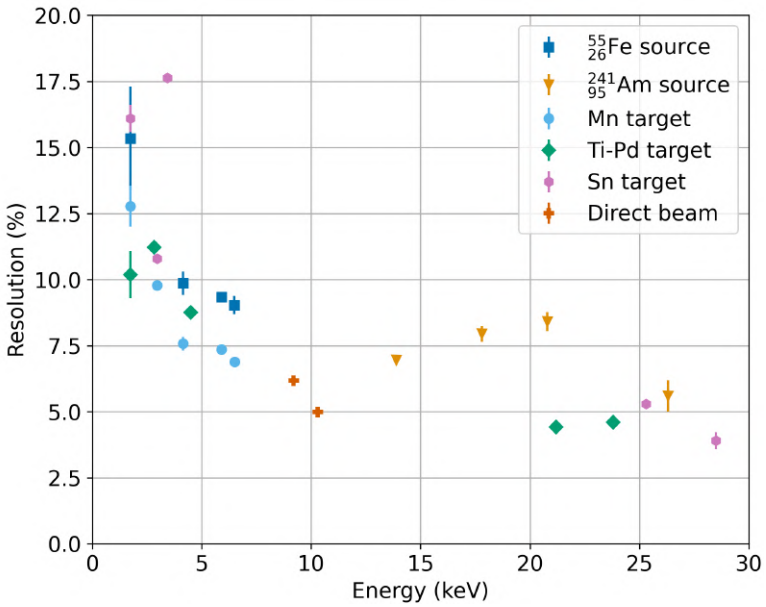

Figure 4.32: Energy resolution as a function of the incident photon energy for all the collected points. Different colours and shapes indicate the spectrum from which the data are retrieved.

The mean position of all the measured peaks as a function of the incident photon energy is shown in fig. 4.33. Different colours and shapes identify the spectrum from which the points are obtained. The black line represents the response calibration as

obtained from the $^{55}_{26}$Fe source spectrum. This calibration was chosen as a reference due to the widespread use of $^{55}_{26}$Fe as the standard calibration spectrum, with well known characteristics.

The points from each spectrum alone exhibit linearity. However, when the complete set of 23 points is considered, multiple distinct calibration behaviours emerge. With respect to the reference calibration from the $^{55}_{26}$Fe source a systematic increase of the mean measured value of the peak is observed. This feature is possibly due to temperature-related effects, that are investigated in the following section. In fact, the absence of an active temperature control system for the sensor during the data acquisition might have resulted in temperature variations over the course of the measurements, that for most of the spectra were more than 10 hours long.

Considering the set of points from the tin target spectrum, that is the one with the highest energies, a linearity of the energy response up to 28.5 keV is demonstrated.

The overall behaviour demonstrates an excellent detector response to X-rays from 1.73 keV (silicon fluorescence emission) to 28.5 keV (tin Kβ emission).

This work was extended by conducting a similar XRF measurement campaign on the babyMOSS prototype, with photons with energies up to 43.0 keV, which showed a gradual loss of linearity for energies above 21.2 keV [87].

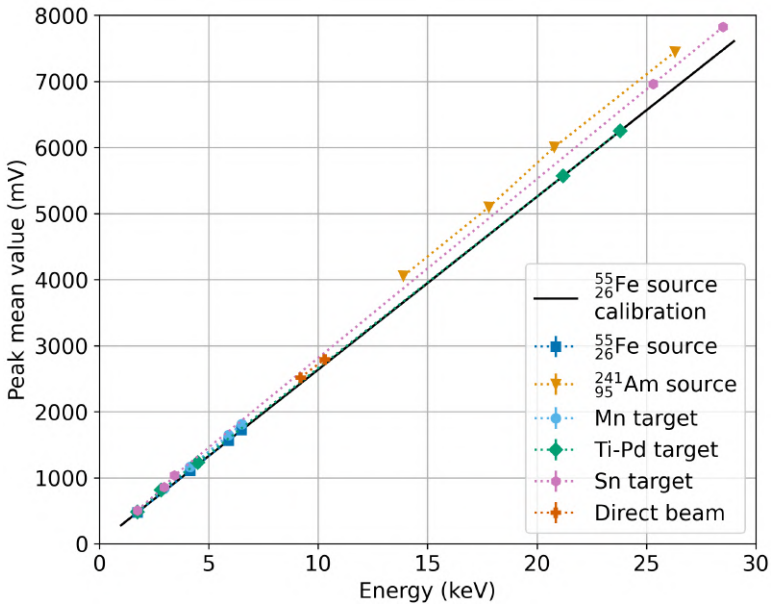

Figure 4.33: Measured peak mean position as a function of the incident photon energy for all the collected points. Different colours and shapes indicate the spectrum from which the data are retrieved.

4.2.4 Temperature dependence of the energy measurements

The measurements done at the Instrumentation & Detectors Laboratory and at the OptImaTo facilities were performed without active temperature control of the DPTS under test. Thus, the possible impact on the results of temperature variation during the acquisition have been subsequently studied by adding to the setup a cooling jig (see sec.2.3.1.4), which allows to keep constant over time the temperature of the detector. The DPTS performance when illuminated with a $^{55}_{26}$Fe radioactive source has been

studied at 20 °C, 25 °C and 30 °C. The operating parameters have ben kept the same for the three measurements.

For each temperature a measurement of the threshold and of the electronic noise was done. The mean matrix threshold and noise as a function of the temperature are shown in fig. 4.34a and 4.34b, respectively. The threshold decreases as the temperature increases, as expected from the increase of the thermal noise with the temperature. However, the measured noise increases between 20 °C and 30 °C, but has a minimum at 25 °C. This unexpected trend of the noise might be due to additional sources of noise (see chapter 3) not temperature dependent.

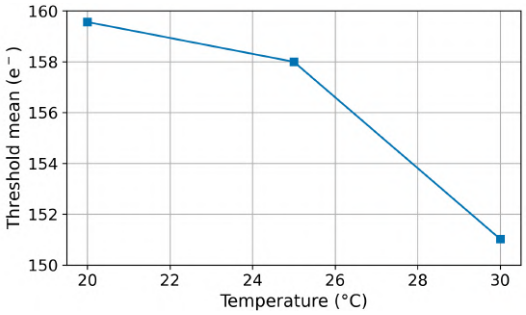

(a) Mean measured threshold of the matrix as a function of the temperature.

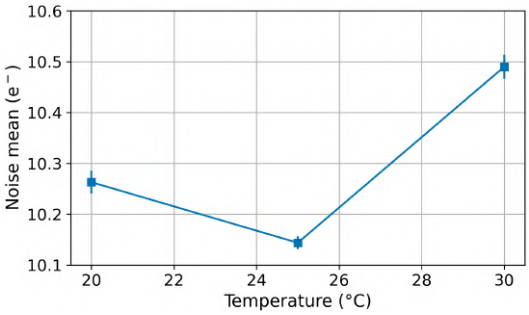

(b) Mean measured electronic noise of the matrix as a function of the temperature.

Figure 4.34

The ToT pixel-to-pixel calibration has been done for each temperature. The relation between the matrix mean value of the measured ToT and the injected pulse V_H is shown in fig. 4.35. The experimental range of V_H is from 0 to 1000 mV, values of ToT for V_H higher than 1000 mV were obtained by extending the relation found for V_H below 1000 mV. The slope of the curve is increasing for lower temperatures, therefore, with the same injected signal, the ToT will be higher for lower temperatures.

The spectra of $^{55}_{26}$Fe , which were measured with the DPTS at 20 °C, 25 °C and 30 °C, were pre-analysed with the procedure described in sec. 4.2.2 and are shown in fig. 4.36. All the three spectra resolve the four peaks which are expected (see sec. 4.1.3.1). The temperature does not impact significantly on the spectrum, except for a shift of the Mn-K_α and Mn-K_β, whose mean value is decreasing with temperature increasing.

Each spectrum was analysed using the same procedure described in sec. 4.2.3.1. The mean position of the peaks that was obtained from the fit is shown in fig. 4.37 for each peak. A systematic decrease of the mean peak position as the temperature increases is observed. On the other hand, the calibration line shows only a difference of few percent at high energies for different temperatures, as shown in fig. 4.38. At the same temperature, the associated measured value is lower for higher temperatures.

Eventually, fig. 4.39 shows the resolution of the four peaks as a function of the temperature. The values remain compatible within the errors.

4.2.5 Single pixel energy calibration

A high statistics spectrum was measured using the fluorescence photons from an iron-titanium target to do a single pixel calibration of the energy response directly from the raw ToT spectrum. The measured calibrated spectrum from the matrix is shown in fig. 4.40. The iron characteristic emission peaks are resolved (Fe-K_α, Fe-K_β) between

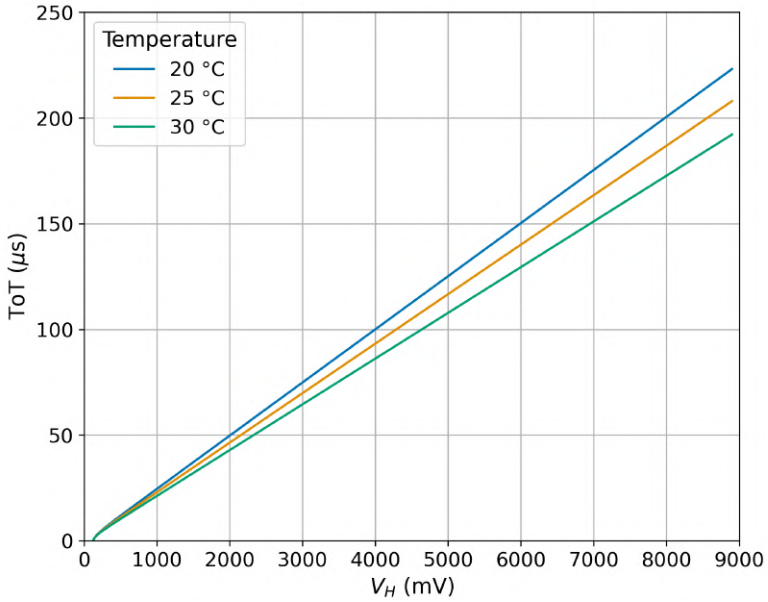

Figure 4.35: Measured mean matrix ToT as a function of the injected pulse V_H for the ToT pixel-to-pixel calibration.

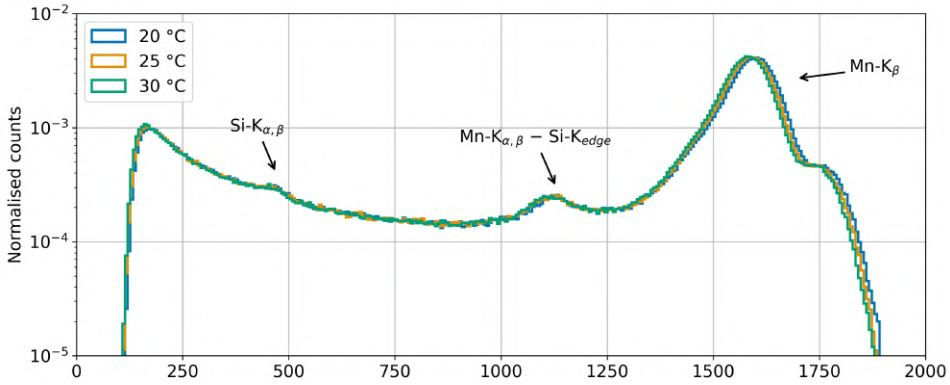

Figure 4.36: Measured spectrum from a $^{55}_{26}$Fe radioactive source. The colours identify the temperature at which the sensor was operated. The manganese characteristic emission peaks (Mn-K$_\alpha$ and Mn-K$_\beta$), the corresponding escape peak (Mn-K$_{\alpha,\beta}$ − Si-K$_{\text{edge}}$) and the silicon fluorescence peak (Si-K$_{\alpha,\beta}$) are resolved in all the spectrum.

1300 mV and 1700 mV, as well as the titanium characteristic emission peak Ti-K$_\alpha$ at around 1000 mV and the silicon fluorescence peak (Si-K$_{\alpha,\beta}$) at around 400 mV. The titanium Ti-K$_\beta$ is overlapping with the Ti-K$_\alpha$ and thus it is not visible. The silicon escape peak from Ti-K$_\alpha$ is visible, peaked at around 650 mV. One additional peak at around 1800 mV is associated to scattered Cu-K$_\alpha$ from the primary source. Thanks to the high statistics of around 4M events in total, it is possible to retrieve for each pixel the position of the most populated peaks, i.e. Ti-K$_\alpha$ and Fe-K$_\alpha$. Fig. 4.41 shows an example of a single pixel spectrum, where each of the two peaks has been fitted with a Gaussian distribution:

$$f(x) = A\ e^{-\frac{(x-\mu)^2}{2\sigma^2}} \tag{4.38}$$

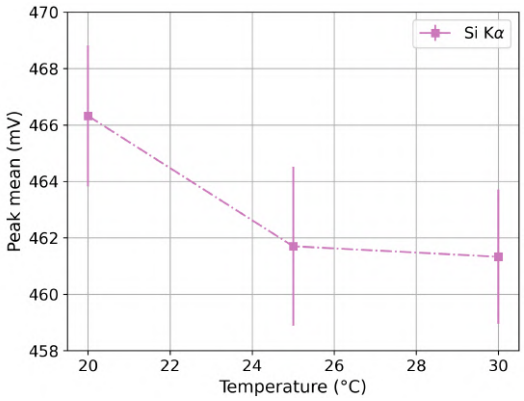

(a) Mean position of the Si Kα peak as a function of the temperature.

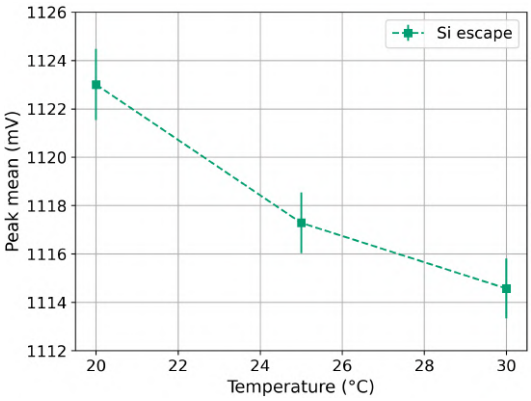

(b) Mean position of the Si escape peak as a function of the temperature.

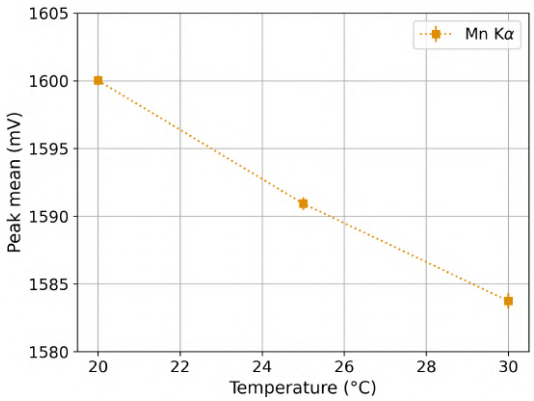

(c) Mean position of the Mn Kα peak as a function of the temperature.

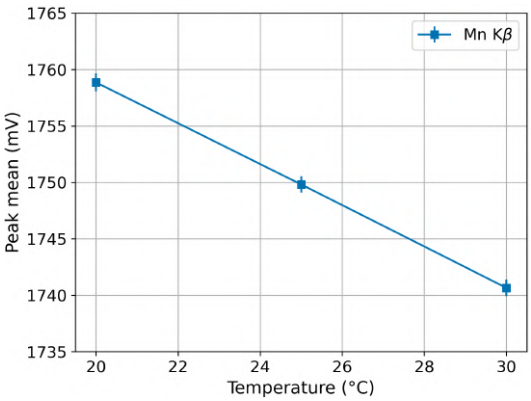

(d) Mean position of the Mn Kβ peak as a function of the temperature.

Figure 4.37

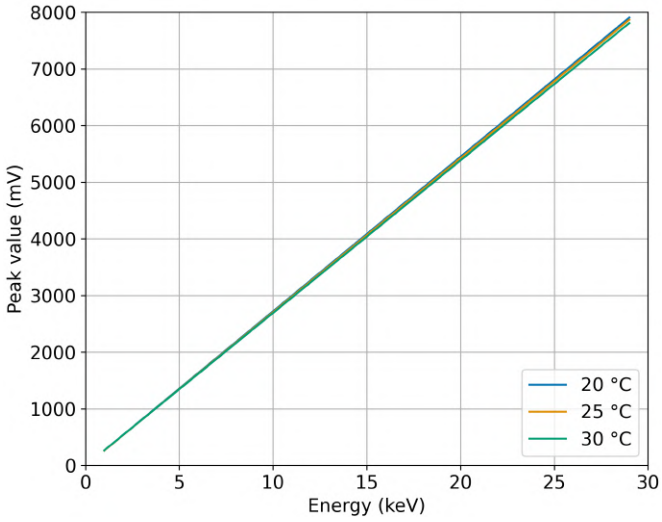

Figure 4.38: Comparison of the energy calibration lines at 20 °C, 25 °C and 30 °C.

In the hypothesis of a linear relation between the measured ToT in μs and the energy of the detected photon, the slope m and the offset q for each pixel are computed

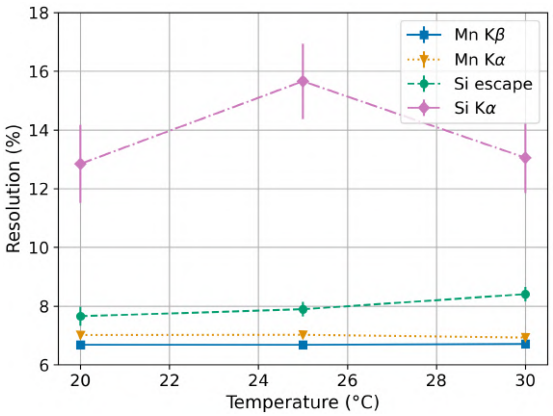

Figure 4.39: Peak resolutions as a function of the temperature. Different colours identify the four peaks.

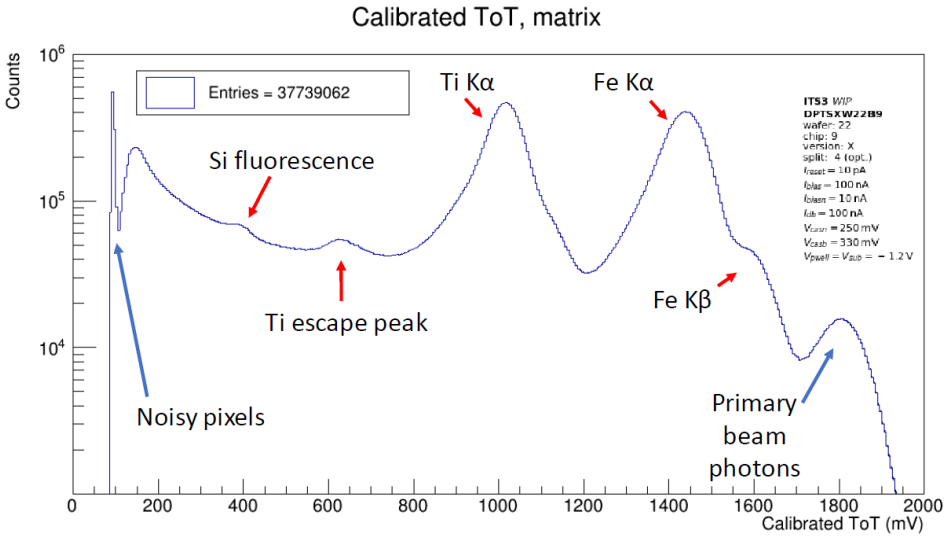

Figure 4.40: Measured spectrum of fluorescence X-rays emitted from an iron-titanium target. The iron characteristic emission peaks are resolved (Fe-K_α, Fe-K_β), as well as the titanium characteristic emission peak (Ti-K_α) and the silicon fluorescence peak (Si-$K_{\alpha,\beta}$). The silicon escape peak from Ti-K_α is visible. One additional peak at around 1800 mV is associated to scattered Cu-K_α from the primary source.

as:

$$m = \frac{\mu_{Fe-K\alpha} - \mu_{Ti-K\alpha}}{E_{Fe-K\alpha} - E_{Ti-K\alpha}} \tag{4.39}$$

$$q = \mu_{Fe-K\alpha} - m \cdot E_{Fe-K\alpha} \tag{4.40}$$

The distribution of m and q for the matrix are shown in fig. 4.42a and 4.42b, respectively. Both show a Gaussian distribution.

A possible correlation between the offset, the slope and the threshold was investigated and shown in fig. 4.43. There is no correlation between the offset and the slope. A hint of correlation is visible between the slope and the threshold and the offset and the threshold, indicating that pixels with a higher threshold shows a higher offset and a higher slope.

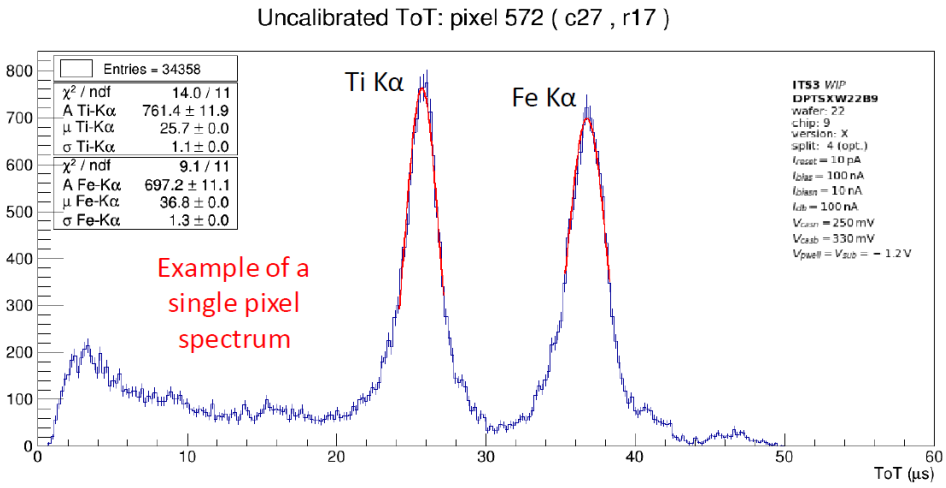

Figure 4.41: Measured spectrum of fluorescence X-rays emitted from an iron-titanium target for a single pixel. The iron characteristic emission peak Fe-K$_\alpha$ is resolved, as well as the titanium characteristic Ti-K$_\alpha$.

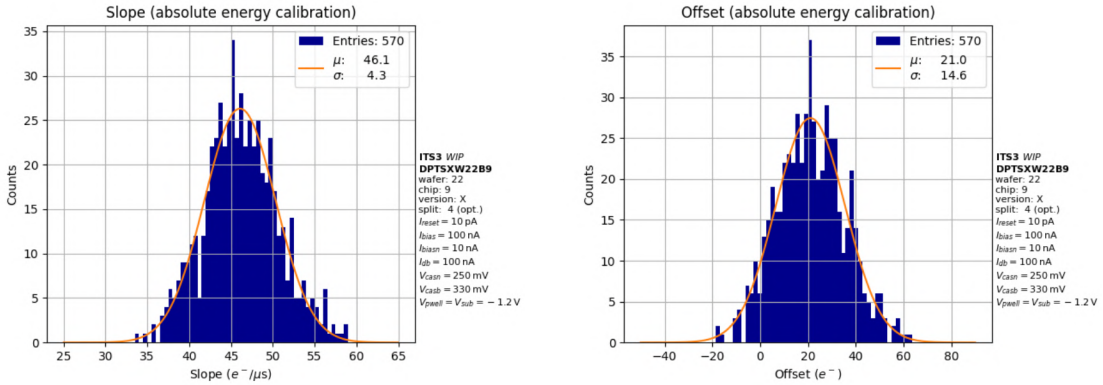

(a) Slope distribution for all the matrix pixels, for the single pixel energy calibration.

(b) Offset distribution for all the matrix pixels, for the single pixel energy calibration.

Figure 4.42

These parameters can be used to perform an energy calibration of the pixel response directly from μs to e$^-$, without the need of the ToT pixel-to-pixel calibration. This calibration is referred to as *absolute* in the following. The spectrum calibrated with the absolute calibration (blue spectrum) and the one obtained with the normal procedure (orange spectrum), which is described in sec. 4.2.2, are compared in fig. 4.44. The loss of linearity for low signals (<400 e$^-$) is not considered by the absolute calibration, thus there are signals even below the threshold, which is set at ∼100 e$^-$. Otherwise, the position of the peaks and their width is compatible between the two spectra, except for a shift of the mean position of the iron Kα and iron Kβ emissions, which might be due to a temperature effect.

The energy resolution of the resolved peaks in the two spectra is reported in tab. 4.12. The silicon fluorescence and the silicon escape peaks have the same energy resolution, whereas a slightly better resolution is observed for the absolute calibrated spectrum in the other peaks. The comparable results in terms of the energy resolu-

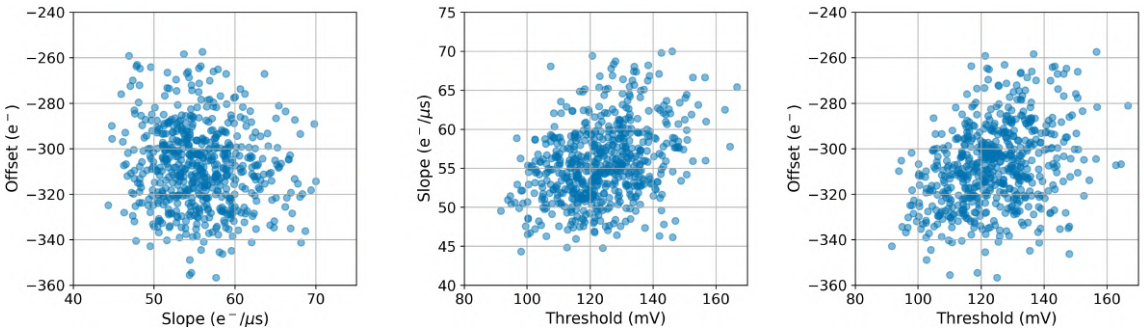

(a) (b) (c)

Figure 4.43: Correlations between the absolute calibration slope, offset and the threshold.

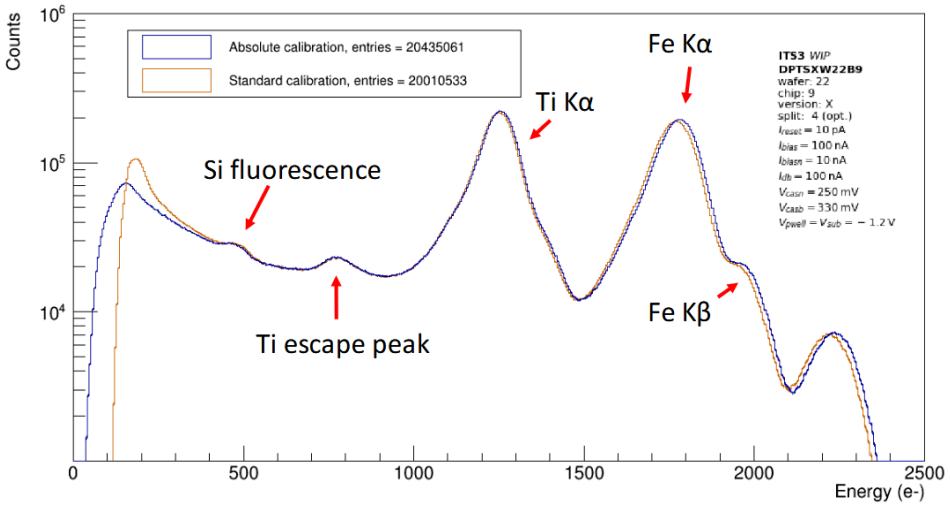

Figure 4.44: Measured spectrum of fluorescence X-rays emitted from an iron-titanium target for a single pixel. In orange is shown the calibrated spectrum, which is obtained with the standard calibration procedure, instead in blue it is shown the spectrum obtained with the absolute calibration.

tion between the two spectra demonstrates how the ToT pixel-to-pixel calibration is effective in correcting the variation of the response from pixel to pixel.

Table 4.12: Summary of all the quantities of interest for the peaks of the spectrum of fluorescence X-rays emitted from a iron-titanium target.

Peak	Photon energy (keV)	Energy resolution (%) standard calibration	Energy resolution (%) absolute calibration
Si_{fl}	1.74	13.2 ± 0.3	13.2 ± 0.3
Si escape from Ti	2.77	11.9 ± 0.1	11.9 ± 0.1
Ti-Kα	4.51	9.19 ± 0.03	9.10 ± 0.03
Fe-Kα	6.40	7.51 ± 0.01	7.34 ± 0.01
Fe-Kβ	7.06	7.23 ± 0.03	7.06 ± 0.04

4.3 Ion energy loss measurements with babyMOSS

The Time-over-Threshold (ToT) energy measurement capabilities of the babyMOSS have been exploited to investigate the prototype response to heavily ionising particles. In particular, measurements were performed with Helium and Carbon ions. The aim of this study is to evaluate the charge collection efficiency and the energy response linearity of the babyMOSS when operated with ions of different mass and energy.

4.3.1 Setup

A mixed ion beam composed of Carbon, Helium and Oxygen ions was provided at GSI [148]. The composition of the beam was approximately 50% Carbon, 45% Helium and 5% Oxygen, with an energy of 225 MeV/amu for all ions. The babyMOSS prototype was tested within a telescope composed of eight detection planes, including two babyMOSS modules and six ALPIDE sensors [58, 59, 60]. The telescope configuration allowed reconstructing the particle trajectory and correlating the signals recorded by the different planes.

A dedicated acquisition system with NIM and VME modules was developed specifically to control the data acquisition and to handle the trigger signals provided by the scintillators, ensuring proper synchronization of all detector planes in the telescope as well as with the scintillators themselves.

4.3.1.1 Modules calibration

The two VME modules used in the experiment, the QDC, for recording the charge deposited in the scintillators, and the TDC, for measuring the time of flight (TOF) between the scintillators, were calibrated prior to data acquisition. In particular, the QDC pedestal and the TDC timing characteristics were measured.

QDC pedestal The pedestal of the QDC, which represents the baseline signal in the absence of any particle-induced charge, is measured for both channels used to read out the scintillators. To characterize the pedestal, a random trigger was employed, allowing the acquisition of the QDC baseline amplitude in the absence of any particle interaction. The resulting distributions for the two channels are then fitted with a Gaussian distribution to determine the mean value, corresponding to the pedestal of each channel. These distributions are shown in fig. 4.45. The pedestal values thus obtained are subsequently subtracted from the real particle signals during data acquisition, ensuring that the measured charges reflect only the energy deposited by the particles in the scintillators.

TDC calibration The calibration of the TDC is performed by injecting a signal with a known time delay into the channel. By comparing the measured TDC values with the corresponding input delays, a linear relationship between the TDC output and the actual time intervals is established. The resulting calibration curve is shown in fig. 4.46.

4.3.2 Beam characteristics

The measurements performed with the scintillators were initially used to study the characteristics of the beam. This section presents the main properties of the beam as determined from these data.

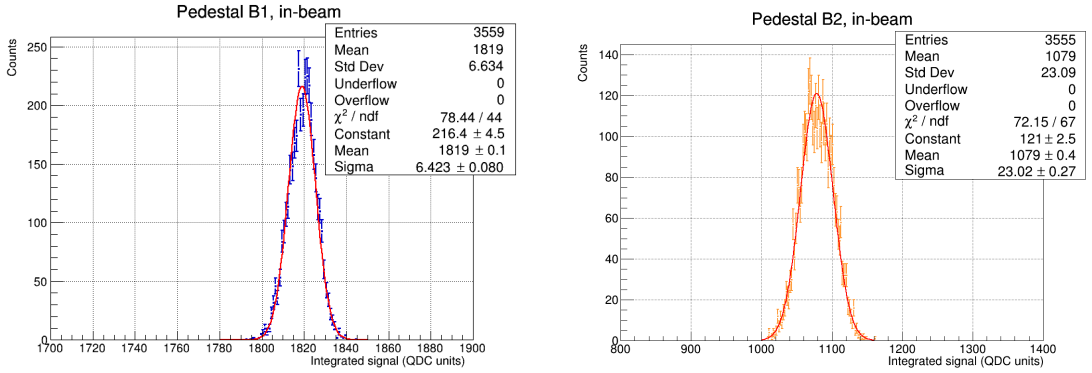

(a) (b)

Figure 4.45: Distribution of the QDC pedestal for the two scintillator channels, measured using a random trigger. The Gaussian fit applied to the distributions allows the determination of the mean pedestal, which is then subtracted from the real particle signals.

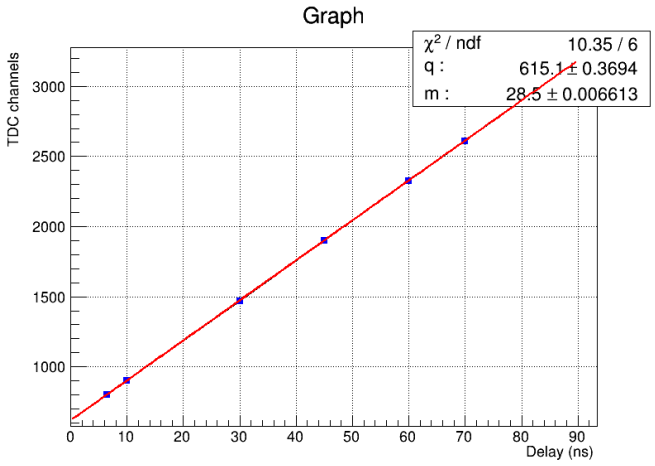

Figure 4.46: Calibration curve of the TDC. The measured TDC values are plotted as a function of known input delays. A linear fit demonstrates the direct proportionality between the TDC output and the actual time interval.

The energy spectrum measured by the first scintillator provides information on the composition of the beam in terms of particle species. The spectrum exhibits three distinct peaks, corresponding to helium, carbon, and oxygen nuclei, as shown in fig. 4.47. By performing a fit on these peaks, the relative contribution of each species to the beam can be quantified. The fitting results indicate that the beam is composed of 42.8% helium, 55.0% carbon, and 2.1% oxygen nuclei, reflecting the dominant presence of carbon and helium and a minor percentage of oxygen. This analysis allows for a clear characterization of the beam composition prior to further studies.

The peaks in the energy spectrum measured by the downstream scintillator, shown in fig. 4.48, appear smeared compared to those in the front scintillator. This widening of the spectrum is a consequence of the particles traversing the telescope before reaching the detector, including an additional layer of plastic placed in front of the back scintillator, which induces energy loss fluctuations and multiple scattering.

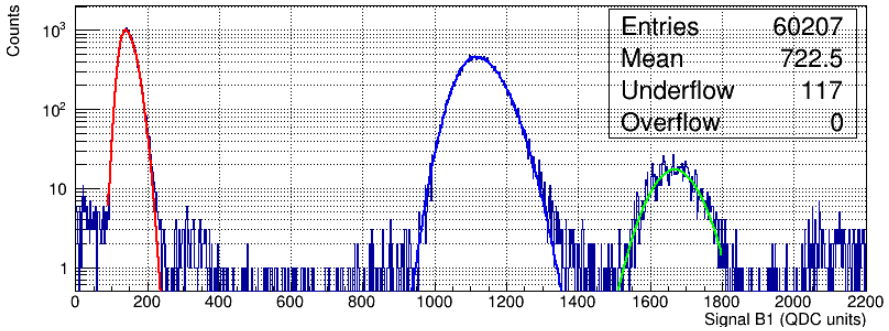

Figure 4.47: Energy spectrum measured by the scintillator in front of the telescope. The three distinct peaks correspond to different particle species in the beam. A fit of these peaks allows the determination of the relative contributions of each component.

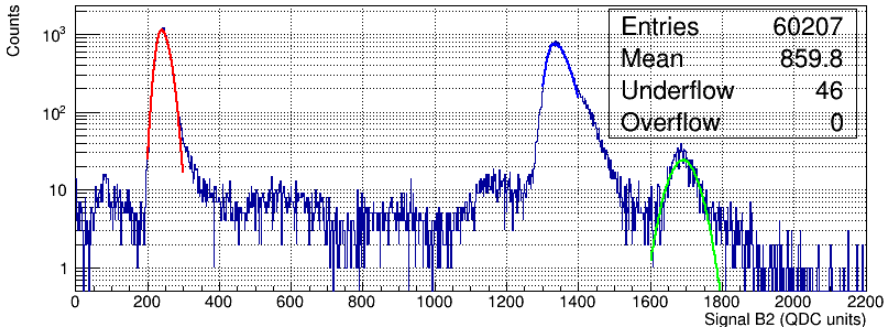

Figure 4.48: Energy spectrum measured by the downstream scintillator.

In fig. 4.49 the correlation between the energy response of the two scintillators in the telescope is shown. The front scintillator measures the initial energy deposition, while the downstream scintillator, placed behind an additional layer of plastic, receives particles that have traversed this material. This plastic layer, introduced in front of the thicker downstream scintillator, acts as a degrader and allows for better separation of energy losses, making it possible to resolve different isotopes of carbon in addition to the main particle species. In the correlation plot, the three primary components of the beam, i.e. helium, carbon, and oxygen, are clearly identifiable, with carbon isotopes forming distinguishable substructures. As expected, very few oxygen events are observed, consistent with the beam composition measured in the front scintillator.

The correlation between the signal measured by the front scintillator and the time-of-flight (TOF) data, shown in fig. 4.50, allows for particle separation as well. By combining the energy deposited in the scintillator with the measured TOF between the two detectors, it is possible to distinguish different particle species and perform a clean selection of events. This approach allows to isolate specific groups of particles, reducing background and improving the accuracy of further analyses based on the scintillator signals.

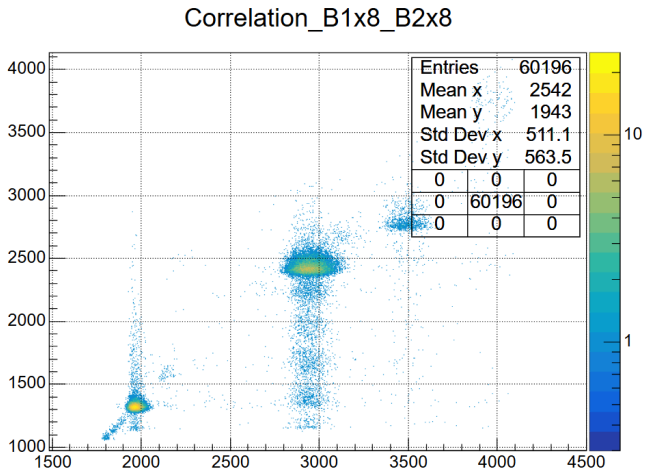

Figure 4.49: Correlation between the analogue signals of the front and downstream scintillators. The three main particle species clusters (He, C, and O) are clearly visible. Thanks to the additional layer of plastic placed in front of the back scintillator, different carbon isotopes can also be distinguished below the main carbon cluster. As expected, oxygen events are very few.

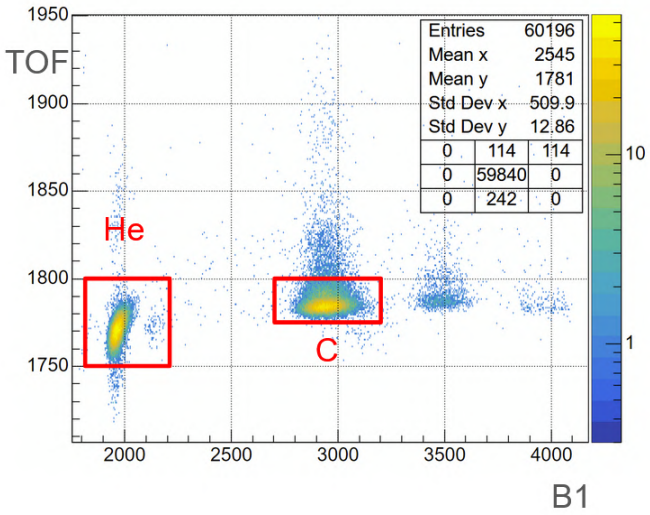

Figure 4.50: Correlation between the energy deposited in the front scintillator and the time-of-flight (TOF) measured between the two scintillators. This correlation allows the identification and selection of different particle species based on their energy loss and velocity.

4.3.3 PID with babyMOSS ToT

The ALPIDE planes of the telescope were used to reconstruct the particle tracks. By combining this tracking information with the scintillator data presented in the previous section, it is possible to associate each event recorded by the babyMOSS sensor with a particle trajectory, a time-of-flight measurement and the corresponding energy loss in the scintillators. Moreover, since the scintillators allow for particle identification, each event could also be assigned to a specific particle species, in order to verify the PID

capabilities offered by the babyMOSS detector ToT measurement.

Fig. 4.51 shows the ToT measured by the babyMOSS for all events, without any track reconstruction or particle association. Three peaks are visible: the first peak is interpreted as background from particles produced by the primary beam, the second corresponds to helium, and the third to carbon.

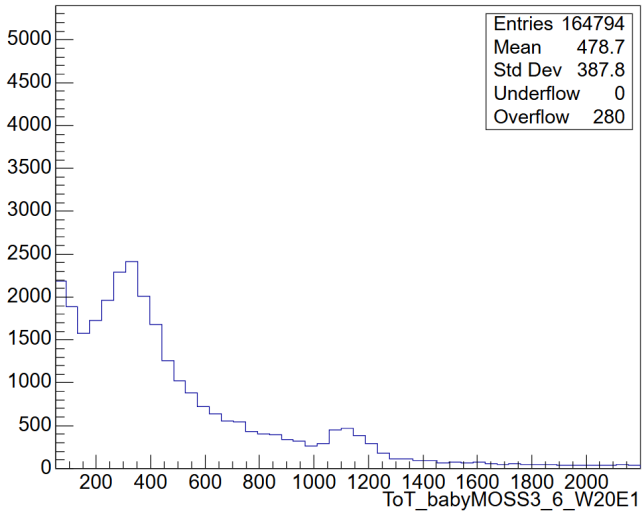

Figure 4.51: Measured Time-over-Threshold (ToT) distribution on the babyMOSS sensor for all events, without track reconstruction or particle association. Three peaks are visible: the first corresponds to background from secondary particles produced by the primary beam, the second to helium, and the third to carbon.

By combining the tracking information provided by the ALPIDE planes with the particle identification obtained from the scintillators, it is possible to select only those events that can be attributed to helium and carbon ion detections. This selection allows the study of the corresponding energy loss distributions on the babyMOSS sensor, which are shown in fig. 4.52a for helium and fig. 4.52b for carbon. Focusing on these identified species enables a more precise evaluation of the babyMOSS response and its potential for particle identification.

Despite the low statistics, mainly attributed to a misalignment of the telescope identified in the subsequent analysis, it is still possible to fit the two distributions with a convolution of a Landau and a Gaussian function, as expected from theory (see Sec. 4.1.1.3), in order to extract the Maximum Probable Value (MPV) of the distributions. The measured MPV for helium is slightly lower than the mean theoretical expectation (31 keV), consistent with the properties of the Landau distribution. In contrast, the carbon MPV is significantly lower than expected mean value (276 keV), suggesting that a saturation effect in the detector response, either due to the collection process or the in-pixel electronics, may be occurring.

Despite the observed saturation effect, further investigated in chapter 5, the babyMOSS sensor is still able to distinguish between helium and carbon ions through the energy loss measurements provided by the ToT. These preliminary studies, together with the experience gained, will be valuable for future test beam campaigns.

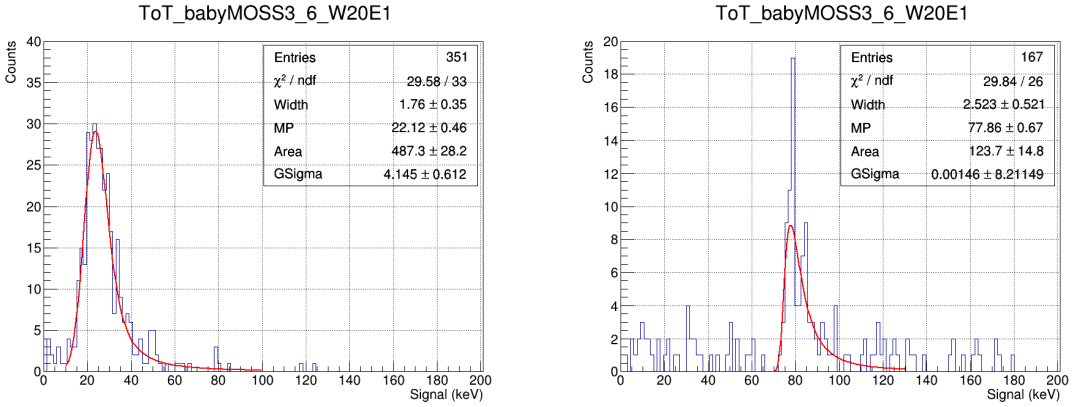

(a) (b)

Figure 4.52: Energy loss spectra measured by the babyMOSS sensor for helium (a) and carbon (b) ions. The distributions are fitted with a convolution of a Landau and a Gaussian function.

Chapter 5

Charge collection process simulation

In order to complement the experimental characterisation presented in the previous Chapters and to a complete understanding of the signal formation mechanism in the studied devices, a comprehensive simulation of the charge collection process has been carried out and is presented in this chapter. After a brief introduction of the simulation tools, the procedure to define the doping profile and the electric field in a pixel with similar characteristics to the DPTS and the MOSS pixels is presented, together with the results. Simulations of the response to MIPs, Xrays and light ions are discussed and compared to the experimental results. Finally, a transient simulation of the charge collection process for energy depositions up to 300 keV is presented to investigate the effect of large energy losses on the pixel electric field and thus on the signal.

5.1 Simulation tools

Two software packages have been used for different purposes in the simulation. TCAD is used to simulate the electric field inside the pixel, while Garfield++ is used to simulate the charge collection process in an array of pixels.

5.1.1 TCAD

Technology Computer Aided Design (TCAD) [149] is a powerful simulation tool to develop and optimise semiconductor fabrication processes and device operation. It can be used to predict the electrical, thermal and mechanical properties of devices before the fabrication. In this thesis work, it has been exploited to simulate the electric field of a DPTS-like pixel and of a pixel with the characteristics of the babyMOSS top region, with the goal of validating the results of the energy-loss measurements presented in chapter 4.

TCAD simulations are based on a finite element procedure, which first provides the splitting of the structure into a grid using a mesh and then the computation of the physical properties of each mesh point by using fundamental physics models. These two steps are usually performed by two different TCAD tools. The Sentaurus Structure Editor [150] tool is used to simulate the semiconductor fabrication process, defining the doping profile of the pixel and the mesh. The Sentaurus Device [151] is used to simulate the electrical properties of the semiconductor.

5.1.1.1 Doping profile simulation

The Sentaurus Structure Editor allows for the geometrical definition of the doping profile features of the semiconductor. Another TCAD tool allows for the simulation of the whole fabrication process to obtain the sensor doping profile, going through all the necessary steps: ion implantation, diffusion, growth and etching. However, despite giving more precise results, it is more time consuming and above all it requires the knowledge of the exact fabrication process, which is trade secret for the ITS3 prototypes. Therefore, the geometric approach offered by the Sentaurus Structure Editor was employed for this study.

The definition of a mesh is part of the doping profile simulation stage. The simulation is more accurate if a finer mesh is used, however, the finer the mesh, the longer the simulation takes. Thus a trade-off between the simulation duration and its accuracy has to be made. Usually the mesh precision follows the gradient of the doping profile: the mesh is finer where the gradient is larger.

5.1.1.2 Electric field simulation

The Sentaurus Device tool is used to simulate the electric field inside the structure, once the doping profile and the mesh have been defined via the Sentaurus Structure Editor. The drift-diffusion model is the basis of the Sentaurus Device. Firstly the Poisson equation is solved at each mesh point [152]:

$$\nabla \cdot \mathbf{E} = -\nabla^2 \phi = \frac{\rho}{\varepsilon} \tag{5.1}$$

where $\mathbf{E}$ is the electric field, ϕ is the electric potential, ρ is the electric charge density and ε is the permittivity. The two continuity equations for electrons and holes are solved self-consistently with the Poisson equation:

$$\frac{\partial n}{\partial t} = \frac{1}{q}\nabla \cdot \mathbf{J}_n - R_n + G_n \tag{5.2}$$

$$\frac{\partial p}{\partial t} = \frac{1}{q}\nabla \cdot \mathbf{J}_p - R_p + G_p \tag{5.3}$$

where J is the current density, R is the recombination rate, G is the generation rate and n and p are the electron and hole densities. The subscripts n and p identify the quantities for the electrons and holes, respectively.

Eq. 5.1, 5.2 and 5.3 are solved self-consistently for the electrostatic potential and the electron and hole densities using an iterative method. An initial guess is used to begin the process, which then continues until the convergence criteria have been reached.

The system of equations can be solved for steady bias and time conditions if no external voltage is applied to the sensor. In the ITS3 prototypes the reverse bias voltage is applied, as well as an additional voltage level applied onto the collection electrode. Thus the three equations have to be solved with a quasi-stationary procedure, that ramps a parameter until the defined goal is reached. For each step the system is solved for a steady state.

Once the electric field of the pixel has been obtained, it can be exported from TCAD to be used in other software for the particle interaction simulation. The interaction of particles and the signal formation can be simulated in TCAD as well, but it is more time-consuming, due to the fact that the physical properties of the device are computed

at each step of the simulation. Thus another software, Garfield++, which employs the fixed electric field computed by TCAD, has been chosen to investigate the pixel charge collection properties with high statistics simulations.

5.1.2 Garfield++

The particle interaction with the device and the signal formation and collection are simulated with Garfield++ [153], an object-oriented toolkit for the detailed simulation of particle detectors based on semiconductors.

Garfield allows for the simulation of the interaction of charged particles and photons. In this thesis work a simulation of the photon and ions interaction was carried out. The Garfield simulation can be divided in 4 steps:

1. Creation of a silicon pixel, or a matrix of pixels, importing the TCAD electric field;
2. Simulation of the incident particle and of its interaction with the device, in particular the energy lost by the particle is simulated in terms of created e^-/h^+ pairs;
3. Simulation of the drift and the diffusion of the e^-/h^+ which were created by the incident particle, by taking into account the electric field in the pixel cell;
4. Simulation of the signal induced on the collection electrode by the e^- and h^+ motion.

The creation of an electric field with TCAD has been approached in the previous section, while the physics of the particle interaction with matter has been extensively discussed in chapter 4. The charge diffusion and the signal formation in the pixel cell are discussed below.

5.1.2.1 Transport of e^- and h^+

The mean energy necessary to create an electron/hole pair in silicon is of $E_{pair} = 3.6$ eV, thus meaning that an incident particle that is releasing an energy ΔE inside the detector will create $\Delta E/E_{pair}$ pairs of electrons and holes. Such particles are subject to the electric field inside the detector, therefore their motion is a combination of thermal diffusion and drift.

In general, the motion of electrons and holes under an electric field $\mathbf{E}$ is described by the following equation:

$$\dot{\mathbf{r}} = \mathbf{v}_\mathrm{d}(\mathbf{E}(\mathbf{r})) \tag{5.4}$$

where $\mathbf{r}$ is the position and $\mathbf{v}_\mathrm{d}$ is the drift velocity, that given a mobility μ_e for the electrons and μ_h for the holes is defined as:

$$\mathbf{v}_\mathrm{d}^{\mathrm{e,h}} = \mu_{e,h}\mathbf{E} \tag{5.5}$$

Eq. 5.4 is solved stochastically, by computing a drift step $\Delta\mathbf{s} = \mathbf{v}_\mathrm{d}\Delta\mathrm{t}$ and a random diffusion step and adding them vectorially. The random diffusion step is computed taking into account the two Gaussian distributions of the random motion parallel and transverse to the drift velocity.

Fig. 5.1 shows an example of the e^-/h^+ transport simulated with Garfield in silicon with a vertical uniform electric field. The effect of the diffusion is visible in the increasing spread of the charges while moving away from their origin.

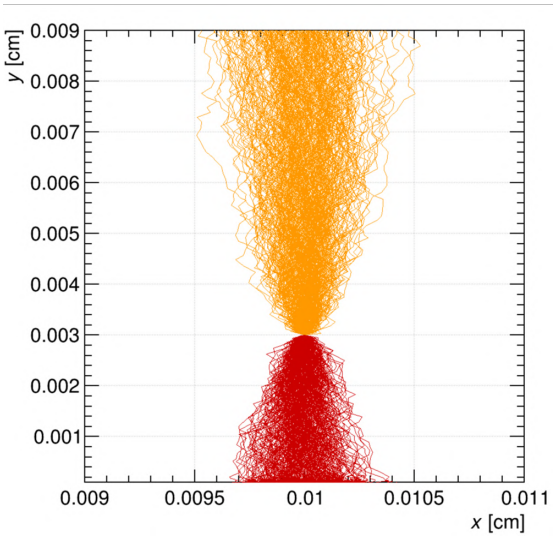

Figure 5.1: Example of drift and diffusion of electrons (orange lines) and holes (red lines) in a generic p-n silicon junction with a uniform electric field along the vertical direction.

5.1.2.2 Charge collection and signal formation

The signal formation is described by the Shockely-Ramo theorem, from which follows that the instantaneous current i induced on the electrode by a charge q in motion with a velocity $\mathbf{v}$ is:

$$i = -q\mathbf{v} \cdot \mathbf{E}_W(\mathbf{r}) \tag{5.6}$$

where $\mathbf{E}_W$ is the weighting field that is obtained by applying unit potential to the measurement electrode and zero to all the others.

Following eq. 5.6 the charge induced by a particle moving from $\mathbf{r}_1$ to $\mathbf{r}_2$ is:

$$\int_{t_1}^{t_2} i(t)dt = q[\phi_W(\mathbf{r}_2) - \phi_W(\mathbf{r}_1)] \tag{5.7}$$

where ϕ is the weighting potential.

Fig. 5.2 shows an example of the induced signal (dark blue line) on a 3D DPTS-like pixel. The electrons contribution to the total signal is shown in orange and the holes contribution is shown in red.

5.2 Doping profile and electric field definition

The electric field inside the pixel of the sensor has been simulated with TCAD, using the tools presented in sec. 5.1.1. The electric field is directly related to the doping profile. Since the doping profile of the ITS3 prototypes is under trade secret, an initial guess has to be made and then optimised by looking qualitatively at the resulting electric field. A comparison between simulated MIP and $^{55}_{26}$Fe source spectra and experimental results is performed to assess the compatibility of the selected electric field with the sensor response.

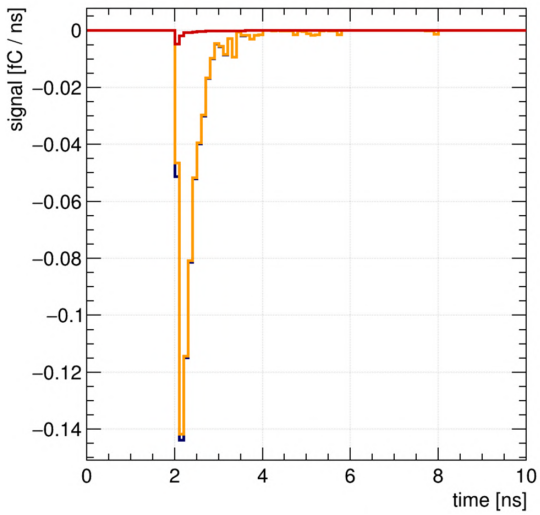

Figure 5.2: Example of induced signal on the collection electrode of a DPTS-like 3D pixel. The electrons contribution is shown in red, the holes one is shown in orange and the total one in dark blue.

5.2.1 Tuning of the doping profile

A 3D DPTS-like pixel and a 3D babyMOSS top region pixel have been simulated. The doped regions and their thickness as implemented in TCAD are shown in the lateral cross section of a pixel in fig. 5.3. The figure is not in scale. Fig. 5.4 shows a top view of the pixel with the relative dimensions, highlighting the differences between the DPTS and the babyMOSS pixel, i.e. the larger pixel pitch and gap size in the babyMOSS pixel.

The core of the pixel is the p-n junction formed by the highly n^+ doped collection electrode and the p^- epitaxial layer. In the ITS3 prototypes studied for this work an additional n^- doped implant is added just below the collection electrode to allow for the extension of the depleted region over the whole epitaxial layer, thus providing a more efficient and faster charge collection. The deep p^+ wells hosting the CMOS in-pixel logic on top of the sensor are included in the simulation as well, since they impact on the shape of the depleted region. Finally the thick p^+ substrate under the epitaxial layer is simulated to allow for a precise simulation of the charge collection process, including the contribution of the charge released in the substrate to the signal. In fact, despite the substrate contribution is negligible when simulating MIP particles, it is important for higher energy depositions, as in the case of photons from an $^{55}_{26}$Fe source [154]. A draw back of a thick substrate is the increase in the simulation time, thus its thickness can be reduced down to only 1 μm for faster, but less precise, simulations.

An initial guess of the doping levels of the implants in the pixel has been made starting from the knowledge about the order of magnitude of the doping levels in the ALPIDE chip [154]. The doping optimisation is achieved by tuning, one at a time, the doping levels of the deep pwell, the epitaxial layer and the additional n-type implant, which have the largest impact on the shape of the depleted region. The extension of the depleted region before and after applying the reverse bias voltage is evaluated for each combination of doping levels and the one that yields the most extended depletion in the epitaxial layer is chosen to be used in the subsequent simulation steps. The effect

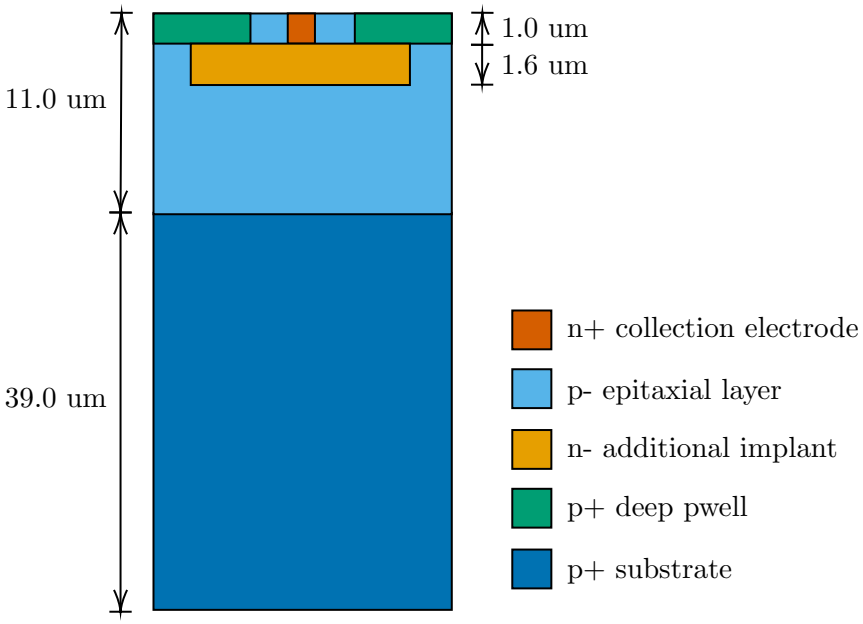

Figure 5.3: Lateral cross section not in scale of a DPTS and of a babyMOSS pixel. The implant depths indicated in the figure are approximative.

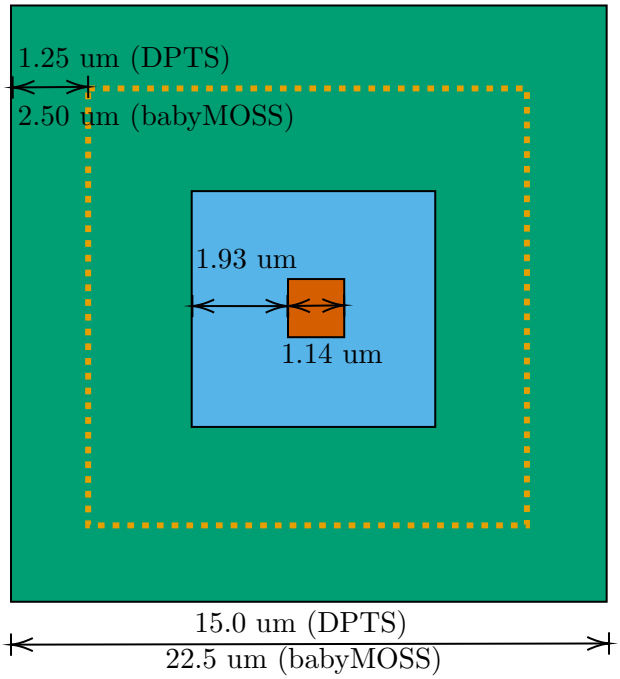

Figure 5.4: Top view not in scale of a DPTS and of a babyMOSS pixel. Colours are referred to the legend in fig. 5.3. The yellow dashed line indicates the position of the additional n^- implant.

of the variation of the doping profile is illustrated below with an example.

Fig. 5.5 shows a 2D plot of the electric field near the collection electrode simulated in the babyMOSS 3D pixel for a fixed doping level of the deep p-well and for varying doping concentration of the additional n-type implant (increasing from left to right)

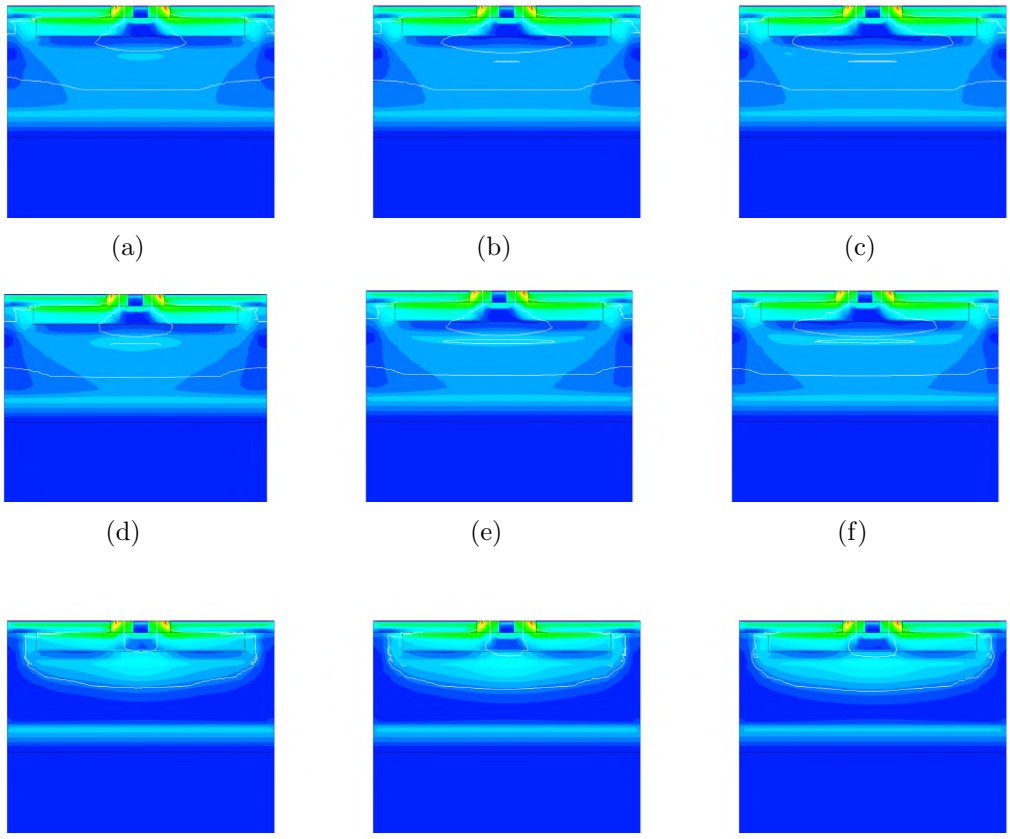

Figure 5.5: Simulated electric field in a babyMOSS pixel with a fixed doping of the deep pwell. The additional n-type implant doping is increased from left to right and the one of the epitaxial layer is increased from top to bottom. No reverse bias voltage is applied, to better highlight the effects of the doping profile variation. The simulation is not based on actual doping profiles and geometry and implant depths are approximative.

and the epitaxial layer (increasing from top to bottom). The white line represents the depleted region borders. No reverse bias is applied.

Although the final doping combination is chosen by looking at the electric field with reversed voltage applied, removing the reverse bias allows the effects of doping variations in the different implants on the electric field to be seen more clearly. An increase of the additional n-type implant doping leads to the enlargement of the undepleted region around the collection electrode, thus worsening the electric field in the pixel. An increase in the epitaxial layer doping reduces the undepleted region around the collection electrode, but at the same time reduces the expansion of the depleted region in the epitaxial layer itself. Thus a trade-off between these two doping concentrations must be found.

Fig. 5.6 shows the electric field for the same doping concentration combinations of additional n-type implant and epitaxial layer, but with a deep p-well concentration increased by a factor of 10. The effect of varying the additional n-type implant and the epitaxial doping is the same discussed above. However it is less pronounced, as the higher doping of the deep p-well helps to keep the undepleted region around the

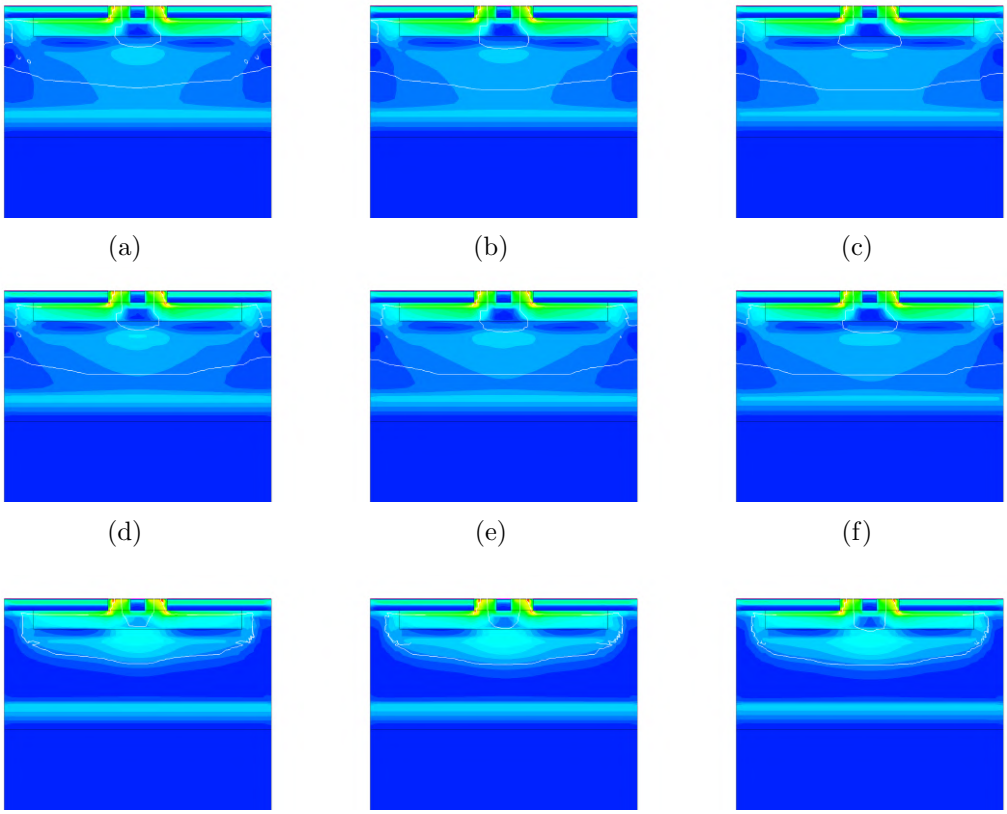

Figure 5.6: Simulated electric field in a babyMOSS pixel with a doping of the deep pwell fixed to a value which is a factor of 10 larger than the one used in fig. 5.5. The additional n-type implant doping is increased from left to right and the one of the epitaxial layer is increased from top to bottom. No reverse bias voltage is applied, to better highlight the effects of the doping profile variation. The simulation is not based on actual doping profiles and geometry and implant depths are approximative.

collection electrode small.

5.2.2 Electric field

The choice of the doping profile is based on the extension of the depleted region around the collection electrode shown in the previous section. The doping profile that is generating the largest depleted region around the collection electrode, while covering as much as possible of the epitaxial layer, is selected. A 2D view of the final 3D doping profile and the resulting electric field chosen for particle simulations in the DPTS and the babyMOSS are shown in fig. 5.7 and 5.8, respectively. The different doping level colours in fig. 5.7a and 5.7b allow the identification of the pixel features schematised in fig. 5.3, whose boundaries are also indicated by the black lines. The two electric fields give a depleted region with the same shape, covering most of the epitaxial layer. Moreover, the electric field is larger as it approaches the collection electrode. As expected, in the substrate no electric field is present, thus meaning that the charges released here will move only by diffusion.

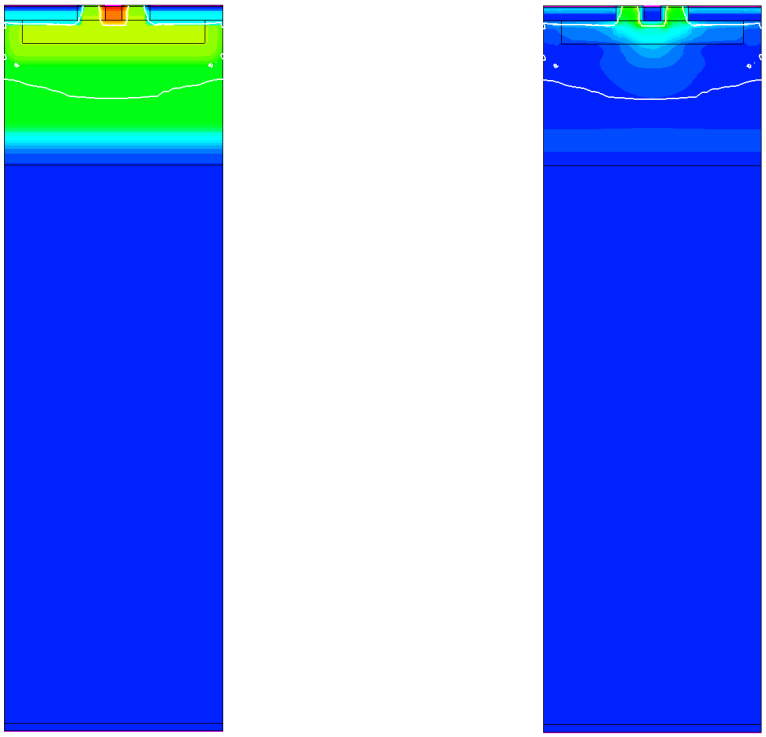

(a) (b)

Figure 5.7: Simulated doping profile and electric field in a DPTS pixel. The white line delimits the depleted region boundaries. The simulation is not based on actual doping profiles and geometry and implant depths are approximative.

5.3 Particle simulation

The goal of the simulation is an in-depth study of the charge collection process. Thus, the reproduction of the energy-loss measurement results, which give a direct knowledge on the signal experimentally collected by the pixel, is of great interest. The measured pixel signal depends on both the charge collection process and the subsequent amplification and shaping performed by the in-pixel logic. The comparison between simulated charge collection and acquired experimental data will give the opportunity to separate the two contributions.

The compatibility between the real sensor response and the electric fields discussed in sec. 5.2.2 and used in simulations to predict energy-loss measurement results, is verified by comparing the simulation output with MIP energy loss measurements for the DPTS and $^{55}_{26}$Fe radioactive source measurements for the babyMOSS. These measurements have been chosen as reference since the characteristics of the MIP and $^{55}_{26}$Fe spectra are well known.

5.3.1 MIP simulation with DPTS

The electric field extracted for the DPTS pixel through the described procedure is then evaluated by comparing the simulated response to the experimental one. A matrix of 3×3 pixels is simulated in Garfield, using the electric field obtained from the TCAD simulation. The dimension of the simulated matrix is chosen to allow for the study of

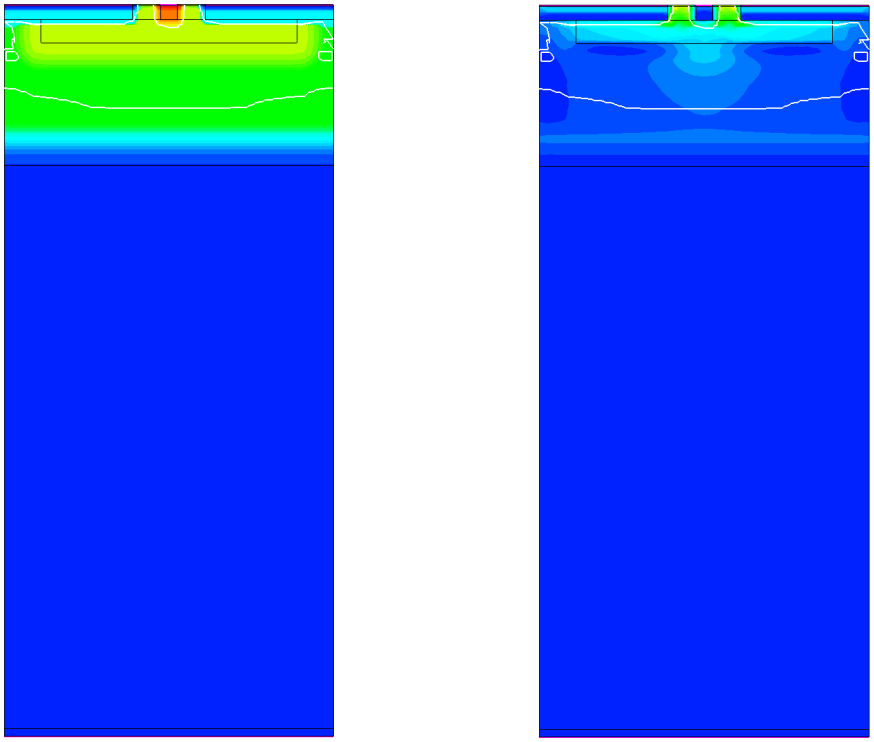

(a) (b)

Figure 5.8: Simulated doping profile and electric field in a pixel of the babyMOSS top half unit. The simulation is not based on actual doping profiles and geometry and implant depths are approximative.

the cluster size, which is experimentally measured as around 1 pixel on average [83]. Fig. 5.9 shows a section of the electric field contour lines of three pixels. The TCAD simulation is done with a reduced substrate to shorten the simulation time. A pion

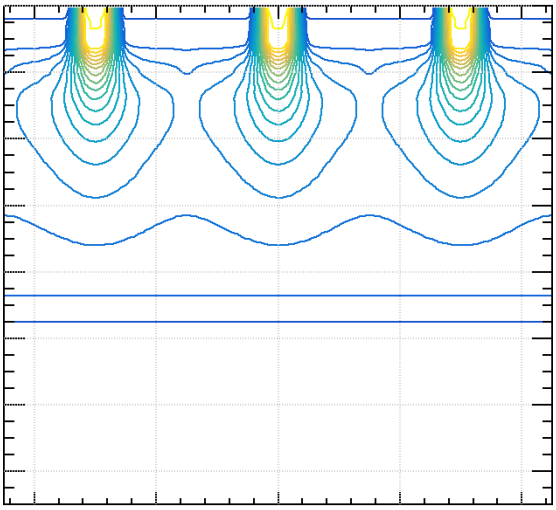

Figure 5.9: Section of the 3×3 pixel matrix simulated with Garfield to reproduce the MIP energy loss spectrum with DPTS. The electric field contour lines are shown.

beam of 10 GeV, impinging perpendicularly the central pixel, is simulated to reproduce the beam test measurements performed with the DPTS at the CERN PS facility (see sec. 2.5). The crossing location of the pions is uniformly distributed across the central pixel in the matrix.

Fig. 5.10 shows the comparison between the simulated seed pixel spectrum of 10 GeV positive pions and the experimental data. Both distributions are fitted with a convolution of a Landau and a Gaussian function, which is expected to describe the MIP energy loss in a thin layer of silicon (see sec. 4.1.1.3). The fit results are compatible, thus confirming that the electric field selected for the DPTS gives results which are consistent with the experimental ones.

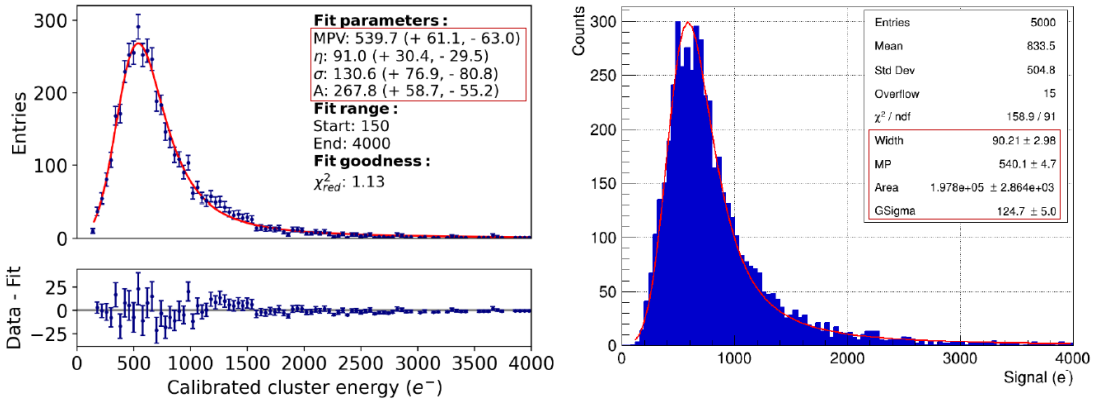

Figure 5.10: Seed pixel simulated spectra of 10 GeV pions in a 3×3 DPTS pixel matrix compared with the experimental result. The noise and the electronics transfer function are not taken into account. Figure on the left from [88].

5.3.2 $^{55}_{26}$Fe simulation with babyMOSS

The babyMOSS pixel electric field simulated with TCAD is evaluated by comparing the simulated spectrum of $^{55}_{26}$Fe source to the experimental one. A matrix of 3×3 pixels is simulated in Garfield, following the procedure described in the previous section for the DPTS. Incident photons of 5.9 keV and 6.5 keV, corresponding to the Kα and Kβ emissions of the $^{55}_{26}$Fe source (see sec. 4.1.3.1), are directed perpendicular to the central pixel of the array with a random incident position. The transport of the photons in the detector is simulated by the TrackHeed class of Garfield.

The simulated seed pixel spectra with and without electronic noise are shown in fig. 5.11. The electronic noise is simulated from a Gaussian distribution with mean $\mu = 0$ and $\sigma = 18\ e^-$, corresponding to the noise mean value [155] as measured in a threshold scan (see sec. 2.4.1.1). A threshold of 0 e^- is set in the simulation. The main $^{55}_{26}$Fe emission peaks are visible at large signal charge values. An additional lower peak is visible at $\sim$1100 e^-, corresponding to the silicon escape peak (see sec. 4.1.3.1). The silicon fluorescence peak is not simulated.

Fig. 5.12 shows the comparison between the babyMOSS $^{55}_{26}$Fe simulated spectra and the measured one. Despite the spectrum shape, including three peaks superimposed to a continuous background, is correctly reproduced in simulation, the peak smearing of the measured spectrum is larger with respect to the one of the simulated spectrum.

The simulated spectrum reproduces also the slight rise for signals just below the two

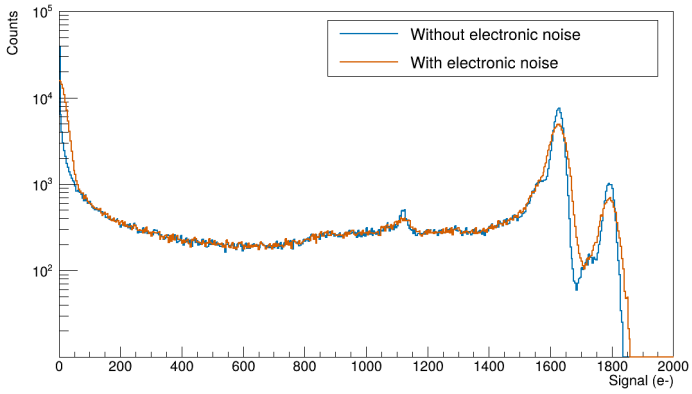

Figure 5.11: Seed pixel simulated spectra of $^{55}_{26}$Fe Kα (5.9 keV) and Kβ (6.5 keV) emissions with and without electronic noise.

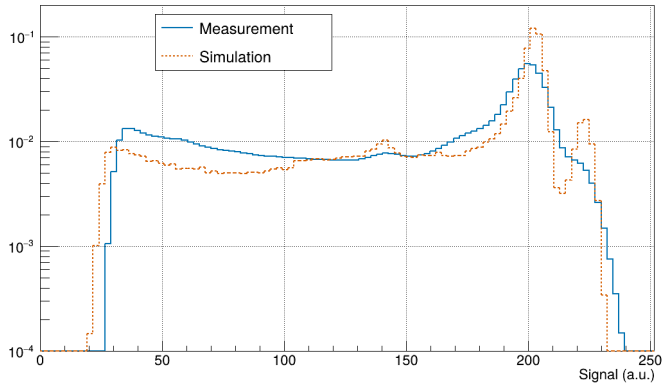

Figure 5.12: Comparison between the seed pixel simulated spectra of $^{55}_{26}$Fe Kα (5.9 keV) and Kβ (6.5 keV) emissions with the babyMOSS measured spectrum from [87].

$^{55}_{26}$Fe emissions, which is more visible in the spectrum without noise shown in fig. 5.11. The same feature was also observed in some of the XRF measurements presented in chapter 4, adding an unknown background component in the peak energy range, which makes it incompatible with a Gaussian fit function. Hence the understanding of the source of such a shoulder in the distribution is of particular interest and is discussed in the following section.

5.3.2.1 Signal dependence on the photon absorption position

The correlation between the location where the energy is released, defined as the mean position of the released charge cloud, and the location where the signal is collected by the pixel is studied to understand the origin of some spectrum features, including the shoulder for signal values just below the main peaks.

The contribution of signals originated in the substrate consists in a continuous background extending up to below the main $^{55}_{26}$Fe emission, as it can be see in fig. 5.13, while the rest of the pixel contributes both to the background range and to the emission peaks, as expected from previous studies [154]. The electronic noise is not added to

the spectrum to better resolve the spectrum features.

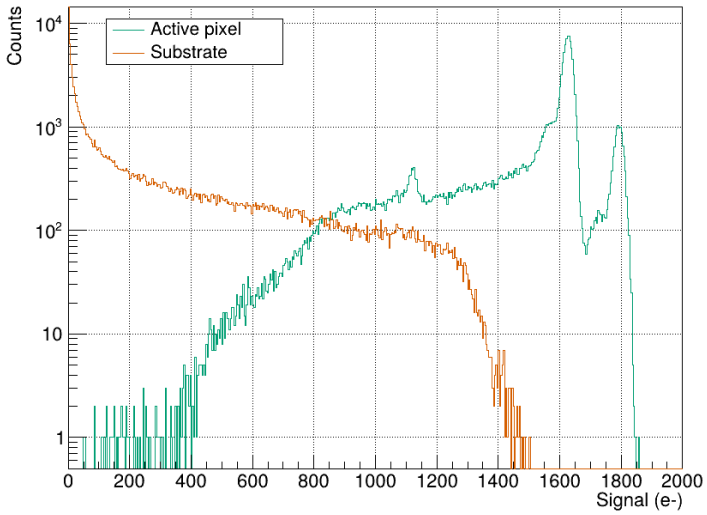

Figure 5.13: Substrate and active volume contributions to the simulated seed pixel spectra of $^{55}_{26}$Fe.

The contributions coming from the implants at the top of the pixel as schematised in fig. 5.3, from the deep p-well and from the collection electrode, respectively, are shown in fig. 5.14. The peaks in the spectrum of the deep p-well is systematically shifted downwards with respect to the spectrum of the active volume, which is comprising the epitaxial layer, the additional n-type implant and the substrate. Similarly, signals generated inside the collection electrode are shifted downwards the actual position of the peak.

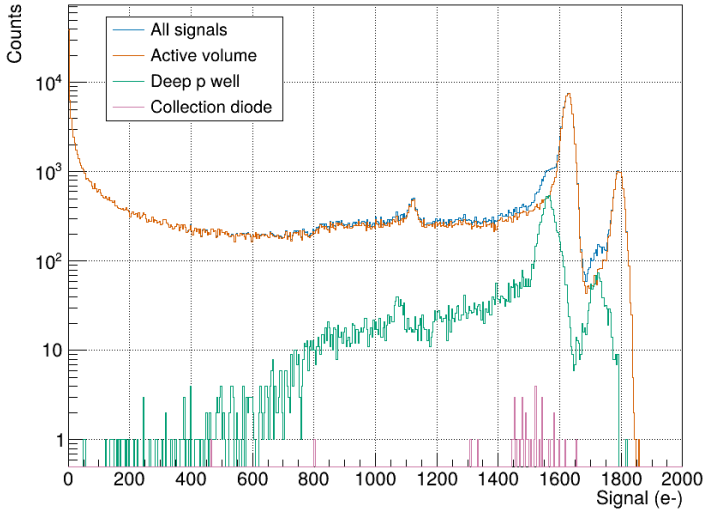

Figure 5.14: Implants contribution to the seed pixel simulated spectra of $^{55}_{26}$Fe.

The possible reason of the shift of the spectra is further investigated by looking

at the transport of the signal electrons and holes in the pixel. Fig. 5.15a shows an example of the transport of electrons and holes generated in the epitaxial layer, in the ideal case. The electrons drift to the collection electrode, while the holes drift towards the substrate, where they keep moving by diffusion only. The corresponding generated signal shown in blue in fig. 5.15b is equal to the sum of the electron and hole signals in amplitude and shorter than 1 ns in duration. As expected from their reduced mobility, holes, compared to electrons, contribute with a longer signal.

Instead, when the charge release happens in the deep p-well as shown in fig 5.16a, the electrons drift to the collection electrode, while the holes remain inside the deep p-well. The total signal, shown in fig 5.16b, is equal to the electron signal and is about ten times longer than the signal observed for energy depositions in the epitaxial layer. The spectrum shift towards lower values might be related to the recombination in the heavily doped layers of some of the generated electrons that are slowly moving by diffusion.

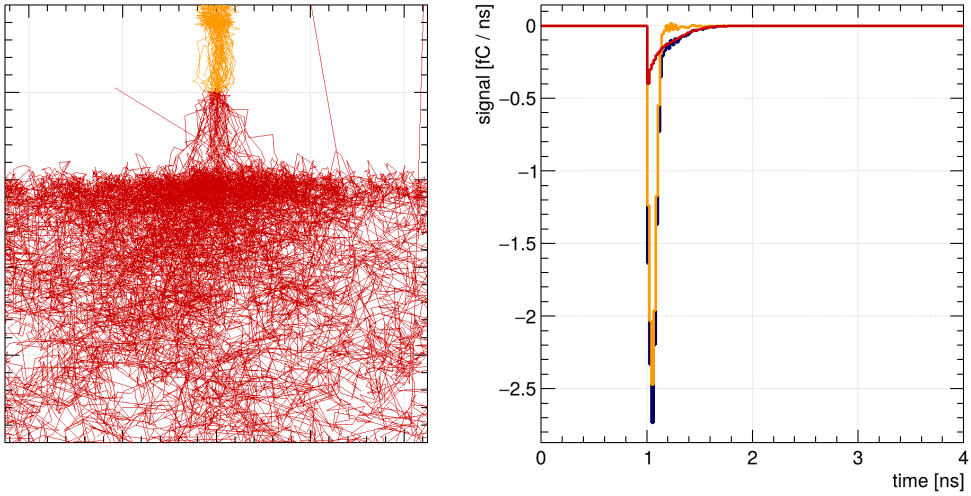

(a) (b)

Figure 5.15: 2D projection of drift and diffusion (a) of electrons (orange) and holes (red) in the pixel generated by an energy deposition in the epitaxial layer and the corresponding signal (b). In blue the total signal. Only a small fraction of electrons and holes are shown in the left plot for visualisation purposes.

The same behaviour is observed for the energy deposition happening in the collection electrode, asshown in fig. 5.17a. However, in this case the electrons are not subject to drift, as they are immediately collected, while the holes drift towards the substrate. The resulting signal, shown in fig. 5.17b, is equal to the hole signal with a small contribution from the electrons. The duration of the signal is doubled with the respect to the ideal case of an energy deposition in the epitaxial layer.

Finally, when the charge is released in the substrate as shown in fig. 5.18, only electrons diffused to the epitaxial layer contribute to the total signal. The duration of the signal is two order of magnitude larger than the duration of the signal of a charge release in the epitaxial layer.

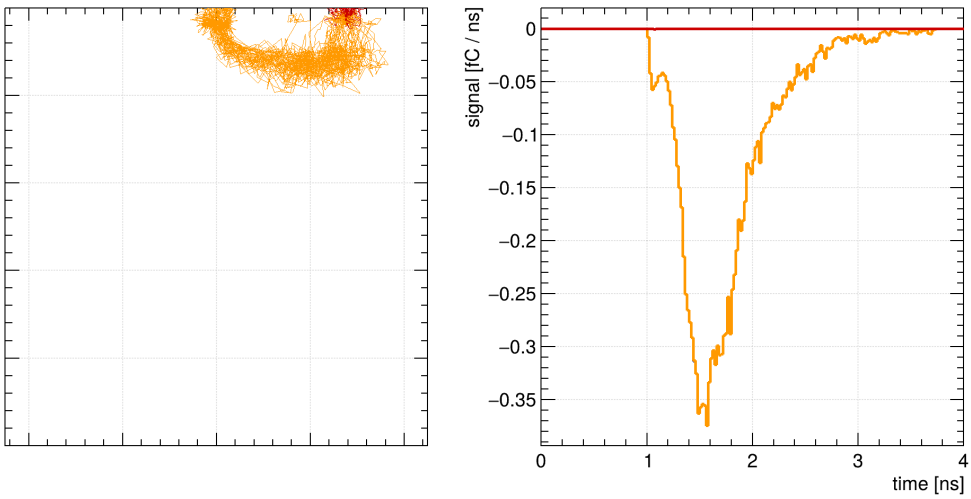

(a) (b)

Figure 5.16: 2D projection of drift and diffusion (a) of electrons (orange) and holes (red) in the pixel generated by an energy deposition in the deep p-well and the corresponding signal (b). The total signal correspond to the electron signal. Only a small fraction of electrons and holes are shown in the left plot for visualisation purposes.

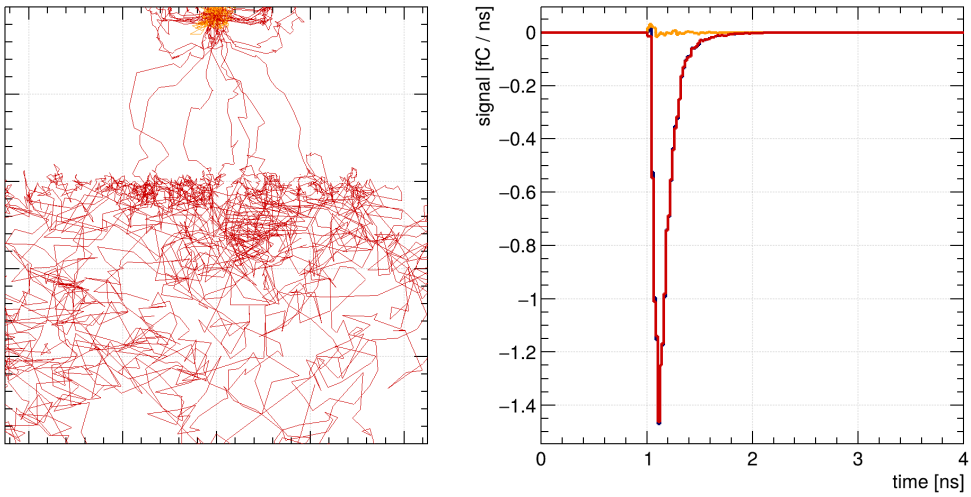

(a) (b)

Figure 5.17: 2D projection of drift and diffusion (a) of electrons (orange) and holes (red) in the pixel generated by an energy deposition in the collection electrode and the corresponding signal (b). In blue the total signal, mostly corresponding to the signal of the holes. Only a small fraction of electrons and holes are shown in the left plot for visualisation purposes.

5.3.3 XRF measurement simulation

As shown in [87], the babyMOSS energy calibration was obtained from XRF measurements performed at the OptImaTo source using targets producing fluorescence up to 43.0 keV (gadolinium Kα emission). A gradual loss of linearity was observed starting at

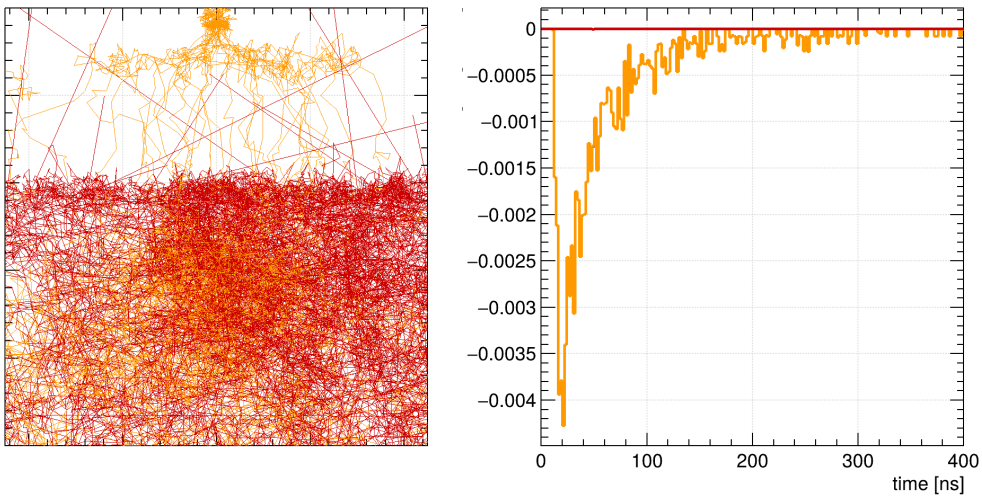

(a) (b)

Figure 5.18: 2D projection of drift and diffusion (a) of electrons (orange) and holes (red) in the pixel generated by an energy deposition in the substrate and the corresponding signal (b). The total signal corresponds to the one of the electrons. Note that the time scale of the signals is two orders of magnitude larger than in the previous plots. Only a small fraction of electrons and holes are shown in the left plot for visualisation purposes.

21.2 keV. To understand whether this effect was caused by charge-collection processes, such as the long path of photoelectrons in silicon relative to the pixel dimensions or partial energy loss in the substrate, or, alternatively, by an in-pixel circuit limitation, a dedicated simulation study is performed. A matrix of 5×5 babyMOSS pixels, including the full substrate, is implemented in Garfield++ to simulate the signals corresponding to the main measured energy-loss peaks, which are reported in tab. 5.1 along with their corresponding energies.

Table 5.1: Energies of the characteristic peaks [147] of the targets used at the laboratory OptImaTo to characterise the babyMOSS energy response.

Peak	Energy (keV)
Ti Kα	4.51
Mn Kα	5.90
Pb Lα	10.55
Pd Kα	21.18
Sn Kα	25.27
Ba Kα	32.19
Gd Kα	43.00

The simulated spectra of the seed pixels are shown in fig. 5.19 for all considered energies. In the simulations, the threshold is set to zero, and no electronic noise was added, since noise affects only the peak width and not its mean, which is the quantity of interest for the simulation of the energy calibration. The overall shape of the spectra resembles the iron source measurement presented in the previous section, with a con-

tinuous exponential background extending up to the main peak at large signal values. For lower-energy emissions, a small secondary peak appears at below the mean peak energy, corresponding to the silicon escape peak also observed in the iron spectrum. The simulated spectra are not directly compared with experimental data, because the measured spectra include a significant background contribution from the composition of the primary beam used to excite the fluorescence photons.

A Gaussian fit is applied to the main peak of each spectrum to extract its mean position and derive the energy calibration. The resulting calibration from the simulation is shown in fig. 5.20, together with the experimentally measured values for comparison. While the simulation preserves linearity across the full energy range, the measurements clearly show the previously mentioned gradual deviation from linearity, indicating that this effect is not related to the charge collection process but rather to limitations in the in-pixel circuitry.

5.3.4 Helium and carbon ions energy-loss simulations

A dedicated test beam at the GSI/FAIR facility with a mixed helium-carbon ion beam, discussed in sec. 4.3, was performed and a saturation of the signal response was observed. A simulation is carried out using a 5×5 matrix of babyMOSS pixels, including the full substrate, to investigate whether saturation effects originate from the pixel charge collection. Both helium and carbon ions at 225 MeV/amu, corresponding to total energies of 0.9 GeV and 2.7 GeV respectively, are simulated to study the energy-loss spectrum in the sensor.

Figure 5.21 shows the energy loss spectra of the seed pixels for helium (a) and carbon (b) ions. The spectra are well reproduced by a Landau distribution convoluted with a Gaussian, in agreement with theoretical expectations (see Sec. 4.1.1.3), except for the left side of the spectra, where an additional contribution builds up. The average energy loss in the epitaxial layer estimated from tabulated data is expected to be 31 keV for helium and 276 keV for carbon.

The simulated mean energy loss for helium ions is found to be consistent with the expected value, with a mean of 31 keV. For carbon ions, however, the simulated mean

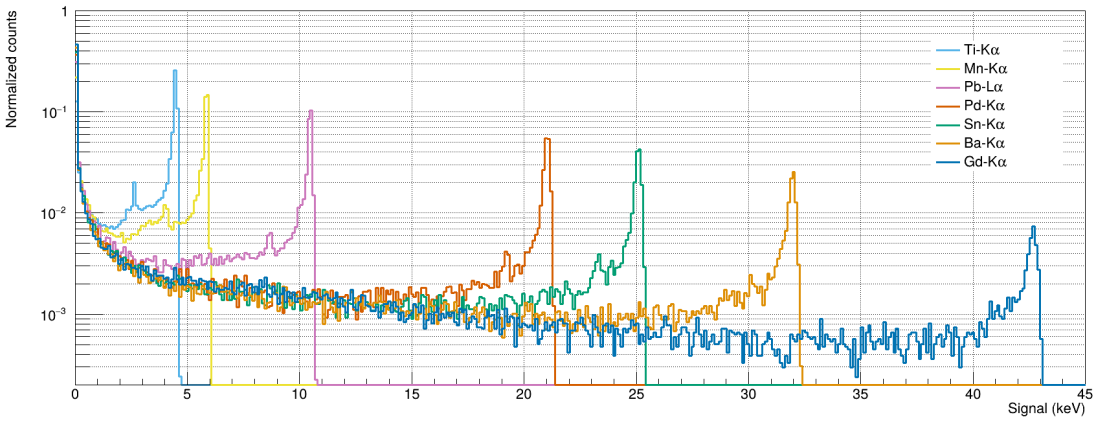

Figure 5.19: Simulation of the seed pixel emission spectra measured at the OptIMaTo laboratory using the babyMOSS sensor, corresponding to the peaks reported in Tab. 5.1.

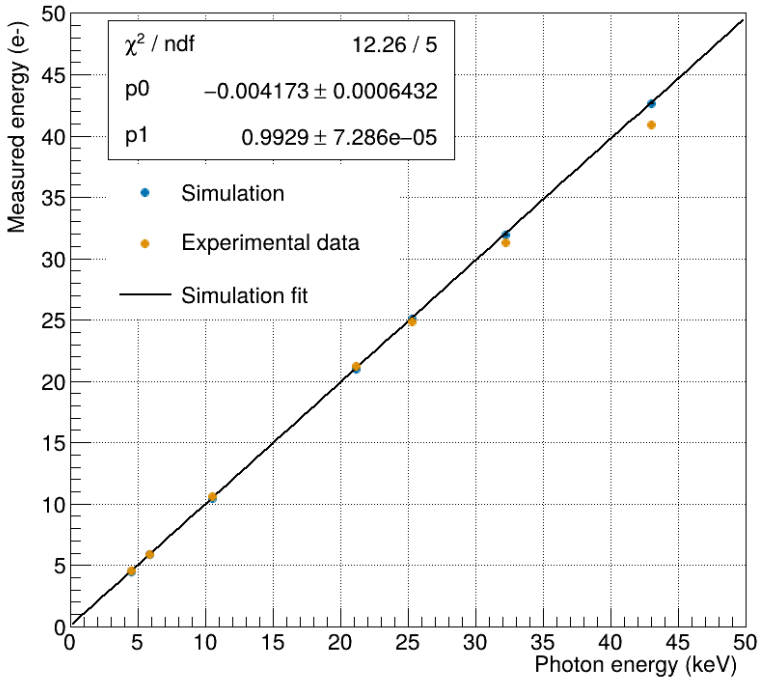

Figure 5.20: Comparison of the energy calibration obtained from the simulated spectra with the experimental measurements. The mean position of the main peak in each seed pixel simulated spectrum was determined via a Gaussian fit. While the simulation preserves linearity across the full energy range, the measured values show a gradual deviation from linearity.

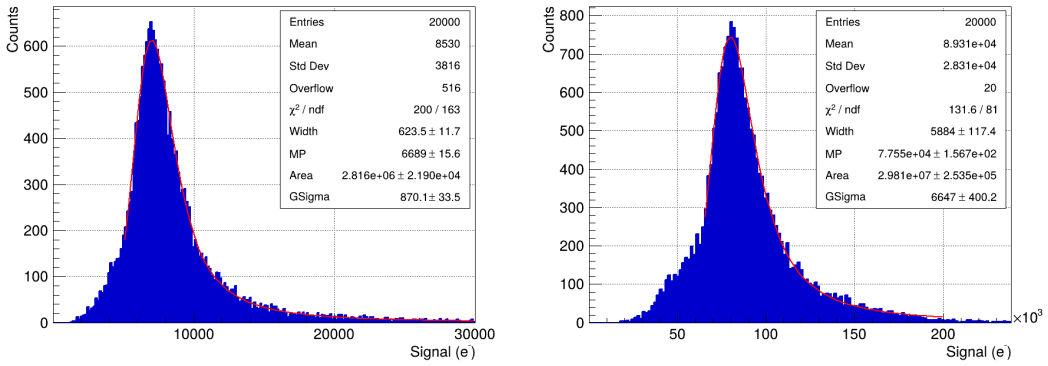

(a) (b)

Figure 5.21: Simulated energy-loss spectra of helium (a) and carbon (b) ions at 225 GeV/amu in a 5×5 babyMOSS pixel matrix. The distributions are fitted with a convolution of a Landau with a Gaussian function.

energy loss is higher than the tabulated prediction, resulting in an average value of 322 keV. This excess can be explained by an additional contribution from the substrate, which increases the total collected signal. The higher ionisation density produced by carbon ions enhances the probability of diffusion of charge carriers from the substrate into the epitaxial layer, effectively extending the charge collection volume of the pixel

matrix.

The Most Probable Value (MPV) obtained from the fits is (24.08 ± 0.06) keV for helium and (279.2 ± 0.6) keV for carbon. These values can be compared with the experimental MPVs presented in sec. 4.3.3, which are (22.1 ± 0.5) keV for helium and (77.9 ± 0.7) keV for carbon. Although slightly lower, the measured helium value is consistent with the simulated result. In contrast, the measured carbon MPV is significantly lower than the simulation, proving that a saturation of the detector response is occurring already at energies below 80 keV.

As for the measurements discussed in the previous section, Garfield++ has the limitation of not accounting for variations in the pixel electric field induced by large charge deposits, since the simulation must remain computationally efficient. For this reason, the results are further investigated using TCAD transient simulations, which include the full electric field evolution and allow a more accurate evaluation of the detector response.

5.3.5 TCAD simulation of large charge deposits

TCAD was exploited to simulate large charge deposits, taking into account the possible modifications to the electric field induced by the generated charge carriers. Transient simulations are performed for local energy deposits up to 300 keV, allowing for a time-dependent evaluation of all relevant pixel properties, including the electric field distribution and the charge carrier density. The main drawback of this approach is the considerably longer computation time, which limits the simulation to a single charge deposition event at a given energy. Nevertheless, this method provides a more realistic description of the detector response under high ionisation conditions, complementing the results obtained with Garfield++.

The absolute value of the signals simulated with TCAD on the collection electrode are shown in fig. 5.22 for different energy deposits. The signals are generated by a localised charge deposition at the centre of the epitaxial layer, representing the ideal case of signal formation. As expected, both the signal amplitude and its width increase with the deposited energy.

As an example, figs. 5.23 and 5.24 show the time evolution of the electron density distribution in the pixel for 10 keV and 100 keV energy deposits, respectively. The maps are shown every 0.2 ns, illustrating the gradual collection of the generated charge. In agreement with the signal durations discussed above, for a 10 keV deposit the charge is collected after about 1.6 ns, while for 100 keV this occurs after approximately 2 ns.

The time evolution of the electric field was also investigated and is shown in fig. 5.25 and 5.26. The frames correspond to the initial time steps of those presented previously for the electron density distribution. Fewer frames are displayed, since the effect of the deposited charge on the electric field is visible only during the early stages of the signal formation.

The signals shown in fig. 5.22 are integrated to obtain an energy calibration of the sensor, allowing to assess whether the observed modifications of the electric field affect the collected charge. The result of the calibration is shown in Fig. 5.27 and exhibits linearity, demonstrating that charge deposits up to 300 keV do not significantly impact the electric field and therefore do not alter the signal collection.

This finding supports the validity of the results obtained with the Garfield++ simulations in the previous sections and indicates that, in principle, these sensors can

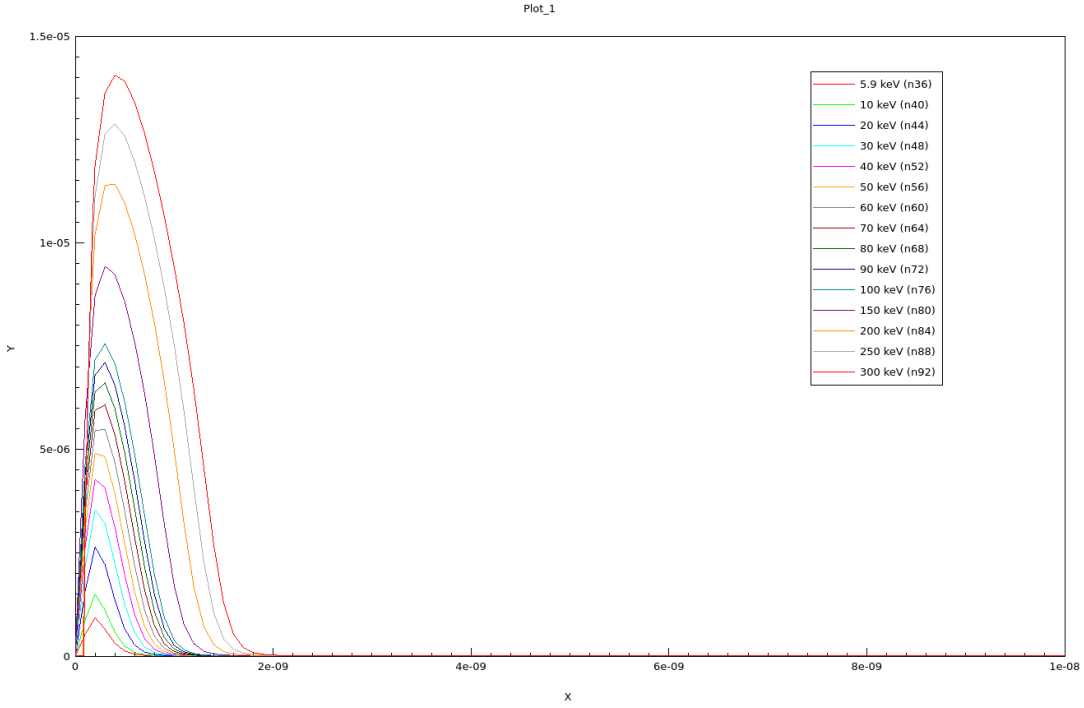

Figure 5.22: Absolute value of the signals simulated with TCAD on the collection electrode for various deposited energies in different colours, as a function of time (expressed in seconds). The signal amplitude and width increase with energy.

be employed for precise energy measurements, with the practical limitation being the potential saturation of the in-pixel circuitry.

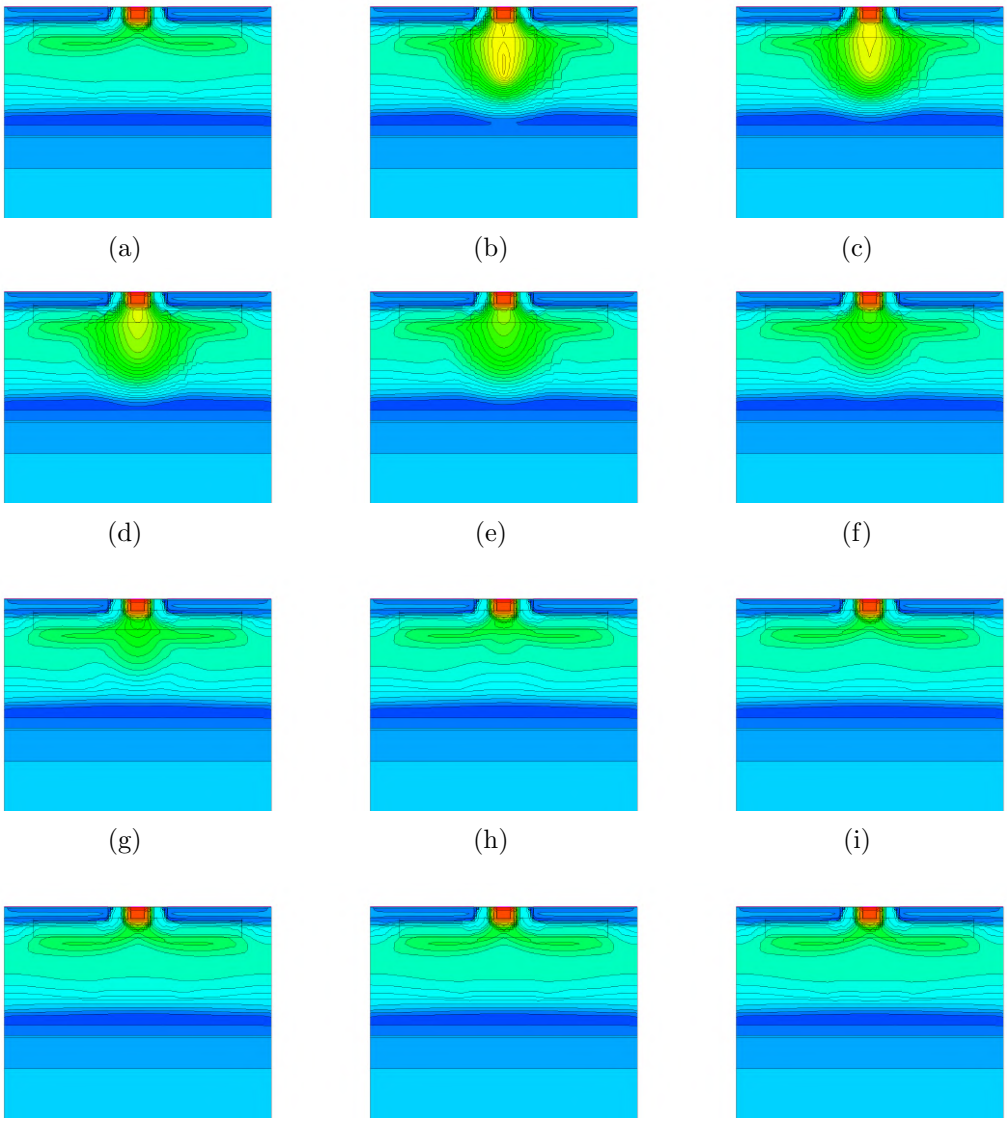

Figure 5.23: Temporal evolution of the simulated electron density in a babyMOSS pixel after a simulation of a 10 keV charge release in the middle of the epitaxial layer. The frames are taken every 0.2 ns. The simulation is not based on actual doping profiles and geometry and implant depths are approximative.

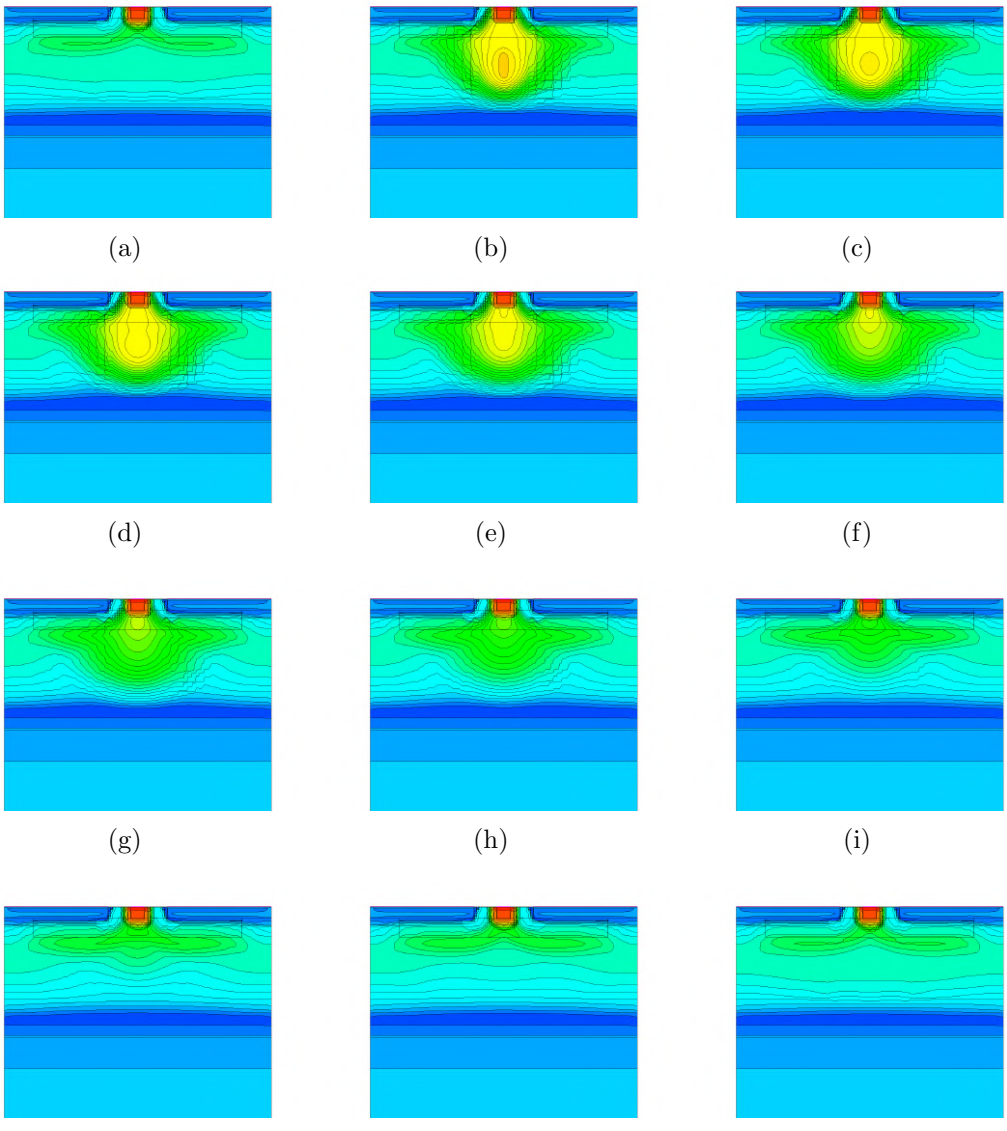

Figure 5.24: Temporal evolution of the simulated electron density in a babyMOSS pixel after a simulation of a 100 keV charge release in the middle of the epitaxial layer. The frames are taken every 0.2 ns. The simulation is not based on actual doping profiles and geometry and implant depths are approximative.

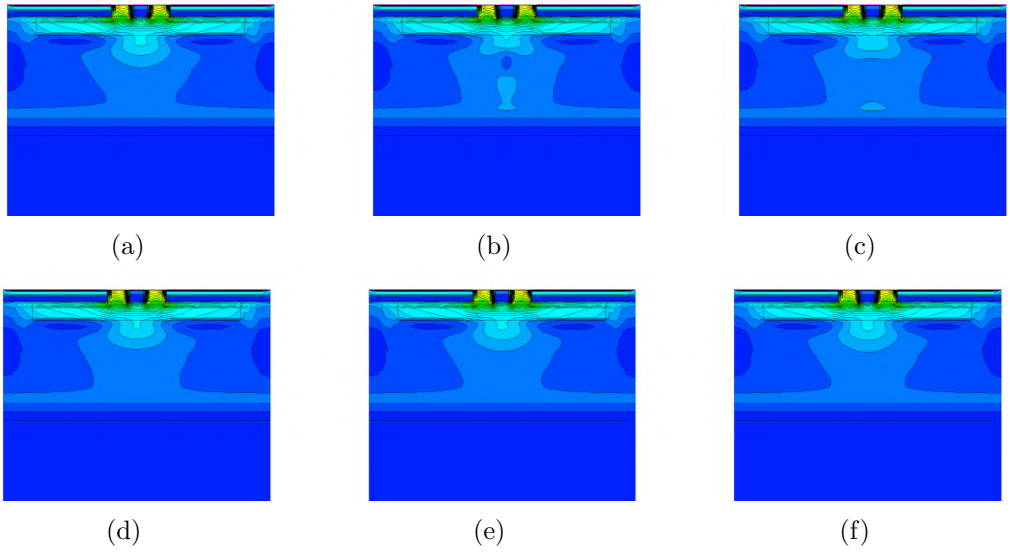

Figure 5.25: Temporal evolution of the simulated electric field in a babyMOSS pixel after a simulation of a 10 keV charge release in the middle of the epitaxial layer. The frames are taken every 0.2 ns. The simulation is not based on actual doping profiles and geometry and implant depths are approximative.

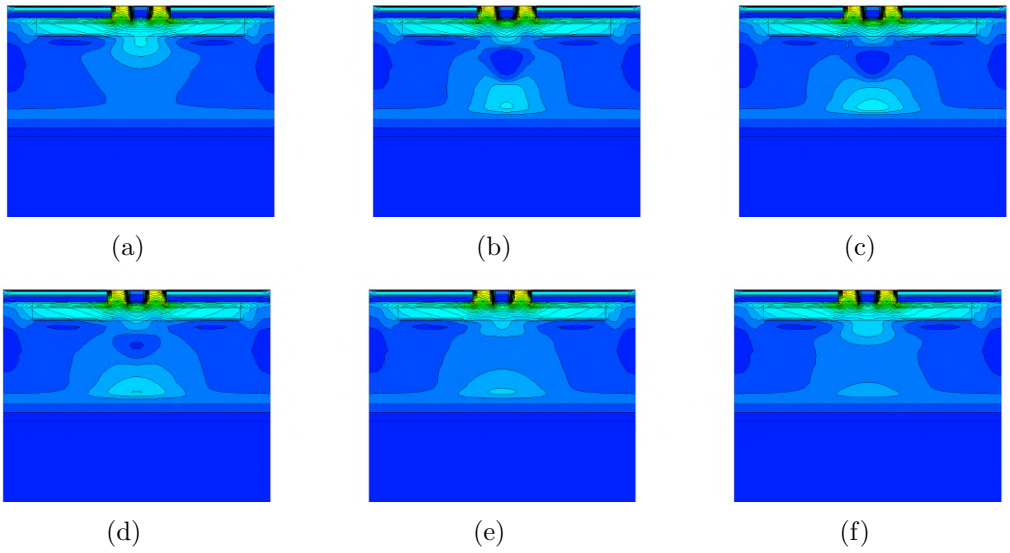

Figure 5.26: Temporal evolution of the simulated electric field in a babyMOSS pixel after a simulation of a 100 keV charge release in the middle of the epitaxial layer. The frames are taken every 0.2 ns. The simulation is not based on actual doping profiles and geometry and implant depths are approximative.

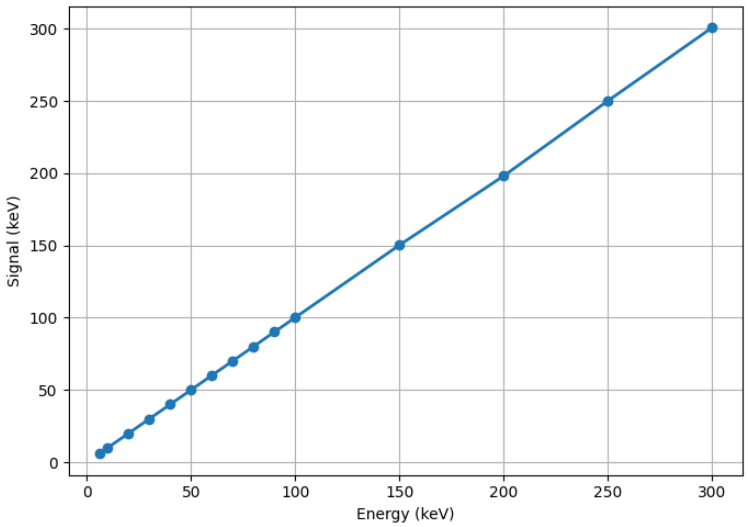

Figure 5.27: Energy calibration of the sensor obtained from TCAD simulations. The integrated signal amplitudes are plotted as a function of the deposited energy, showing a linear response up to 300 keV.

Chapter 6

Conclusions

The ALICE Inner Tracking System (ITS) will be upgraded to the ITS3 during the LHC long shutdown 3 (2026-2029). This upgrade will significantly enhance both the tracking efficiency and the pointing resolution, thereby improving the precision of measurements in the heavy-flavour sector and bringing another set of fundamental observables among the main objectives of the ALICE physics program into reach. These improvements will be achieved by positioning the new detector closer to the interaction point, from 22.4 mm to 19 mm, and by reducing the average material budget per layer, from 0.35% X_0 to 0.09% X_0. The ITS3 represents a benchmark application of the most advanced Monolithic Active Pixel Sensor (MAPS) technology. It will employ flexible, large-area MAPS sensors fabricated in the 65 nm CMOS imaging process and implementing a stitched design. With the aim of validating the application of stitching technology and 65 nm CMOS process to high-energy physics and to evaluate the performance and radiation hardness of the prototypes, an extensive characterisation campaign is being carried out.

This thesis aims to demonstrate the feasibility of an ultra-thin (50 μm) large-area (26×28 cm^2) MAPS detector realised in the 65 nm CMOS process to be operated in a tracker placed in a high radiation load environment. The complete characterisation of two ITS3 sensor prototypes, the Digital Pixel Test Structure (DPTS) and the MOnolithic Stitched Sensor (MOSS), was carried out through laboratory and in-beam measurements. Designed both to achieve a high detection efficiency with a fine granularity (pixel pitch $< 30\mu$m), the DPTS focuses on validating the 65 nm CMOS process, while the MOSS represents the first large-scale stitched MAPS to validate the stitching technique itself. Moreover, the energy-loss measurement capability, a specific feature of the DPTS and MOSS prototypes, which relies on encoding the analogue Time-over-Threshold (ToT) signal into the digital output, was exploited to complement and strengthen the standard laboratory and in-beam characterisation results. Although not foreseen to be featured in the final ITS3 sensor design, the study allowed for a better understanding of the signal generation and treatment in the CMOS sensor, while exploring the potential of these sensors for applications beyond high-energy physics. The experimental results were complemented by developing a simulation of the in-pixel charge collection process.

Within this thesis work, a dedicated software for sensor characterization was developed, and an exhaustive and comprehensive test procedure was defined to establish the optimal operating range for DPTS and MOSS. Laboratory measurements were used to define a preliminary threshold range satisfying the ITS3 fake-hit rate requirement

($< 10^{-1}$hit/pixel/s). Subsequently, the in-beam performance of a set of MOSS sensors has been evaluated in terms of detection efficiency as a function of the applied threshold. The radiation hardness of the ITS3 prototypes up to 1 Mrad of Total Ionising Dose (TID) and up to 10^{13} 1 MeV n_{eq} cm^{-2} Non Ionizing Energy Loss (NIEL), corresponding to the expected radiation load for the ITS3, has been studied. The results confirmed that all tested sensors maintained a detection efficiency above the required 99% in a threshold range of at least 20 e^-, thus demonstrating the radiation hardness of the ITS3 prototypes.

The origin of the noise affecting the prototype sensor performance was investigated. For the DPTS, the frequency-dependent *1/f* noise was identified as the dominant component for a small fraction ($< 5\%$) of the pixel matrix, which can be masked out in the analysis. In the MOSS, a pick-up noise was investigated and attributed to the electrical coupling between on-chip metal lines distributing the analogue bias and the acquisition window signal, providing important feedback to the chip designers in view of the final ITS3 sensor design.

The ToT measurement capability of the DPTS was exploited to study its response to X-rays over a broad energy range, using both radioactive sources such as $^{55}_{26}$Fe and $^{241}_{95}$Am, and fluorescence photons produced by XRF (X-Ray Fluorescence) targets of titanium, manganese, iron and tin illuminated with an X-ray beam. These measurements demonstrated the linearity of the DPTS energy response up to 28.5 keV. A similar XRF measurement campaign with photons up to 43.0 keV was conducted with the babyMOSS and showed that a gradual loss of linearity begins to appear at 21.2 keV. The ToT measurement capability featured by the babyMOSS was also investigated during a dedicated test beam at the GSI/FAIR facility with a mixed helium-carbon ion beam, demonstrating the babyMOSS potential use as a particle identification (PID) detector, while also revealing a saturation limit of the circuit response at around 80 keV injected energy.

Finally, TCAD simulations of the electric field inside DPTS-like and babyMOSS-like pixels were developed. The resulting fields were used in a custom Garfield++ simulation, implemented for this work, to model the charge collection process for X-rays and for minimum ionising particles and heavy ions. A simulation of the absorption of photons up to 43.0 keV was performed for comparison with the babyMOSS XRF measurements. The simulation showed a linear response, in contrast to the gradual loss of linearity observed experimentally, demonstrating that the non-linearity is likely due to in-pixel logic limitations related to the transistor operating range rather than to charge-collection effects. The measurements with helium and carbon ions were also reproduced in the simulation to determine whether the observed saturation could be attributed to charge-collection effects. The results indicate that the saturation is not caused by charge-collection limitations. Since Garfield++ does not account for potential modifications of the electric field within the pixel caused by a large energy deposition, a TCAD transient simulation was performed including energy losses in the epitaxial layer up to 300 keV, above the expected energy loss of the carbon ion in the ITS3 prototypes (270 keV). The simulation showed a linear response, demonstrating that energy depositions up to 300 keV do not distort the charge collection process.

Appendix A

X-ray fluorescence measurements

A.1 $^{241}_{95}$Am spectrum

The $^{241}_{95}$Am radioactive source spectrum is shown in fig. A.1. Four out of the six expected peaks that are reported in tab. 4.6 are visible: the neptunium $L\alpha$ characteristic peak is placed around 4000 mV, the neptunium $L\beta$ is peaked at ∼5000 mV, the neptunium Lγ emission is centred around 6000 mV and the neptunium transition $\gamma_{2,1}$ can be found around 7500 mV. The neptunium transitions $\gamma_{1,0}$ and $\gamma_{2,0}$, that have an energy higher than the other peaks, are not visible, possibly because of the exponentially decreasing detection efficiency of the thin silicon sensor for X-rays above 10 keV (see fig. 4.5b). A continuous background is visible, as in the $^{55}_{26}$Fe source and manganese target spectra, probably related to partial charge collection from the substrate.

The fits of the peaks are described in detail in the following.

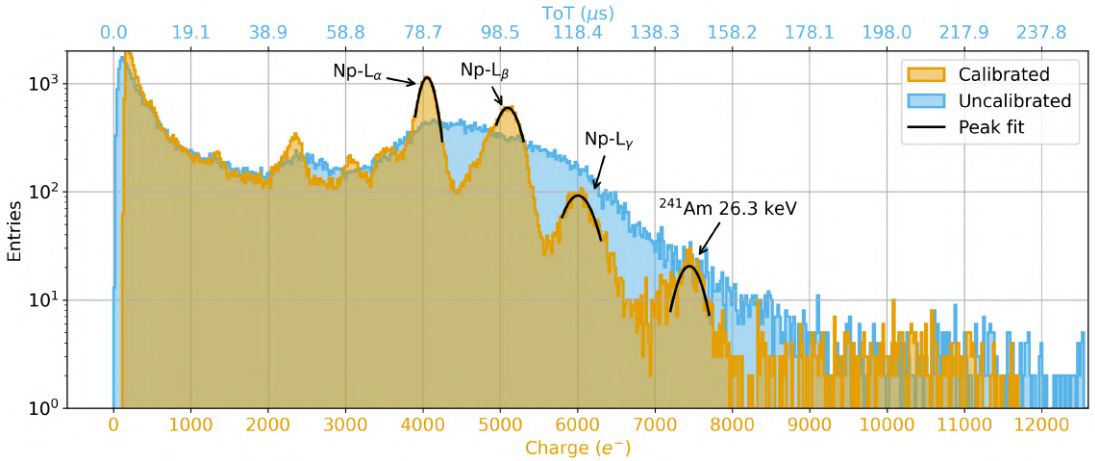

Figure A.1: Measured spectrum of an $^{241}_{95}$Am radioactive source. The neptunium characteristic emission peaks (Np-L$_\alpha$, Np-L$_\beta$, Np-γ_α and $\gamma_{2,1}$(Np)) are resolved. The most probable neptunium $\gamma_{2,0}$ at 59.5 keV is not visible, possibly because of the low detection efficiency for such photon energies.

Neptunium Lα, Lβ, Lγ, $\gamma_{2,1}$ The neptunium Lα, Lβ, Lγ and $\gamma_{2,1}$ peaks have an energy of 13.9 keV, 17.8 keV, 20.8 keV and 26.3 keV respectively. Each peak is fitted

with a Gaussian distribution (figd. A.2a, A.2b, A.2c and A.2d):

$$f(x) = A_1 \; e^{-\frac{(x-\mu_1)^2}{2\sigma_1^2}} \tag{A.1}$$

The background was not evaluated for these peaks, as their proximity prevents the selection of a region with only background and no signal on the sides of the peaks. However, the Gaussian distributions describe well the shape of the peaks, as can be seen from the reduced χ^2 in the plots in fig. A.2.

The variables of interest and the derived quantities for the neptunium emissions are reported in tab. A.1.

Table A.1: Summary of the key parameters of the peaks in the X-ray spectrum of an $^{241}_{95}$Am radioactive source.

Peak	Photon energy (keV)	μ (mV)	σ (mV)	Yield (%)	Energy resolution (%)
Np 1	13.90	4053.4 ± 1.4	119.9 ± 1.9	51.82 ± 0.48	6.95 ± 0.11
Np 2	17.80	5095.5 ± 3.9	172.3 ± 6.5	39.24 ± 0.40	7.95 ± 0.30
Np Lg	20.80	6005.2 ± 6.4	214.8 ± 9.2	7.55 ± 0.15	8.41 ± 0.36
Am 1	26.30	7445.3 ± 12.7	177.3 ± 18.9	1.39 ± 0.06	5.60 ± 0.60

Energy calibration with the $^{241}_{95}$Am spectrum The comparison between the mean peak position μ and the corresponding photon energy (see tab. A.1) is shown in fig. A.3 for the $^{241}_{95}$Am spectrum. The trend of the points deviates from the linear relation, especially at energies higher than 20 keV. This is possibly related to the low statistics of the two most energetic peaks and the absence of a background description for all the peaks.

A.2 Titanium-palladium target spectrum

The spectrum of fluorescence X-rays emitted from a target made by a foil of titanium and one of palladium which were placed side by side is shown in fig. A.4. The expected characteristic emission peak of titanium Ti-$K_{\alpha,\beta}$ is resolved between 1000 mV and 1200 mV, the characteristic emissions of palladium Pd-K_α and Pd-K_β can be found at ∼5400 mV and ∼6200 mV, respectively, while the palladium Pd-L_α is peaked around 800 mV. The silicon fluorescence peak is visible at ∼400 mV. Additional peaks in the spectrum between 1400 mV and 3000 mV are attributed to Compton and Rayleigh scattered X-rays from the primary beam. Since the exact energy of these scattered photons cannot be determined precisely, they are excluded in the following analysis. As observed in the previously discussed spectrum, a continuous background characterises the spectrum, possibly related to partial charge collection of photons that converted outside the depleted region of the sensor.

The fits of the peaks are described in detail in the following.

Silicon fluorescence peak from Ti-Pd target spectrum The silicon fluorescence, with an energy of 1.74 keV, is associated to the peak at ∼400 mV in the titanium-palladium spectrum. The fit of the signal and of the background is done as previously

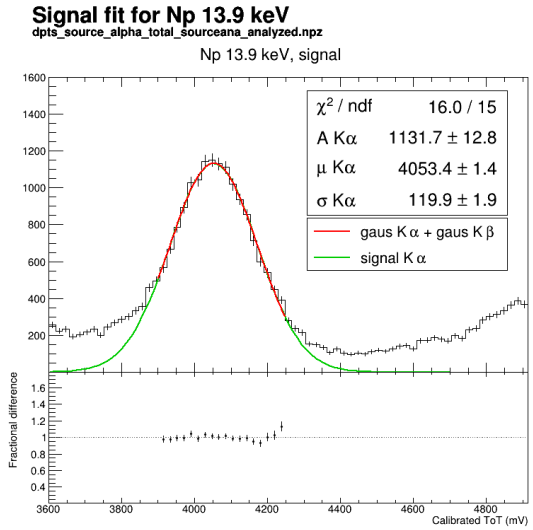

(a) Fit of the neptunium Lα peak in the spectrum of a $^{241}_{95}$Am radioactive source with a Gaussian distribution.

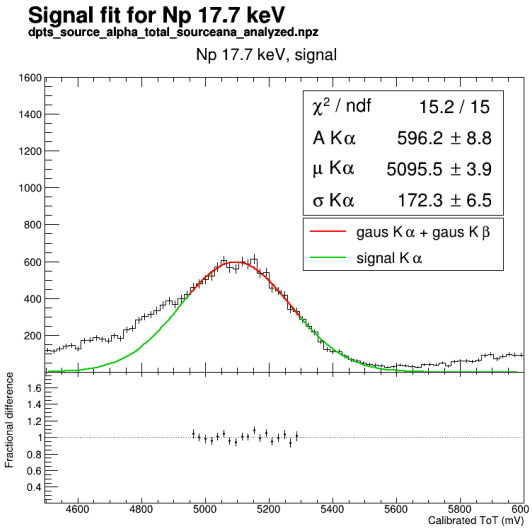

(b) Fit of the neptunium Lβ peak in the spectrum of a $^{241}_{95}$Am radioactive source with a Gaussian distribution.

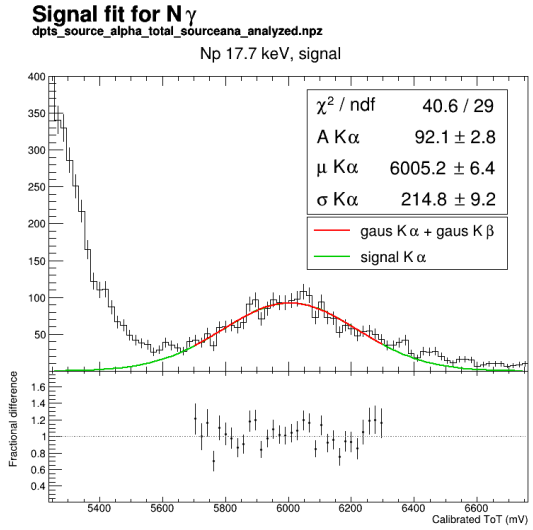

(c) Fit of the neptunium Lγ peak in the spectrum of a $^{241}_{95}$Am radioactive source with a Gaussian distribution.

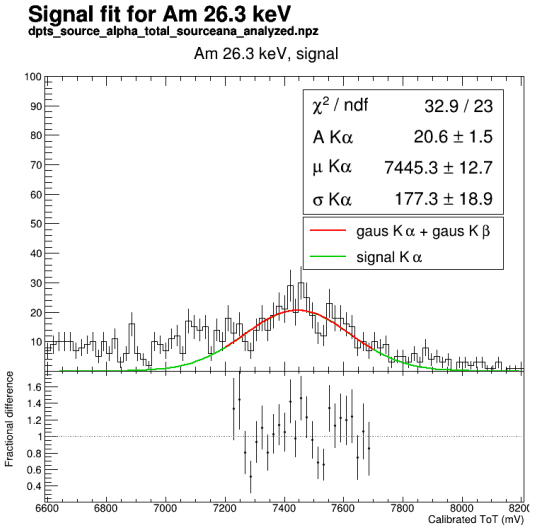

(d) Fit of the neptunium $\gamma_{2,1}$ peak in the spectrum of a $^{241}_{95}$Am radioactive source with a Gaussian distribution.

Figure A.2

discussed in sec. 4.2.3.1, using an exponential function for the background (fig. A.5 left) and a Gaussian distribution summed with the background for the signal (fig. A.5 right).

The variables of interest and the derived quantities for the silicon fluorescence peak are reported in tab. A.2.

Palladium Lα and Titanium Kα peaks from Ti-Pd target spectrum The palladium Lα emission has an energy of 2.84 keV and is associated to the peak at ∼800 mV in the palladium-titanium fluorescence spectrum, while the titanium Kα

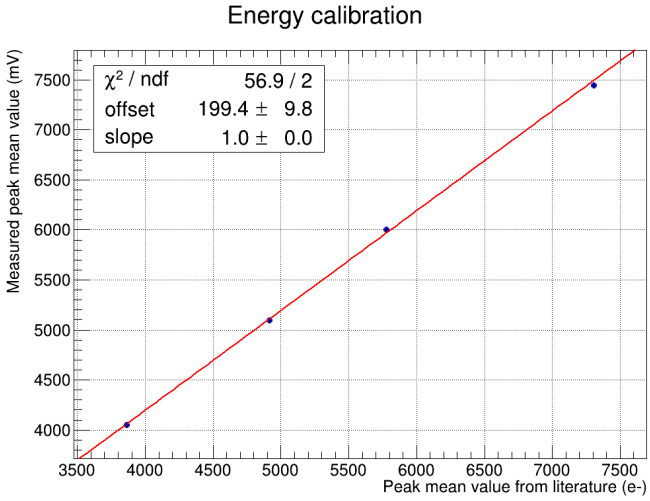

Figure A.3: Energy calibration plot for the $^{241}_{95}$Am spectrum.

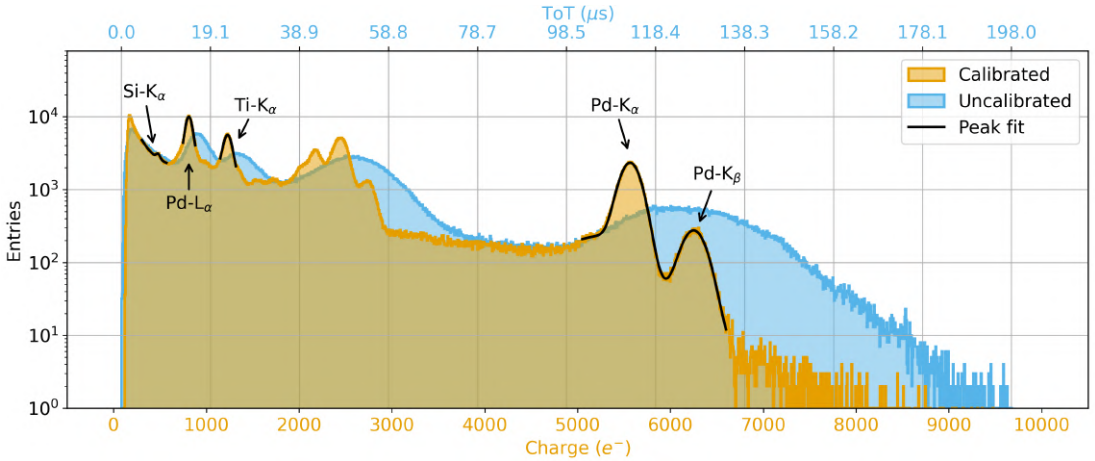

Figure A.4: Measured spectrum of fluorescence X-rays emitted from a palladium-titanium target. The titanium characteristic emission peak (Ti-K$_{\alpha,\beta}$), the palladium characteristic emission peaks (Pd-K$_\alpha$, Pd-K$_\beta$ and Pd-L$_\alpha$) and the silicon fluorescence peak (Si-K$_{\alpha,\beta}$) are resolved. Additional peaks in the spectrum are attributed to Compton and Rayleigh scattered X-rays from the primary beam.

emission has an energy of 4.51 keV, and is associated to the peak centred at ∼1200 mV. The same analysis applies to both peaks and is detailed below. The background that is underlying the peak is described by a linear function:

$$bkg(x) = p_0 + p_1 x \tag{A.2}$$

where p_0 and p_1 are the parameters to be estimated. The data in the side bands of the signal are fitted with this function, excluding the peak itself (fig. A.6 and fig. A.7 left). The signal is then fitted with the sum of a Gaussian distribution and the linear background which was previously evaluated (fig. A.6 and fig. A.7 right):

$$f(x) = bkg(x) + A\ e^{-\frac{(x-\mu)^2}{2\sigma^2}} \tag{A.3}$$

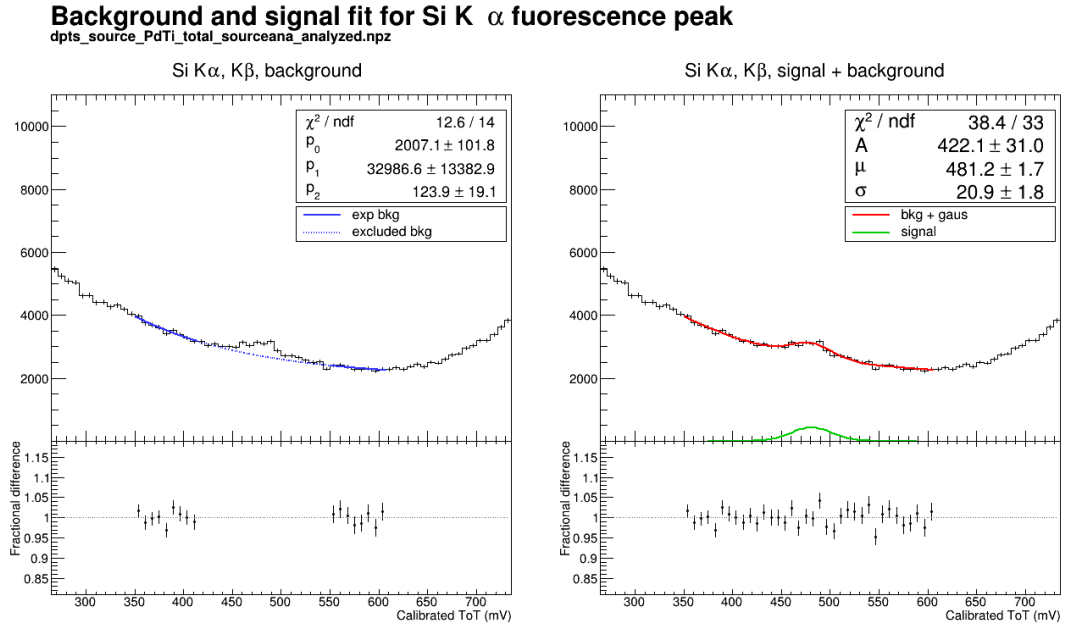

Figure A.5: Fit of exponential background (left) and sum of background and signal (right) for the silicon fluorescence peak in the spectrum of fluorescence X-rays emitted from a titanium-palladium target. The data under the dashed line was excluded in the fit of the background.

The variables of interest and the derived quantities for the palladium Lα and the titanium Kα peaks are reported in tab. A.2.

Palladium Kα and Kβ peaks from Ti-Pd target spectrum The palladium Kα and Kβ emissions have an energy of 21.2 keV and 23.8 keV, respectively, and are associated to the two rightmost peaks in the calibrated spectrum from the titanium-palladium target. An exponential background has been considered:

$$bkg(x) = p_0 + p_1 \; e^{-\frac{x}{p_2}} \tag{A.4}$$

which was used to fit the sidebands of the signals (fig. A.8 left). Below the two characteristic palladium emissions, a third broad peak is visible. This feature of the spectrum is possibly related to Compton scattered photon of the primary beam. Thus, the signal is fitted with a sum of three Gaussian distributions (fig. A.8 right):

$$f(x) = bkg(x) + A_1 \; e^{-\frac{(x-\mu_1)^2}{2\sigma_1^2}} + A_2 \; e^{-\frac{(x-\mu_2)^2}{2\sigma_2^2}} + A_3 \; e^{-\frac{(x-\mu_3)^2}{2\sigma_3^2}} \tag{A.5}$$

The variables of interest and the derived quantities for the palladium Kα and Kβ peaks are reported in tab. A.2.

Energy calibration with the Ti-Pd target spectrum The mean peak position μ as a function of the detected photon energy (see tab. A.2) is shown in fig. A.9 for the titanium-palladium target spectrum.

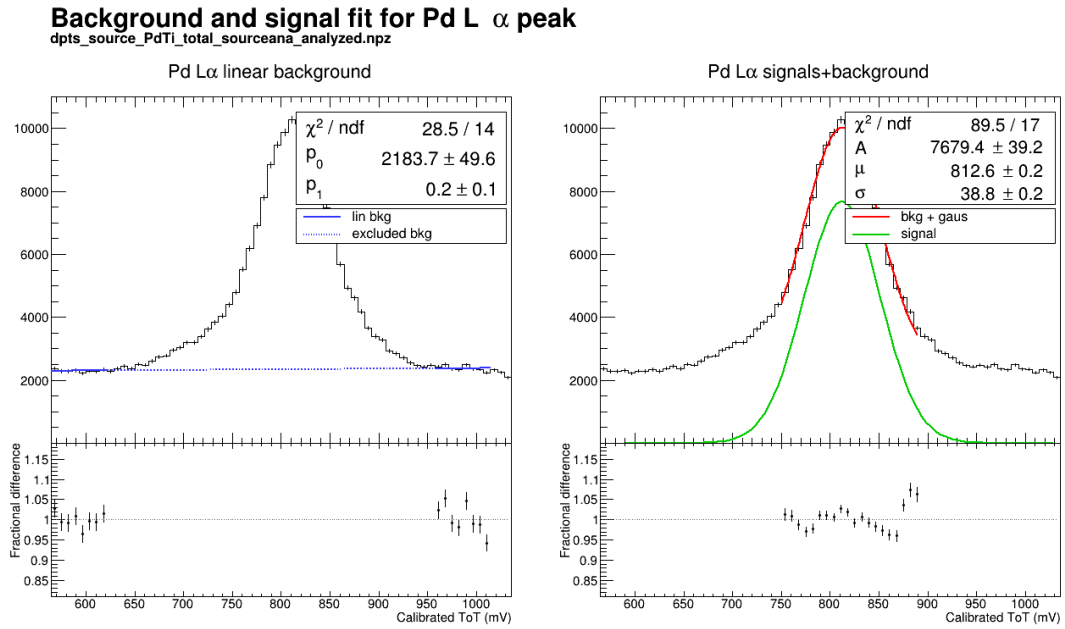

Figure A.6: Fit of linear background (left) and sum of background and signal (right) for the palladium Lα peak in the spectrum of fluorescence X-rays emitted from a titanium-palladium target. The data under the dashed line was excluded in the fit of the background.

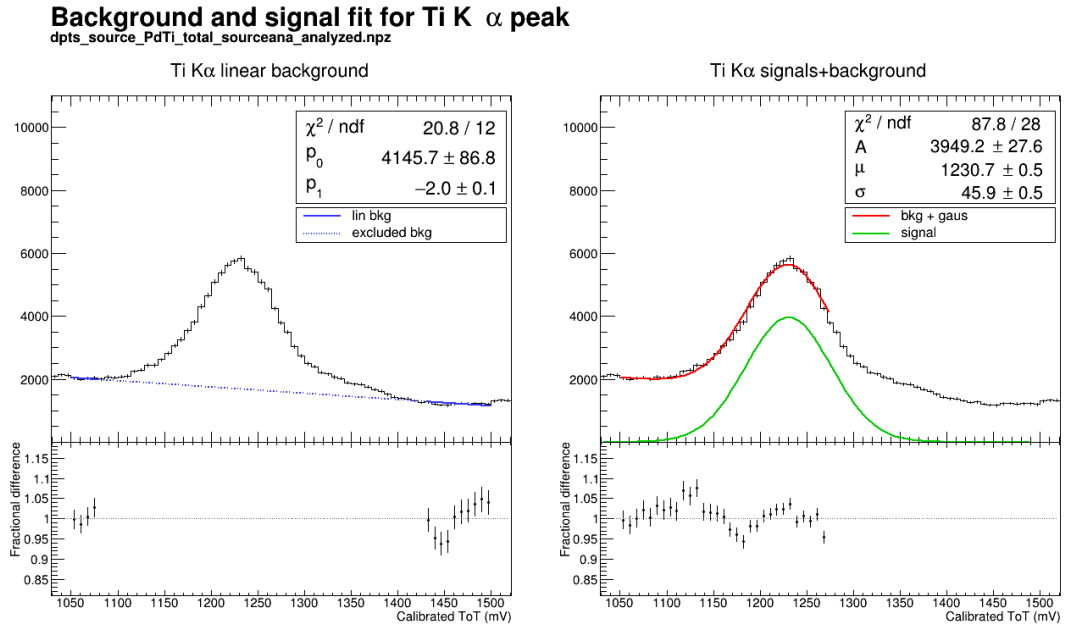

Figure A.7: Fit of linear background (left) and sum of background and signal (right) for the titanium Kα peak in the spectrum of fluorescence X-rays emitted from a titanium-palladium target. The data under the dashed line was excluded in the fit of the background.

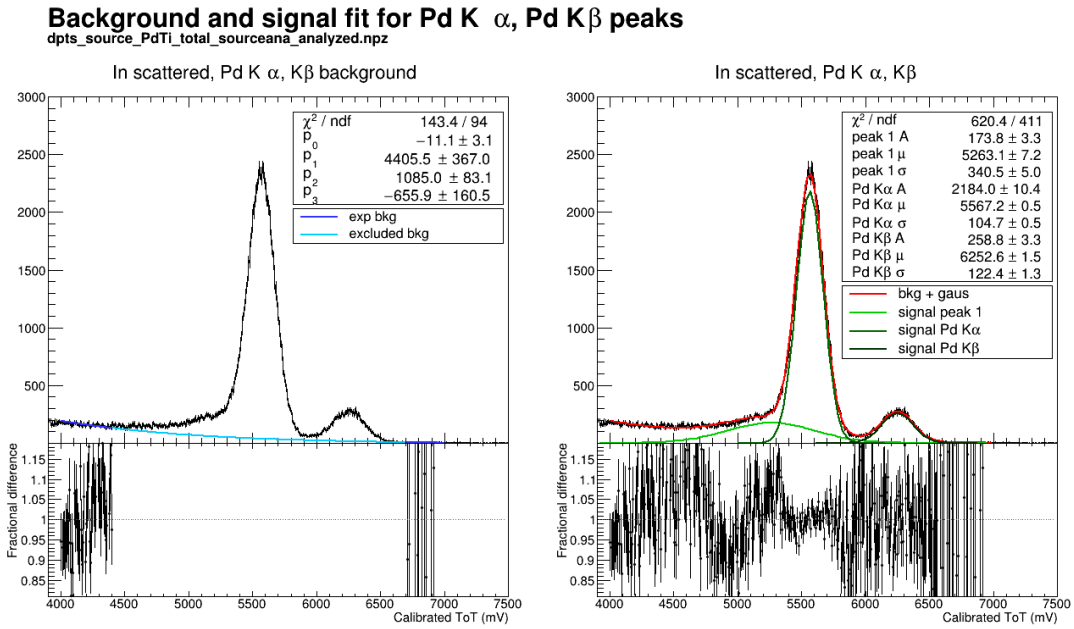

Figure A.8: Fit of the exponential background (left) and sum of background and three Gaussian distribution (right) for the palladium Kα and Kβ peaks in the spectrum of fluorescence X-rays emitted from a titanium-palladium target. The data under the dashed line was excluded in the fit of the background. The broadest Gaussian distribution fits a peak which is possibly related to Compton scattered X-rays from the primary source.

Table A.2: Summary of the key parameters of the peaks in the spectrum of fluorescence X-ray emitted by a titanium-palladium target.

Peak	Photon energy (keV)	μ (mV)	σ (mV)	Yield (%)	Energy resolution (%)
Si Ka	1.74	481.2 ± 1.7	20.9 ± 1.8	1.18 ± 0.02	10.18 ± 0.89
Pd La	2.84	812.6 ± 0.2	38.8 ± 0.2	39.81 ± 0.15	11.22 ± 0.06
Ti Ka	4.51	1230.7 ± 0.5	45.9 ± 0.5	24.22 ± 0.11	8.76 ± 0.10
Pd Ka	21.20	5567.2 ± 0.5	104.7 ± 0.5	30.56 ± 0.12	4.42 ± 0.02
Pd Kb	23.80	6252.6 ± 1.5	122.4 ± 1.3	4.23 ± 0.04	4.60 ± 0.05

A.3 Direct beam spectrum

The spectrum of the direct beam of the OptImaTo X-ray source is shown in fig. A.10. Out of the six characteristics peaks of the primary beam (see tab. 4.7) only Ga-K$_\alpha$ and Ga-K$_\beta$ are resolved between 2200 mV and 3000 mV. A possible hint of indium K_α is visible around 6500 mV. The low statistics for the indium characteristic emission and the absence of the tin emission lines is attributable to the low rate of these emissions if compared to the ones of gallium in the primary beam (see fig. 4.11).

Ga-Kα and Ga-Kβ peaks from the direct beam spectrum The Ga-K$_\alpha$ and Ga-K$_\beta$ emissions have an energy of 9.2 keV and 10.3 keV, respectively. Below these two

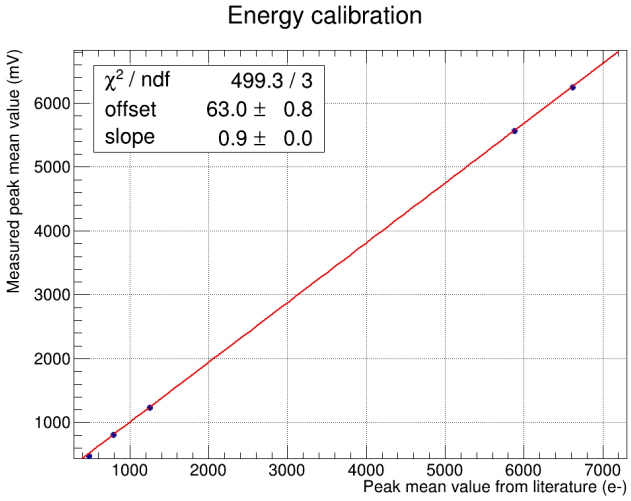

Figure A.9: Energy calibration plot for the titanium-palladium target spectrum.

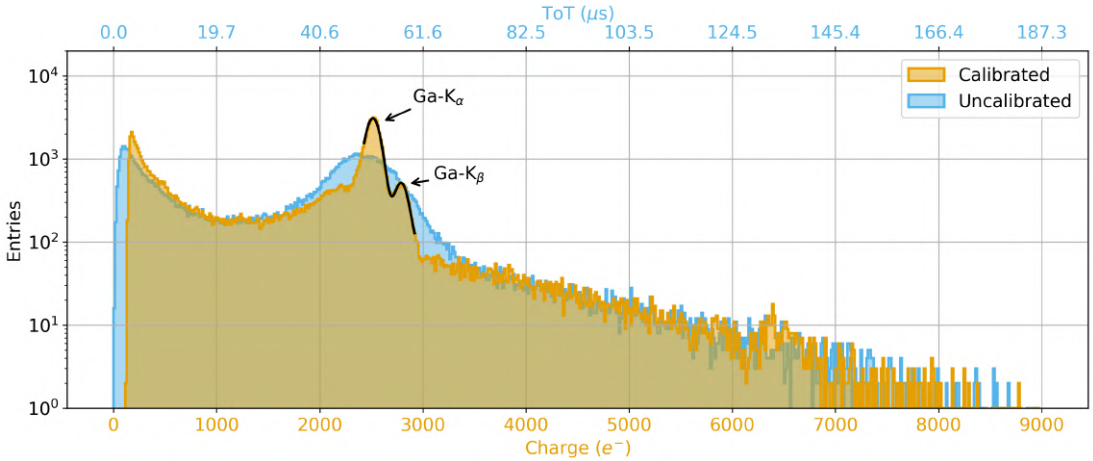

Figure A.10: Measured spectrum of the direct beam of the OptImaTo X-ray source. The gallium characteristic emission peaks (Ga-K$_\alpha$, Ga-K$_\beta$) are resolved. A possible hint of In-K_α is visible at around 6500 mV.

emissions a third broad peak is visible. It is included in the background description, that thus is parametrised with a sum of an exponential and a Gaussian function (fig. A.11 left):

$$bkg(x) = p_0 + p_1\ e^{-\frac{x}{p_2}} + p4\ e^{-\frac{(x-p5)^2}{2p6^2}} \tag{A.6}$$

The signals are then fitted with a sum of two Gaussian distributions on top of the background which was previously evaluated (fig. A.11 right):

$$f(x) = bkg(x) + A_1\ e^{-\frac{(x-\mu_1)^2}{2\sigma_1^2}} + A_2\ e^{-\frac{(x-\mu_2)^2}{2\sigma_2^2}} \tag{A.7}$$

The variables of interest and the derived quantities for the gallium Kα and Kβ peaks are reported in tab. A.3.

As there are only two points in the direct beam spectrum, the slope m and the

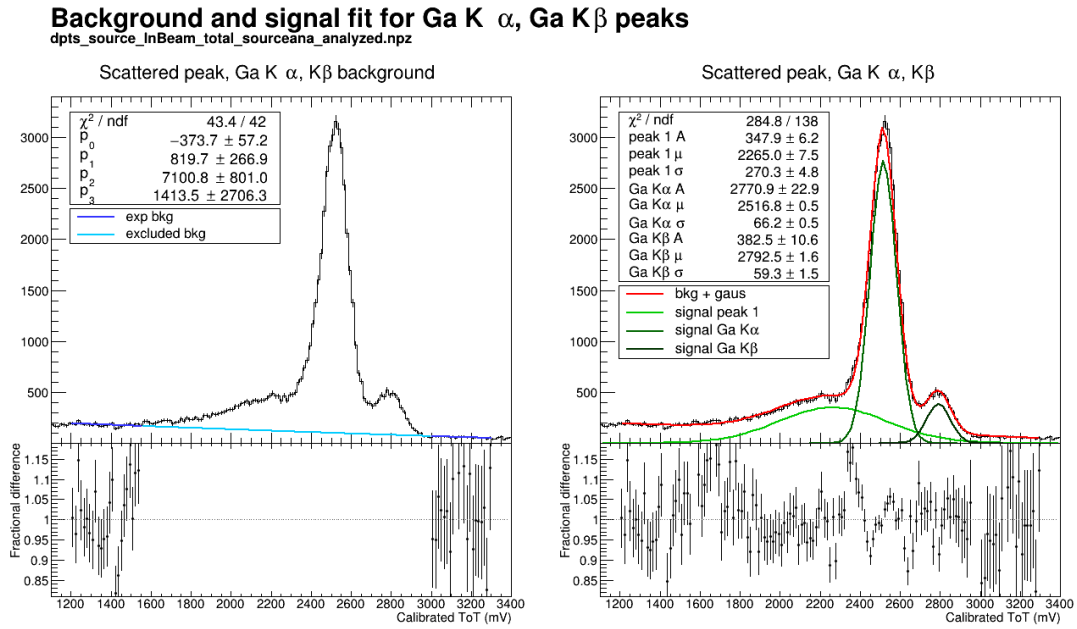

Figure A.11: Fit of the background with the sum of an exponential function and a Gaussian distribution (left) and sum of the background and three Gaussian distributions (right) for the gallium Kα and Kβ peaks in the spectrum of the direct beam of the OptImaTo X-ray source. The data under the dashed line was excluded in the fit of the background.

Table A.3: Summary of the key parameters of the peaks in the direct spectrum of the X-ray source at the OptImaTo laboratory.

Peak	Photon energy (keV)	μ (mV)	σ (mV)	Yield (%)	Energy resolution (%)
Ga Ka	9.25	2516.8 ± 0.5	66.2 ± 0.5	33.89 ± 0.31	6.18 ± 0.05
Ga Kb	10.26	2792.5 ± 1.6	59.3 ± 1.5	66.11 ± 0.47	4.99 ± 0.13

offset q for the energy calibration have been computed directly as:

$$m = \frac{\mu_{Ga-K\beta} - \mu_{Ga-K\alpha}}{E_{Ga-K\beta} - E_{Ga-K\alpha}} \tag{A.8}$$

$$q = \mu_{Ga-K\alpha} - m \cdot E_{Ga-K\alpha} \tag{A.9}$$

where $E_{Ga-K\alpha}$ and $E_{Ga-K\alpha}$ are the energies of the Ga-Kα and Ga-Kβ photons, respectively. The errors have been computed using the error propagation rules and the final results are:

$$m = (274.0 \pm 1.7) \text{ mV/keV} \tag{A.10}$$

$$q = (-16 \pm 15) \text{ keV} \tag{A.11}$$

Bibliography

[1] Frank Wilczek. "Quantum field theory". In: *Reviews of Modern Physics* 71.2 (Mar. 1999). Publisher: American Physical Society, S85–S95. DOI: 10.1103/RevModPhys.71.S85.

[2] The ALICE Collaboration. "The ALICE experiment at the CERN LHC". In: *Journal of Instrumentation* 3.08 (2008), S08002–S08002. DOI: 10.1088/1748-0221/3/08/s08002. URL: https://doi.org/10.1088/1748-0221/3/08/s08002 (visited on 06/08/2025).

[3] Particle Data Group *et al.* "Review of Particle Physics". In: *Progress of Theoretical and Experimental Physics* 2022.8 (Aug. 2022), p. 083C01. ISSN: 2050-3911. DOI: 10.1093/ptep/ptac097. eprint: https://academic.oup.com/ptep/article-pdf/2022/8/083C01/49175539/ptac097.pdf.

[4] David J. Gross and Frank Wilczek. "Ultraviolet Behavior of Non-Abelian Gauge Theories". In: *Physical Review Letters* 30.26 (June 1973). Publisher: American Physical Society, pp. 1343–1346. DOI: 10.1103/PhysRevLett.30.1343.

[5] H. David Politzer. "Reliable Perturbative Results for Strong Interactions?" In: *Physical Review Letters* 30.26 (June 1973). Publisher: American Physical Society, pp. 1346–1349. DOI: 10.1103/PhysRevLett.30.1346.

[6] Kenneth G. Wilson. "Confinement of quarks". In: *Physical Review D* 10.8 (Oct. 1974). Publisher: American Physical Society, pp. 2445–2459. DOI: 10.1103/PhysRevD.10.2445.

[7] Roman Pasechnik and Michal Šumbera. "Phenomenological Review on Quark–Gluon Plasma: Concepts vs. Observations". In: *Universe* 3.1 (Mar. 2017). Publisher: Multidisciplinary Digital Publishing Institute, p. 7. ISSN: 2218-1997. DOI: 10.3390/universe3010007.

[8] A. Bazavov et al. "Chiral crossover in QCD at zero and non-zero chemical potentials". In: *Physics Letters B* 795 (2019), pp. 15–21. ISSN: 0370-2693. DOI: https://doi.org/10.1016/j.physletb.2019.05.013.

[9] Eemeli Annala et al. "Evidence for quark-matter cores in massive neutron stars". In: *Nature Physics* 16.9 (Sept. 2020). Publisher: Nature Publishing Group, pp. 907–910. ISSN: 1745-2481. DOI: 10.1038/s41567-020-0914-9.

[10] Adam Bzdak et al. "Mapping the phases of quantum chromodynamics with beam energy scan". In: *Physics Reports*. Mapping the phases of quantum chromodynamics with beam energy scan 853 (Apr. 2020), pp. 1–87. ISSN: 0370-1573. DOI: 10.1016/j.physrep.2020.01.005.

[11] Mikhail Kapishin. "The fixed target experiment for studies of baryonic matter at the Nuclotron (BM@N)". In: *The European Physical Journal A* 52.8 (Aug. 2016), p. 213. ISSN: 1434-601X. DOI: 10.1140/epja/i2016-16213-0.

[12] V. Golovatyuk et al. "The Multi-Purpose Detector (MPD) of the collider experiment". In: *The European Physical Journal A* 52.8 (Aug. 2016), p. 212. ISSN: 1434-601X. DOI: 10.1140/epja/i2016-16212-1.

[13] T. Ablyazimov et al. "Challenges in QCD matter physics –The scientific programme of the Compressed Baryonic Matter experiment at FAIR". In: *The European Physical Journal A* 53.3 (Mar. 2017), p. 60. ISSN: 1434-601X. DOI: 10.1140/epja/i2017-12248-y.

[14] Enrico Scomparin. "The NA60+ experiment at the CERN SPS: physics goals and prospects". In: *PoS* HardProbes2020 (2021), p. 050. DOI: 10.22323/1.387.0050.

[15] Chiara De Martin. "Understanding the production mechanisms of particles with strangeness in pp collisions with the ALICE experiment at the LHC". PhD thesis. URL: https://repository.cern/records/27zwc-xjf23 (visited on 08/13/2025).

[16] Wit Busza, Krishna Rajagopal, and Wilke van der Schee. "Heavy Ion Collisions: The Big Picture and the Big Questions". In: *Annual Review of Nuclear and Particle Science* 68.Volume 68, 2018 (Oct. 2018). Publisher: Annual Reviews, pp. 339–376. ISSN: 0163-8998, 1545-4134. DOI: 10.1146/annurev-nucl-101917-020852.

[17] Peter Koch, Berndt Müller, and Johann Rafelski. "From strangeness enhancement to quark–gluon plasma discovery". In: *International Journal of Modern Physics A* 32.31 (Nov. 2017). Publisher: World Scientific Publishing Co., p. 1730024. ISSN: 0217-751X. DOI: 10.1142/S0217751X17300241.

[18] The ALICE Collaboration. "The ALICE experiment: a journey through QCD". In: *The European Physical Journal C* 84.8 (Aug. 2024), p. 813. ISSN: 1434-6052. DOI: 10.1140/epjc/s10052-024-12935-y.

[19] HotQCD Collaboration et al. "Equation of state in ($2+1$)-flavor QCD". In: *Physical Review D* 90.9 (Nov. 2014). Publisher: American Physical Society, p. 094503. DOI: 10.1103/PhysRevD.90.094503.

[20] S. Wheaton, J. Cleymans, and M. Hauer. *THERMUS*. arXiv:1108.4588 [hep-ph]. Aug. 2011. DOI: 10.48550/arXiv.1108.4588.

[21] Michal Petráň et al. "Hadron production and quark-gluon plasma hadronization in Pb-Pb collisions at $\sqrt{{s}_{\mathit{NN}}}=2.76$ TeV". In: *Physical Review C* 88.3 (Sept. 2013). Publisher: American Physical Society, p. 034907. DOI: 10.1103/PhysRevC.88.034907.

[22] Volodymyr Vovchenko and Horst Stoecker. "Thermal-FIST: A package for heavy-ion collisions and hadronic equation of state". In: *Computer Physics Communications* 244 (Nov. 2019), pp. 295–310. ISSN: 0010-4655. DOI: 10.1016/j.cpc.2019.06.024.

[23] A. Andronic, P. Braun-Munzinger, and J. Stachel. "Thermal hadron production in relativistic nuclear collisions: The hadron mass spectrum, the horn, and the QCD phase transition". In: *Physics Letters B* 673.2 (Mar. 2009), pp. 142–145. ISSN: 0370-2693. DOI: 10.1016/j.physletb.2009.02.014.

[24] The ALICE collaboration. "Performance of the ALICE VZERO system". In: *Journal of Instrumentation* 8.10 (Oct. 2013), P10016. ISSN: 1748-0221. DOI: 10.1088/1748-0221/8/10/P10016.

[25] Michael L. Miller et al. "Glauber Modeling in High-Energy Nuclear Collisions". In: *Annual Review of Nuclear and Particle Science* 57.Volume 57, 2007 (Nov. 2007). Publisher: Annual Reviews, pp. 205–243. ISSN: 0163-8998, 1545-4134. DOI: 10.1146/annurev.nucl.57.090506.123020.

[26] ALICE Collaboration. "Performance of the ALICE experiment at the CERN LHC". In: *International Journal of Modern Physics A* 29.24 (Sept. 2014). Publisher: World Scientific Publishing Co., p. 1430044. ISSN: 0217-751X. DOI: 10.1142/S0217751X14300440.

[27] ALICE Collaboration. "Centrality Dependence of the Charged-Particle Multiplicity Density at Midrapidity in Pb-Pb Collisions at $\sqrt{s_{\mathrm{NN}}} = 5.02$ TeV". In: *Physical Review Letters* 116.22 (June 2016). Publisher: American Physical Society, p. 222302. DOI: 10.1103/PhysRevLett.116.222302.

[28] Ulrich Heinz and Raimond Snellings. "Collective Flow and Viscosity in Relativistic Heavy-Ion Collisions". In: *Annual Review of Nuclear and Particle Science* 63.Volume 63, 2013 (Oct. 2013). Publisher: Annual Reviews, pp. 123–151. ISSN: 0163-8998, 1545-4134. DOI: 10.1146/annurev-nucl-102212-170540.

[29] Ekkard Schnedermann, Josef Sollfrank, and Ulrich Heinz. "Thermal phenomenology of hadrons from 200A GeV S+S collisions". In: *Physical Review C* 48.5 (Nov. 1993). Publisher: American Physical Society, pp. 2462–2475. DOI: 10.1103/PhysRevC.48.2462.

[30] ALICE Collaboration. "Multiplicity dependence of pion, kaon, proton and lambda production in p–Pb collisions at $\sqrt{s_{\mathrm{NN}}} = 5.02$ TeV". In: *Physics Letters B* 728 (Jan. 2014), pp. 25–38. ISSN: 0370-2693. DOI: 10.1016/j.physletb.2013.11.020.

[31] The ALICE collaboration. "Anisotropic flow of identified particles in Pb-Pb collisions at $\sqrt{s_{\mathrm{NN}}} = 5.02$ TeV". In: *Journal of High Energy Physics* 2018.9 (Sept. 2018), p. 6. ISSN: 1029-8479. DOI: 10.1007/JHEP09(2018)006.

[32] *ALICE figure repository*. URL: https://alice-figure.web.cern.ch/ (visited on 08/08/2025).

[33] K. Aamodt et al. "Suppression of charged particle production at large transverse momentum in central Pb–Pb collisions at $\sqrt{s_{\mathrm{NN}}} = 2.76$ TeV". In: *Physics Letters B* 696.1 (Jan. 2011), pp. 30–39. ISSN: 0370-2693. DOI: 10.1016/j.physletb.2010.12.020.

[34] The CMS Collaboration. "Study of high-pT charged particle suppression in PbPb compared to pp collisions at $\sqrt{s_{\mathrm{NN}}} = 2.76$ TeV". In: *The European Physical Journal C* 72.3 (Mar. 2012), p. 1945. ISSN: 1434-6052. DOI: 10.1140/epjc/s10052-012-1945-x.

[35] B. Abelev et al. "Transverse momentum dependence of inclusive primary charged-particle production in p–Pb collisions at $\sqrt{s_{\mathrm{NN}}} = 5.02$ TeV". In: *The European Physical Journal C* 74.9 (Sept. 2014), p. 3054. ISSN: 1434-6052. DOI: 10.1140/epjc/s10052-014-3054-5.

[36] STAR Collaboration. "Evidence from $d+Au$ Measurements for Final-State Suppression of High-p_{T} Hadrons in $Au+Au$ Collisions at RHIC". In: *Physical Review Letters* 91.7 (Aug. 2003). Publisher: American Physical Society, p. 072304. DOI: 10.1103/PhysRevLett.91.072304.

[37] The ALICE Collaboration. "The ALICE experiment at the CERN LHC". In: *Journal of Instrumentation* 3.08 (Aug. 2008), S08002. ISSN: 1748-0221. DOI: 10.1088/1748-0221/3/08/S08002.

[38] The ALICE Collaboration. "Upgrade of the ALICE Experiment: Letter Of Intent". In: *Journal of Physics G: Nuclear and Particle Physics* 41.8 (July 2014), p. 087001. ISSN: 0954-3899. DOI: 10.1088/0954-3899/41/8/087001.

[39] The ALICE Collaboration. "ALICE upgrades during the LHC Long Shutdown 2". In: *Journal of Instrumentation* 19.05 (May 2024). Publisher: IOP Publishing, P05062. ISSN: 1748-0221. DOI: 10.1088/1748-0221/19/05/P05062.

[40] The ALICE collaboration. *Technical Design report for the ALICE Inner Tracking System 3 - ITS3 ; A bent wafer-scale monolithic pixel detector*. 2024. URL: https://cds.cern.ch/record/2890181 (visited on 06/13/2024).

[41] *Technical Design Report of the ALICE Forward Calorimeter (FoCal)*. 2024. URL: https://cds.cern.ch/record/2890281 (visited on 08/16/2025).

[42] ALICE Collaboration. *Letter of intent for ALICE 3: A next generation heavy-ion experiment at the LHC*. Letter of Intent CERN-LHCC-2022-009, LHCC-I-038. 2022. URL: https://cds.cern.ch/record/2803563 (visited on 08/08/2025).

[43] *Technical Design Report for the Muon Forward Tracker*. 2015. URL: http://cds.cern.ch/record/1981898 (visited on 08/16/2025).

[44] *Upgrade of the ALICE Time Projection Chamber*. Tech. rep. 2013. URL: https://cds.cern.ch/record/1622286 (visited on 08/16/2025).

[45] "The ALICE Transition Radiation Detector: Construction, operation, and performance". In: *Nuclear Instruments and Methods in Physics Research Section A: Accelerators, Spectrometers, Detectors and Associated Equipment* 881 (Feb. 2018), pp. 88–127. ISSN: 0168-9002. DOI: 10.1016/j.nima.2017.09.028.

[46] *ALICE Time-Of-Flight system (TOF)*. 2000. URL: http://cds.cern.ch/record/430132 (visited on 08/16/2025).

[47] P Cortese. *ALICE Time-Of Flight system (TOF)*. Place: Geneva Series: Technical design report. ALICE. 2002. URL: http://cds.cern.ch/record/545834 (visited on 08/16/2025).

[48] François Piuz et al. *ALICE high-momentum particle identification*. Place: Geneva Series: Technical design report. ALICE. 1998. URL: https://cds.cern.ch/record/381431 (visited on 08/16/2025).

[49] P. Cortese et al. *ALICE Electromagnetic Calorimeter Technical Design Report*. 2008. URL: http://cds.cern.ch/record/1121574 (visited on 08/16/2025).

[50] J Allen et al. *ALICE DCal: An Addendum to the EMCal Technical Design Report Di-Jet and Hadron-Jet correlation measurements in ALICE*. 2010. URL: http://cds.cern.ch/record/1272952 (visited on 08/16/2025).

[51] V I Man'ko et al. *ALICE Photon Spectrometer (PHOS)*. Place: Geneva Series: Technical design report. ALICE. 1999. URL: https://cds.cern.ch/record/381432 (visited on 08/16/2025).

[52] *ALICE dimuon forward spectrometer*. Place: Geneva Series: Technical design report. ALICE. 1999. URL: https://cds.cern.ch/record/401974 (visited on 08/16/2025).

[53] Livia Terlizzi. "Operation and performance of the ALICE Muon IDentifier RPCs during LHC Run3". In: *Nuclear Instruments and Methods in Physics Research Section A: Accelerators, Spectrometers, Detectors and Associated Equipment* 1077 (Aug. 2025), p. 170518. ISSN: 0168-9002. DOI: 10.1016/j.nima.2025.170518.

[54] Wladyslaw Henryk Trzaska. "New Fast Interaction Trigger for ALICE". In: *Nuclear Instruments and Methods in Physics Research Section A: Accelerators, Spectrometers, Detectors and Associated Equipment*. Proceedings of the Vienna Conference on Instrumentation 2016 845 (Feb. 2017), pp. 463–466. ISSN: 0168-9002. DOI: 10.1016/j.nima.2016.06.029.

[55] G. Puddu et al. "The zero degree calorimeters for the ALICE experiment". In: *Nuclear Instruments and Methods in Physics Research Section A: Accelerators, Spectrometers, Detectors and Associated Equipment*. VCI 2007 581.1 (Oct. 2007), pp. 397–401. ISSN: 0168-9002. DOI: 10.1016/j.nima.2007.08.013.

[56] P Buncic, M Krzewicki, and P Vande Vyvre. *Technical Design Report for the Upgrade of the Online-Offline Computing System*. 2015. URL: https://cds.cern.ch/record/2011297 (visited on 08/16/2025).

[57] The ALICE Collaboration. "Technical Design Report for the Upgrade of the ALICE Inner Tracking System". In: *Journal of Physics G: Nuclear and Particle Physics* 41.8 (July 2014), p. 087002. ISSN: 0954-3899. DOI: 10.1088/0954-3899/41/8/087002.

[58] M. Šuljić. "ALPIDE: the Monolithic Active Pixel Sensor for the ALICE ITS upgrade". In: *J. Inst.* 11.11 (2016), p. C11025. DOI: 10.1088/1748-0221/11/11/c11025.

[59] Gianluca Aglieri Rinella. "The ALPIDE pixel sensor chip for the upgrade of the ALICE Inner Tracking System". In: *NIM-A* 845 (2017), pp. 583–587. ISSN: 0168-9002. DOI: 10.1016/j.nima.2016.05.016.

[60] M. Mager. "ALPIDE, the Monolithic Active Pixel Sensor for the ALICE ITS upgrade". In: *NIM-A* 824 (2016), pp. 434–438. ISSN: 0168-9002. DOI: 10.1016/j.nima.2015.09.057.

[61] The ALICE Collaboration. "Technical Design Report for the Upgrade of the ALICE Inner Tracking System". In: (2014). DOI: 10.1088/0954-3899/41/8/087002. URL: https://cds.cern.ch/record/1625842 (visited on 06/08/2025).

[62] J. Schambach et al. "A Radiation-Tolerant Readout System for the ALICE Inner Tracking System Upgrade". In: *2018 IEEE Nuclear Science Symposium and Medical Imaging Conference Proceedings (NSS/MIC)*. ISSN: 2577-0829. Nov. 2018, pp. 1–6. DOI: 10.1109/NSSMIC.2018.8824419.

[63] The ALICE Collaboration. *Expression of Interest for an ALICE ITS Upgrade in LS3*. 2018. URL: https://cds.cern.ch/record/2644611 (visited on 06/03/2025).

[64] The ALICE Collaboration. *Letter of Intent for an ALICE ITS Upgrade in LS3*. Letter of Intent CERN-LHCC-2019-018, LHCC-I-034. 2019. URL: https://cds.cern.ch/record/2703140 (visited on 06/03/2025).

[65] The ALICE Collaboration. *Upgrade of the ALICE Inner Tracking System during LS3: study of physics performance*. 2023. URL: https://cds.cern.ch/record/2868015 (visited on 06/03/2025).

[66] David d'Enterria and Constantin Loizides. "Progress in the Glauber Model at Collider Energies". In: *Annual Review of Nuclear and Particle Science* 71.Volume 71, 2021 (Sept. 2021). Publisher: Annual Reviews, pp. 315–344. ISSN: 0163-8998, 1545-4134. DOI: 10.1146/annurev-nucl-102419-060007.

[67] The ALICE Collaboration. "Measurement of prompt D_s^+-meson production and azimuthal anisotropy in Pb–Pb collisions at $\sqrt{s_{NN}}$=5.02 TeV". In: *Physics Letters B* 827 (Apr. 2022), p. 136986. ISSN: 0370-2693. DOI: 10.1016/j.physletb.2022.136986.

[68] The ALICE Collaboration. "Measurement of beauty-strange meson production in Pb–Pb collisions at $\sqrt{s_{NN}}$=5.02 TeV via non-prompt D_s^+ mesons". In: *Physics Letters B* 846 (Nov. 2023), p. 137561. ISSN: 0370-2693. DOI: 10.1016/j.physletb.2022.137561.

[69] The CMS Collaboration. "Observation of B_s^0 mesons and measurement of the B_s^0/B^+ yield ratio in Pb–Pb collisions at $\sqrt{s_{\mathrm{NN}}} = 5.02$ TeV". In: *Physics Letters B* 829 (June 2022), p. 137062. ISSN: 0370-2693. DOI: 10.1016/j.physletb.2022.137062.

[70] S. Plumari et al. "Charmed hadrons from coalescence plus fragmentation in relativistic nucleus-nucleus collisions at RHIC and LHC". In: *The European Physical Journal C* 78.4 (Apr. 2018), p. 348. ISSN: 1434-6052. DOI: 10.1140/epjc/s10052-018-5828-7.

[71] Anton Andronic et al. "The multiple-charm hierarchy in the statistical hadronization model". In: *Journal of High Energy Physics* 2021.7 (July 2021), p. 35. ISSN: 1029-8479. DOI: 10.1007/JHEP07(2021)035.

[72] Min He and Ralf Rapp. "Charm-baryon production in proton-proton collisions". In: *Physics Letters B* 795 (Aug. 2019), pp. 117–121. ISSN: 0370-2693. DOI: 10.1016/j.physletb.2019.06.004.

[73] P. Skands, S. Carrazza, and J. Rojo. "Tuning PYTHIA 8.1: the Monash 2013 tune". In: *The European Physical Journal C* 74.8 (Aug. 2014), p. 3024. ISSN: 1434-6052. DOI: 10.1140/epjc/s10052-014-3024-y.

[74] Jesper R. Christiansen and Peter Z. Skands. "String formation beyond leading colour". In: *Journal of High Energy Physics* 2015.8 (Aug. 2015), p. 3. ISSN: 1029-8479. DOI: 10.1007/JHEP08(2015)003.

[75] S. et all Acharya. "Constraining hadronization mechanisms with $^{+}_{c}$/D^{0} production ratios in Pb–Pb collisions at $\sqrt{s_{NN}}$=5.02 TeV". In: *Physics Letters B* 839 (Apr. 2023), p. 137796. ISSN: 0370-2693. DOI: 10.1016/j.physletb.2023.137796.

[76] A. M. et all Sirunyan. "Production of Λ_c^+ baryons in proton-proton and lead-lead collisions at $\sqrt{s_{NN}}$=5.02 TeV". In: *Physics Letters B* 803 (Apr. 2020), p. 135328. ISSN: 0370-2693. DOI: 10.1016/j.physletb.2020.135328.

[77] The LHCb collaboration. "Measurement of the Λ_c^+ to D^0 production ratio in peripheral Pb-Pb collisions at $\sqrt{s_{NN}}$=5.02 TeV". In: *Journal of High Energy Physics* 2023.6 (June 2023), p. 132. ISSN: 1029-8479. DOI: 10.1007/JHEP06(2023)132.

[78] S. et all Acharya. "Λ_c^+ production in Pb–Pb collisions at $\sqrt{s_{NN}}$=5.02 TeV". In: *Physics Letters B* 793 (June 2019), pp. 212–223. ISSN: 0370-2693. DOI: 10.1016/j.physletb.2019.04.046.

[79] STAR Collaboration. "First Measurement of Λ_c Baryon Production in $Au+Au$ Collisions at $\sqrt{s_{NN}}$=100 GeV". In: *Physical Review Letters* 124.17 (May 2020). Publisher: American Physical Society, p. 172301. DOI: 10.1103/PhysRevLett.124.172301.

[80] S. Holland and H. Spieler. "A monolithically integrated detector-preamplifier on high-resistivity silicon". In: *IEEE Transactions on Nuclear Science* 37.2 (Apr. 1990), pp. 463–468. ISSN: 1558-1578. DOI: 10.1109/23.106663.

[81] W. Snoeys et al. "A new integrated pixel detector for high energy physics". In: *IEEE Transactions on Nuclear Science* 39.5 (Oct. 1992). Conference Name: IEEE Transactions on Nuclear Science, pp. 1263–1269. ISSN: 1558-1578. DOI: 10.1109/23.173188.

[82] Michele Verdoglia. "Characterisation of bent Monolithic Active Pixel Sensors (MAPS) in 65 nm CMOS process for the ALICE ITS3". MA thesis. Trieste U., 2023.

[83] Gianluca Aglieri Rinella et al. "Digital pixel test structures implemented in a 65 nm CMOS process". In: *Nuclear Instruments and Methods in Physics Research Section A: Accelerators, Spectrometers, Detectors and Associated Equipment* 1056 (Nov. 2023), p. 168589. ISSN: 0168-9002. DOI: 10.1016/j.nima.2023.168589.

[84] Gianluca Aglieri Rinella et al. *Further Characterisation of Digital Pixel Test Structures Implemented in a 65 nm CMOS Process*. arXiv:2505.05867 [physics]. Oct. 2025. DOI: 10.48550/arXiv.2505.05867.

[85] Gianluca Aglieri Rinella et al. "A Compact Front-End Circuit for a Monolithic Sensor in a 65-nm CMOS Imaging Technology". In: *IEEE Transactions on Nuclear Science* 70.9 (Sept. 2023). Conference Name: IEEE Transactions on Nuclear Science, pp. 2191–2200. ISSN: 1558-1578. DOI: 10.1109/TNS.2023.3299333.

[86] Walter Snoeys et al. “Optimization of a 65 nm CMOS imaging process for monolithic CMOS sensors for high energy physics”. In: *Proceedings of 10th International Workshop on Semiconductor Pixel Detectors for Particles and Imaging — PoS(Pixel2022)*. Vol. 420. Conference Name: 10th International Workshop on Semiconductor Pixel Detectors for Particles and Imaging. SISSA Medialab, May 2023, p. 083. DOI: 10.22323/1.420.0083.

[87] Giovanni Vecil. “Characterisation of the energy response of Monolithic Active Pixel silicon Sensors”. MA thesis. Trieste U., 2025.

[88] Marius Wilm Menzel. “Energy-straggling analysis of the Digital Pixel Test Structure, a MAPS prototype produced in 65 nm TPSCo CMOS technology towards ALICE ITS3”. MA thesis.

[89] P. Ahlburg et al. “EUDAQ—a data acquisition software framework for common beam telescopes”. In: *J. Inst.* 15.01 (2020), P01038. DOI: 10.1088/1748-0221/15/01/p01038.

[90] D. Dannheim et al. “Corryvreckan: a modular 4D track reconstruction and analysis software for test beam data”. In: *J. Inst* 16.03 (2021), P03008. DOI: 10.1088/1748-0221/16/03/P03008.

[91] V. Blobel. “A new fast track-fit algorithm based on broken lines”. In: *NIM-A* 566.1 (2006), pp. 14–17. ISSN: 0168-9002. DOI: 10.1016/j.nima.2006.05.156.

[92] Gianluca Aglieri Rinella et al. “Characterization of analogue Monolithic Active Pixel Sensor test structures implemented in a 65 nm CMOS imaging process”. In: *Nuclear Instruments and Methods in Physics Research Section A: Accelerators, Spectrometers, Detectors and Associated Equipment* 1069 (Dec. 2024), p. 169896. ISSN: 0168-9002. DOI: 10.1016/j.nima.2024.169896.

[93] Håkan Wennlöf et al. “Simulating monolithic active pixel sensors: A technology-independent approach using generic doping profiles”. In: *NIM-A* 1073 (2025), p. 170227. ISSN: 0168-9002. DOI: 10.1016/j.nima.2025.170227.

[94] M. J. Buckingham. *Noise in electronic devices and systems*. Chichester [West Sussex, England] : E. Horwood ; New York : Halsted Press, 1983. URL: http://archive.org/details/noiseinelectroni0000buck.

[95] D. A. Bell. “Distribution Function of Semiconductor Noise”. In: *Proceedings of the Physical Society. Section B* 68.9 (Sept. 1955), p. 690. ISSN: 0370-1301. DOI: 10.1088/0370-1301/68/9/416.

[96] J. B. Johnson. “Thermal Agitation of Electricity in Conductors”. In: *Nature* 119.2984 (Jan. 1927). Publisher: Nature Publishing Group, pp. 50–51. ISSN: 1476-4687. DOI: 10.1038/119050c0.

[97] J. B. Johnson. “Thermal Agitation of Electricity in Conductors”. In: *Physical Review* 32.1 (July 1928). Publisher: American Physical Society, pp. 97–109. DOI: 10.1103/PhysRev.32.97.

[98] W. Schottky. “Über spontane Stromschwankungen in verschiedenen Elektrizitätsleitern”. In: *Annalen der Physik* 362.23 (1918), pp. 541–567. ISSN: 1521-3889. DOI: 10.1002/andp.19183622304.

[99] Frederick J. Beutler and Oscar A. Z. Leneman. “The spectral analysis of impulse processes”. In: *Information and Control* 12.3 (Mar. 1968), pp. 236–258. ISSN: 0019-9958. DOI: 10.1016/S0019-9958(68)90327-6.

[100] Helmuth Spieler. *Semiconductor Detector System*. Clarendon Press, Oxford, 2005.

[101] H. Schönfeld. "Beitrag zum 1/f-Gesetz beim Rauschen von Halbleitern". In: *Zeitschrift für Naturforschung A* 10.4 (Apr. 1955). Publisher: De Gruyter, pp. 291–300. ISSN: 1865-7109. DOI: 10.1515/zna-1955-0407.

[102] A. Van Der Ziel. "Flicker Noise in Electronic Devices". In: *Advances in Electronics and Electron Physics*. Ed. by L. Marton and C. Marton. Vol. 49. Academic Press, Jan. 1979, pp. 225–297. DOI: 10.1016/S0065-2539(08)60768-4.

[103] R. N. Hall. "Electron-Hole Recombination in Germanium". In: *Physical Review* 87.2 (July 1952). Publisher: American Physical Society, pp. 387–387. DOI: 10.1103/PhysRev.87.387.

[104] W. Shockley and W. T. Read. "Statistics of the Recombinations of Holes and Electrons". In: *Physical Review* 87.5 (Sept. 1952). Publisher: American Physical Society, pp. 835–842. DOI: 10.1103/PhysRev.87.835.

[105] Christian Monzio Compagnoni et al. "Statistical Model for Random Telegraph Noise in Flash Memories". In: *IEEE Transactions on Electron Devices* 55.1 (Jan. 2008). Conference Name: IEEE Transactions on Electron Devices, pp. 388–395. ISSN: 1557-9646. DOI: 10.1109/TED.2007.910605.

[106] V. Radeka. "Signal Processing for Particle Detectors". In: *Particle Physics Reference Library: Volume 2: Detectors for Particles and Radiation*. Ed. by Christian W. Fabjan and Herwig Schopper. Cham: Springer International Publishing, 2020, pp. 439–484. DOI: 10.1007/978-3-030-35318-6_10.

[107] F. S. Goulding and D. A. Landis. "Signal Processing for Semiconductor Detectors". In: *IEEE Transactions on Nuclear Science* 29.3 (June 1982). Conference Name: IEEE Transactions on Nuclear Science, pp. 1125–1141. ISSN: 1558-1578. DOI: 10.1109/TNS.1982.4336332.

[108] V. Radeka. "Optimum Signal-Processing for Pulse-Amplitude Spectrometry in the Presence of High-Rate Effects and Noise". In: *IEEE Transactions on Nuclear Science* 15.3 (June 1968). Conference Name: IEEE Transactions on Nuclear Science, pp. 455–470. ISSN: 1558-1578. DOI: 10.1109/TNS.1968.4324970.

[109] V. Radeka. "Signal, Noise and Resolution in Position-Sensitive Detectors". In: *IEEE Transactions on Nuclear Science* 21.1 (Feb. 1974). Conference Name: IEEE Transactions on Nuclear Science, pp. 51–64. ISSN: 1558-1578. DOI: 10.1109/TNS.1974.4327444.

[110] F. S. Goulding. "Pulse-shaping in low-noise nuclear amplifiers: A physical approach to noise analysis". In: *Nuclear Instruments and Methods* 100.3 (May 1972), pp. 493–504. ISSN: 0029-554X. DOI: 10.1016/0029-554X(72)90828-2.

[111] SciPy. URL: https://scipy.org/ (visited on 08/19/2024).

[112] *Candece Virtuoso*. URL: https://www.cadence.com/en_US/home.html (visited on 08/08/2025).

[113] William R. Leo. *Techniques for Nuclear and Particle Physics Experiments: A How-to Approach*. Berlin, Heidelberg: Springer Berlin Heidelberg, 1994. DOI: 10.1007/978-3-642-57920-2.

[114] Jens Lindhard and Allan H. So/rensen. “Relativistic theory of stopping for heavy ions”. In: *Physical Review A* 53.4 (Apr. 1996). Publisher: American Physical Society, pp. 2443–2456. DOI: 10.1103/PhysRevA.53.2443.

[115] Steven P. Ahlen. “Theoretical and experimental aspects of the energy loss of relativistic heavily ionizing particles”. In: *Reviews of Modern Physics* 52.1 (Jan. 1980). Publisher: American Physical Society, pp. 121–173. DOI: 10.1103/RevModPhys.52.121.

[116] S. P. Ahlen and K. Kinoshita. “Calculation of the stopping power of very-low-velocity magnetic monopoles”. In: *Physical Review D* 26.9 (Nov. 1982). Publisher: American Physical Society, pp. 2347–2363. DOI: 10.1103/PhysRevD.26.2347.

[117] *ICRU Report 49, Stopping Power and Ranges for Protons and Alpha Particles – ICRU*. URL: https://www.icru.org/report/stopping-power-and-ranges-for-protons-and-alpha-particles-report-49/ (visited on 09/02/2025).

[118] H. Bichsel. “Shell corrections in stopping powers”. In: *Physical Review A* 65.5 (Apr. 2002). Publisher: American Physical Society, p. 052709. DOI: 10.1103/PhysRevA.65.052709.

[119] H. H. Andersen and J. F. Ziegler. “Hydrogen. Stopping powers and ranges in all elements”. In: (1977). URL: https://inis.iaea.org/records/nex01-8ea67 (visited on 09/02/2025).

[120] J. Lindhard, M. Scharff, and H. E. Schioett. “Range concepts and heavy ion ranges (notes on atomic collisions, II)”. In: *Kgl. Danske Videnskab. Selskab. Mat. Fys. Medd.* Vol: 33: No. 14 (Dec. 1962). Institution: Originating Research Org. not identified. URL: https://www.osti.gov/biblio/4153115 (visited on 09/02/2025).

[121] J. Lindhard. “the THE properties of a gas of charged particles”. In: *Kgl. Danske Videnskab. Selskab Mat.-fys. Medd.* Vol: 28, No. 8 (Dec. 1953). Institution: Univ. of Copenhagen, Denmark. URL: https://www.osti.gov/biblio/4405425 (visited on 09/02/2025).

[122] J. P. Biersack and J. F. Ziegler. “The Stopping and Range of Ions in Solids”. In: *Ion Implantation Techniques*. Ed. by Heiner Ryssel and Hans Glawischnig. Berlin, Heidelberg: Springer, 1982, pp. 122–156. DOI: 10.1007/978-3-642-68779-2_5.

[123] James F. Ziegler and Jochen P. Biersack. “The Stopping and Range of Ions in Matter”. In: *Treatise on Heavy-Ion Science: Volume 6: Astrophysics, Chemistry, and Condensed Matter*. Ed. by D. Allan Bromley. Boston, MA: Springer US, 1985, pp. 93–129. DOI: 10.1007/978-1-4615-8103-1_3.

[124] James F. Ziegler, M. D. Ziegler, and J. P. Biersack. “SRIM – The stopping and range of ions in matter (2010)”. In: *Nuclear Instruments and Methods in Physics Research Section B: Beam Interactions with Materials and Atoms*. 19th International Conference on Ion Beam Analysis 268.11 (June 2010), pp. 1818–1823. ISSN: 0168-583X. DOI: 10.1016/j.nimb.2010.02.091.

[125] *James Ziegler - SRIM & TRIM*. URL: http://www.srim.org/index.htm (visited on 09/03/2025).

[126] "56 - On the energy loss of fast particles by ionisation". In: *Collected Papers of L.D. Landau*. Ed. by D. Ter haar. Pergamon, Jan. 1965, pp. 417–424. DOI: 10.1016/B978-0-08-010586-4.50061-4.

[127] P. V. Vavilov. "Ionization Losses of High-Energy Heavy Particles". In: *Sov. Phys. JETP* 5 (1957), pp. 749–751.

[128] Hans Bichsel. "Straggling in thin silicon detectors". In: *Reviews of Modern Physics* 60.3 (July 1988). Publisher: American Physical Society, pp. 663–699. DOI: 10.1103/RevModPhys.60.663.

[129] Glenn F. Knoll. *Radiation detection and measurement*. 4th ed. Hoboken, N.J: John Wiley, 2010.

[130] "XCOM: Photon Cross Sections Database". In: *NIST* (Sept. 2009). Last Modified: 2024-08-14T11:59-04:00. URL: https://www.nist.gov/pml/xcom-photon-cross-sections-database (visited on 08/27/2025).

[131] Kramida, A., Ralchenko, Yu., Reader, J., and NIST ASD Team. *NIST Atomic Spectra Database (ver. 5.9)*. 2021. URL: https://physics.nist.gov/asd (visited on 08/08/2025).

[132] M. J. Berger et al. *Binding energy table*. 2010. URL: https://xdb.lbl.gov/Section1/Table_1-1.pdf (visited on 08/08/2025).

[133] *Caracteristic X-rays*. URL: https://physics.nist.gov/PhysRefData/XrayTrans/Html/search.html (visited on 08/08/2025).

[134] A. G. Karydas and T. Paradellis. "A study of silicon escape peaks for X-ray detectors with various crystal dimensions". In: *AIP Conference Proceedings* 475.1 (1999), pp. 858–861. URL: https://aip.scitation.org/doi/abs/10.1063/1.59058 (visited on 08/08/2025).

[135] *Escape Peak*. URL: https://cxc.harvard.edu/cal/Acis/Cal_prods/matrix/notes/Fl-esc.html (visited on 09/08/2025).

[136] "Stopping-Power & Range Tables for Electrons, Protons, and Helium Ions". In: *NIST* (Oct. 2009). Last Modified: 2024-10-11T12:05-04:00. URL: https://www.nist.gov/pml/stopping-power-range-tables-electrons-protons-and-helium-ions (visited on 08/26/2025).

[137] Claude Leroy and Pier-Giorgio Rancoita. *Principles of radiation interaction in matter and detection*. Singapore: World Scientific, 2011. DOI: 10.1142/5578.

[138] E. Helgemo. *Study of Deexcitation Intensities to the K-Shell in Iron 55*. 2022.

[139] M. M. Bé et al. *Table of Radionuclides (Vol. 3)*. 2006.

[140] M. Šuljić. "Characterisation of Monolithic Active Pixel Sensors for the upgrade of the ALICE Inner Tracking System detector". In: (2013).

[141] M. M. Bé et al. *Table of Radionuclides (Vol. 2)*. 2004.

[142] *X-ray Data for the Elements*. URL: https://xraydb.xrayabsorption.org/element/ (visited on 09/12/2025).

[143] "X-Ray Transition Energies Database". In: *NIST* (July 2009). Last Modified: 2024-10-11T12:08-04:00. URL: https://www.nist.gov/pml/x-ray-transition-energies-database (visited on 09/12/2025).

[144] Elettra Sincrotrone Trieste. URL: https://www.elettra.eu/it/index.html (visited on 05/08/2024).

[145] Instrumentation and detectors lab. URL: https://www.elettra.eu/lightsources/labs-and-services/instrumentation-and-detectors-lab/welcome-to-instrumentation-and-detectors-laboratory.html (visited on 09/13/2025).

[146] Vittorio Di Trapani et al. "Speckle-based imaging (SBI) applications with spectral photon counting detectors at the newly established OPTIMATO (OPTimal IMAging and TOmography) laboratory". In: *Journal of Instrumentation* 19.01 (2024), p. C01018. DOI: 10.1088/1748-0221/19/01/C01018.

[147] A.C. Thompson. *X-ray Data Booklet*. Lawrence Berkeley National Laboratory, University of California, 2009. URL: https://xdb.lbl.gov/ (visited on 08/08/2025).

[148] *GSI*. URL: https://www.gsi.de/en/start/news (visited on 08/08/2025).

[149] *Technology Computer Aided Design (TCAD) — Synopsys*. URL: https://www.synopsys.com/manufacturing/tcad.html (visited on 10/13/2025).

[150] *Sentaurus™ Structure Editor User Guide*. 2024.

[151] *Sentaurus™ Device User Guide*. 2024.

[152] Matthew Daniel Buckland. "Simulation and evaluation of HV-CMOS pixel sensors for the CLIC vertex detector". PhD thesis. Liverpool U., 2018. URL: http://cds.cern.ch/record/2633983 (visited on 03/14/2024).

[153] *https://garfieldpp.web.cern.ch/documentation/UserGuide.pdf*. URL: https://garfieldpp.web.cern.ch/documentation/UserGuide.pdf (visited on 01/29/2025).

[154] Miljenko Suljic. "Study of Monolithic Active Pixel Sensors for the Upgrade of the ALICE Inner Tracking System". PhD thesis. Trieste U., 2017. URL: https://cds.cern.ch/record/2303618 (visited on 03/14/2024).

[155] Omar Abdelrahman et al. *Characterisation of the first wafer-scale prototype for the ALICE ITS3 upgrade: the monolithic stitched sensor (MOSS)*. arXiv:2510.11463 [physics]. Oct. 2025. DOI: 10.48550/arXiv.2510.11463.